Étude numérique de la formation de domaines dans les biomembranes : des vésicules biphasiques aux récepteurs viraux.

Julie Cornet

Université Fédérale
Toulouse Midi-Pyrénées

THÈSE

En vue de l'obtention du
DOCTORAT DE L'UNIVERSITÉ DE TOULOUSE

Délivré par l'Université Toulouse 3 - Paul Sabatier

Présentée et soutenue par

Julie CORNET

Le 20 octobre 2020

Étude numérique de la formation de domaines dans les biomembranes : des vésicules biphasiques aux récepteurs viraux.

Ecole doctorale : **SDM - SCIENCES DE LA MATIERE - Toulouse**

Spécialité : **Physique**

Unité de recherche :
LPT-IRSAMC - Laboratoire de Physique Théorique

Thèse dirigée par
Manoel MANGHI et Nicolas DESTAINVILLE

Jury

M. Pierre SENS, Rapporteur
Mme Ana-Sunčana SMITH, Rapporteure
M. Pierre-Emmanuel MILHIET, Examinateur
Mme Laurence SALOMÉ, Examinatrice
M. Manoel MANGHI, Directeur de thèse
M. Nicolas DESTAINVILLE, Co-directeur de thèse

Remerciements

Il ne sera pas aisé, voire impossible, de dresser une liste de personnes que je souhaiterais remercier par ordre “d'importance”. Je voudrais remercier énormément de monde qui, d'une manière ou d'une autre, consciemment ou inconsciemment, ont participé à ce que cette aventure de thèse soit belle, mais également celles et ceux qui ont joué un rôle dans le fait que je sois arrivée jusque là. Je vais donc choisir d'adopter une démarche chronologique pour ces remerciements ! Il ne va pas s'agir d'un récit biographique depuis ma naissance, rassurez-vous, mais je suis convaincue que c'est grâce à un ensemble d'éléments de sa vie et à diverses rencontres que l'on devient qui l'on est et que l'on fait ce que l'on fait.

Je vais donc commencer par mes parents qui m'ont permis, entre autres, d'avoir une éducation riche et variée depuis le plus jeune âge. Grâce à eux ainsi qu'à ma Mamie Colette et à mon Papy Georgio, j'ai pu visiter nombre de musées et expositions qui ont suscité chez moi un intérêt pour les sciences, et je me rends compte a posteriori de l'importance que cela a eu (d'où le métier que je fais à présent). Ils m'ont tous les quatre suivie de près pendant ma scolarité et mes études, en m'accompagnant et m'encourageant, et m'ont transmis leurs goûts pour les mathématiques, la physique, la biologie. Je n'oublierai jamais combien mes grands-parents m'ont aidée avec mes devoirs, de la petite école à... la fin de la licence ! Il y a une époque où des exercices d'algèbre, des révisions d'un partiel de mécanique des fluides et un match de rugby de l'ASM était un samedi après-midi tranquille et classique à Durtol ! À croire qu'ils m'ont également transmis la “fibre enseignante”, tout comme ma Petite Mamie, avec qui j'étais complice, et que j'ai eu la chance de connaître jusqu'à ses 100 ans et de voir heureuse d'avoir été institutrice. J'étais toujours impressionnée lorsque l'on croisait des “mamies” de 70 ans dans la rue qui interpellaient mon arrière-grand-mère, lui disant qu'elle avait été leur maîtresse il y a très longtemps et qu'elles en avaient toujours gardé un bon souvenir ! Plus généralement, je remercie tous les membres de ma famille qui m'ont toujours soutenue dans mes études et dans mes projets, et particulièrement ma Mamie Mado. Elle était de fait moins familière avec mon domaine d'études que mes autres grands-parents issus de ce milieu, mais elle m'a toujours encouragée de tout son cœur et a toujours été fière de moi, et elle aurait été encore plus fière à la fin de ma thèse, bien qu'elle se demandait ce que les chercheurs cherchaient.

Au fil de ma scolarité, au-delà des amis que je n'ai pas quittés pour certains depuis l'école primaire ou le collège, je tiens aussi à remercier mes enseignants, de l'école à la fac, qui, pour beaucoup, ont aussi joué des rôles importants dans mon attrait pour les sciences et ma réussite dans cette voie. Leur travail n'est malheureusement pas reconnu à leur juste valeur bien qu'ils soient d'une importance cruciale par tous les jeunes et future citoyens qui passent par les bancs de l'école ! Je tiens donc à leur rendre hommage et à remercier mes enseignants pour ce qu'ils m'ont apporté ! Je suis également reconnaissante envers mes parents de m'avoir inscrite aux colos “Aventures Scientifiques” avec ma fidèle amie d'enfance Mélanie, dès nos 9 ans et jusqu'au BAFA

et au passage de “l’autre côté de la barrière” ! Là aussi pendant mon enfance, des animateurs géniaux et des ateliers autour des sciences qui sont loins d’avoir été anodins dans l’affirmation de mes centres d’intérêt, et dans mon goût pour l’animation, visiblement ! Enfin, comment ne pas adresser une mention spéciale à Marion, ma fidèle amie et camarade de classe, de la 6ème à la L3 ! Sans notre entraide, notre motivation mutuelle et sa bonne humeur inébranlable, les études en licence de Physique auraient sans aucun doute été plus dures à vivre. Elle a égayé notre quotidien et amené de l’enthousiasme dans le travail ! Je pense également à mes camarades de Peip et de Licence, bienveillants et toujours prêts à aider comme ma chère Lauriane, fidèle binôme de TP. Bienveillants et toujours prêts à aider l’ont été aussi les collègues de labo de mon père que j’avais toujours plaisir à croiser et sur qui j’ai pu compter, et j’aimerais remercier pour cela particulièrement Fabrice, Jérémi et Matthieu, que je n’oublierai pas.

Font ensuite leur entrée les acteurs de mon départ pour Toulouse : Sebastian dans un premier temps puis Stéphane, Richard et Jacques ! Merci d’avoir consacré tout ce temps à se poser tranquillement avec moi pour me parler du domaine de la physique appliquée à la biologie et du Master Physique du Vivant de Toulouse. Grâce à ça, j’ai retrouvé un goût pour les études et une motivation, que j’avais un peu perdue après mon passage à l’INSA de Lyon. Je remercie mes parents qui m’ont encouragée et m’ont aidée à me remobiliser pour mes études à ce moment-là. J’en profite au passage pour remercier du fond du cœur les amis que j’ai rencontrés lors de cette année compliquée à Lyon, qui se sont montrés d’un soutien incroyables, comme une deuxième famille, et que j’espère revoir tous un jour, en France, en Espagne, en Colombie ou ailleurs !

Il faut à ce stage remercier Manoel (qui reviendra bien sûr par la suite) qui ne me connaissait pas encore et qui a eu la patience de répondre à mes montagnes de questions concernant le Master PV alors que j’hésitais à m’y inscrire. Il a apparemment su me convaincre puisqu’à la rentrée suivante, je quittais mon Auvergne natale et posais mes valises à Toulouse, ville qui nous faisait rêver lorsque l’on était ado avec mes fidèles amies et camarades de stade Pauline et Astrid, et où je n’avais au final toujours pas mis les pieds. Mes montagnes de questions, ce sont mes nouveaux “petits camarades” de Master, comme les appelait Nicolas, qui n’ont pas tardé à les découvrir en cours. Là aussi et encore plus que jamais, la bonne entente et l’entraide entre les étudiants a été plus que déterminante dans ces deux années intenses. Il me faut remercier Hadrien, Fanny, Diego et Lyne pour leur amitié et collaboration en M1, et Charlène et Christine, sans qui les TP de chimie n’auraient en aucun cas pu être drôles (ni compréhensibles) et m’auraient probablement faite fuir. L’année de M2, je crois que l’on peut dire que nous l’avons réussie tous ensemble, et je remercie infiniment Hadrien pour toute l’aide, la patience et l’humour qu’il nous a apportés ainsi que Romain pour tout le temps passé ensemble à travailler et papoter, toujours dans la bonne humeur ! Je souhaite que notre belle amitié ainsi que notre désormais traditionnel voyage annuel se poursuivent ! Ce master m’a réellement beaucoup plu et intéressée, c’est pourquoi j’ai toujours remercié Stéphane, Richard et Jacques de m’avoir permis de le découvrir. Mais au-delà de ça, c’est pour leur bienveillance et les échanges toujours extrêmement riches que je les remercie, que ce soit en cours ou en dehors, tout comme l’ensemble de la “team Roffiac” ! Les discussions avec cette belle équipe sont toujours très enrichissantes, je regrette d’avoir manqué de temps durant

la thèse pour y prendre plus part, mais je sais que l'on se retrouvera pour de nouveaux projets !

On se rapproche des années de thèse et je vais donc arriver aux acteurs principaux de celle-ci. L'histoire a commencé en M1, lorsque, visiblement pas effrayé par mes montagnes de questions, Manoel m'a proposé de faire un stage avec lui et Nicolas. C'était un stage de 2 mois seulement, non obligatoire. On pourrait penser que c'est très court et peu important. Pour moi, ce stage a été extrêmement important et même déterminant. J'ai pu découvrir le travail de recherche, à l'interface entre la physique et la biologie, encadrée par une super équipe de personnes en blouse, Raïssa, Loïc et Sophie pour le côté "bio" que je remercie énormément pour tout ce qu'ils m'ont apporté en stage et pour leur encadrement intéressant et leur accueil, ainsi que les membres du plateau d'imagerie et du CPTP. Ce stage m'a permis de pratiquer concrètement l'analyse de données, la modélisation, l'interdisciplinarité, et de confirmer mes goûts pour celles-ci. Sur le plan humain, ce stage m'a également beaucoup apporté, puisque j'ai découvert et beaucoup apprécié le travail (et les temps de pause) avec Nicolas et Manoel, un duo complice et complémentaire ! Je ne peux que les remercier de m'avoir donné cette opportunité et de m'avoir fait confiance dès le M1. Rien n'était écrit, mais avant même le M2, j'avais déjà en tête le fait que j'avais envie de réaliser mon stage de M2 puis ma thèse avec cette équipe. J'ai été très heureuse de constater que c'était visiblement réciproque lorsqu'ils m'ont proposé le stage puis le sujet de thèse. De plus en plus intéressée par les problématiques d'organisation des biomembranes et m'entendant très bien avec l'équipe, je ne pouvais qu'avoir envie de me lancer dans cette aventure ! Manquait une chose importante : le financement... mais nous n'avons rien lâché et avons fini par l'obtenir ! Je suis très reconnaissante, encore une fois, envers Jacques qui a tout fait pour m'aider à obtenir une bourse de thèse pour ce sujet pour lequel il avait compris mon intérêt. C'était donc parti pour 3 ans de plus sur cette thématique et dans cette équipe !

Un élément clé dans mon appropriation du sujet et du code a été l'accompagnement de Guillaume qui, bien que très occupé après sa thèse, a consacré énormément de temps au passage de témoin avec patience et je lui en suis extrêmement reconnaissante ! Je tiens sincèrement à remercier tous les membres du LPT et plus généralement de l'IRSAMC pour leur accueil dans le labo. Depuis le M1, en tant que fille et jeune, et donc minoritaire dans cet "écosystème physicien", j'ai toujours été très bien accueillie, respectée et considérée et je me suis toujours sentie à ma place, et rapidement "comme à la maison". Je ne pourrai pas citer tous les membres, mais je suis extrêmement heureuse d'avoir connu bon nombre de personnes du 3R1 durant ces 4,5 années, et la bienveillance et la bonne mentalité de toutes ces personnes ont indéniablement participé à rendre cette expérience très positive. Je sais qu'il n'en est pas toujours de même dans tous les labos et je m'estime chanceuse d'avoir pu évoluer dans un tel environnement. Le bâtiment est certes vieux et moche, mais l'habit ne fait pas le moine ! Je me dois tout de même de mentionner Bertrand, directeur du labo qui m'a particulièrement bien accueillie et qui a soutenu mes démarches. Comment ne pas parler de Malika ? La "maman" des doctorants (et parfois de certains permanents), si attentionnée et serviable, et toujours là pour nous aider lorsque nous étions perdus devant des procédures administratives, pour nous plus difficiles à comprendre que des lignes de code. Et toujours là tout simplement pour participer à la bonne humeur et bienveillance

générale du labo ! Merci également à Patricia pour son accueil chaleureux à l'IRSAMC pendant toutes ces années ! Enfin, on ne pourrait tout simplement pas faire notre travail de recherche sans la personne de Sandrine, notre informaticienne extrêmement compétente et disponible, toujours là quand on avait besoin d'assistance technique (souvent !), et également là pour partager des moments conviviaux et des pauses thé "entre filles". Merci aussi à David qui n'était pas "sensé" m'aider mais qui l'a toujours fait lorsque j'étais coincée, et qui était bien présent également pour les moments conviviaux ! Merci à tous les membres du 3R1 pour les discussions intéressantes et sympathiques à la cantine du CNRS ou à la cafet autour de Jean-Marc et de ses oiseaux !

Être à l'interface entre deux disciplines, cela permet de rencontrer des personnes variées et de différents labos ! Encore une fois, depuis le M1 et jusqu'à la fin de la thèse, je remercie tous les membres de l'IPBS qui m'ont bien accueillie et avec qui j'ai pu avoir des interactions riches, je pense notamment à Laurence, Catherine, Evert, Fabrice, et bien sûr Adrien, Guillaume et Matthieu, avec qui j'ai eu grand plaisir à travailler (et à partir en conférence à Madrid !). Je remercie tous les membres de mon jury qui ont accepté d'en faire partie dans un contexte sanitaire plus que compliqué et qui se sont adaptés aux conditions pour la soutenance, et en particulier Pierre-Emmanuel Milhiet qui a bien voulu être le président de mon jury. Grâce à lui, j'avais pu participer à ma première école d'été au début de ma thèse, une expérience très enrichissante sur le plan scientifique et également sur le plan humain. J'avais d'ailleurs rencontré ma copine et "camarade de conf" et de thèse à distance, Pauline, que je remercie pour sa complicité durant le reste de la thèse ! Je remercie aussi Marie Brut et Jean-François Georgis qui m'ont fait confiance et donné la chance de vivre mes premières expériences en tant qu'enseignante, un exercice que j'ai beaucoup apprécié ! Au-delà de l'enseignement, j'ai eu la chance de découvrir pendant la thèse les aspects de médiation scientifique. Grâce à des personnes comme Pierre Bonnefond, les membres de la Compagnie du Code, ou encore Tania et Nicolas de Délires d'Encre, j'ai pu m'immerger dans ce domaine, et je les remercie pour leur confiance et pour les discussions et expériences riches ! Merci à mes directeurs de thèse d'avoir compris que j'avais une passion pour ces activités et de m'avoir permis de les concilier avec la thèse. C'est grâce à tout cela que j'ai pu trouver ma voie vers mon "avenir post-thèse".

La thèse, tout le monde le sait, c'est une aventure humaine. Il y a l'équipe officielle qui est très importante et pour laquelle j'ai été gâtée, mais il y a également l'équipe "officieuse", sur qui il est important de pouvoir compter ! Et sur ce plan-là non plus, je n'ai pas été déçue. De mon M1 à la fin de ma thèse, j'ai connu plusieurs "générations" de doctorants et de post-docs et presque toujours le même constat : des personnes sur qui on peut compter lorsque l'on a besoin d'aide dans le travail et également dans la vie hors du labo ! On ne travaillait pas sur les mêmes sujets, mais dès que l'un avait besoin d'aide, un autre arrivait avec des astuces de code, un calcul, ou tout simplement une discussion. Ils savent combien je les remercie pour tous ces moments, Benjamin Senior et Junior, Olivier, Maxime(s), Bertrand, mes camarades de bureau et de thèse Jojo et Huhu, Nicolas, Francesca, Annaël, Théo, Yassir, Faedi, Claire, Julie, Adrien, Gaby, Natnat..., ainsi que les "jeunots", Nico et Thibault, et tous les stagiaires et étudiants de PV tels que Sruthi, Anaïs et Carole qui sont passés contribuer quelques mois à la bonne humeur

et à la richesse du groupe ! Bravo à Nico et Nelly d'avoir, chacun à leur manière, repris joliment le sujet en stage et bon courage pour la thèse / le M2. Dès le début, malgré son air ronchon probablement dû à son grand âge, Benjamin Senior était là pour m'aider lorsque, petite étudiante de M1, je n'arrivais pas à ouvrir Mathematica. Je garderai le souvenir de moi en train de me propulser dans le bureau sur ma chaise à roulettes vers lui pour aller lui poser une question et lui de me renvoyer à l'expéditeur lorsqu'il avait fini de m'expliquer. Les grandes discussions autour d'un chaï (en Français) et petites discussions en Russe avec Junior resteront aussi de bons souvenirs tout comme les sorties balades, concerts, crêpes, Quai des Savoirs... Spasibo bol'shoye Natalia (ou Huguette par adoption) pour tous les bons moments partagés en rentrant du cours de Russe, à la salle de sport ou en voyage, et pour les discussions autour de la thèse aidant à garder la motivation ! S'il fallait être proportionnel, il me faudrait écrire des pages entières pour remercier Olivier pour tout ce qu'il a fait pour moi pendant la thèse. Des heures à m'aider à débeuguer des codes (même mon LaTeX de ce manuscrit en SAV alors qu'il n'était même plus au labo !) à m'aider à réfléchir à mes problèmes, et à me faire découvrir des outils techniques qui m'ont énormément apporté et qui me serviront dans le futur. Mais c'est aussi tous ces moments partagés en dehors du travail, le vendredi soir à 22h à attendre que l'un ou l'autre ait fini de lancer ses jobs pour le weekend, les balades à vélo avec les racines, les joggings avec les ragondins, et les sorties, expos et restau avec l'équipe des "jeunes du LPT", autant de moments qui resteront de chouettes souvenirs des années de thèses !

Also big thanks to Alasdair, qui a eu la gentillesse et la patience de m'aider pour certaines tournures de phrases en anglais dans ce manuscrit et de répondre à toutes mes questions sur la grammaire anglaise, qui se montre parfois aussi étrange que lui !

Enfin, pendant tout ce temps-là, il a été toujours présent pour moi et m'a soutenue dès que j'en avais besoin. Merci à mon compagnon, Ben, qui partage ma vie depuis maintenant presque 6 ans, qui a dû me supporter pendant la thèse (et surtout pendant un confinement et une rédaction combinés !) et qui a dû dire pendant 4 ans combien il trouvait jolies "mes vésicules" qui étaient en réalité pour lui "des boules bleus et rouges biscornues toutes pareilles". Il a toujours été à mes côtés et c'est aussi grâce à ça que je me suis sentie bien pendant ces années.

Je ne remercie par contre pas Annaël (humour) d'avoir eu l'idée de me proposer un chaton de 2 mois mal sevré, trouvé abandonné dans son jardin, en plein mois d'août 2020 et en pleine fin de rédaction de thèse ! Cette boule de poils dénommée Buzz a vite pris ses habitudes dans son nouveau chez lui et a décidé de consacrer ses journées à dormir sur moi alors qu'il faisait 39 degrés ou à insérer des caractères spéciaux dans mon fichier .tex en marchant sur mon clavier (ou encore à se coincer dans un arbre à 7 mètres de haut pendant que je préparais ma soutenance). Mais il a égayé cette période et continue de le faire aujourd'hui !

Si vous avez lu ces remerciements jusqu'ici, je pense que vous aurez compris que cette thèse a été pour moi une aventure plus que positive et je suis sincèrement heureuse de l'avoir menée. Si cela a été si positif, c'est grâce à tout ce que j'ai mentionné ci-dessus, mais tout cela a été rendu possible par mes 2 directeurs de thèse que je remercie du fond du cœur. Vous avez été un peu mes "papa et maman" de thèse, toujours extrêmement disponibles.

Manoel, même si je n'étais pas la meilleure étudiante du Master, que j'étais plus intéressée par le numérique, que je n'étais pas aussi fan d'analytique que tu l'aurais aimé, et que j'étais supportrice de Clermont, tu m'as fait confiance depuis le stage de M1, tu as su m'apprécier pour les qualités que j'avais, et on a appris à se comprendre toujours mieux au fil des années. J'ai grandement apprécié travailler avec toi en tant que physicien mais également côtoyer la personne très gentille et intéressante que tu es !

Nicolas, dès le M1, les projets numériques et les TP de biomembranes étaient mes matières préférées, pour le sujet en lui-même et pour ta manière d'enseigner, et en découvrant ta personnalité, j'ai très vite compris qu'on allait bien s'entendre ! J'ai beaucoup apprécié ta franchise, ta simplicité, ton humour, et ton impressionnante capacité à toujours voir à ma tête ce que j'avais compris ou non ! Ton enthousiasme pour la recherche et ta bonne humeur sont apparemment contagieux, cela m'a apporté beaucoup de motivation pour ce travail.

Pendant toutes ces années, on a bien travaillé mais aussi bien rigolé tous les 3 et je n'oublierai pas les bons moments passés à la cantine ou à la cafet, et la manière dont vous m'avez accueillie pleinement dans l'équipe dès le début alors même que je n'étais "qu'une stagiaire de M1". Les autres doctorants étaient taquins et moqueurs de notre complicité, mais je dirais que c'est parce qu'ils étaient jaloux ;) Vous êtes de très bons scientifiques mais ce sont aussi vos qualités humaines qui font que votre équipe avance si bien, et pendant ma thèse j'ai avancé avec la motivation suscitée par l'intérêt pour mon sujet mais aussi celle générée par l'idée d'apporter à cette équipe que j'aimais tant. Je suis très heureuse d'avoir pu participer à un bout de chemin avec vous sur la compréhension des mécanismes des biomembranes, et, même si je vais m'éloigner de ces dernières, j'espère sincèrement continuer à vous recroiser pour que vous me donniez des nouvelles de vous et de "mes vésicules" !

Numerical study of patterning in biomembranes: from bicomponent vesicles to virus receptors.

Julie Cornet

Ph.D. supervisors: Manoel MANGHI and Nicolas DESTAINVILLE

Defense date: 10/20/2020

Laboratoire de Physique Théorique de Toulouse (LPT)
CNRS, Université Paul Sabatier

Contents

Introduction

Contents

Biological membranes

The plasma membrane [Alb+02] forms a selective barrier for the cell, yet its role goes far beyond a mere frontier delimiting the cell interior and exterior. Indeed, it plays a crucial role in biological functions [BS18] such as cell adhesion, signalling, transport of solutes, viral and bacterial infection or immune response. In eukaryotic cells, it is made up of a lipid bilayer (amphiphilic molecules, mainly phospholipids, sphingolipids and cholesterol) which features various inclusions made of peripheral or integral proteins that can represent up to 50% of its mass. Glycolipids and glycoproteins are also important membrane components (see Fig. 1). In this work we focus on eukaryotic mammalian cell membranes, plant or prokaryotic ones being even more complex systems. Eukaryotic cells are typically 10 μm or more in diameter [Nel13], their surface can then be estimated at around 300 μm^2 and their volume at 500 μm^3.

The surface occupied by a lipid in the membrane depends on the lipid type. The average area per lipid is 0.72 nm^2 for DOPC and 0.63 nm^2 for DLPC [BS18], for example. With an approximate area per lipid value of 1 nm^2, a 10 μm diameter vesicle membrane can then contain up to $\sim 10^9$ lipid molecules. The lipid bilayer thickness is on the order of a few nanometers, making it a quasi-two-dimensional object at the cell scale. It also directly depends on the lipid composing the membrane. For example, a pure DOPC membrane is measured to be 2.68 nm thick and a pure DLPC one, 2.09 nm [BS18]. Lipid mixtures have been shown to present in mammalian cells two main distinct phases, termed liquid-disordered (Ld phase, cholesterol-poor) and liquid-ordered (Lo phase, cholesterol-rich) [KA14; Mou05; Mar09; Sch17] that undergo phase separation [CL95; Onu02; VK05; HVK09] for a specific composition range and below $T \sim 20 - 30°C$ depending on the nature of the lipid mixture, as it was already understood in the 1980's [Ips+87]. The minimal requirement for such liquid phase coexistence seems to be a ternary mixture of low- and high-melting temperature lipids, and cholesterol [Heb+10]. For instance, a DOPC/DPPC/chol mixture with composition 2:1:1 is miscible above approximately 30°C and

phase separates below [VK03]. Notably the more ordered phases are typically 1 nm thicker than the disordered ones [Ceb+18].

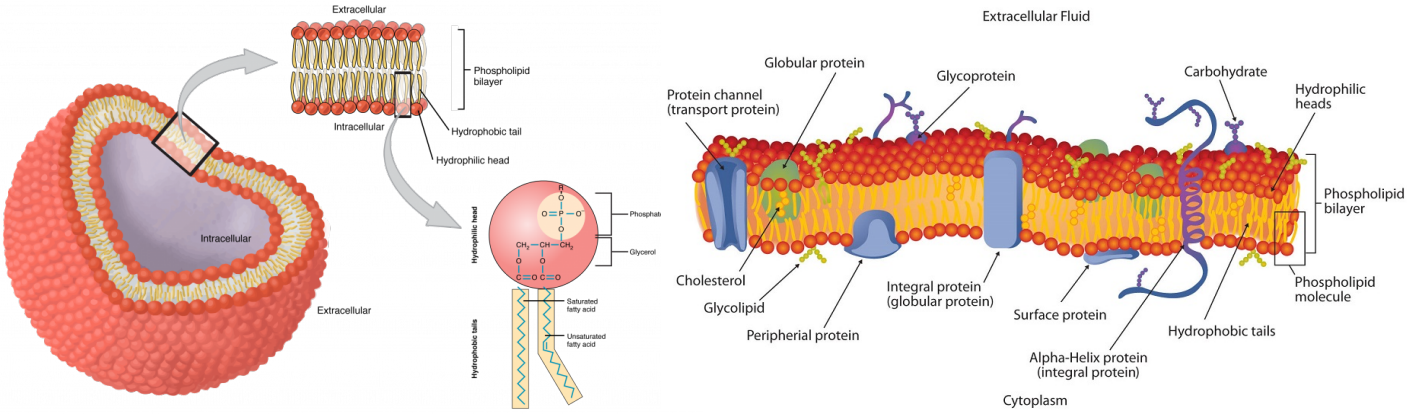

FIGURE 1 – **Left:** Lipid vesicle. Lipids are amphiphilic molecules with hydrophilic heads and hydrophobic tails that spontaneously assemble into enclosed bilayers or vesicle [Big+20], minimizing contact between water and the hydrophobic tails. **Right:** Biological membrane composed of two lipid leaflets, cholesterol and peripheral and integral proteins [Wik12].

Membrane component organization into domains or modulated phases

Thanks to recent *in vivo* and *in vitro* experimental developments such as single particle tracking (SPT) [IKK01; Dau+03; Esp+08], fluorescence (or Förster) resonance energy transfer (FRET) [Heb+10; FB01], atomic force microscopy (AFM) [GCS07; Gra+11; Con+13; LM13; WP15; HKP16], super-resolution microscopy techniques (STED, PALM, STORM, SIM, see [Hou+18] and the review [LR10]) or small-angle neutron scattering (SANS) [Heb+13; Nic+15; Use+17b], it has been observed and it is now widely agreed that cell membrane components are heterogeneously distributed, and are generically organized into functional lipid and protein sub-micrometric or nanoscopic domains (nanodomains for short) [Ceb+18], as illustrated in Fig. 2. They form dynamic supramolecular assemblies the size of which ranges from few dozens to several hundreds of nanometers, in which certain lipid and/or protein species are segregated [KA14; JL16; Sez+17]. A common view pictures lipid nanodomains as lipid "rafts" [JMA07; Sez+17; Mou05; VK05; LS10], a consensual definition of which was formulated in 2006 [Pik06]. They are molecular assemblies of nanometric length-scale (10 to 200 nm) enriched in sphingolipids and cholesterol (the above Lo phase) within a "sea" of Ld phase. Their lipid composition can be asymmetric in the two leaflets [KWT09]. Specific proteins are supposed to be targeted to them to perform their biological functions. However, the concept of "raft" remains controversial, especially in living cells [Sch17; VK05; LS10; Hee02; Mun03; Har03; Han06; Pov+08; Les11; KS13; Hon+14; LV16].

Hence cell plasma membranes are now seen as patterned two-dimensional systems, but the physico-chemical mechanisms accounting for these observations are not consensual today [Les11; LV16; Sch17; DMC18]. In particular the reason why membrane domains are as small as dozens of

nanometers is still matter of debate. Phase separation is a widespread phenomenon in biomembranes, that helps to concentrate locally particular lipids and/or proteins and thus permits the creation of specialized membrane platforms needed to perform specific cellular processes. However phase separation solely cannot account for the small size of these domains and some other ingredients need to be introduced to understand the mechanisms leading to this membrane patterning. These domains have proven to be key players in the above-mentioned biological functions. It is then clear that the understanding of their formation is a central point.

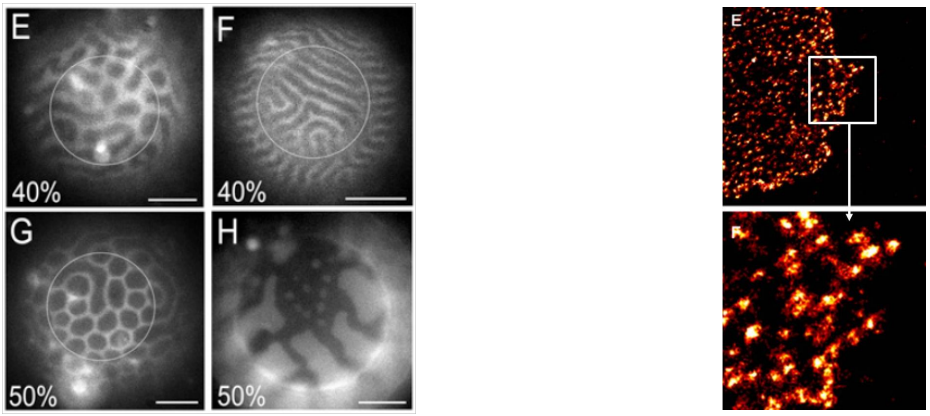

FIGURE 2 – **Left:** Different patterns observed in GUVs at room temperature (fluorescence microscopy). Images drawn from [GAF13] The composition ratio DSPC/(DOPC+POPC)/CHOL is 0.283/0.45/0.267 and the percentage given is the DOPC/(DOPC+POPC) ratio. Scale bars are 10 μm. **Right:** Clusters of transmembrane proteins (LFA-1) in T-lymphocyte cell membrane (super resolution dSTORM microscopy). The square zoom side length is about 1 μm. Courtesy of Raïssa Houmadi.

State of the art and objectives of the present work

Using statistical physics tools, we study biomembranes as complex dynamic systems with a mesoscopic approach. Based on a previous Ph.D. work by Guillaume Gueguen [Gue16], the present work studies one physical mechanism for this membrane organization in a simple model vesicle, combining numerical simulations and analytical tools.

Different simulation scales are available to study biomembranes and their component organization [Ing+16; Mar+19]. At the lower scale, all-atom simulations allow one to study in detail lipid-lipid or protein-lipid interactions with molecular dynamics, but the computation power needed to simulate a system including a large number of atoms is massive. Therefore, these simulations are limited to dozens of nanometers in size and can reach the microsecond as simulation time. They show to be very useful though in studying local membrane component interactions [Wu+14; KK15; MK15]. In a recent study, Singharoy et al. (2019) handled simulations of vesicles on the order of 60 nm with all-atom simulations. In order to study systems with more particles and to be able to simulate larger and longer systems, the hint is to use coarse-grained simulations. In this method, several atoms are combined into a single bead, the interactions are calibrated and motion equations are solved for the beads, significantly reducing the number of particles at play, hence the computation power needed. With this method, one can reach hundreds of nanometers

and simulate up to a millisecond of time. Coarse-grained methods are helpful to study local membrane phenomena involving a patch of membrane such as protein clusters [CDS16; Dun+17; Cha+18] or a rather small vesicle [Lou+10; KKS15; Hol+16]. However, one has to run very long and expensive simulations with these descriptions in order to reach equilibrium to characterize membrane phenomena such as phase separation and membrane patterning. If one wants to tackle the simulations of bigger systems such as vesicles of several micrometers or cells, one needs to use other methods such as the mesoscale and continuous models. In these models, a patch contains up to thousands of lipid molecules and several protein inclusions and the simulation methods study the system in equilibrium [NP95; GGL09; HWL11; AF14; GDM17]. Thus, this latest method allows one to simulate large systems and to reach equilibrium at the expense of molecular details. Ingolfsson et al. (2016) provide an illustration comparing the typical simulation times and sizes of these different methods that we reproduce in Fig. 3.

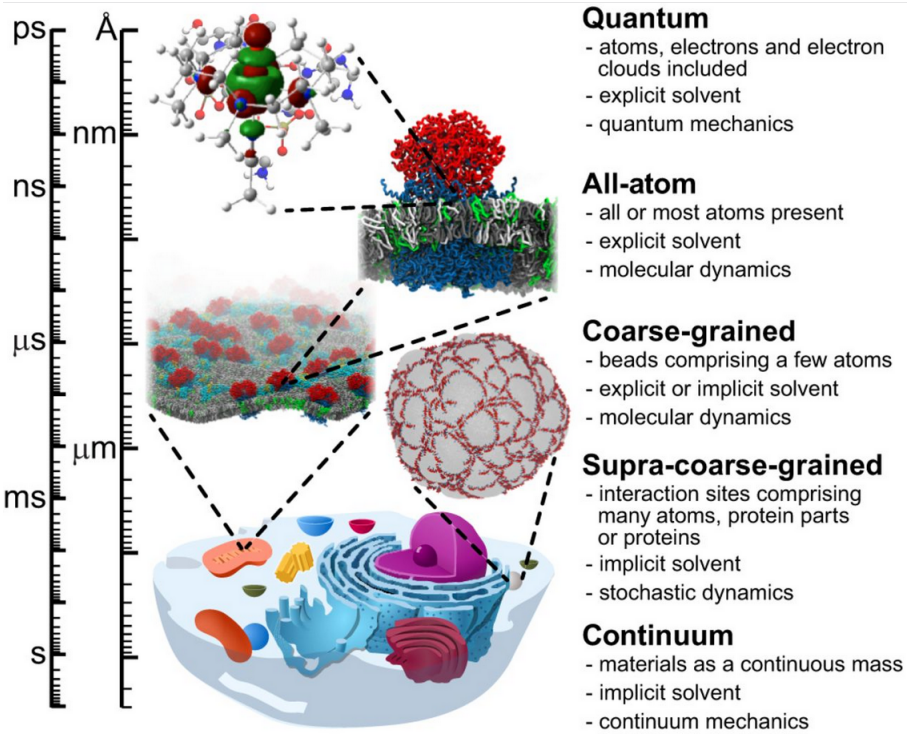

FIGURE 3 – Systems reachable with the different simulation methods in terms of simulation times and system sizes. The figure is taken from [Ing+16].

In my Ph.D., inspired by the works previously conducted in the team, the main object under study is an equilibrated vesicle of several μm of radius on timescales up to several minutes. Hence, to tackle the questions raised above at these length scales, we use mesoscale Monte Carlo simulations. Thanks to our collaboration started during my Master 2 internship with Matthieu Chavent (IPBS, Toulouse) who works on molecular dynamics simulations (notably MARTINI), we also got the opportunity to address these questions at the lower scale and worked on bridging the two scales, in order to propose a mechanism accounting for membrane patterning dwelling on realistic parameters ensuing from lower-scale simulations.

A common general physical mechanism describes patterning in various soft-matter contexts and for a wide range of length scales [SA95]: short-range attraction that drives monomer association competes with weaker, however longer-range repulsion and thermal agitation that counters the segregation and limits the aggregate size. This mechanism gives rise to modulated phases as we term them in this work. In this way, membrane patterning can result from the energy competition between two mechanisms: on one hand, species interactions and intra-species affinity (short-range attraction) leads to phase separation under a critical temperature (the system tends to separate in two distinct phases with a boundary ruled by line tension). On the other hand, this mixture being coupled to membrane shape fluctuations, local symmetry breaking induces energy cost not favorable to large domains since the cost related to membrane elastic energy overcomes the cost in line energy. This leads to the formation of smaller structures which repel each others (long-range repulsion). The symmetry breaking can be generated by local curvature and can occur because of the presence of different lipid species and/or non-symmetric proteins in the leaflets (Fig. 4). The curvature generated can reach 10^{-2} nm^{-1} when the asymmetry arises from lipid composition difference in the leaflets [Ste+20], 10^{-1} nm^{-1} when imposed by glycolipids [Das+18] and up to a few 10^{-1} nm^{-1} when it is imposed by proteins [ZK06; BSL14].

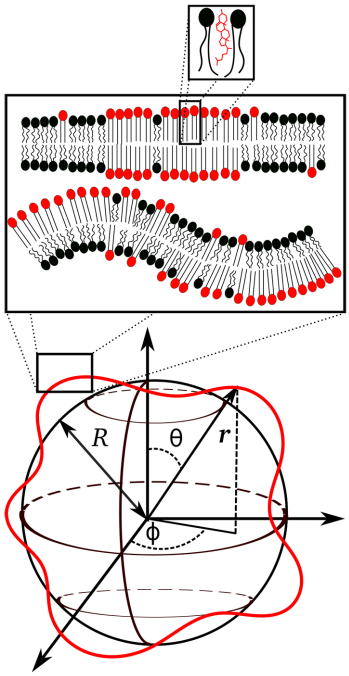

FIGURE 4 – Symmetry breaking in the membrane leaflets leading to domain formation. The figure is taken from [Gue16].

In our model, the elastic properties of the membrane, such as its curvature, its bending modulus, and its surface tension, are taken into account in the Canham-Helfrich free energy [Can70; Hel73]. We describe the energy of species interaction in the frame of Landau's theory. We introduce the composition-curvature coupling by assuming that the local spontaneous curvature and/or the bending modulus directly depend on the local composition as sketched in Fig. 4. The so-obtained coupled model, accounting for both composition and shape fluctuations, was studied analytically by Guillaume Gueguen during his Ph.D. in our research group [Gue16]. He also

developed the numerical tesselated vesicle model used in the present manuscript. My objectives were (i) to couple this tesselated discrete model to a 2D Ising model on the lattice formed by the vesicle vertices, in order to account for the composition-dependent terms of the Hamiltonian; (ii) to confront my numerical observations to the analytical findings; and (iii) to apply this model to situations of experimental interest, in order either to provide a theoretical interpretation to experimental observations, or to predict yet unobserved behaviors of biophysical models or even live cells.

In this model, assumed to be a binary mixture for sake of simplicity, one of the molecular species, named A, imposes a local spontaneous curvature to the elastic membrane while the other species, named B, does not. In biologically relevant situations, A is assumed to be the minority species. When species aggregate below the demixing temperature, A-domains acquire a curved shape. The membrane being under tension, this leads to the increase of the surface tension term in the elastic energy which can eventually make too large domains, and a fortiori macrophases, unstable. This results in an effective long-range repulsion between A-species molecules and to the formation of thinner structures in equilibrium [WD13; DMC18]. This mechanism thus explains the formation of meso-domains or labyrinthine structures (stripes), depending on A-species concentration. An additional interest of such a mechanism is that it remains efficient *above* the demixing temperature, where membrane shape fluctuations stabilize structured composition fluctuations (see Ref. [GDM14] and references therein).

We thus perform Monte Carlo simulations of a bicomponent, tessellated (i.e. triangulated) membrane with two types of degrees of freedom: the vertex displacements and the Ising variables, discretized version of the position and composition fields respectively. These two types of degrees of freedom are coupled since one of the species imposes a local spontaneous curvature to the membrane. We suppose for sake of simplicity that the bending modulus κ_0 is uniform on the whole membrane. We choose $\kappa_0 = 20\ k_\mathrm{B}T$ (where $k_\mathrm{B}T \simeq 4 \times 10^{-21}$ J is the thermal energy at room temperature), a typical value for biomembrane lipids [Mou05; PM15]. The situation where κ_0 also depends on local composition [GDM14; DMC18; DM06] is briefly tackled at the end of this manuscript.

We run simulations for different membrane parameters and study the equilibrium states in terms of membrane shape and component repartition. Domains form for a certain regime of parameters (species affinity, spontaneous curvature, surface tension). Beyond considering the visual results obtained, we compute different observables, such as correlation functions and domain size distributions. We draw phase diagrams to identify the parameter regimes leading to modulated phases in the membrane.

One important interest of our numerical model is that, contrary to alternative models [HWL11; AF14; Pen+15], the area is not locally constrained at the scale of elementary triangles but globally controlled by surface tension and imposed volume [GDM17]. Consequently, the imposed surface tension is known exactly and is not affected by local constraints in an ill-controlled manner. Controlling the surface tension permits the direct comparison with analytical results. Indeed, one of our goals here is to propose a numerical verification of the analytical studies provided for example in Refs. [Lei86; HMI98; KGL99; Sch12; GDM14], which relied upon some approximations. In particular, the Gaussian or mean-field theories studied there were not expected to be valid

below or close to the mixture critical temperature, and we also intend to address the system properties in this case of potential biophysical interest. Note that it is possible to derive some exact analytical solutions below the critical temperature [JLS00], however, this requires to neglect thermal fluctuations and to assume restrictive symmetries.

We recover numerically the phase diagrams predicted by analytical calculations, displaying four characteristic phases: macro-, disordered (or dilute), "structured disordered" (or microemulsion), and "structured ordered" (or meso-) phases. The two last ones are the modulated phases, above and below the demixing temperature, respectively. In addition, analytical predictions are based on the calculation of structure factors that give access to typical wavelengths of modulated phases. However, they do not provide any information on the shape of patterns that can be roundish domains, elongated ones, stripes or even more complex, labyrinthine morphologies. Our numerical simulations can give access to such information, which will be of particular importance below when addressing the effects of protein overexpression on domain shape.

Furthermore, it is our ambition to propose a model able to explain the experimentally observed size of nano-domains on the surface of eukaryotic cells, below the diffraction limit. At a *qualitative* level, we have argued in Ref. [DMC18] that a model based upon the competition between attraction at short range and weak repulsion at longer range likely explains the existence of such nano-domains. Using realistic values of the numerical parameters entering the model, this work will demonstrate that such an approach remains realistic at a *quantitative* level, in vesicles. To our knowledge, this has never been achieved so far in this context.

It is also worth mentioning that at the level of coarse-graining of the model, where an elementary membrane patch represents many molecules, the model embrasses several experimental situations: A-species can either represent a different lipid phase, e.g. liquid-ordered domains in a liquid-disordered sea [Sez+17; HD20], in which some curving molecules can also be incorporated [SIT16]; or an otherwise homogeneous lipid phase locally enriched in some curving proteins. For example, interesting recent experiments by Shimobayashi et al. (2016) show that externally added glycolipids insert preferentially in the Lo phase and the asymmetry that they induce triggers the fragmentation of the Lo macrophase into smaller curved domains. Motivated by these findings and in order to base our mesoscale model on realistic parameters drawn from a lower scale, we perform MARTINI coarse-grained simulations of a patch of membrane of a lipid mixture undergoing Lo-Ld phase separation in which are inserted glycolipids, in the upper leaflet only. We extract membrane parameters from these simulations and connect them to the mesoscale ones.

As already mentioned, our model allows one to study the shape of the emerging domains. In some experiments, it has been noticed that protein domains seemed to be more elongated when the proteins were overexpressed in the membrane, i.e. when their concentration was increased, whereas they were more roundish at basal concentrations. It has notably been observed by Fabrice Dumas and his coworkers (IPBS, Toulouse) in the case of HIV receptors in Single Particle Tracking (SPT) experiments. We develop a quantitative tool based on the computation of the aspect ratio of the domains in order to characterize domain shape and draw a comparison with our simulations so as to propose a mechanism accounting for this phenomenon.

We are also interested by the effect of external forces in the mesocale membrane model.

Motivated by biological cases where forces are exerted on the membrane such as mitosis, we explore their effect on vesicle shape and component spatial rearrangement.

These different aspects of my work will be treated in the successive chapters of the present manuscript, as follows.

Organization of the manuscript

In the first part of the manuscript we present the analytical model used to describe biomembranes and the coupling of their composition to their shape. We then develop the numerical model and the methods used to perform mesoscale and coarse-grained simulations in the second chapter along with the quantitative analysis tools used in this work. We also tackle the numerical tesselation bias that we encountered and detail the method elaborated to correct it, which has been an important part of the work. In Chapter 3, we present the results obtained with our mesoscale model. After studying the role of each membrane parameter, we characterize the parameter sets leading to meso-patterning in the membrane by building phase diagrams. Chapter 4 describes the measurements of simulations at the lower scale, coarse-grained molecular dynamics simulations. We consider a lipid bilayer in which local stronger curvature is imposed by glycolipids (GM1) inserted in the outer leaflet only, an example case of curvature generation corresponding to our mesoscale model, from which we extract membrane parameters and establish the connexion between the two scales. In Chapter 5 we focus on the numerical analysis of the SPT experimental data of our collaborators and their comparison with simulation results concerning domain shape in function of the concentration. We are interested in quantifying the domain shape of HIV receptors when they are more or less expressed in a cell membrane. In the 6^{th} and last chapter, the behavior of bicomponent vesicles with curvature coupling under the application of external forces is explored in the frame of our mesoscale model. We also present the preliminary results of the study of the effect of bending modulus-composition coupling in our model. We conclude by a discussion about the present results and the outlook for the future studies about bio-membrane structuring.

Chapter 1

Membrane modeling

Contents

This chapter is an introduction to the physics of membranes presenting the widespread ways of modeling biomembranes and the corresponding analytical description mainly relying on the previous works carried out by Gueguen et al. (2014).

A model biomembrane can be seen as a bidimensional fluid mosaic and viewed as a surface, ruled by the elastic free energy of its surface and the interaction free energy of its components.

1.1 Elastic free energy

In the Monge gauge, a globally planar membrane can be described by a height function $h(\mathbf{r})$ measuring the distance to a reference plane. The Canham-Helfrich elastic free energy of the membrane is defined as [Can70; Hel73]

$$H_{\text{Helf}} = \frac{1}{2}\int_{\mathcal{A}} \kappa(2H - C)^2 dS + \sigma\mathcal{A} \tag{1.1}$$

over the whole membrane area $\mathcal{A}$. Here $H = \frac{1}{2}(\frac{1}{r_1} + \frac{1}{r_2})$ is the local mean curvature with r_1 and r_2 being the radii of curvature in the principal normal directions. The first term of the right-hand side of Eq. (1.1) is the elastic contribution, with the bending modulus κ, constraining locally the membrane to its preferential or spontaneous curvature C. This local curvature in the membrane can result from leaflet composition asymmetries or the effect of integral or peripheral proteins with particular shapes, as we will discuss it below.

When membrane fluctuations remain small, one can write $H \simeq -\Delta h/2$ in planar geometry. Note that with this sign convention curvature is assumed to be positive when the membrane is convex.

The membrane surface tension is denoted by σ which appears as a Lagrange multiplier controlling the membrane area. An area deformation $\delta\mathcal{A}$ of a surface $\mathcal{A}$ can be written as $\delta\mathcal{A} \simeq \frac{1}{2}(\nabla h)^2\mathcal{A}$ and the ensuing elastic energy associated with surface tension is then $\delta F = \frac{1}{2}\sigma(\nabla h)^2\mathcal{A}$.

In the case of a closed vesicle of interest in this work, the membrane is described by a height function $u(\theta,\varphi)$ measuring the relative distance to a reference sphere of radius R with $\mathbf{r}(\theta,\varphi) = R[1+u(\theta,\varphi)]\mathbf{e}_r$ the position of the membrane. In the case of weak membrane fluctuations, we write $H \simeq \frac{1}{R}[1-u-\frac{1}{2}(\partial_\theta^2 u + \frac{1}{\sin^2\theta}\partial_\varphi^2 u) + \mathcal{O}(u^2)]$ (see for instance [GDM14]). The bending modulus κ typically falls in the 10 to 100 $k_\mathrm{B}T$ interval for biomembranes [Mou05; Sch17; Dim14]. There exist several alternative definitions of the surface tension, coinciding in the high tension limit [GDM17]. It is imposed by external constraints, and cannot exceed the so-called "lysis" tension, on the order of 10^{-2} N.m^{-1} (or J.m^{-2}) for usual lipids such as DOPC from which membrane can tear. Here we consider values of σ on the order of 10^{-8} J.m^{-2} allowing moderate shape fluctuations [BSL14]. The vesicle is then considered to have a quasi-spherical shape fluctuating around the sphere of radius R corresponding to the minimum of surface free energy.

1.2 Species interaction free energy

We consider a membrane made of a binary mixture of two species, A and B, and their corresponding composition fields are ϕ_A and ϕ_B. We note $\phi = \phi_A$ (thus $\phi_B = 1-\phi$). In this part ϕ is constant and does not depend on the position. In the frame of the mean-field Flory theory [Flo53], the free energy of the mixture (interparticle interaction energy and mixing entropy) is written as follows

$$F_\mathrm{Flory} = \frac{\nu}{2}\phi(1-\phi)\left[-J_{AA}+2J_{AB}-J_{BB}\right] + k_BT\left[\phi\ln\phi + (1-\phi)\ln(1-\phi)\right] \tag{1.2}$$

where J_{ij} is the species affinity parameter and ν is the number of neighbors of each molecule. In a simple 2D liquid with approximate local hexagonal symmetry, $\nu \simeq 6$. We call Flory parameter the quantity

$$\chi = \nu\left[J_{AB} - \frac{J_{AA}+J_{BB}}{2}\right] \tag{1.3}$$

arising from molecular short-range interactions (London, van der Waals), lipid-lipid or lipid-protein interactions, notably hydrophobic ones. We can introduce the positive energetic parameter J that favors lipids of the same type being together and disfavors the species mixing with $J_{AA} = J_{BB} = -J$ and $J_{AB} = J$, and we get

$$\chi = 2\nu J \tag{1.4}$$

The mixture has a critical point at $\chi_c = 2k_BT$ and for $\phi_c = \frac{1}{2}$ if T is fixed, that is to say $T_c = \frac{\nu J}{k_B}$ if J is fixed. When $\chi > \chi_c$ ($T < T_c$) the mixture undergoes phase separation and we get two separate phases, one rich in A and the other one rich in B (Fig. 1.1). In this case, one can define the line tension λ which corresponds to the energy cost of the interface per unit length and is proportional to $|T-T_c|^{\nu_c}$ close to T_c with the critical exponent $\nu_c = 1$ in the 2D Ising

universality class [CL95; Hon+08; EPS11]. In the strong segregation limit, the line tension is related to J and χ via $\lambda = 2J/a = \chi/(a\nu)$, a being the lattice parameter. For example, in the strong segregation limit with a line tension of a few pN and a lattice parameter corresponding to 1 nm, $\chi \approx 10 k_B T$ [DMC18]. For $\chi < \chi_c$ ($T > T_c$) the homogeneous mixture is more favorable.

Typical values of realistic lipid mixture transition temperatures range from 0 to more than 60°C, strongly depending on the lipid nature [VK03].

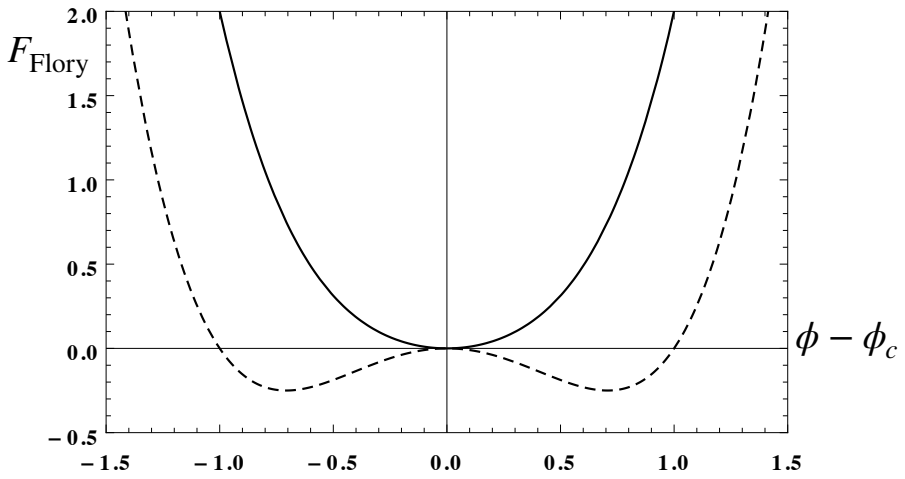

FIGURE 1.1 – Flory free energy with respect to the concentration ϕ, ϕ_c is the critical concentration. For $\chi < \chi_c$ ($T > T_c$, solid line) the homogeneous mixture is more favorable. When $\chi > \chi_c$ ($T < T_c$, dashed line) there are two minima and the system experiences phase separation. Figure adapted from [Gue16].

Alternatively, one can describe the mixture free energy using a coarse-grained field ϕ which is the local average of the composition values on a small patch. The lipid-lipid interactions in the mixture can then be described by the more general Ginzburg-Landau Hamiltonian [CL95]. At the Gaussian order (above the critical temperature T_c), the field theory writes

$$H_{\text{GL}}[\phi] = \int_{\mathcal{A}} \mathrm{d}S \left[\frac{m}{2}(\phi - \phi_c)^2 + \frac{b}{2}(\nabla\phi)^2 \right] \tag{1.5}$$

where $\phi(\mathbf{r}) \in [0, 1]$ is the composition field, and $\phi_c = 1/2$ is the critical composition. The mixture undergoes a phase transition at a critical temperature T_c. The potential $\frac{m}{2}(\phi - \phi_c)^2$ ensures a homogeneous phase for high enough temperatures $T > T_c$ ($m > 0$) and a phase separation for lower temperatures $T < T_c$ ($m < 0$). Close to T_c, the theory "mass" $m \propto k_B(T - T_c)/a^2$ where a is a microscopic (UV) cutoff. The term $\frac{b}{2}(\nabla\phi)^2$ characterizes the energy cost ensuing from the local variation of composition, where b is the so-called stiffness, and gives rise to line tension below T_c. More precisely, this parameter results from the energy cost of the presence of B species in the A phase and vice-versa hence from interactions between these molecules. One can write b as $b = \int_{l_0}^{\infty} \mathrm{d}r V(r) r^4$ and for example, for the van der Waals potential $V(r) = -c/r^6$, c being a constant, one gets $b = c/l_0$ with l_0 the molecule typical size. It weakly varies with T, we thus consider it here as constant with T. Note that below T_c positive terms in ϕ^4 need to be considered in the free energy 1.5 to enable the partition function to converge that would diverge otherwise.

1.3 Composition - shape fluctuations coupling

From a biophysical perspective, we consider that the locally higher curvature of the membrane can either be induced by lipid mixture symmetry-breaking [Mou05; HD20; Ste+20] or be imposed by integral or peripheral proteins [ZK06; BSL14]. In both cases, $\phi(\mathbf{r})$ then measures the local density of the curving molecules, lipids or proteins, that we call A-species in this work. To introduce the coupling between the composition and the membrane curvature, it is usually considered that the local spontaneous curvature and/or the bending modulus are functions of the local concentration, $C(\phi)$ and $\kappa(\phi)$. As a first approximation, one can choose a linear form of the couplings, as in [GDM14]:

$$C = C_0 + C_1\phi \tag{1.6}$$

$$\kappa = \kappa_0 + \kappa_1\phi \tag{1.7}$$

In the present work (except in Section 6.2) we assume that the bending modulus is not dependent on the phase, i.e. $\kappa_1 = 0$. The term C_1 is the difference between the spontaneous curvatures of the two phases, pure A ($C_0 + C_1$) and pure B (C_0) as illustrated in Fig. 1.2. Hence in Eq. (1.1) we include a term accounting for the coupling:

$$\frac{\kappa_0}{2}(2H - C)^2 = \frac{\kappa_0}{2}[2H - (C_0 + C_1\phi)]^2 \tag{1.8}$$

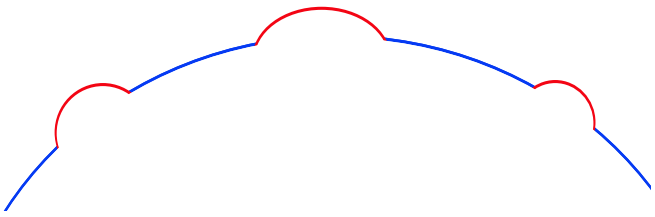

FIGURE 1.2 – The two different species impose different local spontaneous curvatures to the membrane. In this example, the preferred radius of curvature of the blue species is the radius of the reference sphere R, the blue species then have a spontaneous curvature of $C_0 = 2/R$. The red species impose a higher spontaneous curvature than the blue ones, i.e. their spontaneous curvature is higher than $C_0 = 2/R$ and their preferred radius of curvature has a value lower than R. The term C_1 denotes the difference of curvature between the red species and the blue ones so that the red species curvature is given by $C_0 + C_1$. That is the description of the case that is mainly studied in this work.

Developing this square, one gets the coupling term also called "coupling strength": $-\kappa_0 C_1$, and the following expression can then be introduced in the free energy expression to account for the coupling between the fields H and ϕ (see [DMC18]):

$$-\kappa_0 C_1 \int_{\mathcal{A}} H\phi \, \mathrm{d}S \tag{1.9}$$

In addition, developing the square gives a ϕ^2 term that has been discussed in Destainville et al.

(2018) and in references therein to play an important role, even though some authors wrongly neglect it. Indeed, in the two extreme cases $\phi = 0$ and 1 the spontaneous curvature should be respectively C_0 and $C_0 + C_1$.We shall discuss its role again in Section 3.1.1 below.

Finally, in our particular case, we always consider the spontaneous curvature of the majority B-species as being the spontaneous curvature of the sphere of radius R, i.e. $C_0 = 2/R$.

1.4 Bicomponent elastic membrane analytical description

The analytical study of the lipid binary mixture was carried out in [GDM14]. Our case in the current numerical work corresponds to this description with only one composition field ϕ ($\phi - \phi_c$ is noted ψ_- in [GDM14]). In order to study the influence of the different parameters on the formation of modulated phases in the membrane, we will construct a phase diagram. To do so, we will first study the structure factor of the system that provides information about its degree of structure – and also characterizes the amplitude of the response of the local composition to an external perturbation owing to the Green-Kubo theorem as discussed later in Section 6.1. Indeed, when a system features domains, it holds underlying order, i.e. modulated density fluctuations.

We recall that the vesicle is considered to have a quasi-spherical shape being fluctuating around a sphere of radius R. Dimensionless parameters are introduced and presented below, the lengths being divided by the radius R and the energies by $k_\mathrm{B}T$ or κ_0.

TABLE 1.1 – The following dimensionless parameters are used in this manuscript, the lengths being divided by the vesicle radius R. The $\hat{.}$ notation indicates that the energies are divided by the average bending modulus κ_0 whereas the $\tilde{.}$ notation indicates that they are divided by $k_\mathrm{B}T$. The last expression defines a dimensionless parameter α_0.

Parameter	Expression
Spontaneous curvature	$c_0 = C_0 R$; $c_1 = C_1 R$
Bending modulus	$\tilde{\kappa}_0 = \kappa_0 / k_\mathrm{B}T$
Surface tension	$\tilde{\sigma} = \sigma R^2 / k_\mathrm{B}T$; $\hat{\sigma} = \sigma R^2 / \kappa_0$
Ising parameter	$\tilde{J}_I = J_I / k_\mathrm{B}T$ [1] $\hat{J} = 2\sqrt{3} J_I / \kappa_0$
Ginzburg-Landau parameter (mass)	$\hat{m} = m R^2 / \kappa_0$ $= \alpha_0 N (1 - J_I / J_{I,c}) / \tilde{\kappa}_0$

The fixed concentration in A-species in the vesicle is

$$\bar{\phi} = \frac{1}{\mathcal{A}} \int_{\mathcal{A}} \phi(\mathbf{r}) \mathrm{d}S \tag{1.10}$$

By rotational symmetry, the angular correlation function of the composition field fluctuation $\psi = \phi - \bar{\phi}$ is a function of the angle between any two points on the vesicle. It writes (see [GDM14]

1. see Chapter 2 for the definition of J_I.

for further details)

$$\langle \psi(\theta)\psi(0)\rangle = \frac{k_B T}{4\pi\kappa_0}\sum_{l\geq 1}\frac{(2l+1)P_l(\cos\theta)}{M(l)} \tag{1.11}$$

where the P_l are Legendre polynomials [ASR88] and $M(l)$ the coefficient in this basis.

In [GDM14], the total quadratic Hamiltonian $H[u,\phi]$ is written as the sum of 3 contributions:

— $H_{\text{Helf}}[u]$, the Helfrich Hamiltonian describing height fluctuations and membrane elasticity;

— $H_{\text{GL}}[\phi]$, the Ginzburg-Landau Hamiltonian accounting for lipid-lipid (or protein-lipid) interactions in the binary mixture;

— $\delta H[u,\phi]$, the coupling contribution.

In order to write the structure factor, the total Hamiltonian is decomposed in the spherical harmonics basis. The height function u becomes

$$u(\theta,\varphi) = \frac{u_{00}}{\sqrt{4\pi}} + \sum_{\lambda} u_{lm} Y_l^m(\theta,\varphi) \tag{1.12}$$

where $\sum_\lambda = \sum_{l=1}^{l_{\max}}\sum_{m=-l}^{l}$ with $l_{\max}$ the ultraviolet cutoff. The same holds for ϕ, with coefficients ϕ_{lm}. We recall that the spherical harmonics are defined as [ASR88]

$$Y_l^m(\theta,\varphi) = (-1)^m\sqrt{\frac{2l+1}{4\pi}\frac{(l-m)!}{(l+m)!}}P_l^m(\cos\theta)e^{im\varphi} \tag{1.13}$$

where P_l^m are the Legendre functions here defined as

$$P_l^m(x) = \sqrt{(1-x^2)^m}\frac{\mathrm{d}^m}{\mathrm{d}x^m}P_l(x) \qquad (-1\leq x\leq 1). \tag{1.14}$$

$H_{\text{Helf}}[u]$, $H_{\text{GL}}[\phi]$ are written in this new basis, where they are now diagonal quadratic forms, of respective diagonal coefficients $h_{\text{Helf}}(l) = \frac{\kappa_0}{2}[l(l+1)-2]\left[l(l+1)+\hat{\sigma}-c_0\left(2-\frac{c_0}{2}\right)\right]$ and $h_{\text{GL}}(l) = \frac{mR^2+\kappa_0 c_1^2}{2} + Jl(l+1)$. The coefficient of the term $\delta H[u,\phi]$ becomes $\delta h(l) = -\kappa_0 c_1[l(l+1)+2-2c_0]$ that couples the u_{lm} and ϕ_{lm} thus coupling the concentration field and the local curvature. Again in our particular case, we always considered the spontaneous curvature of the major species as being the spontaneous curvature of the sphere of radius R, that is to say $C_0 = \frac{2}{R}$ and $c_0 = 2$. The quadratic Hamiltonian $H[u,\phi]$ can now be integrated on u and we get after simplifications the coefficient $M(l)$ of the total effective Hamiltonian in the Legendre polynomial basis. We have

$$H_{\text{tot,eff}} = \frac{\kappa_0}{2}\sum_{\lambda} M(l)|\phi_{l,m}|^2 \tag{1.15}$$

with

$$M(l) = \hat{m} + \frac{c_1^2\hat{\sigma}}{l(l+1)-2+\hat{\sigma}} + 2\hat{J}l(l+1) \tag{1.16}$$

Note that the vesicle description being isotropic, it is independent of the spherical coordinate φ and $m=0$ in the Y_l^m description. We then only consider

$$Y_l^0(\theta) = \sqrt{\frac{2l+1}{4\pi}}P_l(\cos\theta) \tag{1.17}$$

We compute the following expression for the coefficients in the Legendre polynomials basis when measuring the correlation function $\langle\psi(\theta)\psi(0)\rangle$ in our simulations

$$S(l) = \int_{-1}^{1} g(x)P_l(x)dx = \int_{0}^{\pi} g(\cos\theta)P_l(\cos\theta)\sin(\theta)d\theta \quad \text{with} \quad g(\cos\theta) = \langle\psi(\theta)\psi(0)\rangle \tag{1.18}$$

leading to the structure factor of the composition field ϕ, defined as the coefficient of the Legendre polynomials in Eq. (1.11):

$$S(l) = \frac{k_B T}{2\pi\kappa_0}\frac{1}{M(l)} \tag{1.19}$$

In the following, we fit the structure factors obtained numerically with this expression.

Chapter 2

Numerical methods

Contents

This chapter presents the numerical methods used to simulate membrane systems and the statistical measurements that we used to quantitatively characterize pattern formation in our systems. The first sections (2.1.1 and 2.1.2) describe the discretization of the system in terms of membrane shape and component repartition and is the fruit of the work of Guillaume Gueguen during his Ph.D. The main aspects useful to the understanding of the next chapters are presented here, however one can refer to his manuscript to get all the detailed description [Gue16] as well as the article [GDM17]. My work in the numerical developments begins with the coupling of the two membrane fields, height and composition, and in the collaboration with Matthieu Chavent in order to supplement our mesoscale simulations with MARTINI coarse-grained molecular dynamics simulations at the lower scale.

2.1 Mesoscale Monte Carlo simulations

2.1.1 Discretization of the membrane model

In order to perform numerical simulations, one needs discretized space, time and free energy description. We then consider the vesicle as a tessellated sphere composed of N vertices [GDM17]. On each vertex stands a patch of one of the two species delineated to the Voronoï cell associated to the vertex (Fig. 2.1). The size of this patch, both in terms of diameter and number of molecules, is tunable and depends on the vesicle radius R. In the case of weak shape deformations, the area of a patch A_0 can approximately be written as the area of the reference sphere of radius

R over the number of sites N so that $A_0 \simeq 4\pi R^2/N$. We can get different system sizes N by choosing the number of times that we iterate the subdivision process in the sphere tessellation (see Section 2.1.6 and [GDM17]). As an example, for a simulation with $N = 2562$ sites, in a vesicle of radius 10 μm, a patch contains $\sim 10^6$ lipids.

To create this discretized sphere, an initial icosahedron is tesseled successively. This leads to a restricted list of accessible values for the total number of vertices (see [GDM14]). An important point to notice is that this discretization also leads to a few defects in the structure. Indeed, the coordination number of all the vertices is not equal to 6 for all of them, because of the 12 vertices of the initial icosahedron that only have 5 neighbors. This feature has to be taken into account when computing the local energy (Helfrich or Ising) of a vertex. The numerical issues ensuing from these topological aspects are described in Section 2.1.6.

Helfrich free energy

The elastic free energy in Eq. (1.1) is discretized as follows, with the help of the Laplace-Beltrami operator for the curvature term which is a 3D generalization of the 2D Laplacian operator, here discrete:

$$H_{\text{Helf}} = \frac{1}{2}\sum_i \kappa_0[2H_i - C_i]^2\mathcal{A}_i + \sigma\sum_i \mathcal{A}_i \tag{2.1}$$

with $\mathcal{A}_i$ the area associated to a vertex. The term $2H_i$ is the signed norm of the Laplace-Beltrami operator $\mathbf{K}_i$ (total curvature) computed following [Mey+03] as

$$\mathbf{K}_i = \frac{1}{2\mathcal{A}_i}\sum_j (\cot\alpha_{ij} + \cot\beta_{ij})(\mathbf{x}_i - \mathbf{x}_j) \tag{2.2}$$

where $\mathbf{x}_i$ is the position of vertex i and the sum is taken over the neighbors j of i. The angles α_{ij} and β_{ij} are the angles of the two triangles sharing the edge $\mathbf{x}_i\mathbf{x}_j$ and opposite to this edge. See [GDM17] and Fig. 2.1 for illustration.

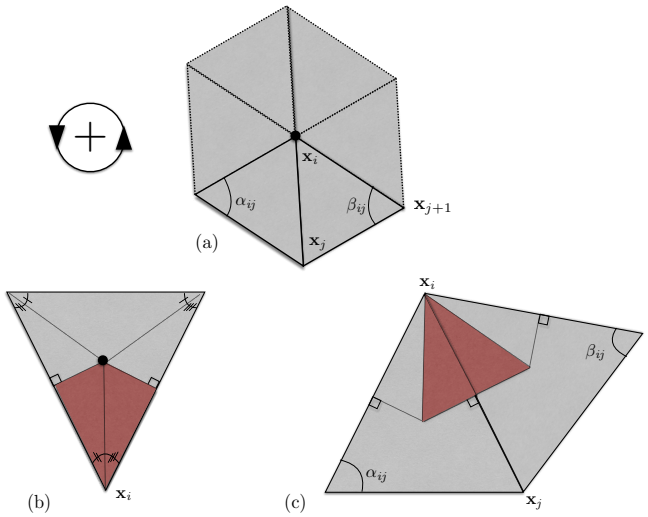

FIGURE 2.1 – Voronoï area associated to a vertex taken into account in the curvature free energy calculation (the sum of the red surfaces of neighboring triangles) and definition of the angles α_{ij} and β_{ij}. Figure from [Gue16].

The uniform bending modulus is set to $\kappa_0 = 20\ k_\mathrm{B}T$, a typical value for biomembranes. In our simulations, the vesicle volume is fixed close to the volume of the initial sphere V_0 by a hard quadratic constraint. By contrast the total vesicle area is constrained by a soft constraint and controlled by the surface tension, acting as a Lagrange multiplier and allowing the surface to fluctuate reasonably:

$$H_\mathrm{c} = \sigma\mathcal{A} + \frac{1}{2}K_v\left(\frac{V}{V_0} - 1\right)^2 \tag{2.3}$$

where $K_v = 2 \times 10^6 k_\mathrm{B}T$. Contrary to other studies [HWL11; AF14; Pen+15] we impose a global constraint on the total vesicle area and do not introduce local constraints on the triangle edge lengths. Such local bounds induce resulting forces on the edges, thus influencing the surface tension and making its value difficult to control while it plays a crucial role in membrane spatial organization [GDM17]. Since we are here interested in weak shape deformations and considering the vesicle in equilibrium, we are not concerned about dynamical aspects and thus allowing edge flipping in the tesselated system is not required. This turns needful if one wishes to study membrane dynamics and large deformations as the ones at play in phenomena such as crumpling [GK95].

In our model, a site of the lattice site is not assigned to a specific patch of lipids. Consequently, the lipid patches are free to diffuse on the lattice as in the usual lattice gas model, accounting for membrane fluidity, and without inducing any shear stress. A comparative image can be found in the sea where some buoys are sometimes anchored and tethered all together in the water, forming a lattice, for example to measure the characteristic of waves. The water is still fluid and able to diffuse freely under them although the buoy network is more static. In a similar way, when simulating membranes in planar geometry (Monge gauge), a square mesh-grid is used, the topology of which remains unchanged throughout the simulation, and no shear stress is believed to ensue.

Note that in order to prevent the vesicle from globally diffusing throughout the Monte Carlo process (see below), its center of position is bound to the origin by a quadratic potentiel [Gue16; GDM17].

Species interaction

The discrete two-dimensional Ising (or lattice-gas) model, very relevant to study phase transition phenomena, is used to describe the binary mixture. It belongs to the same universality class as the Ginzburg-Landau continuous theory in Eq. (1.5) and these two models are equivalent above T_c in the continuous limit [CL95]. Note that it has been experimentally checked in Ref. [Vea+08] that lipids mixtures of interest in this contest indeed belong to the 2D Ising universality class. The discrete Hamiltonian between nearest-neighbor sites on the lattice is:

$$H_\mathrm{Ising} = -J_I \sum_{\langle i,j\rangle} s_i s_j \tag{2.4}$$

where $s_i = \pm 1$. The average composition on any vertex i of the tessellated lattice is $\phi_i = 0$ or 1, related to s_i through $\phi_i = (1 + s_i)/2$. The sum runs on N lattice vertices, most of which have $\nu = 6$ nearest neighbors. The Ising parameter $J_I > 0$ measures the tendency of the species to

demix. It is related to the parameter b of Eq. (1.5) via $b = 4\sqrt{3}J_I$ on a triangular lattice (see below). Note that only the first neighbors come into play, mimicking short range (e.g., van der Waals) interactions between membrane constituents. In our case, we work at fixed concentration, the system is studied in the frame of the canonical ensemble.

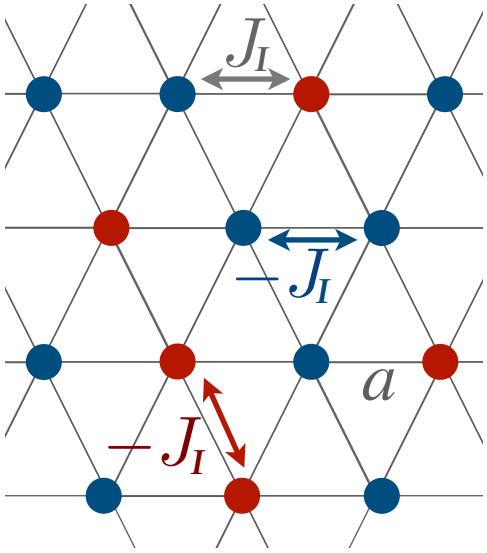

FIGURE 2.2 – 2D Ising model on a triangular lattice of parameter a with J_I the Ising coupling parameter. Blue and red dots respectively represent 0 and 1 composition values ϕ_i. Ensuing nearest neighbors energies are indicated.

Varying the temperature in the simulations of a pure Ising model amounts to tuning the species affinity via the interaction parameter J_I. In our simulations we rather fix the temperature T at room temperature and vary the value of J_I. In this way, the temperature of the fluctuating membrane is kept fixed. For $J_I < J_{I,c}$ (respectively $J_I > J_{I,c}$) we have a disordered (resp. ordered) phase with the critical value $J_{I,c} = (\ln 3/4)k_\mathrm{B}T \simeq k_\mathrm{B}T/3.64$ on an infinite triangular lattice [Bax82]. We introduce the dimensionless Ising parameter varying in our simulations $\tilde{J}_I = J_I/k_\mathrm{B}T$ and then $\tilde{J}_{I,c}^{-1} \simeq 3.64$. We have measured numerically the critical value of $\tilde{J}_I$ by computing the specific heat at $\bar{\phi} = 0.5$ without curvature coupling (pure Ising model), see below. Consistently, it has a maximum at $\tilde{J}_{I,c}^{-1} \simeq 3.62$. Of course it is different from the value found with mean-field $\tilde{J}_{I,c}^{-1} = 6$, the number of first neighbors in a triangular lattice. One can relate m and J_I through $\hat{m} = \frac{\alpha_0 N}{\tilde{\kappa}_0}(1 - \frac{J_I}{J_{I,c}})$ with $\alpha_0 > 0$. A mean-field approximation for α_0 can be drawn from Flory theory [Flo53], $\alpha_0 = 1/\pi$ (see below).

Owing to renormalization issues [AF14], close enough to its critical value, the Ising parameter depends on the coarse-graining level. We denote by

- a the simulation lattice spacing at the mesoscale, $a = (8\pi/\sqrt{3})^{\frac{1}{2}}\, R/\sqrt{N}$,
- $l_0 \sim 1$ nm the typical distance between two lipid molecules,
- $J_{I,0}$ the Ising interaction parameter at the molecular scale, related to the Flory parameter χ via Eq. (1.4).

We assume that the interaction network at the molecular scale can be assimilated to a triangular lattice, owing to the symmetries of bidimensional liquids. Close to the critical point, one gets

$$J_I - J_{I,c} = \frac{a}{l_0}\,(J_{I,0} - J_{I,c}) \tag{2.5}$$

relating the two scales [AF14]. This relation will be useful to relate MARTINI simulation results and mesoscale parameters in Chapter 4. Note that on this lattice $k_{\rm B}(T_c - T) = (4/\ln 3)\,(J_{I,0} - J_{I,c})$, where $T_c - T$ can be measured either in experiments or in molecular dynamics simulations.

The bending modulus κ_0, for its part, depends logarithmically on the scale a [Saf18], and we consider it as constant for sake of simplicity. The renormalization of σ will be tackled in Section 3.3.

We can also make the connection between the parameters of the discrete Ising (lattice gas) model on a triangular lattice, and those of the continuous Ginzburg-Landau theory. The interaction energy between nearest-neighbor sites of the triangular lattice in the Ising model is given by Eq. (2.4) and at the Gaussian order, valid below the critical Ising parameter $\tilde{J}_{I,c}$, the continuous field theory gives Eq. (1.5). In [GDM14] b is denoted by $2J$ (not to be confused with $J_{\rm I}$ above), the factor 2 coming from the fact that there are initially two composition fields, one for each leaflet. The Ginzburg-Landau parameter playing the same role as our m is m_- but we shall denote it as m because they have the same meaning. In [GDM14], dimensionless quantities are introduced, namely

$$\hat{J} \equiv \frac{J}{\kappa_0} = \frac{b}{2\kappa_0} \quad \text{and} \quad \hat{m} \equiv \frac{mR^2}{\kappa_0} \tag{2.6}$$

We want to express these quantities in function of our model parameters. In the tessellation, we consider an elementary triangle of vertices denoted by i, j and k bearing the three compositions ϕ_i, ϕ_j and $\phi_k \in \{0, 1\}$. We identify $\|\nabla\phi\|$ with the slope of the plane defined by the points (i, ϕ_i), (j, ϕ_j) and (k, ϕ_k): $\nabla\phi(x, y) = (-\alpha/\gamma; -\beta/\gamma)$ for the plane of equation $\alpha x + \beta y + \gamma z = C$ with C a constant. We compute its normal vector and get its coordinates, $\alpha = \sqrt{3}(\phi_j - \phi_i)/(2a)$, $\beta = (\phi_j + \phi_i)/(2a) - \phi_k/a$ and $\gamma = -\sqrt{3}/2$ where $a \propto R/\sqrt{N}$ is still the lattice spacing. After a short calculation, one gets

$$\|\nabla\phi\|^2 = \frac{4}{3a^2}\left(\phi_i^2 + \phi_j^2 + \phi_k^2\right)^2 - \frac{4}{3a^2}(\phi_i\phi_j + \phi_i\phi_k + \phi_j\phi_k) \tag{2.7}$$

The elementary triangle has average area $\sqrt{3}a^2/4$. Thus skipping irrelevant squares ϕ_i^2 of trivial integral, we obtain

$$\begin{aligned} \frac{b}{2}\int (\nabla\phi)^2 {\rm d}S &\simeq -\frac{b}{2}\sum_{\text{triangles}} \frac{\sqrt{3}a^2}{4}\frac{4}{3a^2}(\phi_i\phi_j + \phi_i\phi_k + \phi_j\phi_k) \\ &= -\frac{b}{\sqrt{3}}\sum_{\langle i,j\rangle}\phi_i\phi_j, \end{aligned} \tag{2.8}$$

where a factor 2 arises from the fact that each triangle edge belongs to two elementary triangles. Owing to the relation $\phi_i = (1+s_i)/2$, and now skipping irrelevant linear terms, we finally conclude

that $b = 4\sqrt{3}J_{\mathrm{I}}$. It follows that

$$\hat{J} = \frac{2\sqrt{3}J_I}{\kappa_0}. \tag{2.9}$$

Alternatively, we could have used a more rigorous, but more technical, Hubbard-Stratonovitch transformation [Ala+16] to reach the same conclusion.

As far as $\hat{m}$ is concerned, we need the expression of the "mass" m of the Ising model on a triangular lattice, assuming that the 12 sites of coordination number 5 are negligible in the large N limit. The Ising energy is an intensive quantity and thus scales as N. The contribution of m in the Ginzburg-Landau energy is proportional to the surface and then scales as mR^2, with R fixed in our simulations. Combining these scalings implies that m has to scale as N/R^2. In addition, we know that $m \propto (1 - J_I/J_{I,c})$ [CL95]. It follows that $m = \alpha_0\, k_{\mathrm{B}}T\,(1 - J_I/J_{I,c})\, N/R^2$ where $\alpha_0 > 0$ is a non-universal dimensionless coefficient and thus that

$$\hat{m} = \alpha_0 \frac{N}{\tilde{\kappa}_0}\left(1 - \frac{J_I}{J_{I,c}}\right) \tag{2.10}$$

In order to obtain an approximate value for α_0, we expand F_{Flory}/N given in Eq. (1.2) to the second order close to ϕ_c and $J_{I,c}^{-1}$ and identify the prefactor of $(\phi - \phi_c)^2$ in both theories which leads to $\alpha_0 = 1/\pi$. This value is only a rough estimate because this mean-field theory is not rigorous close to the critical point.

Curvature coupling

As explained previously, we write the spontaneous curvature coupling as

$$C_i = C_0 + C_1\phi_i \tag{2.11}$$

with C_i the curvature assigned to a vertex computed with Eq. (2.2). We used the program developed by G. Gueguen to simulate fluctuating vesicles and modified it so to account for membrane composition and its coupling to membrane shape. This model with two distinct states describes a membrane made of only one leaflet or two leaflets containing lipids of opposite spontaneous curvatures in register. We can also consider that it models a lipid bilayer with transmembrane proteins or particular lipids imposing local curvature [SIT16].

2.1.2 Monte Carlo simulations - Metropolis/Kawasaki algorithm

For our numerical simulations we use Monte Carlo method and we have implemented in C language the Metropolis algorithm applied to our system, containing two coupled subsystems: membrane height fluctuations and membrane composition. More precisely, since a system with conserved order parameter $\bar{\phi}$ is considered (the species transformation is forbidden, hence the composition fractions are constant throughout the simulation), we use the Kawasaki algorithm [NB99] for the composition field, which is a special case of the Metropolis one. The method we used for the Monte Carlo simulations is described in details in G. Guegen Ph.D. thesis [Gue16].

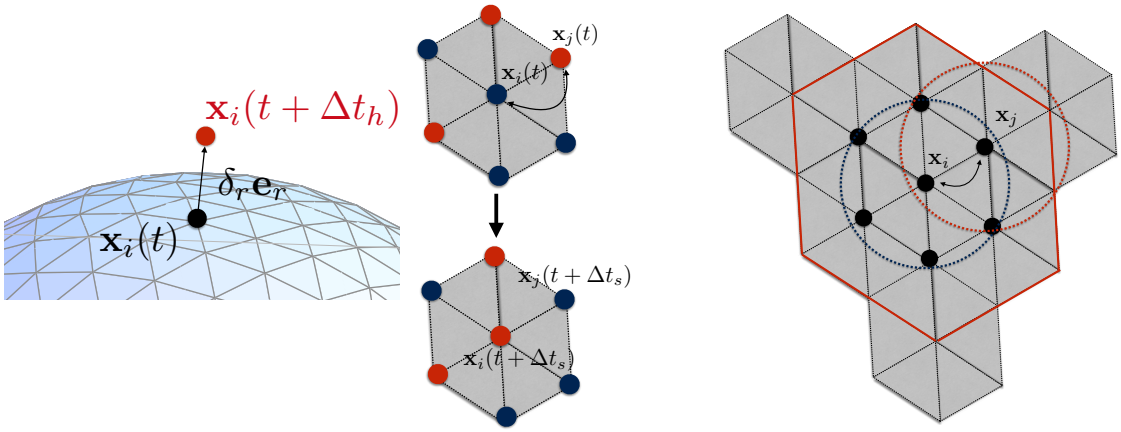

FIGURE 2.3 – **Left:** Metropolis and Kawasaki algorithm local moves. Displacement of a vertex and swap of two vertices composition values. **Right:** The two subsystems of vertices influenced by the different Monte Carlo changes. When the vertex $\mathbf{x}_i$ undergoes a radial displacement, the elastic energy is affected and has to be computed for all the sites included in the red hexagon and on its boundary. When the two composition values of the sites $\mathbf{x}_i$ and $\mathbf{y}_i$ are swapped, the Ising energy is modified and has to be computed for all the sites included in both circles centered in $\mathbf{x}_i$ and $\mathbf{x}_j$. Figures taken from [Gue16].

At each step of the program, two local moves are applied to the vesicle on random vertices: (1) a vertex undergoes a small radial displacement $\pm dr$, which locally modifies the elastic energy; (2) the spin values of two neighbor vertices are swapped, following the Kawasaki prescription, modifying the interaction energy. Figure 2.3 illustrates these two subsystems and the corresponding local moves. The energy difference between before and after these changes is computed $\Delta E = E_{af} - E_{be}$. If $\Delta E < 0$, the move is systematically accepted since it is energetically favorable. If $\Delta E > 0$, the move is going to be accepted with the probability $\mathrm{e}^{-\beta \Delta E} < 1$, reflecting the fact that this change is not energetically favorable but is possible due to thermal energy fluctuations. The iteration of this process converges to the equilibrium three-dimensional conformations of the membrane in terms of shape and component spatial organization (see Fig. 2.4). We used $dr = 0.007R$ as a value for the radial displacement, leading to a reasonable compromise between acceptance rates and simulation times. Considerations about the effects of this value are provided in Appendix B.

One can then study membrane organization according to different sets of input parameters. The concentration $\bar{\phi}$, the curvature coupling c_1, the surface tension $\tilde{\sigma}$ and the Ising parameter $\tilde{J}_I^{-1}$ are the parameters that we vary here and whose combined influence on membrane meso-patterning is studied. We recall that the bending modulus is kept constant when not indicated, set to $\kappa_0 = 20\ k_\mathrm{B}T$.

Triangulating the sphere leads to the construction of triangles of slightly different surfaces (the largest triangles are typically 10% larger than the smallest ones). In our numerical model, the bending energy of a vertex is proportional to the area associated with it [GDM17]. Thus the most curved regions tend to get localized to the smallest triangles, close to the 12 vertices of coordination number 5, which biases the free energy minimisation. We corrected this issue and reduced the main effect by decreasing the triangle area dispersion by a factor ~ 100. However, a slight bias still persists. See Section 2.1.6 for more detailed explanations about this issue.

Note that in our model, since we have no local constraint on individual triangle surfaces,

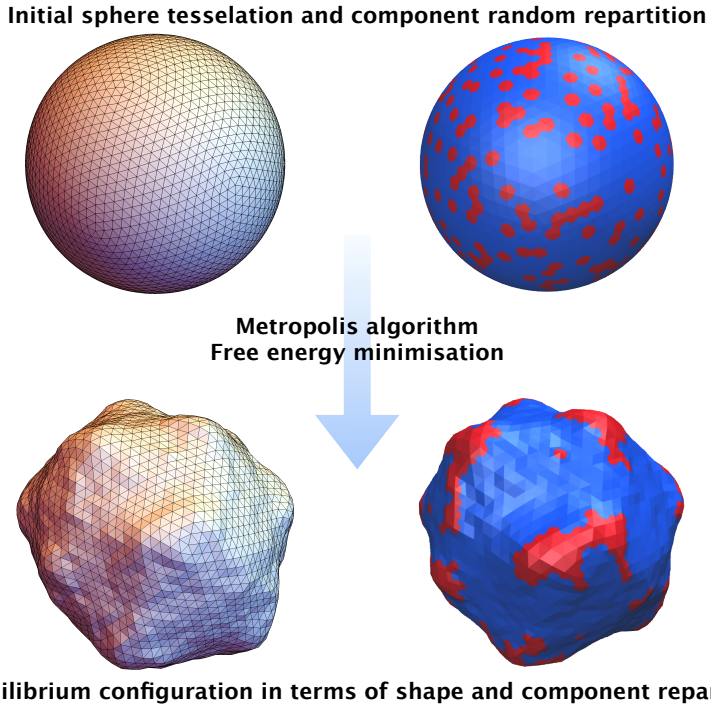

FIGURE 2.4 – Snapshot of a tessellated vesicle before simulation and after (in equilibrium) using the Metropolis/Kawasaki algorithm, showing the membrane height field u (left) and the composition one ϕ (right), A (resp. B) species in red (resp. blue). The algorithm iterations lead to equilibrium state for one set of parameters in terms of shape and species repartition.

one way to minimize the bending free energy when the membrane undergoes strong curvature deformations can result in adopting smaller Voronoï (hence triangle) area (getting closer to the vesicle barycenter). When facing this eventuality, the total A species area is then lower after the free energy minimization than the input fix value $\bar{\phi}$, as if a lipid leakage were at play. However in this work the systems are studied in the canonical ensemble, thus we do not consider membrane component fluxes. We recall that the framework of validity of this work is the case of weak deviations from the reference spherical shape in high surface tension regime. In the following when not specified, we have checked that in the simulations performed, the final A species area was only slightly differing from the imposed concentration. For example in the phase diagram presented in Fig. 3.17 the average ratio of the surface occupied by A species was found to be 0.51 with a dispersion of 1%. In a few systems this is not verified and we then have to be careful in interpreting the results since it is out of the framework of validity of our numerical model (see an example in Fig. 2.5). This can typically occur for low surface tensions and/or high forces (see below).

2.1.3 Force application

In the 6th chapter of this manuscript, Section 6.1, we describe the works carried out with the aim of exploring the effect of external force application on our mesoscale vesicle model. We wrote a version of the program with an external pulling force applied on one vertex or two opposite vertices of the vesicle lattice. To take the force into account in the Monte Carlo simulations, we

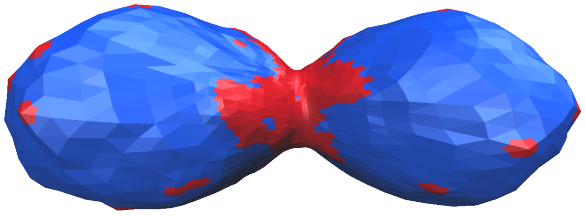

FIGURE 2.5 – Example snapshot of a simulation in which the A species area is not conserved. Here the input concentration is $\bar{\phi} = 0.5$ and the surface ratio of A species is 0.13 at the end of the simulation, thus having decreased by more than 75%. One can note very small red (A) triangles and large blues (B) ones. Other simulations parameters are $\tilde{\sigma} = 300$, $c_1 = 8.0$, $\tilde{J}_I^{-1} = 2.5$ and $\tilde{f} = 100$ (see below for the definition of $\tilde{f}$).

consider the work of the force on a displacement dr. We define the dimensionless applied force as $\tilde{f} = Rf/k_{\mathrm{B}}T$. In the Metropolis random move process on the vertices position, when a site where we apply the force is randomly chosen, we add the potential energy variation associated with the force to the energy variation so that

$$\Delta E = \Delta E_{\mathrm{elastic}} \pm \tilde{f} dr \tag{2.12}$$

where $\Delta E_{\mathrm{elastic}}$ is computed for the elastic energy contribution when no force is applied as described in 2.1.1 and the sign is randomly chosen with equal probability. The force is this way applied outwards the vesicle which is here studied in the f-ensemble (f is fixed). We recall that the vesicle center of position is bound to the origin by a quadratic potentiel acting as the opposing force when applying the external force on one zone of the vesicle only. In that respect, our case is comparable to a theoretical study of a pulling force on a bound vesicle, as it has been done for example in [SSS03].

To prevent the vertices where the force is applied from diverging and getting separated from the rest of the surface in a non-physical way, we apply the force in a distributed manner on a site and on its nearest neighbors. We thus factually apply on these vertices the force per site $\tilde{f}_s = \tilde{f}/(\nu + 1)$, ν being the number of neighbors of the central site.

2.1.4 Model verifications

In this section we present some tests and measurements that were performed on the numerical system described previously in order to validate its behavior before extensively studying the effect of different sets of parameters.

Ising temperature effect without curvature coupling

In this section we focus on the role of temperature of the Ising mixture and on the transition which occurs at its critical value. This is equivalent to studying the effect of J_I as we do further on in this work. As explained above, the lipid binary mixture undergoes a phase transition at a critical temperature T_c with a macrophase separation below T_c and a disordered phase above.

We recall that for a plane Ising system on a triangular lattice, the theoretical value is given by $T_c = 4/\ln 3 \approx 3.64 J_I/k_\mathrm{B}$. At $\bar{\phi} = \bar{\phi}_c = 1/2$, the system undergoes a second order phase transition. We checked that our system was experiencing this expected physical behavior without any coupling as shown in Fig. 2.6.

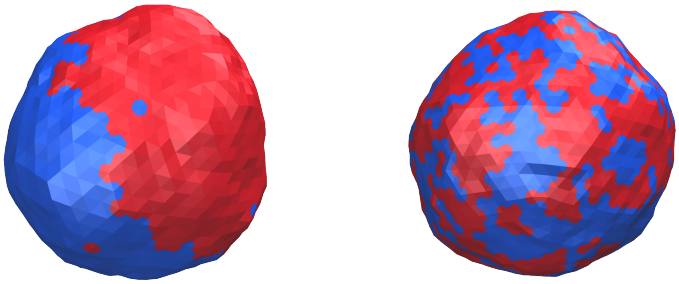

FIGURE 2.6 – Verification of Ising temperature effect on the system below and above $T_c \approx 3.62\, J_I/k_\mathrm{B}$ at $\bar{\phi} = 0.5$ and $\tilde{\sigma} = 300$ with no curvature coupling ($c_2 = c_0 = 2$ i.e. $c_1 = 0$). **Left:** $T = 2.5\, J_I/k_\mathrm{B}$, the system phase separates. **Right:** $T = 5.0\, J_I/k_\mathrm{B}$, the species mix.

When the species fraction differs from $\bar{\phi}_c$, the transition is first order and the transition temperature is expected to be lower (see Fig. 2.7).

Measurements of the different transition Ising temperatures for different concentrations

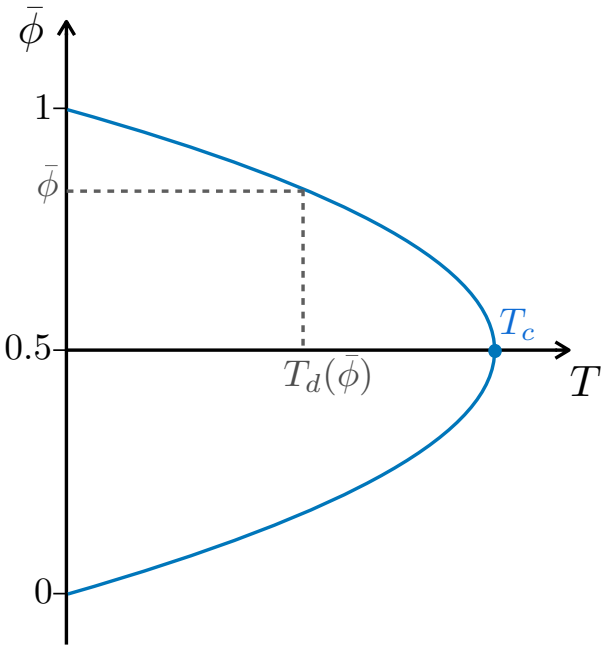

FIGURE 2.7 – Schematic $\bar{\phi}$-T diagram and shape of the transition line (in blue). For $\bar{\phi} < \bar{\phi}_c$ or $\bar{\phi} > \bar{\phi}_c$ with $\bar{\phi}_c = 1/2$ here, the transition is reached at a temperature $T_d(\bar{\phi})$ lower than T_c.

- T_c when $\bar{\phi} = 1/2$:

In our simulations, the measured value of T_c (see below) is slightly different from the theoretical value for an infinite system on a triangular lattice $T_c \simeq 3.64\, J_I/k_\mathrm{B}$ [Bax82]. The first reason for that is that we have a finite system. The second source of error comes from the fact that in our systems, a few vertices have a coordination number of 5 instead of 6 ensuing from the tessellation of the sphere. However, one assumes that this effect becomes negligible in the large N limit.

- T_d when $\bar{\phi} \neq 1/2$:
  For $\bar{\phi}$ varying from 0 to 1, the critical temperature exhibits a maximum at $\bar{\phi}_c = 1/2$. Hence, for $\bar{\phi} < \bar{\phi}_c$ or $\bar{\phi} > \bar{\phi}_c$, the demixing (or transition) temperature is lower than T_c as visible in figure 2.7 and is termed T_d.

Measurement of T_c and T_d :

Then, to check that the value of T_c in our simulations was close to the theoretical one, and to know the value of T_d, we decided to measure them throughout the simulations, via the measurement of the heat capacity C_v of our system. We know that C_v diverges logarithmically at T_c in an infinite system. We have

$$C_v = \frac{\partial E}{\partial T} = \frac{\partial \beta}{\partial T}\frac{\partial E}{\partial \beta} = -\frac{\partial \beta}{\partial T}\mathrm{Var}(E) = \frac{1}{k_B T^2}\mathrm{Var}(E) \tag{2.13}$$

We then implemented the calculation of the variance of the energy related to C_v and computed it for different temperatures around the value expected for T_c or T_d, for Ising systems without any curvature coupling. In the case of a finite system, the plot of C_v over T exhibits a maximum at the critical temperature [NB99], as illustrated in Fig. 2.8.

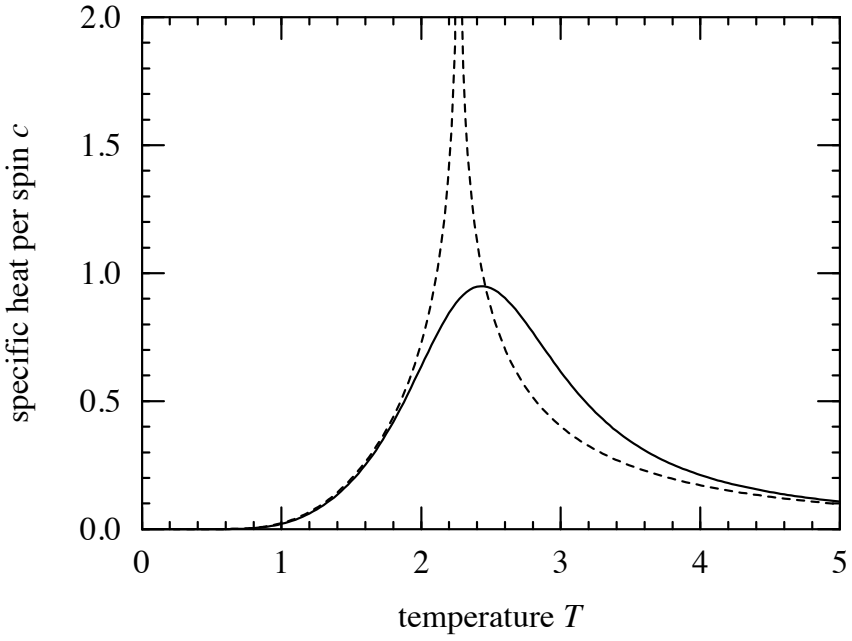

FIGURE 2.8 – Specific heat in function of the temperature. On an infinitely big square lattice (dashed line), the curve diverges at the critical temperature T_c. In a finite-size system (here for a simulation of a 5×5 Ising model on a square lattice in 2D, solid line), the curve exhibits a maximum at $T \simeq T_c$ [NB99].

The fact that we work at fixed order parameter in our simulations (the input numbers of sites of each species are conserved since the composition values can swap between sites but do not transform) implies the formation of macrodomains below T_c and then line tension (proportional to $|T - T_c|$ [CL95]) at the boundaries of these domains. This leads to a non-vanishing term in the derivative of the energy w.r.t. T, that shifts our curve above 0 below T_c as obtained in Fig. 2.9 and contrary to Fig. 2.8 (obtained for a system with a non-conserved order parameter forbidding the formation of macrodomains of the two species below T_c). We found numerically $T_c \approx 3.62 J_I/k_\mathrm{B}$ for the systems with $N = 642$ et $N = 2562$ sites. This method is not very accurate since the shape of C_v around its maximum is not sharp, but we recover a value for T_c close to the theoretical value for an infinite system with no tesselation defect $T_c \approx 3.64 J_I$. As expected, we found a lower value at $\bar{\phi} = 0.2$, $T_d \approx 3.45 J_I/k_\mathrm{B}$ and an even lower one at $\bar{\phi} = 0.1$, $T_d \approx 3.12 J_I/k_\mathrm{B}$ (see figure 2.9). This is consistent with the fact that at $\bar{\phi} \neq \bar{\phi}_c$ the system undergoes a first-order transition at a lower temperature than at $\bar{\phi} = \bar{\phi}_c$ [CL95].

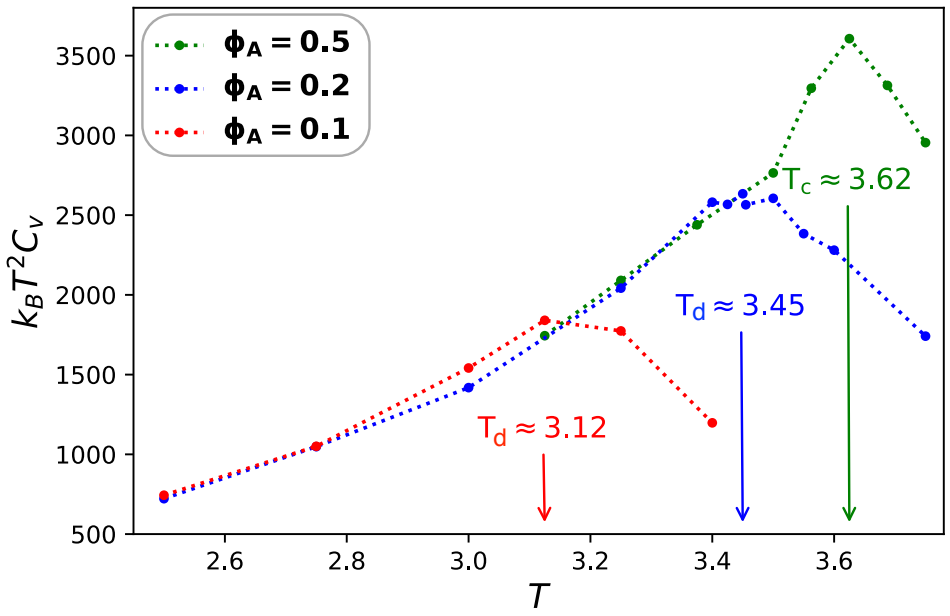

FIGURE 2.9 – Measurement of the transition temperature for different composition fractions via the computations of C_v for a system with $N = 2562$ sites. Here $\bar{\phi}$ is denoted by ϕ_A and the temperatures are in units of J_I/k_B.

2.1.5 Statistical measurements

To compare numerical results to available analytical predictions and experimental data, we regularly compute different observables throughout the simulation, once the system has reached equilibrium. In particular, we measure temporal and spatial correlation functions for the height function u and the composition field ϕ and domain size distribution. This section describes in details the quantitative tools used to analyse the results presented in the following chapters.

Temporal correlation functions

We define the two following correlation functions

$$C_{pos}(\tau) = \langle u(r,t)\, u(r,t+\tau)\rangle - \langle u\rangle^2 \tag{2.14}$$

$$C_{compo}(\tau) = \langle \phi(r,t)\, \phi(r,t+\tau)\rangle - \langle \phi\rangle^2 \tag{2.15}$$

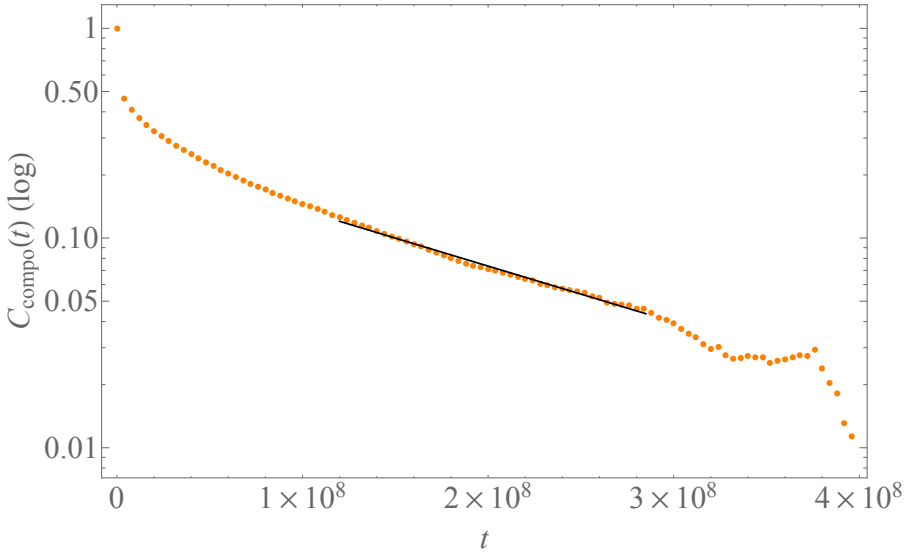

FIGURE 2.10 – Temporal correlation function (log scale) fitted with a linear expression to estimate the correlation time, here $\tau_c \approx 1.6\times10^8$ MC steps. The simulation parameters are $\bar{\phi} = 0.5$, $\tilde{\sigma} = 300$, $c_1 = 3.0$ and $\tilde{J}_I^{-1} = 3.0$. The measurement is noisy at large t, we thus do not fit this part of the curve.

By fitting the temporal correlation functions, we can extract an equilibrium time for both concentration and height fields, which is also the correlation time of the system. We measured correlation times to be typically 10^8 Monte Carlo (MC) steps for both shape and composition fields for a system of $N = 2562$ sites. For high $\tilde{J}_I$ (low Ising temperatures) and low coupling c_1, we checked that the dynamics is slow. Indeed, once a macrophase is formed, the macrocluster exchanges elements with the surrounding dilute phase by Ostwald ripening process only and diffuses slowly [CL95]. In our simulation timescale, this macrocluster cannot explore the whole vesicle area. However, we are not interested in describing the domain diffusion phenomena at these large time scales. We rather focus on the equilibration of cluster size distributions and structure factors as discussed below. We wait about $5\tau_c$ to start performing measurements. All the observables computed are measured every $\tau_c/2$ so that we do not miss uncorrelated information. We thus performed simulations of 10^{10} MC steps each so that we have good sampling for the different measured observables, averaged on at least $\sim 10^2$ independent configurations. We also performed some simulations with $N = 10242$ vertices. However, the excessive simulation time required to obtain good sampling for this system size (around one month on a standard processor) restrained us to a few parameter sets only and lower statistical sampling. All the systems studied in this work are in thermodynamical equilibrium.

We are then able to quantitatively study pattern formation and the morphologies obtained once the system has reached equilibrium thanks to spatial correlation functions (or equivalently their Fourier transform) or cluster size distribution. The aim is to extract information characterizing the emerging membrane patterns, such as their typical size, spacing or number.

Spatial correlation functions and structure factors

Information about membrane shape is provided by the spatial correlation function of the height field:

$$C_{pos}(\mathbf{r}_1, \mathbf{r}_2) = \langle u(\mathbf{r}_1, t)\, u(\mathbf{r}_2, t)\rangle - \langle u\rangle^2 \tag{2.16}$$

When $\mathbf{r}_1 = \mathbf{r}_2$, $\langle u^2\rangle - \langle u\rangle^2$ measures what is termed the rugosity of the membrane.

We compute "lipid-lipid" spatial correlation functions as defined in Eq. (1.11) that provide information about the degree of order in the equilibrium configurations of the system and the typical wavelength of the potentially emerging pattern. For cluster phases, the first peak width reflects domain size and the following oscillations characterize domain spacing [BT16]. When the system is disordered, the correlation function behaves as a decreasing exponential and when the system is phase-separated it decreases regularly from positive to negative values.

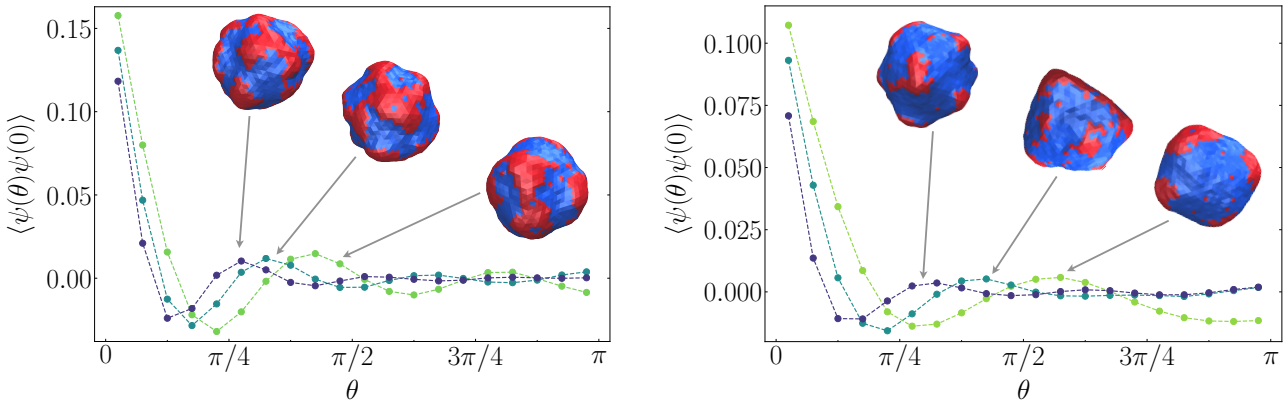

FIGURE 2.11 – Spatial correlation functions at $\bar{\phi} = 0.5$ (left) and $\bar{\phi} = 0.2$ (right) and corresponding system snapshots. The typical pattern wavelength of the system can be identified with this observable. For example here at $\bar{\phi} = 0.2$ for $c_1 = 3.0$ it is approximately 0.6π corresponding roughly to 25 lattice sites and for $c_1 = 6.0$ it is 0.3π corresponding to 12 sites. Other parameters are $\tilde{\sigma} = 300$, $\tilde{J}_I^{-1} = 2.5$ and varying c_1 values. Color lines are guides to the eye.

To have an estimate of the measurement error on the correlation functions, we ran the simulations with exactly the same parameters but different seeds and considered the amplitude of the difference between the corresponding curves. We checked that the results were very similar and that the errors affecting our measurements were relatively low, on the order of the symbol size, except at very high $\tilde{J}_I$ (see Section 3.1.3).

From the composition field correlation function $\langle\psi(\theta)\psi(0)\rangle$, we compute the structure factor $S(l)$ following Eq. (1.18). Note that the physical maximum value $l_{\max}$ of l, related to the UV cut-off satisfies $(l_{\max}+1)^2 = N$ in order to have the same number of degrees of freedom in both direct and reciprocal spaces [GDM14]. For $N = 2562$ it gives $l_{\max} = 49$. In practice the integral Eq. (1.18) is discretized because the correlation function $\langle\psi(\theta)\psi(0)\rangle$ is also discretized.

If the structure factor has a maximum for the first mode $l = 1$, which corresponds to the soft mode $q = 0$ in the planar case ($R \to \infty$) since $\tilde{q}^2 = (Rq)^2 = l(l+1) - 2$ [GDM14], and then decreases monotonously with l, the system is disordered (Fig. 2.12, top-left). For low c_1 in Eq. (1.16), $M(l)$ is almost quadratic in l, which leads to a decreasing exponential correlation function with correlation length $\sqrt{2\hat{J}/\hat{m}}R$. This is the expected Orstein-Zernicke behavior for the structure factor in the disordered phase [CL95]. The excitation of the mode $l = 1$ is also maximum in the macrophase case when one hemisphere is rich in A-species and the other one in B (Fig. 2.12, bottom-left). This corresponds to a divergence of $S(l)$ at $l = 1$ in an infinite-size system. Since we consider a finite-size system, we cannot get any divergence but a maximum of large amplitude in our case. Thus for a finite-size system $S(l)$ has a maximum at $l = 1$ in both cases, disordered and macrophase states. To distinguish them, we decided to consider the ratios of amplitude between the first two modes $\rho = S(1)/S(2)$ and assumed that for $\rho \gg 1$ the structure factor corresponds to macrophase separation and for $\rho \sim 1$ to a disordered phase.

When $S(l)$ exhibits a second maximum for a value $l^* \neq 1$, it is the signal of an underlying structuration, i.e. a modulated phase. The maximum is given by

$$l^*(l^*+1) - 2 = \tilde{q}_c^2 = c_1\sqrt{\frac{\hat{\sigma}}{2\hat{J}}} - \hat{\sigma} \tag{2.17}$$

as discussed in Ref. [GDM14]. The typical inter-domain distance is then $L = 2\pi R/l^*$ [BT16]. This case corresponds to the so-called structured disordered phase (or microemulsion), as described in the Introduction, where composition fluctuations are stabilized by curvature coupling, as illustrated in Fig. 2.12, top-right. Theoretically, another phase has been defined [GDM14; Sch12; SS13], termed structured ordered (or mesophase, visible in Fig. 2.12, bottom-right) defined by the divergence of the structure factor for $l^* \neq 1$. They show well-defined patterns with boundaries ruled by line tension. Again in our case, since we perform numerical simulations of a finite-size system, we cannot observe any divergence and these two phases can hardly be distinguished in practice. Note that this effect is also captured in the computation of C_v in the case of no coupling. As explained in Refs. [GDM14; DMC18], the structured disordered phases appear at large c_1 and small enough $\tilde{J}_I$, because the gain in bending energy is larger than the cost in line energy when creating patterns. The maximum of the structure factor is obtained for a non-zero value of $\tilde{q}^2$ (i.e. $l^* > 1$), when $\tilde{q}_c^2 > 0$, which defines the threshold coupling value c_1^* (see Ref. [GDM14]):

$$c_1 > c_1^* = \sqrt{2\hat{J}\hat{\sigma}} \tag{2.18}$$

signalling the onset of phase modulation. This will be discussed below when exploring phase diagrams. Examples of borderline cases are provided in Fig. 2.13, where it is difficult to distinguish between disordered phase and macrophase (left) and between mesophase and macrophase (right).

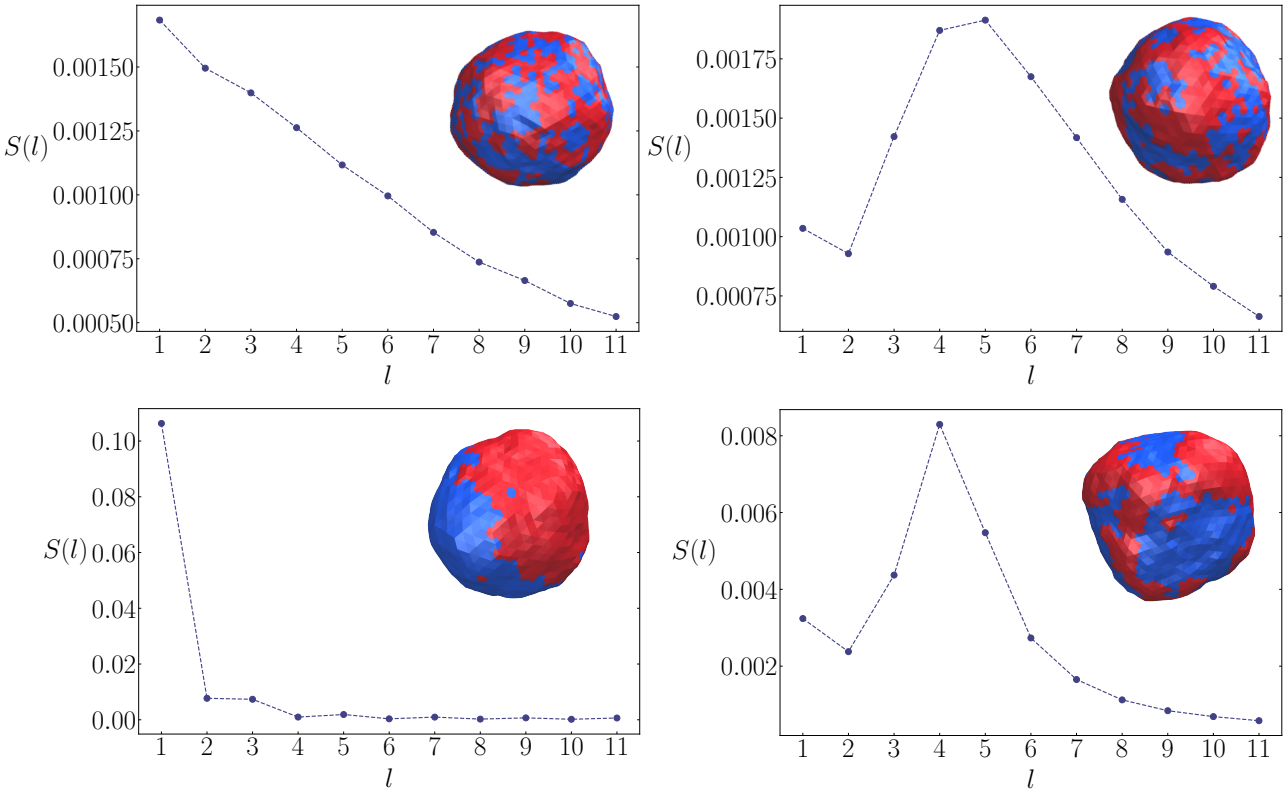

FIGURE 2.12 – Structure factors and corresponding system snapshots. **Top-left:** $c_1 = 0.5$, $\tilde{J}_I^{-1} = 5.0$. Disordered system, where the mixture is homogeneous and features no underlying order. **Bottom-left:** $c_1 = 0$, $\tilde{J}_I^{-1} = 2.5$. Macrophase system, in which the lipid mixture undergoes complete phase separation into two macrophases. **Right:** $c_1 = 3.0$. Modulated phases showing patterns. Upper-right, "Structure disordered" phase ($\tilde{J}_I^{-1} = 4.0$). Lower-right, "Structure ordered" phase ($\tilde{J}_I^{-1} = 3.0$). Other parameters are $\bar{\phi} = 0.5$ and $\tilde{\sigma} = 300$ for all figures.

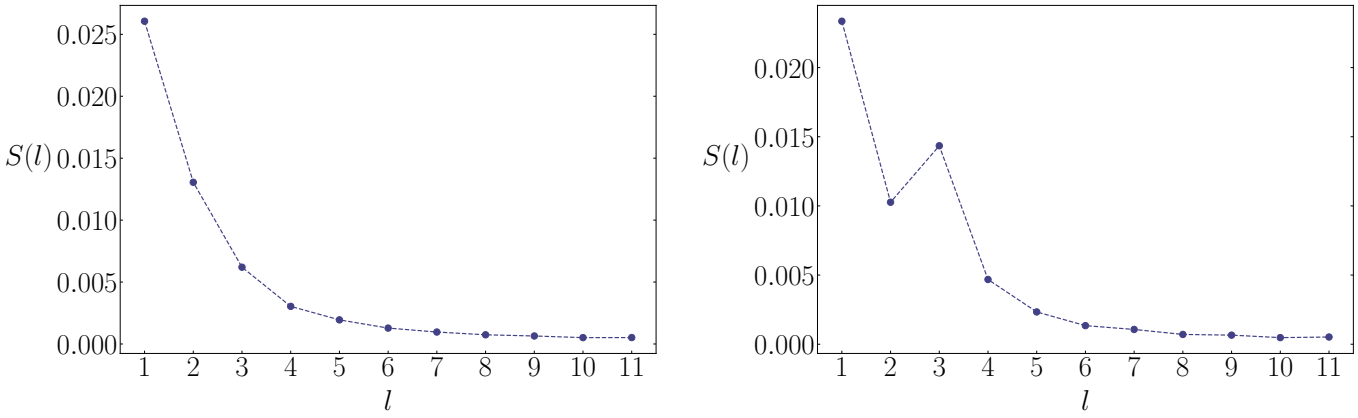

FIGURE 2.13 – Examples of borderline cases at $\bar{\phi} = 0.5$ and $\tilde{\sigma} = 300$. **Left:** $c_1 = 1.0$ and $\tilde{J}_I^{-1} = 3.5$. The decrease between the maximum in $l = 1$ and the value for $l = 2$ is soft with $\rho \approx 2$. **Right:** $c_1 = 2.0$ and $\tilde{J}_I^{-1} = 3.0$, the species mix. The structure factor exhibits a second maximum in $l = 3$ lower than the first maximum in $l = 1$ but of comparable height.

Measurements in the case of force application

In Chapter 6 we are also interested in computing the correlation function between the height field and the composition in an unperturbed system. This function is noted $C_{\{u,\phi\}}(\gamma)$ and is

computed between two randomly chosen sites labelled i and j forming an angle γ such as

$$\gamma = \mathrm{acos}(\cos\theta_i \cos\theta_j + \sin\theta_i \sin\theta_j \cos(\varphi_i - \varphi_j)) \in [0, \pi] \tag{2.19}$$

The correlation function $C_{\{u,\phi\}}(\gamma)$ is then given by

$$C_{\{u,\phi\}}(\gamma) = \langle \phi(\theta_i, \varphi_i) u(\theta_j, \varphi_j) \rangle - \langle \phi(\theta_i, \varphi_i) \rangle \langle u(\theta_j, \varphi_j) \rangle \,. \tag{2.20}$$

To investigate the force application effect on the membrane shape and composition we also compute the angular membrane height and the angular concentration with respect to a "pole". What we term "pole" in the following is one of the vertices on which we apply the force. We define the angular composition function as:

$$s(\gamma) = \langle \phi(\gamma) \rangle - \bar{\phi}$$

where γ is the angle between the "pole" and the vertex where the field is measured, and $\bar{\phi}$ is still the mean A species concentration. In the computation of this function, the site j is chosen randomly but the site i is fixed and is one of the sites on which the force is applied. The equivalent measurement is done for the membrane height field, $u(\gamma)$.

In Chapter 6 we compare this measurement under force application to the above-defined correlation function between the height field and the composition with the aim of attesting the linear response of our system.

Cluster detection and size distribution

We can also characterize the emerging domains in terms of number and size. Cluster detection analysis is performed in order to compare cluster size distributions only for low enough $\bar{\phi}$ to have well-defined disconnected domains termed "clusters". We recall that at high concentration domains merge into labyrinthine structures percolating through the vesicle, as visible in Fig. 3.2 below, upper right-most vesicles. Hence above $\bar{\phi} \approx 0.5$, mesophases and macrophases are hardly distinguishable using the sole cluster size distribution since the onset of percolation is equal to $1/2$ on a triangular lattice [SA94]. At $\bar{\phi} = 0.2$, we implemented a depth-first search (DFS) algorithm in order to identify the different clusters and to index their size in units of number of sites as illustrated by Fig. 2.14.

As it is visible in the figure, the clusters coexist with a population of low-density, dispersed monomers and small multimers, the so-called gas phase. The clusters continuously exchange monomers with this homogeneous gas phase. This can be seen as an analogue of a liquid-gas coexistence [BT16]. While $\tilde{J}_I$ increases, the monomers become increasingly scarce and nearly all condensed into clusters because the line tension is very high and their detachment has a high cost in terms of interfacial energy.

We then plot the size distribution, i.e. the occurrence $p(n)$ of clusters comprising n sites throughout the simulation, after equilibration, as shown in Fig. 2.15. This distribution shows a local maximum at the most probable cluster size. In the case of cluster phases, the distribution is bimodal and the secondary peak position n^* corresponds to the typical domain size, measured

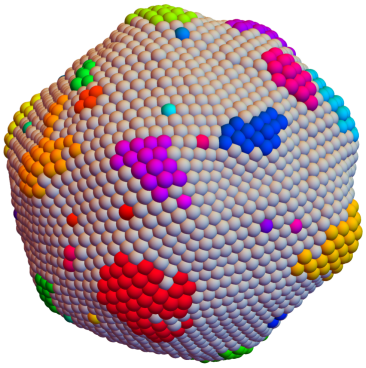

FIGURE 2.14 – Cluster detection analysis performed on a simulated vesicle with the DFS algorithm. Each color indicates a detected cluster.

in units of the number of sites belonging to a same cluster. The first peak of the distribution $p(n)$, corresponding to monomers and small multimers, seems to be well fitted by a power-law (data not shown), which might be explained by the reminiscence of the critical behavior of the Ising model in the vicinity of the critical point [TW87]. To get accurate values of n^* we fit the secondary peak with a Gaussian. Note that in the case of a macrophase, the distribution shows a peak the abscissa of which is close to the total number of A-species, as observed in Fig. 2.15, reflecting the fact that most of the A sites are condensed in a single macro-cluster.

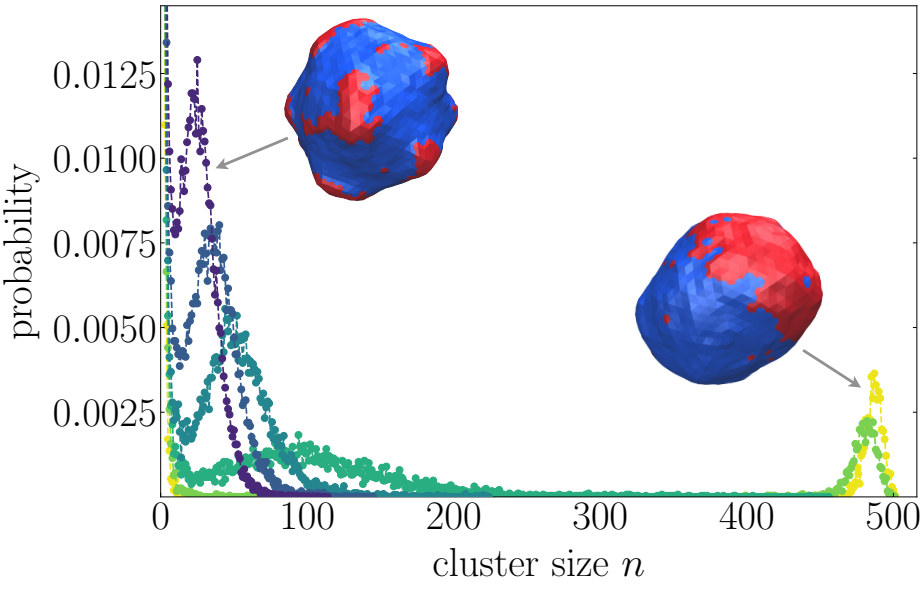

FIGURE 2.15 – Example of phase identification with the size distribution tool. We can distinguish mesophase (left) and macrophase (right) via the position of the peak. The parameters used are $\phi = 0.2$, $\tilde{J}_I^{-1} = 2.5$, $\tilde{\sigma} = 300$ and varying values of c_1, increasing from 1 to 6 (from yellow to purple). Color lines are guides to the eye.

On a triangular lattice, the typical cluster size n^*, the typical inter-cluster distance L and the position l^* of the structure factor maximum are related through

$$n^* = \frac{L^2}{a^2}\bar{\phi} = \left(\frac{2\pi R}{al^*}\right)^2 \bar{\phi} = \frac{\sqrt{3}\pi}{2}\frac{N}{l^{*2}}\bar{\phi} \tag{2.21}$$

owing to $L = 2\pi R/l^*$, a still being the lattice parameter.

When the typical cluster size is very small, this secondary peak might merge into the first one and becomes impossible to spot. To detect it in this case, we use the plot of $n\,p(n)$, the mean occupied surface by clusters of size n, in which the secondary peak will be enhanced and appear as a shoulder in the first peak. This allows one distinguishing small predominant sizes.

We can then study the influence of the different parameters and try to figure out which regimes of parameters lead to either macro, modulated or disordered phases. We can do this quantitatively with the help of the tools that we have introduced here: computation of correlation functions, structure factor and domain size distribution.

2.1.6 Tesselation bias and correction

To create the discretized sphere for the initial configuration, we start from a regular icosahedron. We then subdivide each face of the starting icosahedron by joining the middles of its 3 edges. We then get 4 smaller triangles into each face and reiterate this process (Fig. 2.16). This leads to a restricted list of accessible values for the total number of vertices (see [Gue16]). With s being the number of subdivisions, only the system size N satisfying $N = 10 \times 4^s + 2$ are accessible and leads to $k = 2^s + 1$ sites on an initial edge. An important point to notice is that this discretization also leads to a few defects in the structure. Indeed, the connectivity of all the vertices is not equal to 6 for all of them, because of the 12 vertices of the initial icosahedron that only have 5 neighbors (it is impossible to tile a sphere with only hexagons, pentagons are unavoidable). This feature is taken into account when computing the local energy (Helfrich or Ising) of a vertex, however we understood that this tesselation induces a bias in the simulations.

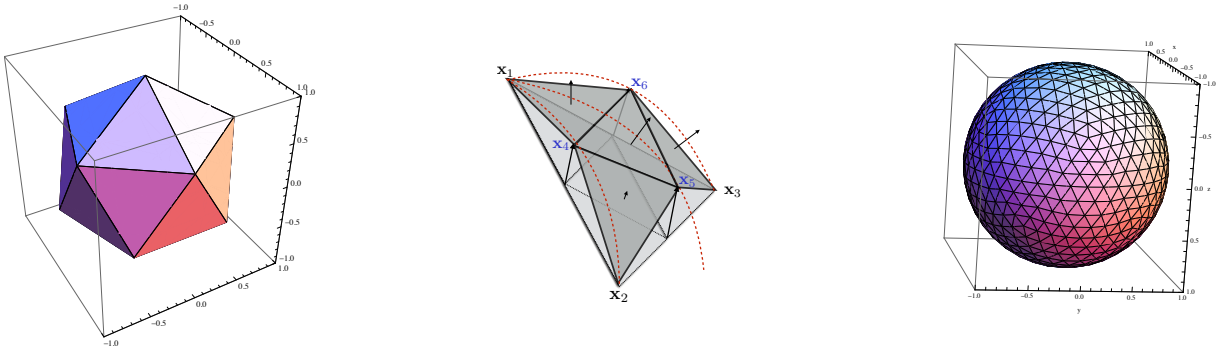

FIGURE 2.16 – Tesselation method. We start form an initial icosahedron (left) whose vertices are on a sphere of radius R. Each triangular face of the icosahedron is subdivided iteratively and the newly created vertices are projected on to the sphere (center). We eventually get a tessellated or triangulated sphere (right) whose total number of vertices N depends on the number of iterations of the subdivision process s as $N = 10 \times 4^s + 2$. Figures are taken from [Gue16].

Local problem due to the icosahedron vertices

As explained above, 12 of the total N vertices forming the tesseled sphere are special, since they belong to the initial icosahedron and have then 5 neighbors instead of 6 for all the other

sites. This has to be taken into account in the Helfrich energy calculation. Indeed, the surface associated to these vertices is smaller than the one for vertices with 6 neighbors. We noticed that in mesophase cases at low concentrations, domains are often localized around a 5-neighbor vertex. We then measured the average ratio of these vertices whose nature is A species and noticed that this ratio was systematically higher compared to the fixed concentration ratio. We first thought that this came from the fact that the surface associated to these vertices taken into account in the local Helfrich energy computation was smaller, leading to a smaller energy and then more favorable MC moves. We tried to correct this bias by multiplying these areas by 6/5 but no significant modification was observed.

The specificity of these vertices also plays a role in the Ising energy: the probability for these vertices to have a certain number of neighbors of the same species is different than in the case of 6 neighbors. We tried to see the effect of this by locally adapting the Ising energy of these vertices but again no effect was observed.

Global and major problem

We eventually realized that one major problem of this tesselation method does not come directly from the twelve 5-neighbor vertices that only have weak and local effects but from a global issue: after each subdivision, the newly created points are projected on the sphere. The

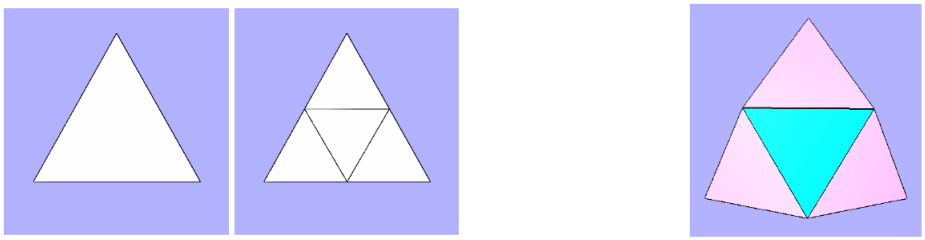

(a) Starting Face (b) Level 1 Face

FIGURE 2.17 – Face subdivision (left). After projection (right), the blue projected triangle has larger area than the pink ones. Figures are taken from [Har12].

triangles projected then have a larger surface than the initial ones (Fig. 2.17). This results in triangles with different areas in the initial sphere. The closer they are to the initial icosahedron vertices, the smaller they are. The triangles close to the centers of the initial icosahedron faces then have a larger surface than the ones close to the initial vertices. This results in triangles with different areas in the lattice, the largest triangles being typically 10% larger than the smallest ones. The Voronoï area associated to each vertex [GDM17] taken into account in the local energy calculations depends on the surrounding triangles. They are consequently locally smaller close to the icosahedron vertices, involving calculated local energies locally lower since the bending energy of a vertex is proportional to the Voronoï area associated with it. Thus the most curved A-species regions tend to get anchored to the smallest triangles, close to the 12 initial vertices, which biases the free energy minimization. Since our algorithm relies on energy minimization, the results are then distorted by this initial tesselation bias in the lattice triangle areas.

To correct this effect, we tried to create an initial discretized sphere with all triangles of equal size. We did not find any deterministic approach to do that and, since it appears to be an open problem [Har12], we tackled this problem numerically and stochastically. We started from the configuration generated by the above-described tesselation. Then, we used a Metropolis algorithm at zero temperature (gradient descent) minimizing the standard deviation of the lattice triangles areas, the local moves of which are small displacements of the vertices on the sphere. We then checked that we obtained a highly peaked distribution around a characteristic triangle area, having reduced triangle area dispersion by a factor ~ 100 (Fig. 2.18). The bias induced by the

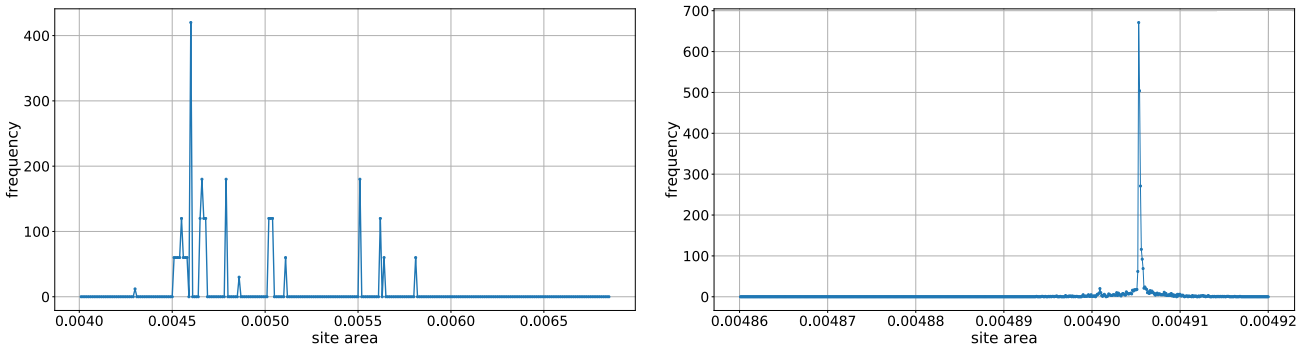

FIGURE 2.18 – Triangle areas distribution before (left) and after correction (right). Note that the x-axis scales are different.

original tessellation is illustrated in Fig. 2.19 by the mean number of domains with respect to the curvature coupling c_1 (see Chapter 3). Around $c_1 = 5.5$, there is a marked shoulder corresponding to systems with mean number of domains close to 12 without correction (in red). The vesicles with a little less and a little more than 12 clusters seem to be constrained to have 12 clusters by the underlying icosahedron because curved domains are anchored to the 12 icosahedron vertices zones. After correction, this shoulder almost disappeared (in green), showing that we significantly improved the triangle area distribution, although a soft shoulder is still present.

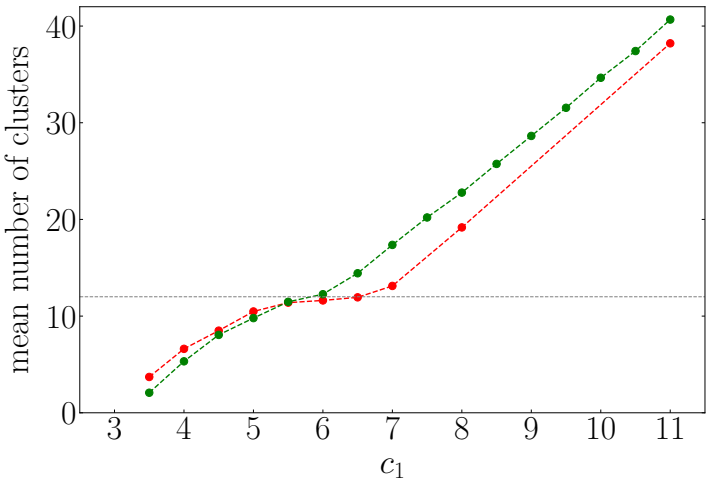

FIGURE 2.19 – Mean cluster number versus curvature coupling c_1 for clusters of size $n \geq 5$ ($\bar{\phi} = 0.2$, $\tilde{\sigma} = 300$ and $\tilde{J}_I^{-1} = 2.0$) with (green) and without (red) correction of the initial triangle area distribution. Lines are guides to the eye.

We can also notice the tesselation effect in the measurement of the angular composition and the membrane height in regards to a pole. These measurements highlight the underlying icosahedron shape. We see in Fig. 2.20 that the effect is strongly reduced with the correction of the tesselation method. Figure 2.21 shows these angular measurements for different c_1 values at

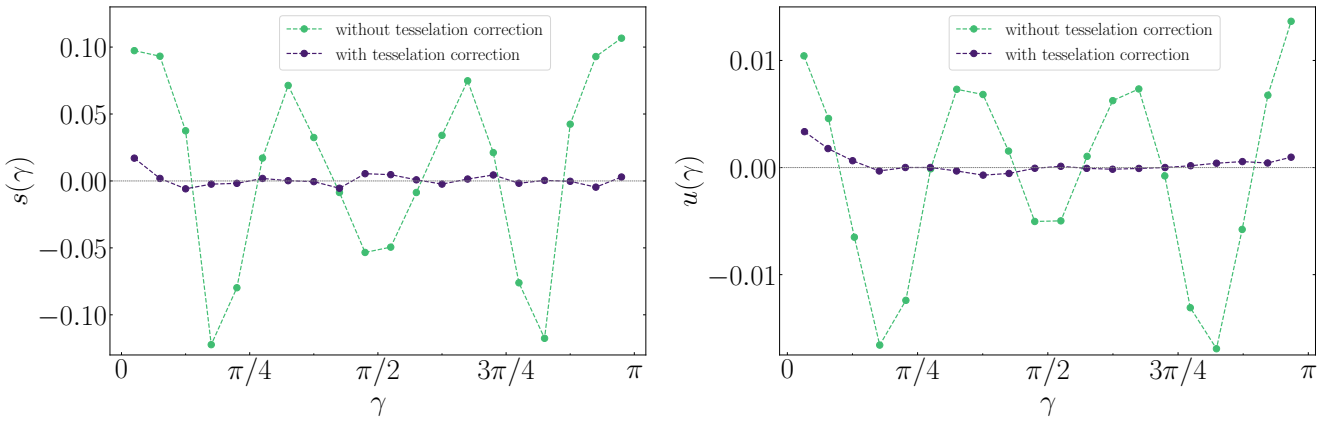

FIGURE 2.20 – Composition with respect to a pole in function of the angle γ (left) and height function with respect to a pole in function of the angle γ (right). $\bar{\phi} = 0.5$, $\tilde{\sigma} = 300$, $c_1 = 6.0$, and $\tilde{J}_I^{-1} = 4.0$. Color lines are guides to the eye.

$\phi = 0.2$ after the correction of the tesselation. Again we clearly see that the effect is the strongest around $c_1 = 5.5$ at this concentration.

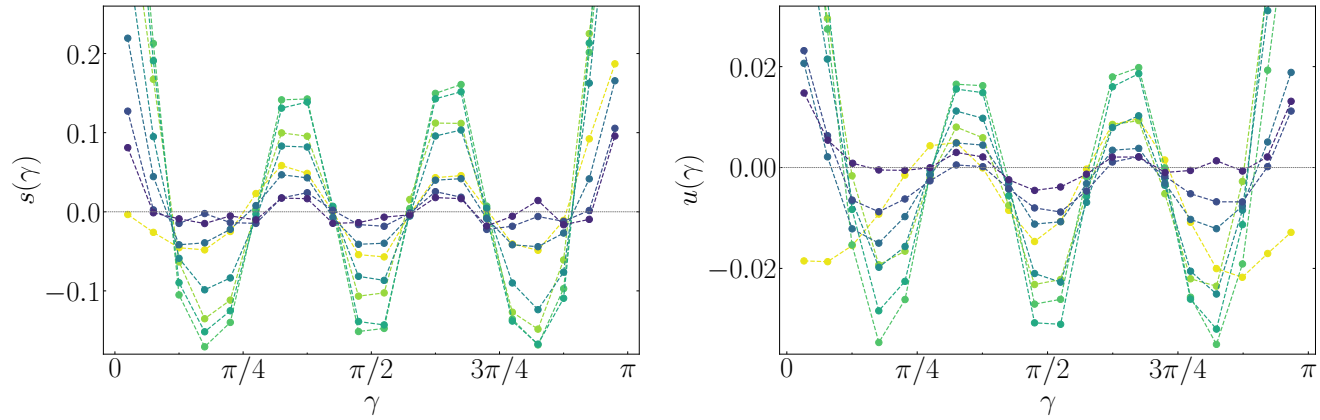

FIGURE 2.21 – Composition with respect to a pole in function of the angle γ (left) and height function with respect to a pole in function of the angle γ (right) for different c_1 values, after tesselation correction. The maximum amplitudes are obtained for the systems where $c_1 \simeq 6$. Other parameter values are $\bar{\phi} = 0.2$, $\tilde{\sigma} = 300$, and $\tilde{J}_I^{-1} = 2.5$. Color lines are guides to the eye.

When exploring the effect of force application on our system (see Secs. 2.1.5 and 6.1), we also face the influence of the tesselation nature on our measurements. We notice that the results are slightly different when applying the force on a site that is a vertex of the initial icosahedron from when applying it on a site that is located close to the center of a face of the initial icosahedron. In Fig. 2.22 we plot the angular membrane height $u(\gamma)$ for a system with no curvature coupling and where the force is applied either on a vertex located close to the center of a face of the initial icosahedron (i.e. of coordination number equal to 6, green) or on a vertex belonging to

the initial icosahedron (i.e. of coordination number 5, orange) for different simulation seeds. We observe that the deformation tends to be of higher amplitude when the force is applied to a vertex belonging to the initial icosahedron than to a face. This suggests that the elastic response to force application is slightly different for these two cases and that vertices belonging to the initial icosahedron might be less rigid and more easily deformable. The higher flexibility of these zones might be a source of insight into the preferential location of more curved domains to them. Note

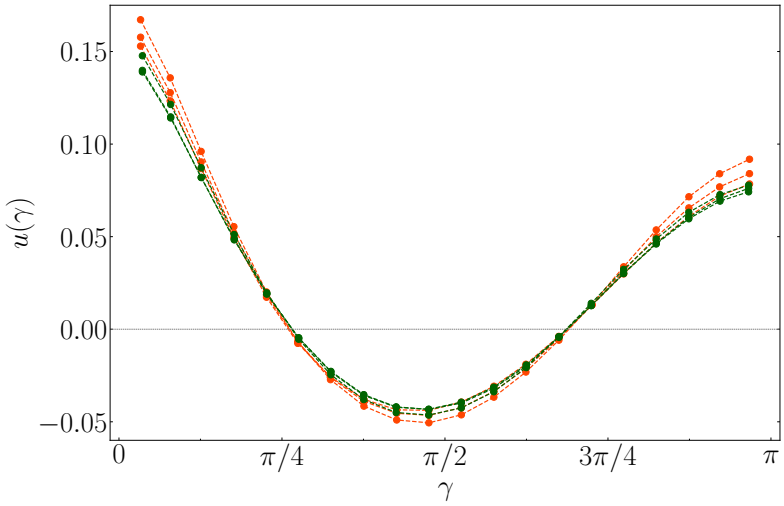

FIGURE 2.22 – Angular membrane height for a system without curvature coupling ($c_1 = 0$) with $\tilde{f} = 100$ for different simulations seeds. The force is applied either on a vertex located close to the center of a face of the initial icosahedron (i.e. of coordination number equal to 6, green) or on a vertex belonging to the initial icosahedron (i.e. of coordination number 5, orange). Other parameters are $\bar{\phi} = 0.2$, $\tilde{\sigma} = 300$ and $\tilde{J}_I^{-1} = 2.5$.

that such a difference of elastic response between the two types of vertices has previously been demonstrated by Widom et al. (2007) in the different, however connected, case of polymerized membranes ensuing from similar tessellations.

The fact that some effects remain after the correction of the tessellation triangle areas indicates that another phenomenon is at play favoring the positioning of the curved domains close to the icosahedron vertices, as if they were pinned by a defect. The difference of elasticities of the sphere when a force is applied to different vertices suggests that the origin is mechanical. In the frame of the linear response theory for Gaussian Hamiltonians, it can easily be proved that in the Fourier space, the response to a local curvature constraint is proportional to the response to a local force. It follows that icosahedron vertices are also probably more compliant to local curvature, which would favor positioning of curving A domains close to them. Even though the energies at play will have to be quantified in the future to ascertain that they are strong enough to partially pin the domains, this might be the cause of the spherical symmetry breaking still observed in the simulations.

2.2 Coarse-grained (MARTINI) molecular dynamics simulations

Molecular dynamics simulations (MD) consist in solving the equations of motion for all the particles present in the system after calibrating their individual interactions from experiments or ab initio calculations. We used coarse-grained molecular dynamics simulations performed using the MARTINI v2.2 force field [Mar+07] and run with GROMACS 2016 software [Abr+15]. Unlike the Monte Carlo simulations in which one single patch corresponds to a large number of lipids, here all the lipids are simulated with one lipid being made of several beads, each representing four heavy atoms. MARTINI was first developed in order to simulate lipid systems. The different kinds of interactions (bonded interactions with harmonic potentials, nonbonded interactions with a Lennard-Jones potential) between the different types of beads (water, nitrogen polar group, phosphate group, ester group, acyl chain beads...) are parametrized and described in [Mar+07]. The force field was then extended so to allow simulating glycolipids following [Lop+13] (the force field that we have used in this work) as well as membrane protein systems [Mon+08; Jon+13]. More recently, MARTINI was even adapted to simulate systems departing from membranes such as polymers. For a review addressing the different applications and the limitations of MARTINI see [MT13]. The latest version of the force field tuned to parametrize proteins more accurately is presented in [Sou+20].
We use the CHARMM-GUI interface [CHA18] to generate the lipid bilayer input system. Water molecules are added to the system (4 water molecules constituting one bead) along with neutralizing ions. We apply the Parrinello-Rahman barostat to control the pressure and the v-rescale thermostat to control the temperature in the system energy minimization before running molecular dynamics simulations. The surface tension is zero in these simulations as explained by the GROMACS documentation [GRO16]. It is defined as:

$$\sigma = L_z \left(P_z - \frac{P_x + P_y}{2} \right) \tag{2.22}$$

where L_z is the height of the simulation box, P_z the normal pressure and P_x and P_y the lateral pressure. Here we have $P_x = P_y = P_z$ hence $\sigma = 0$.

The analysis scripts were written in Python3 using MDAnalysis packages [Gow+16]. In particular we used the LeafletFinder tool that allows one to identify and assign each molecule to the upper or lower leaflet to which it belongs. The simulations were run for a patch of a bilayer of approximately 40 nm side and over 20 μs.

One can again notice the important difference in term of length-scale between the mesocale and the coarse-grained models, hence leading to important differences in term of manageable simulation times.

Chapter 3

Curvature-induced domain formation studied by Monte Carlo simulations

Contents

In this chapter, we present the main results obtained with the mesoscale Monte Carlo simulations of a bicomponent vesicle involving a composition-curvature coupling essentially published in [CDM20] plus some additional results.

3.1 Effects of membrane parameters on modulated phases formation

We performed Monte Carlo simulations of vesicles for various sets of parameters, varying the curvature coupling strength c_1, the surface tension $\tilde{\sigma}$ and the component interaction parameter $\tilde{J}_I$. The theory developed in [GDM14] predicts four different phases arising from the combination of these parameters. At low curvature coupling c_1, the systems are either phase-separated for high $\tilde{J}_I$, or disordered for low $\tilde{J}_I$, reproducing the expected behavior without coupling. At high enough curvature coupling, A-rich domains of various sizes appear, i.e. stable modulated phases.

3.1.1 Curvature-composition coupling effect

At low $\tilde{J}_I < \tilde{J}_{I,c}$, the two species tend to mix at null or low curvature coupling as shown in Fig. 3.1, left, but we observe that strong enough coupling of the composition field to shape fluctuations stabilises more ordered local composition fluctuations as visible in the right-hand vesicle of Fig. 3.1 where $c_1 = 3.0$. Although hardly detectable with the eye, this underlying order is present and can be expressly detected thanks to the computation of the structure factor of the system as described previously in Chapter 2 (see also Fig. 3.4). We see that our numerical results are in quantitative agreement with previous analytical studies [GDM14; Sch12; SS13] (see also the Review article [DMC18]). Note that in the following, we sometimes talk abusively about "domains" at high enough values of the concentration $\bar{\phi}$ so that the red species is dense enough for its repartition to be continuous. In this case we therefore do not observe distinct domains strictly speaking. The more general terms "patterns" or "modulated phases" would be more appropriate.

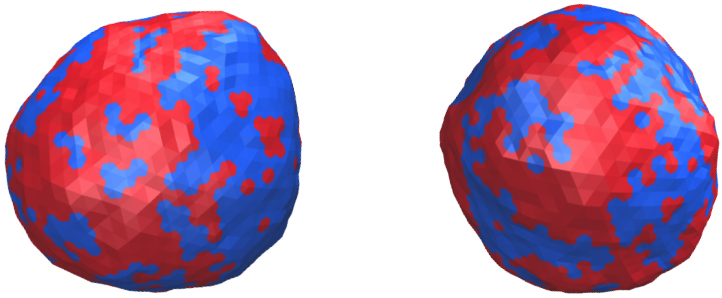

FIGURE 3.1 – Snapshots of simulated vesicles showing the effect of the difference of spontaneous curvature $c_1 = c_2 - c_0$ between the two species at low $\tilde{J}_I$ ($\tilde{J}_I^{-1} = 4.0$, $\bar{\phi} = 0.5$, $\tilde{\sigma} = 300$): $c_1 = 0$ (left) and $c_1 = 3$ (right). For the blue species, $c_0 = 2$ in all the simulations. The two species tend to mix but the coupling c_1 stabilises modulated phases, although difficult to catch with the eye (see text).

At large $\tilde{J}_I > \tilde{J}_{I,c}$, the previous analytical description is not adapted anymore as the functional integrals are no more Gaussian because terms in ϕ^4 must be kept in Eq. (1.5) [GDM14]. Here comes the interest of the numerical study that can extrapolate the model to these cases. Without any curvature coupling, the vesicle mixture undergoes phase separation as expected (Fig. 3.2, upper leftmost vesicle). When we increase the coupling c_1 (from left to right), the large curved domains become unstable and break into smaller ones, getting smaller as c_1 increases. We see that when we couple the concentration field to shape fluctuations, a system in the macrophase regime $\tilde{J}_I > \tilde{J}_{I,c}$ can move over the phase transition and feature domains. We get modulated phases as shown in Fig. 3.2. We also study vesicles at $\bar{\phi} = 0.2$ as shown in Fig. 3.2 (bottom) and 3.8, a concentration that is more illustrative of biological membranes containing curvature-generating proteins or particular lipids [PM15].

We can then consider an effective Ising parameter for the coupled system modified by the curvature coupling that introduces a new term in ϕ^2 in Eq. (1.8). It shifts the mass m to:

$$m' = m + \kappa_0 C_1^2 \tag{3.1}$$

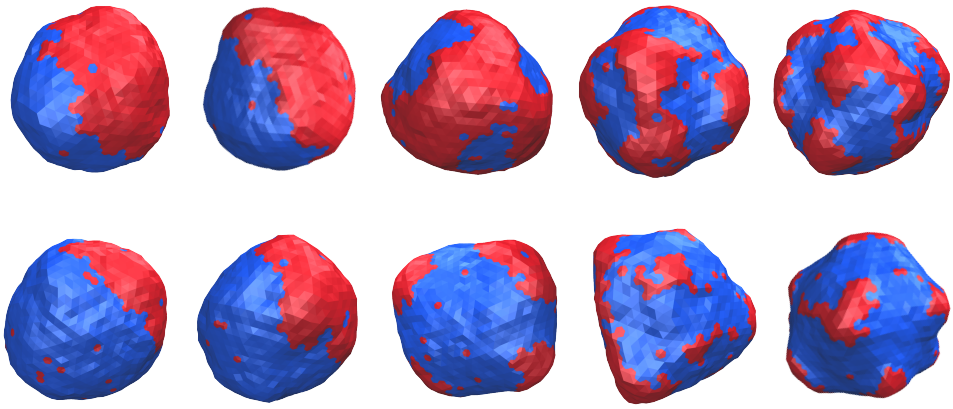

FIGURE 3.2 – Same as Fig. 3.1 at high $\tilde{J}_I$ with $c_1 = 0, 2, 3, 4, 6$ (up) and $c_1 = 0, 1.5, 3, 4, 6$ (bottom), from left to right. Other parameter values are $\tilde{J}_I^{-1} = 2.5$, $\tilde{\sigma} = 300$, $\bar{\phi} = 0.5$ (up) and $\bar{\phi} = 0.2$ (bottom).

The transition in a coupled system now occurs when $m' = 0$, that is to say when $m = -\kappa_0 C_1^2$. One can then express the effective transition Ising parameter for a coupled system as

$$J_{I,c}^{\text{eff}} = J_{I,c}\left(1 + \frac{\tilde{\kappa}_0 c_1^2}{\alpha_0 N}\right) \tag{3.2}$$

The coupling c_1 increases the effective value of the transition Ising parameter as found in Fig. 3.2, allowing the system to move over the transition and thus to undergo phase modulations even above $\tilde{J}_{I,c}$. Increasing further $\tilde{J}_I$ drives macrophase separation by increasing line tension.

To obtain an approximated expression for the domain size, we compute the energy cost due to the area excess ΔA induced by a curved domain of radius r (we assume spherical cap domains at low enough concentration above $\tilde{J}_{I,c}$, as well as spherical vesicle)

$$\begin{aligned} \sigma \Delta A &= 2\pi\sigma[R_2^2(1-\cos\theta_2) - R_0^2(1-\cos\theta_0)] \\ &\simeq \frac{\pi}{16}\sigma r^4 (C_2^2 - C_0^2) \end{aligned} \tag{3.3}$$

where θ_2 and θ_0 are the angles of the domain along the osculatory circles of radii $R_2 = 2C_2^{-1}$ and $R_0 = R = 2C_0^{-1}$ respectively (related through $r = R_0 \sin\theta_0 = R_2 \sin\theta_2$). The second expression in Eq. (3.3), obtained by expanding ΔA at order 4 in r/R_0 and r/R_2, is valid for small domains only, with $r \ll R_2 < R$. This energy penalty is balanced by the line energy $2\pi r\lambda$, which yields

$$r \simeq 2^{5/3}\left(\frac{\lambda}{\sigma}\frac{1}{C_2^2 - C_0^2}\right)^{1/3} \tag{3.4}$$

Even though ignoring the role of translational and conformational entropies [DF08], this explains why an increasing c_1 (or equivalently c_2) favors smaller domains. Since the line tension λ is proportional to $J_I - J_{I,c}$ [Hon+08; EPS11], the higher J_I is, the more difficult it is to form small domains. Note that Eq. (3.4) is very similar to the one obtained by Kawakatsu et al. (1993) (their Eq. (2.12)) in the strong segregation limit, although obtained with a different argument.

Beyond these qualitative results, we now quantitatively study domain formation thanks to spatial correlation functions and domain size distributions. These observables are computed once the system has reached equilibrium. The aim is to classify the vesicle states by extracting information about the emerging membrane patterns, such as their typical size, spacing or number.

Correlation function and structure factor

We compute numerical spatial correlation function of the vesicle composition as defined in Eq. (1.11). From these measurements we compute the structure factor as described in Section 2.1.5.

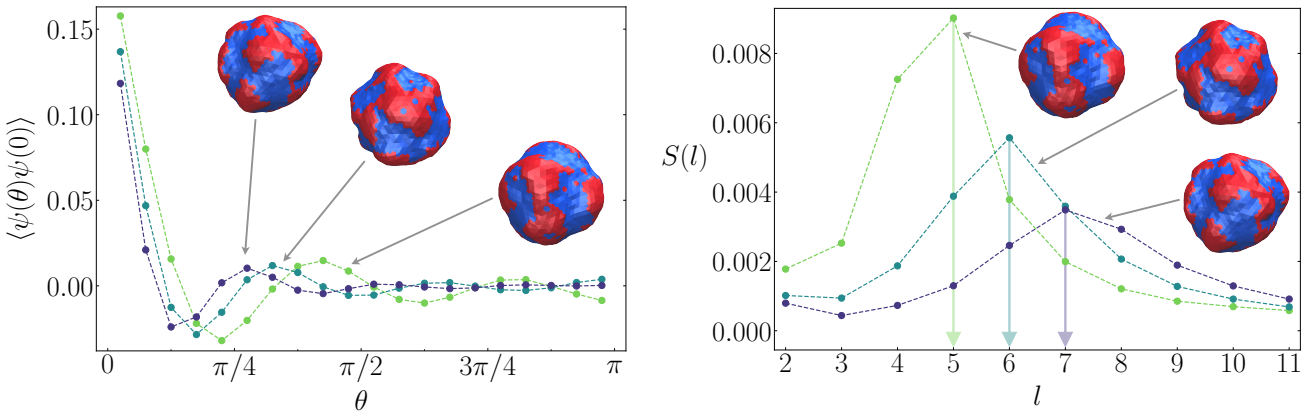

FIGURE 3.3 – Numerical correlation functions (left) and corresponding structure factors (right) for different curvature coupling values $c_1 = 4$, 5 and 6 from green to blue ($\tilde{J}_I^{-1} = 2.5$, $\bar{\phi} = 0.5$, $\tilde{\sigma} = 300$). The structure factors (right) exhibit a maximum for an abscissa l^* (arrows), corresponding to pattern wavelength in real space and correlation function oscillations. Color lines are guides to the eye.

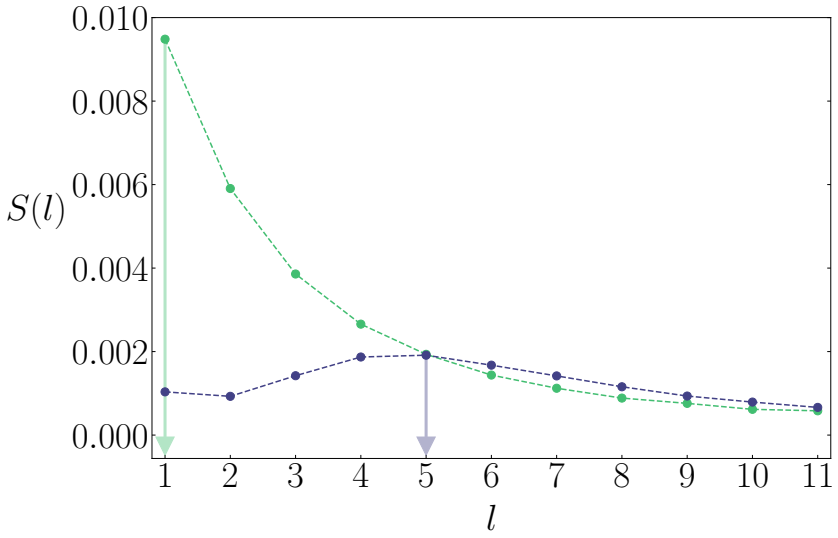

FIGURE 3.4 – Structure factors for two different curvature coupling values $c_1 = 0$ (green, no coupling) and $c_1 = 3.0$ (blue), the ones of the two vesicles presented in Fig. 3.1 at low $\tilde{J}_I$ value below $\tilde{J}_{I,c}$ ($\tilde{J}_I^{-}1 = 4.0$). Color lines are guides to the eye.

Figure 3.3 presents spatial composition correlation functions and respective structure factors for systems with different curvature coupling strength c_1 at large $\tilde{J}_I$. As explained in Section 2.1.5,

the correlation function shows a first peak, the width of which is proportional to pattern typical size. When the vesicle presents modulated phases, it shows oscillations corresponding to the typical pattern wavelength (spacing). As expected, correlation functions with larger c_1 have a smaller first peak width and a smaller wavelength, capturing small pattern size.

Following the definition of the structure factor $S(l)$ in Eq. (1.19), the variance of the concentration is given by $S(0)$. We indeed measure $S(0) = 0$ in our simulations, due to the fact that we have imposed a fixed concentration $\bar{\phi}$ (see Fig. 1 in Appendix A for instance). We used the information provided by the structure factor in order to identify which phase each system belongs to in equilibrium (see Section 2.1.5). We summarize these key points here:

- a disordered phase when the structure factor $S(l)$ has a maximum for the first mode $l = 1$ and $\rho = S(1)/S(2) \sim 1$, for example for the green curve in Fig. 3.4 where $\rho \approx 1.6$;
- a macrophase when the structure factor has a maximum for the first mode $l = 1$ and $\rho \gg 1$;
- a modulated phase when $S(l)$ exhibits a second maximum for a value $l = l^* \neq 1$ (see for example the blue curve in Fig. 3.4 where $l^* = 5$), obtained when the curvature coupling exceeds the threshold value c_1^*. Again, the emergence of phase modulation relies on the condition $c_1 > c_1^* = \sqrt{4\sqrt{3}\tilde{\sigma}\tilde{J}_I/\tilde{\kappa}_0^2}$. This phase includes both theoretically defined "structured ordered" and "structured disordered" phases as described in Section 2.1.5. The typical pattern wavelength is given by $L = 2\pi R/l^*$.

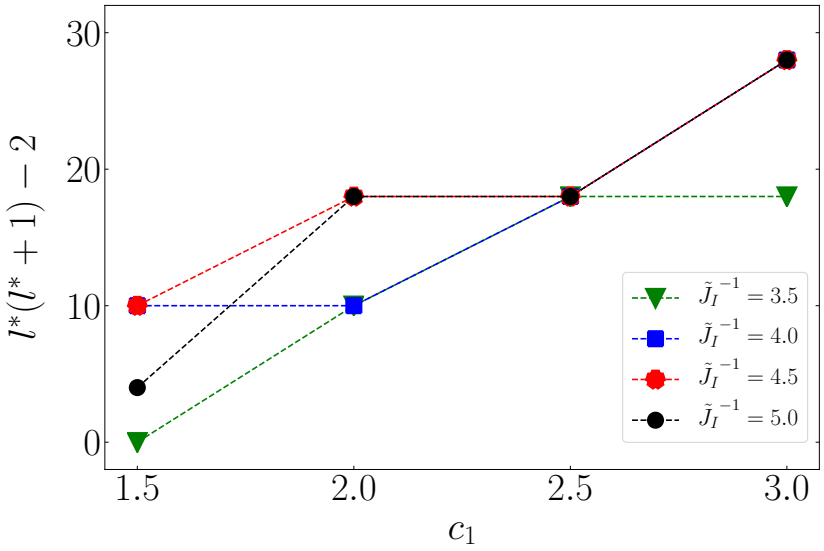

FIGURE 3.5 – Variation of $l^*(l^*+1) - 2$ with c_1, where l^* is the mode corresponding to a maximum in the numerical structure factor, associated with the occurence of the structured disordered phase as shown in Fig. 3.1 right.

In Fig. 3.4 we plot the structure factors of the two systems presented in Fig. 3.1. Although very difficult to distinguish with the unaided eye, as expected, the curvature coupling stabilizes local composition fluctuations, even above the transition, and generates underlying structuring in the vesicle mixture spatial repartition. This effect can be efficiently captured by the structure factor. Indeed, it exhibits a maximum for $l^* = 1$ for the system with $c_1 = 0$, attesting of no

structure in the corresponding system. By contrast, the structure factor of the system with $c_1 = 3.0$ has a maximum for $l^* = 5$, related to pattern wavelength, thus revealing underlying structure. Consistently here $c_1 = 3.0 > c_1^* \simeq 1.1$, inducing phase modulation.

In the structure factors in Fig. 3.3, we observe that the peak position l^* increases when c_1 increases, which leads to a smaller typical wavelength $2\pi R/l^*$ in the structured emerging patterns, with more spaced and thinner patterns, consistent with our results. The l^* are extracted from the numerical structure factors and shown in Fig. 3.5 as a function of c_1. They qualitatively follow Eq. (2.17), i.e. $l^*(l^*+1) - 2$ grossly grows linearly with c_1, although it is difficult to extract any slope due to the integer values taken by l^*.

Fit of the structure factor

We now fit the numerical structure factor with the expression of $S(l)$ given in Eq. (1.19). The simulation parameters involved in the fit are $\hat{J}$, $\hat{m}$ and $\hat{\sigma}$.

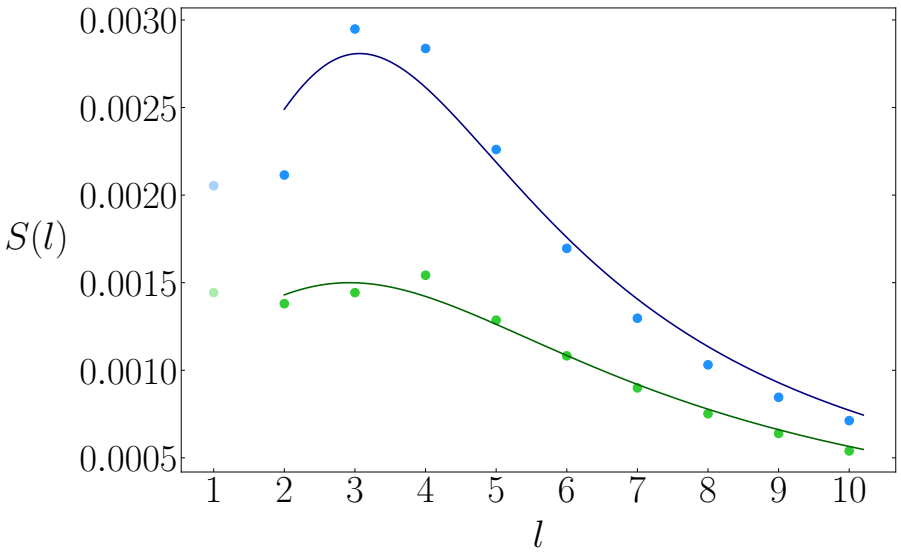

FIGURE 3.6 – Fit of the structure factor for two system sizes $N = 2562$ and $\tilde{\sigma} = 300$ (blue), $N = 10242$ and $\tilde{\sigma} = 1217$ (green). The choice of these surface tension values will be justified in Section 3.3. Here $\tilde{J}_I^{-1} = 4.0$, $\bar{\phi} = 0.5$, $c_1 = 2.0$. The effective surface tension $\tilde{\sigma}_{\text{eff}} \approx 4.2$ in both cases (see Section 3.3). The mode $l = 1$ was not taken into account in the fitting process (see text).

The structure factors $S(l)$ for two different system sizes are shown in Fig. 3.6 for a system featuring modulated phases. We observe that the structure factor amplitude is larger for $N = 2562$ than for $N = 10242$. This is consistent with the fact that $S(l)$ depends on N via $\hat{m} = \frac{\alpha_0 N}{\tilde{\kappa}_0}(1 - \frac{J_L}{J_{I,c}})$ which appears in the denominator of $S(l)$. As explained above, a Flory mean-field approximation for this value is $\alpha_0 = 1/\pi$. The expected theoretical values for $\hat{J}$ and $\hat{m}$ can be drawn from the expressions given in Chapter 1. In Fig. 3.6 the fitted value for $N = 2562$, $\hat{J} \approx 0.045$, is close to the expected one $\hat{J}_{\text{th}} \approx 0.043$. In contrast, the fitted value $\hat{m} \approx 0.19$ differs from the excepted value $\hat{m}_{\text{th}} \approx 4.1$. Note that the surface tension involved in this expression is different from the input value as it is renormalized by curvature coupling and system size as explained below (see also [GDM17]). The fitted value for $\hat{\sigma} \approx 6.4$ also differs from the expected effective surface

tension $\hat{\sigma}_{\text{eff,th}} \approx 0.21$ (see 3.3). This is also noticed for $N = 10242$. The main issue is that fitting the parameters $\hat{m}$ and $\hat{\sigma}$ is very sensitive to numerical data as described in Appendix A. In the fitting process, one minimizes the squares of the distances between the theoretical values and the numerical ones. We used the GOSA software [CCH06; GFR94] that applies simulated annealing to fit the data. We found that the minimum is quasi-degenerate for $\hat{m}$ and $\hat{\sigma}$, in other words we have a valley of quasi-degenerate minima. This implies that if the numerical data are slightly different from the real ones, we will find strong deviations in the fitted parameter values. Another manifestation of this phenomenon are error bars on $\hat{m}$ and $\hat{\sigma}$ on the same order of magnitude as the fitted values, contrary to $\hat{J}$. Indeed, the GOSA code also provides error bars on the fitted parameters, measured during simulated annealing. Even if we were able to acquire precise fitted values of $\hat{m}$ and $\hat{\sigma}$, comparison to theory would be uneasy because of the approximations made in the mean-field calculation of the constant α_0 as underlined above.

Furthermore, the theory developed in [GDM14] is valid in the thermodynamic limit, i.e. for infinite size systems. However, in our case, we study systems with a finite number of sites $N = 2562$ or 10242. This has some consequences on system observables and especially on the structure factor. Above all, the first modes are affected by these finite-size effects since they correspond to large scale phenomena in real space. It is known that for finite systems, the occurence of large macrodomains (corresponding to the mode $l = 1$) is overestimated [TW87]. Note that for this reason, we did not take into account the value for $l = 1$ in the fits of the structure factors. Appendix A provides more detailed explanations about these finite-size effects. Increasing the system size N allows us to reduce this bias and to get more accurate values for the structure factor as shown in Fig. 1 in Appendix A. We then fitted the structure factor for a system of size $N = 10242$ as depicted in Fig. 3.6. However, we encounter numerical limitations since this system size requires considerable simulation time to have good enough sampling for the correlation measurements as mentioned in Section 2.1.5. We then have reduced finite-size effects on the structure factor coefficient measurements with increased system size but poorer precision on the measured values of $S(l \geq 2)$.

Domain number and size distribution

As described in Section 2.1.5, at low enough concentration leading to distinct domains, we identified these different domains and computed their size distribution, showing a peak at the typical cluster size n^*. In Fig. 3.7 we plot the cluster size distribution $p(n)$ of cluster of size n for systems with different c_1 values. The size is measured in units of the number of sites part of a same cluster. We see here that for low c_1 values, the distribution shows a peak whose abscissa is close to the total number of A species, coherent with the fact that all the A patches are condensed into a single macro-cluster, corresponding to a macrophase. In the case of mesophases, we get a peak whose abscissa corresponds to the average typical size of the clusters, and we check here that this abscissa gets smaller and smaller when the coupling is increased, leading to smaller domains.

We also studied the effect of even stronger curvature coupling in order to reach smaller domain sizes. In Fig. 3.8 is shown a simulated vesicle for $\bar{\phi} = 0.2$ and high coupling value, $c_1 = 15$. As explained in Section 3.1.1, we observe many small curved domains. We recall that the typical

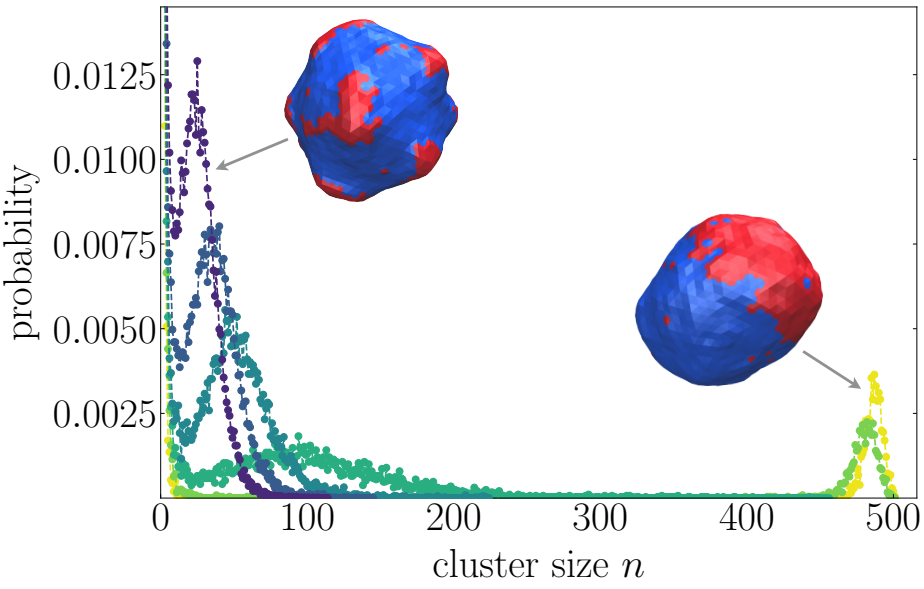

FIGURE 3.7 – Cluster size distributions $p(n)$ for c_1 increasing from 1 to 6 (from yellow to purple). We can distinguish macrophases (right) and mesophases (left) via the peak abscissa which corresponds to the typical cluster size n^*. The size of the clusters is measured in units of number of sites. $\bar{\phi} = 0.2$, $\tilde{J}_I^{-1} = 2.5$ and $\tilde{\sigma} = 300$. Color lines are guides to the eye.)

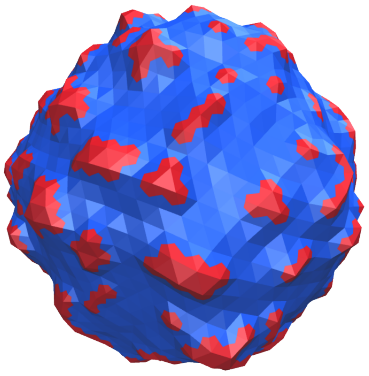

FIGURE 3.8 – Snapshot of a simulated vesicle for $\bar{\phi} = 0.2$ and $c_1 = 15$. ($\tilde{J}_I^{-1} = 2.5$ and $\tilde{\sigma} = 300$). Numerous small curved domains are observed, as expected.

cluster size n^*, the typical inter-cluster distance L and the position l^* of the structure factor maximum are related through Eq. (2.21). For example for the case shown in Fig. 3.8, we find that $l^* = 16$. Using Eq. (2.21) leads to a typical cluster size n^* of 5 sites, which is also the size found using the cluster size distribution secondary peak position. Both approaches are mutually consistent. In a real vesicle with a radius of 10 μm, these domains would have a diameter on the order of 1 μm, the same order of magnitude as the curvature-induced lipid domains observed experimentally in [SIT16].

We now study the domain typical size and their number as a function of the curvature coupling c_1 in Fig. 3.9. As described above, we see that the increase of the coupling leads to the formation of smaller (blue points) and then more numerous curved membrane domains (green points). We

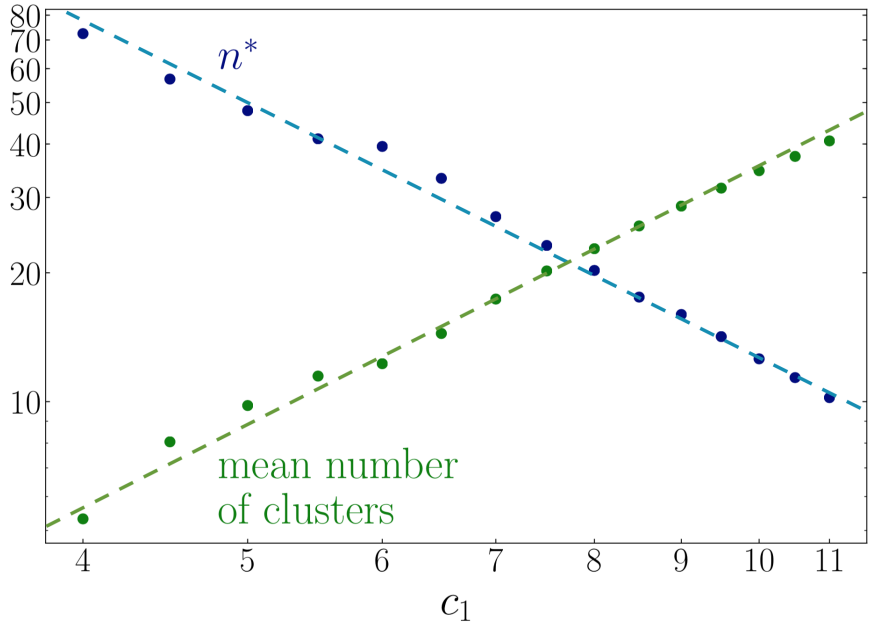

FIGURE 3.9 – Effect of the curvature coupling c_1 on the typical cluster size n^* extracted from Fig. 2.15 and on the mean number of clusters for clusters of size $n \geq 5$ ($\bar{\phi} = 0.2$, $\tilde{J}_I^{-1} = 2.0$ and $\tilde{\sigma} = 300$). Log-log coordinates. The dashes lines have slope 2 and -2, respectively, and are guides to the eye.

note that the typical cluster size (area) n^* scales with c_1 with a power law of -2 exponent. This exponent differs from the one obtained theoretically in Eq. (3.4) which relies on a very simplified and approximate calculation. The authors of [SIT16] recently found an experimental -1 exponent for domains induced by curvature-generating externally added glycolipids in GUVs (see Chapter 4). However their data have significant error bars and this exponent will have to be confirmed in future experiments as well as theoretical works. We also observe that the average number of clusters roughly scales like c_1^2. Together with the scaling $n^* \propto c_1^{-2}$ discussed above, we find that the total number of A sites in clusters is almost constant, as expected at high $\tilde{J}_I$ where most of A sites are condensed into clusters.

Concerning the question raised in the Introduction about the small size of the experimentally observed domain, we propose a scaling law for the typical cluster size n^* in function of the spontaneous curvature c_1 of the minority species ($c_1 = c_2 - c_0 \simeq c_2$ when $c_2 \gg c_0 = 2$), $n^* \simeq 1200/c_1^2$ (for $N = 2562$, as shown in Fig. 3.9). This means that cluster radii are $r = 2R\sqrt{n^*/N} \simeq 1.4/C_1$ in the studied regime of parameters. We cannot go beyond a limiting value of C_1 because r would become comparable or even smaller than the lattice parameter $a \simeq \sqrt{4\pi R^2/N} \simeq 700$ nm for a vesicle radius $R = 10$ μm. However, we can extrapolate the scaling law $r \simeq 1.4/C_1$ beyond the simulated values. A typical size $r \approx 50$ nm, commonly observed by super-resolution microscopy, would lead to $C_1 \approx 0.03$ nm^{-1}. This value is attainable for asymmetric lipid leaflets [PS11; HD20; Ste+20], lipid domains with glycolipid inclusions [Das+18] or protein domains [ZK06; BSL14]. As a consequence, experimentally observed nanodomain sizes can be accounted for by the model presented here.

3.1.2 Surface tension effect

In Fig. 3.10, we show snapshots of simulated vesicles with the same c_1 and $\tilde{J}_I$, but with increasing tension $\tilde{\sigma}$. We see that low tensions allow strong membrane deformations. Therefore the formation of domains, induced by curvature coupling, is favored in highly deformed regions. On the contrary, for high surface tensions the vesicle is constrained to a quasi-spherical shape and patterning along with deformation is therefore attenuated or even prevented. Thus, at a

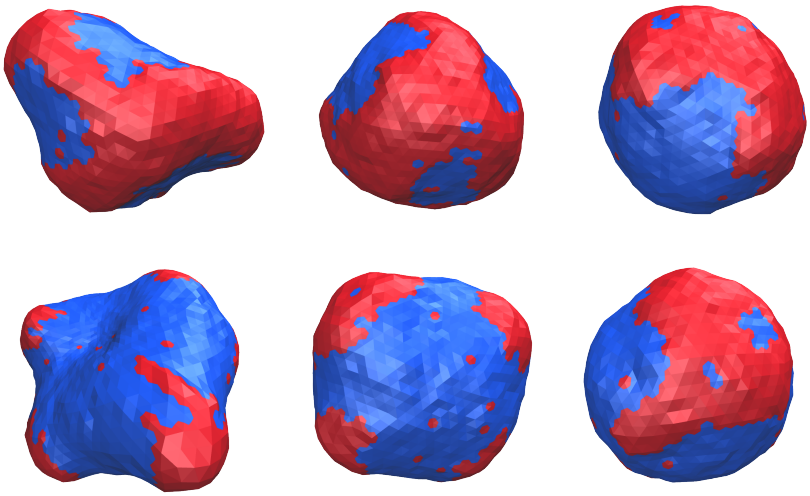

FIGURE 3.10 – Snapshots of simulated vesicles with increasing surface tension $\tilde{\sigma}$ (respectively from left to right 150, 300 and 600). $\bar{\phi} = 0.5$ (top) and $\bar{\phi} = 0.2$ (bottom). Other parameter values are $\tilde{J}_I^{-1} = 2.5$ and $c_1 = 3.0$.

fixed coupling value c_1 leading to mesophases in a low or moderate surface tension regime, the system undergoes macrophase separation as observed in Fig. 3.10 when the surface tension σ is high enough to balance the curvature term $\kappa_0 C_1^2$ in the Helfrich free energy and cancel its effect [AKK92; Kaw+93; DMC18]. Note that Eq. (3.4) is valid for low enough surface tensions such that the domain radius r is smaller than the correlation length $\xi = \sqrt{\kappa/\sigma}$. At higher tensions, the domain shape significantly deviates from a spherical cap of radius $2C_2^{-1}$. Hence Eq. (3.4) applies only to the case of the leftmost snapshots of Fig. 3.10, where $\xi \simeq 0.4R$. In Fig. 3.11 we plot the correlation functions and the structure factors for $\tilde{\sigma} = 300$ and 600. Both functions show the signal of phase modulation at $\tilde{\sigma} = 300$ whereas at $\tilde{\sigma} = 600$ they capture the macrophase predominance. For $\tilde{\sigma} = 150$ the vesicle undergoes strong deformations and its shape is very different from a sphere. This is the signature of the vesicle buckling as described in [GDM17], where the renormalized surface tension becomes negative. In the case of a bicomponent vesicle, the exact analytical expression of the residual tension (coming from the membrane fluctuations) remains to be computed. In this case the spatial angular correlation function is no more meaningful since the global spherical symmetry used to average the measurements is broken.

We also perform cluster detection analysis in order to compare domain size distributions. This effect is as well measurable in Fig. 3.12 where the typical domain size increases up to the total number of A sites condensed into a macrophase when increasing $\tilde{\sigma}$. We then find that when the

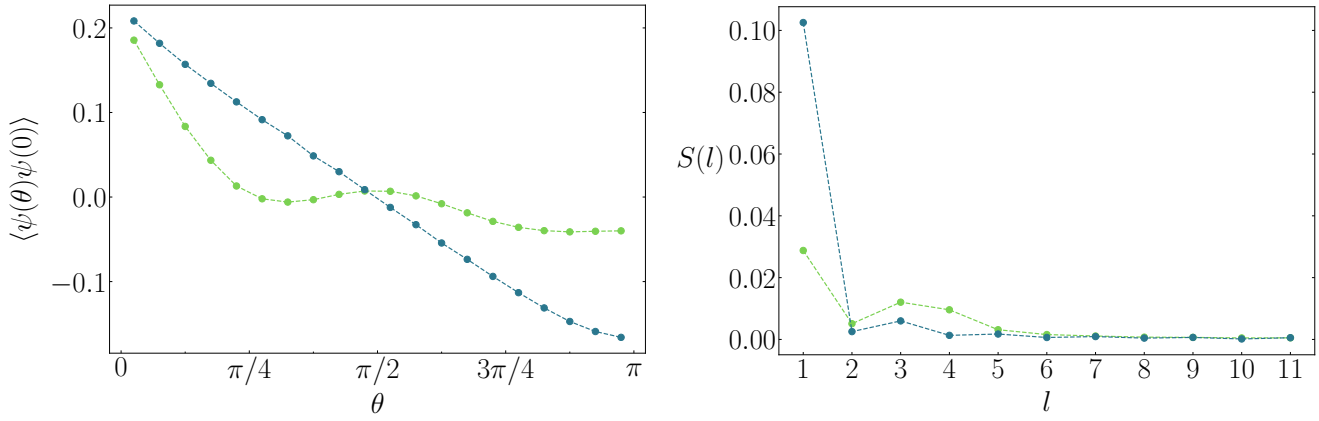

FIGURE 3.11 – Spatial correlation functions (left) and structure factors (right). $\tilde{\sigma} = 300;\ 600$, $\bar{\phi} = 0.5$, $c_1 = 3.0$ and $\tilde{J}_I^{-1} = 2.5$. Color lines are guides to the eye.

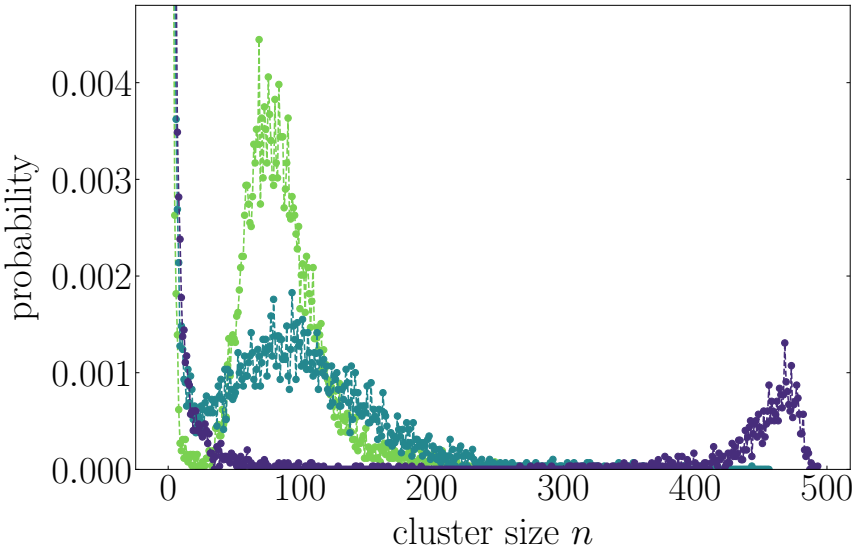

FIGURE 3.12 – Effect of the surface tension on domain formation and on domain size distribution. $\tilde{\sigma} = 150;\ 300;\ 600$. $\bar{\phi} = 0.2$, $c_1 = 3.0$ and $\tilde{J}_I^{-1} = 2.5$. Color lines are guides to the eye.

surface tension is high enough, it tends to stretch the membrane so that the curvature coupling effect is countered. This has also been observed experimentally in Refs. [Sim+19; Ste+20] where tubes and spikes tend to disappear when membrane tension increases.

3.1.3 Ising parameter effect

We also studied the effect of $\tilde{J}_I$ on domain formation using the same measurements. At high enough c_1 coupling, the system features domains getting greater as $\tilde{J}_I$ increases and even fuse into a macrophase when $\tilde{J}_I$ is high enough.

Note that for $\tilde{J}_I^{-1} = 2.5$ and below, we have big clusters that diffuse slowly. With this long time scale, the simulation measurements are potentially affected by larger error bars. Figure 3.14 shows correlation functions and structure factor for different $\tilde{J}_I^{-1}$ values and allows one to measure the decrease of the typical pattern wavelength when $\tilde{J}_I^{-1}$ is increased. We again perform

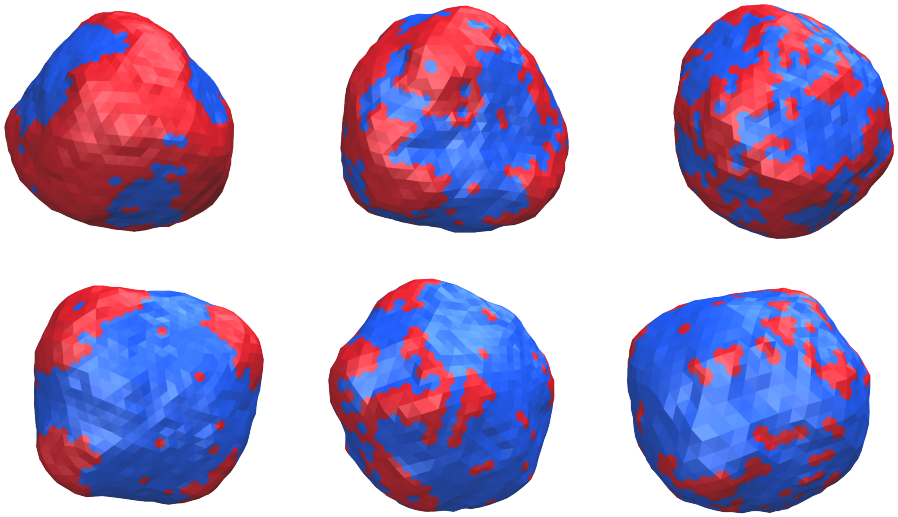

FIGURE 3.13 – Role of Ising parameter in phase separation and domain formation. $\tilde{J}_I^{-1}$ is respectively from left to right 2.5, 3.5 and 4.5. $\bar{\phi} = 0.5$ (top) and $\bar{\phi} = 0.2$ (bottom). Other parameters are $\tilde{\sigma} = 300$ and $c_1 = 3.0$ for all these simulations.

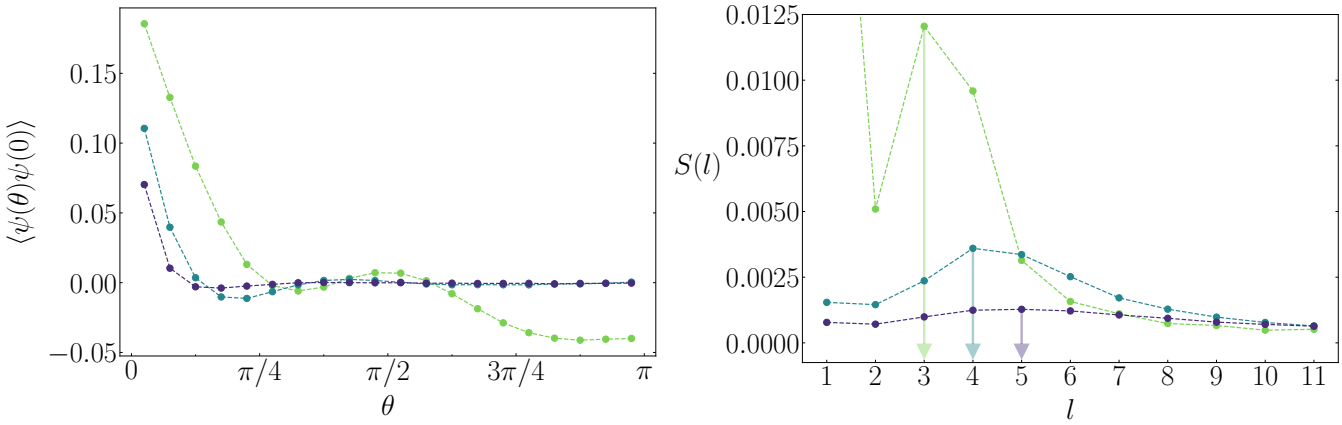

FIGURE 3.14 – Spatial correlation functions (left) and structure factors (right). $\tilde{J}_I^{-1} = 2.5;\ 3.5;\ 4.5$. $\bar{\phi} = 0.5$, $\tilde{\sigma} = 300$ and $c_1 = 3.0$. Color lines are guides to the eye.

cluster detection analysis in order to compare cluster size distributions as shown in Fig. 3.15. As explained in Section 2.1.5, we plot here $n\,p(n)$ giving the occupied surface in terms of number of sites so as to enhance the small peaks and to be able to detect them. We recover the fact that the typical cluster size decreases with $\tilde{J}_I^{-1}$. The lower the temperature is, the more difficult it is to form small domains. Indeed, this implies more numerous domains and then a longer frontier length between the two species at domain boundaries, which results in an increase in line energy. We recall that the line tension is proportional to $|\tilde{J}_{I,c} - \tilde{J}_I|$ close to $\tilde{J}_{I,c}$. We performed simulations with a high curvature coupling ($c_1 = 15.0$) inducing relatively small domains and varied the Ising parameter to see the effect on the domain size as shown in Fig. 3.16, where it is clearly visible that the typical domain size can be even more decreased by increasing $\tilde{J}_I^{-1}$.

We then observe that above the critical Ising parameter, we get systems featuring either a

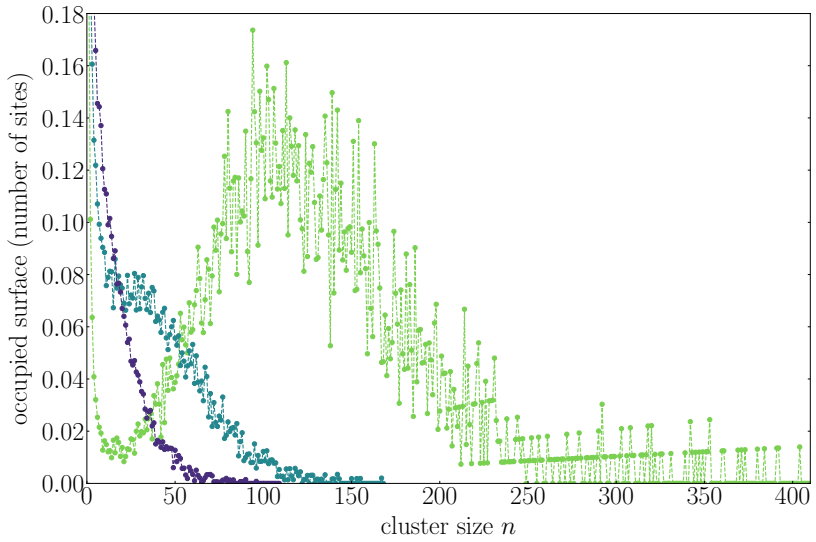

FIGURE 3.15 – Occupied surface in terms of number of sites. Effect of the Ising parameter on domain formation and on domain size distribution. From light green to dark blue, $\tilde{J}_I^{-1} = 2.5;\ 3.5;\ 4.5$. $\bar{\phi} = 0.2$, $\tilde{\sigma} = 300$ and $c_1 = 3.0$. Color lines are guides to the eye.

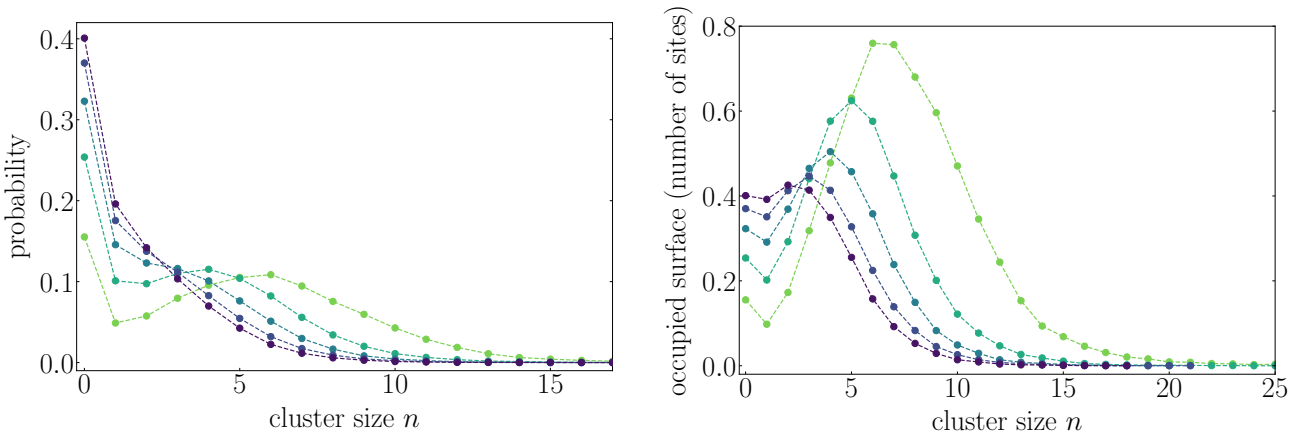

FIGURE 3.16 – Size distribution and occupied surface in terms of number of sites. Effect of the Ising parameter on domain formation and on domain size distribution. $\tilde{J}_I^{-1}$ varies from 1.5 to 3.5 with 0.5 increment from light green to dark blue. Other parameters are $\bar{\phi} = 0.2$, $\tilde{\sigma} = 300$ and $c_1 = 15.0$. Color lines are guides to the eye.

macrophase either domains depending on the range of parameters. We see that high $\tilde{J}_I$ favors phase separation, by increasing line tension. Oppositely, an increasing curvature coupling favors smaller domains whereas surface tension counters this curvature effect. The higher the surface tension is, the higher the cost due to the area excess is (proportional to $\tilde{\sigma}$). High surface tensions then favor phase separation whereas lower ones allow domain formation induced by curvature coupling. Combining the variations of these three key parameters $\tilde{J}_I$, c_1 and $\tilde{\sigma}$, one can get macrophase, disordered or modulated systems that we study in detail below in Section 3.2. In a certain range of parameters that we will characterize further, we get systems featuring mesopatterning: either mesodomains at low concentration $\bar{\phi}$, or labyrinthine mesophases when $\bar{\phi} \geq 0.5$ so that the A-species percolate through the system (see Fig. 3.2, upper right-most vesicles) as predicted for example in Refs. [KGL99; HMO05], by using a one-mode approximation. We

now need to quantify this regime of parameters in order to be able to determine the system state for each set of parameters and to physically characterize the different phase transitions.

3.2 Phase diagrams

In order to study the influence of the different parameters and to compare our results to the analytical predictions [GDM14], we construct a phase diagram. We focus on a 2D phase diagram in the $(c_1,\ \tilde{J}_I^{-1})$ space at fixed surface tension $\tilde{\sigma}$ and for a given concentration $\bar{\phi}$.

3.2.1 Phase diagram at $\bar{\phi} = 0.5$

We first focus on the phase diagram at concentration $\bar{\phi} = 0.5$, since it corresponds to the critical composition, for which analytical study was previously conducted in the group [GDM14]. The diagram shown in Fig. 3.17 compares the competing effects of the curvature coupling c_1 and the species affinity through the Ising parameter $\tilde{J}_I$. We clearly distinguish three regions instead of two in a classical Ising system without coupling:

- a disordered region for low $\tilde{J}_I$ and c_1 values, where the mixture is homogeneous and features no underlying order (blue crosses);
- a macrophase region for high $\tilde{J}_I$ values and low c_1 coupling, in which the lipid mixture undergoes complete macrophase separation (green crosses);
- a modulated phase region for large c_1 and low $\tilde{J}_I$, in which the vesicles feature more than one domain and where the mixture is then modulated (red crosses). This region contains the numerically indistinguishable structured disordered (low $\tilde{J}_I$) and structured ordered (high $\tilde{J}_I$) regions theoretically described in Section 2.1.5 and in [GDM14].

The coupling of the composition field to the shape fluctuations opens a zone in the phase diagram where phase modulation is possible and the transition is continuous through the $\tilde{J}_{I,c}$ crossing.

The vesicle states are classified into these different phases via the observation of the position of the structure factor maximum and its amplitude (see section 2.1.5). In some borderline cases, the distinction is unclear because the maximum position is difficult to determine accurately enough due to measurement errors and discretisation (see examples in Fig. 2.13). Moreover the phase determination has to take into account the finite size of our system, since $S(l)$ has a maximum in both cases disordered and macrophase. To distinguish them, we thus used the criteria for ρ set in 2.1.5. When the value of ρ was in-between, we depicted this with grey crosses. For some systems in the vicinity of the frontier between macrophases (dominant peak at $l = 1$) and structure ordered phases (dominant peak at $l = l^* > 1$), the peaks at $l = 1$ and at $l = l^*$ have comparable heights. We assigned orange crosses to these particular borderline cases.

We derive the analytical expressions of the region frontiers in the phase diagram. The expressions of $M(l)$ and $S(l)$ are given respectively by Eqs. (1.16) and (1.19). The equation of the frontier in the phase diagram between disordered (blue crosses) and structured disordered phases (red crosses) is defined in Eq. (2.18) and reads

$$c_1^* = \sqrt{2\hat{J}\hat{\sigma}}. \tag{3.5}$$

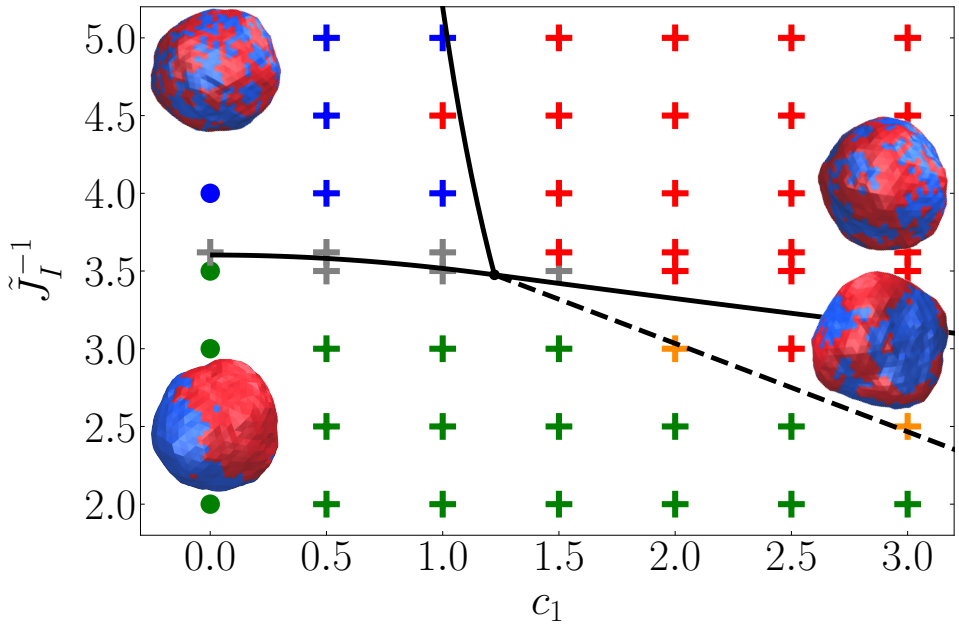

FIGURE 3.17 – Phase diagram in the $(c_1, \tilde{J}_I^{-1})$ parameter space with $\tilde{\sigma} = 300$ and $\bar{\phi} = 0.5$. Green crosses are macrophases, red ones modulated phases and blue ones disordered phases. The dots for $c_1 = 0$ are the case without coupling (exact results [Bax82]). The solid black lines are the analytical expressions, Eqs. (3.5) to (3.7), of the frontiers. The dashed line separates the macrophase and the structured ordered one [GDM14]. The snapshots correspond to the simulation points where they are located in the diagram.

As already mentioned in 2.1.5, the structure factor diverges at $\tilde{q}_c^2 = 0$ when $M(1) = 0$ leading to the equation

$$\hat{m} + c_1^2 + 4\hat{J} = 0 \tag{3.6}$$

that gives the frontier equation between macrophase separation and disordered phase (green/blue, solid line on the left side of the triple point). The equation of the frontier between structured disordered and structured ordered phases (solid line on the right side of the triple point) is obtained when S diverges for $\tilde{q}_c^2 \neq 0$ which leads to

$$\hat{m} + 2c_1^* c_1 - c_1^{*2} + 4\hat{J} = 0. \tag{3.7}$$

Again this theoretical frontier cannot be identified numerically for a finite-size system.

For higher $\tilde{J}_I$, the Gaussian Hamiltonian is no more valid and a term in ϕ^4 should be kept in the theory. This is beyond the scope of this work, thus the frontier between macrophase and structured ordered phases is determined only numerically and approximately shown with a dashed line in Fig. 3.17.

We now write the frontier expressions for Eqs. (3.5) to (3.7) with the dimensionless parameters and express $\tilde{J}_I^{-1}$ in function of c_1. Using Eq. (2.9), Eq. (2.10) and $\hat{\sigma} = \tilde{\sigma}/\tilde{\kappa}_0$, we get for Eq. (3.5)

$$\tilde{J}_I^{-1} = \frac{4\sqrt{3}\tilde{\sigma}}{\tilde{\kappa}_0^2 c_1^2} \tag{3.8}$$

and for Eq. (3.6) we get

$$\tilde{J}_I^{-1} = \frac{\tilde{J}_{I,c}^{-1} - \frac{8\sqrt{3}}{\alpha_0 N}}{1 + \frac{\tilde{\kappa}_0 c_1^2}{\alpha_0 N}} \tag{3.9}$$

For Eq. (3.7) it is more convenient to express c_1 in function of $\tilde{J}_I$:

$$\begin{aligned} c_1 &= -\frac{\alpha_0 N}{4(\sqrt{3}\tilde{\sigma}\tilde{J}_I)^{1/2}} \\ &+ \left(\frac{(\sqrt{3}\tilde{\sigma})^{1/2}}{\tilde{\kappa}_0} - 2\sqrt{\frac{\sqrt{3}}{\tilde{\sigma}}} + \frac{\alpha_0 N}{4\tilde{J}_{I,c}(\sqrt{3}\tilde{\sigma})^{1/2}} \right) \sqrt{\tilde{J}_I} \end{aligned} \tag{3.10}$$

The coordinates of the triple point, corresponding to the intersection of these 3 curves of Eqs. (3.8 - 3.10) are

$$c_1 = \left(\frac{\alpha_0 N \tilde{\sigma}}{\left[\alpha_0 N/(4\sqrt{3}\tilde{J}_{I,c}) - 2\right] \tilde{\kappa}_0^2 - \tilde{\sigma}\tilde{\kappa}_0} \right)^{1/2} \simeq 1.22 \tag{3.11}$$

$$\tilde{J}_I^{-1} = \tilde{J}_{I,c}^{-1} - 4\sqrt{3}\frac{\tilde{\sigma} + 2\tilde{\kappa}_0}{\alpha_0 N \tilde{\kappa}_0} \simeq 3.48 \tag{3.12}$$

with $N = 2562$, $\tilde{\sigma} = 300$, $\tilde{\kappa_0} = 20$, $\alpha_0 = 1/\pi$ and $\tilde{J}_{I,c}^{-1} \simeq 3.64$ on an infinite triangular lattice [Bax82].

Thanks to the phase diagram, we can then predict the mixture phase knowing the species affinity and the curvature at play. To take a realistic example for biomembranes, we can consider an asymmetric lipid mixture as described in [Ste+20]. Assuming that this mixture temperature T is 1 degree below its transition temperature T_c, one can determine the corresponding simulation parameter J_I by writing $k_B(T_c - T) = (4/\ln 3)(J_0 - J_I)$. We have $1 - T/T_c \simeq 1/300$ K. Using Eq. (2.5), we can relate it to $\tilde{J}_I - \tilde{J}_{I,c}$. Considering for example a vesicle radius of 500 nm, one gets the corresponding lattice parameter $a = (8\pi/\sqrt{3})^{\frac{1}{2}} R/\sqrt{N} \simeq 37$ nm for a 2562-vertices lattice and then $\tilde{J}_I - \tilde{J}_{I,c} \simeq 0.04$. Since $\tilde{J}_{I,c} \simeq 0.27$, we can deduce $\tilde{J}_I \simeq 0.31$ and $\tilde{J}_I^{-1} \simeq 3.2$. Considering the spontaneous curvature of this mixture measured to be approximately $C_1 = 0.01$ nm^{-1}, we can deduce the corresponding parameter $c_1 = C_1 R \simeq 5.0$ in the simulations. Extrapolating the phase diagram frontiers, we can predict that this regime of parameters would lead to mesopatterning.

Note that as already mentioned, with the Gaussian theory we do not take into account the terms in ϕ^4, hence $M(l)$ can become negative (see Eq. (1.16)) and in this case the structure factor is thus undefined since, by definition, $S(l) \geq 0$. This would not happen if we took into account all the terms in the Hamiltonian. However, numerically, we can overcome this limitation and we can measure the structure factor even for parameter values for which $M(l)$ is undefined in the Gaussian theory, as depicted in Fig. 3.18.

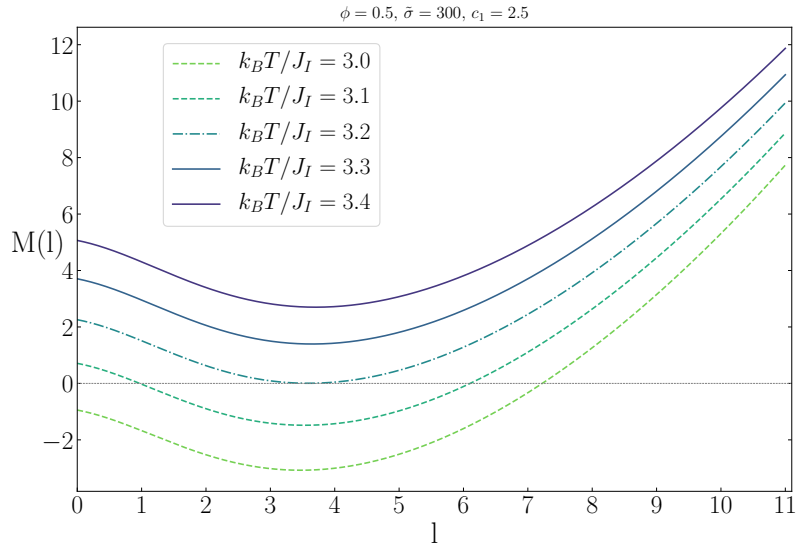

FIGURE 3.18 – $M(l)$ for different $\tilde{J}_I^{-1}$ values. Below $\tilde{J}_I^{-1} \simeq 3.2$, $M(l)$ becomes locally negative and the structure factor is thus undefined with the Gaussian theory approximations but can be measured numerically. Other parameters are $\bar{\phi} = 0.5$, $\tilde{\sigma} = 300$ and $c_1 = 2.5$.

3.2.2 Phase diagram at $\tilde{\sigma} = 600$

We also study the same phase diagram as in Fig. 3.17 at $\bar{\phi} = 0.5$ but at $\tilde{\sigma} = 600$ as presented in Fig. 3.19. As expected the frontiers are affected by this parameter change between the disordered phase and the modulated one (blue/red) and between the macrophase and the modulated one (green/red), respectively ruled by Eqs. 3.8 and 3.10 where $\tilde{\sigma}$ plays a role. The triple point is now obtained for $c_1 \approx 1.76$ and $\tilde{J}_I^{-1} \approx 3.35$. We recover the fact that when $\tilde{\sigma}$ is higher, c_1^* is higher, thus at a fixed $\tilde{J}_I^{-1}$ value one needs a higher curvature coupling c_1 to get modulated phases: increasing surface tension counters the formation of patterns as described in 3.1.2.

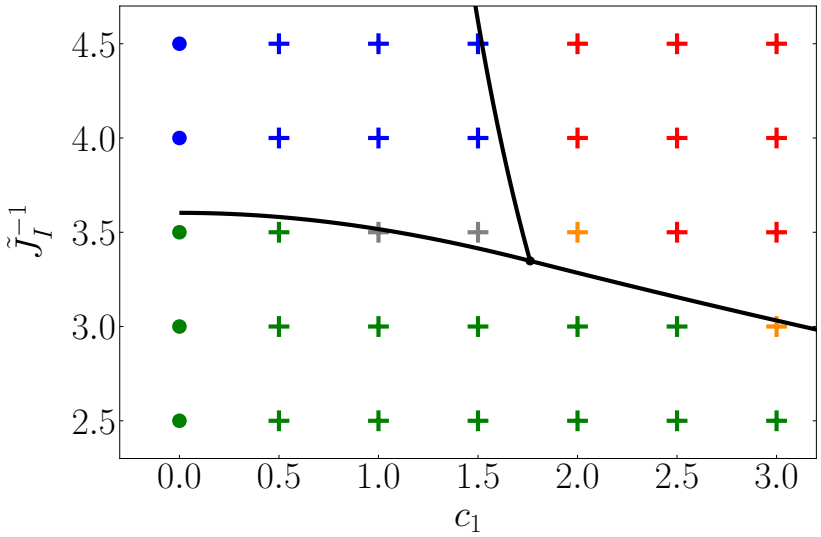

FIGURE 3.19 – Phase diagram in the $(c_1, \tilde{J}_I^{-1})$ parameter space with $\tilde{\sigma} = 600$ and $\bar{\phi} = 0.5$. Same color code as in Fig. 3.17.

3.2.3 Phase diagram at $\bar{\phi} = 0.2$

We also build the same phase diagram as in Fig. 3.17 but at $\bar{\phi} = 0.2$, as shown in Fig. 3.20. Although the theory we used is valid only at $\bar{\phi}_c = 0.5$, we observe that the phase diagrams at $\bar{\phi} = 0.2$ and $\bar{\phi} = 0.5$ are very similar, except in the close vicinity of the frontiers. The grey lines in Fig. 3.20 are the same as the ones in Fig. 3.17, derived from the theory at $\bar{\phi}_c = 0.5$, and are just a guide to the eye. They are quite close to the numerical region frontiers obtained at $\bar{\phi} = 0.2$.

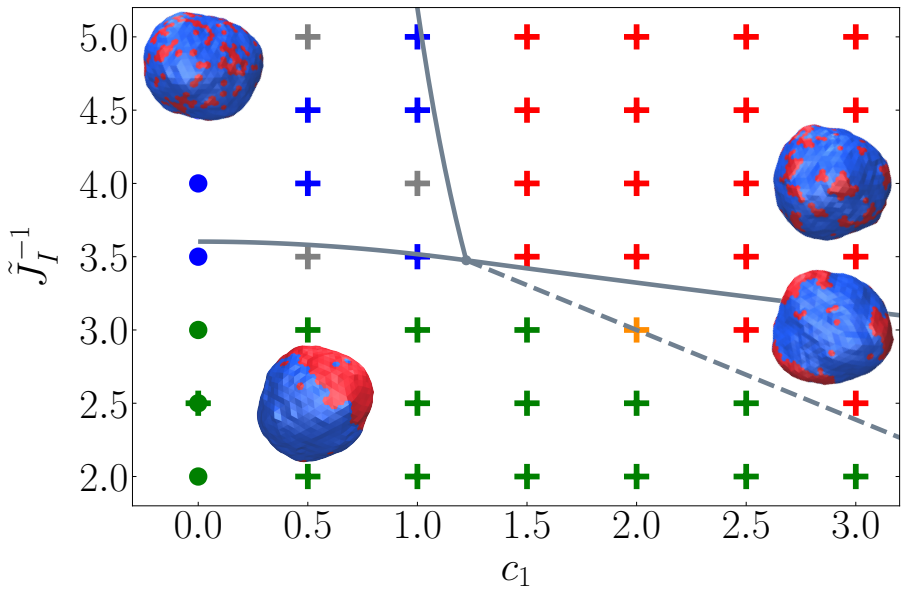

FIGURE 3.20 – Phase diagram in the $(c_1, \tilde{J}_I^{-1})$ parameter space with $\tilde{\sigma} = 300$ and $\bar{\phi} = 0.2$. The color code is the same as in Fig. 3.17. The grey lines are Eqs. (3.5-3.7) plotted with the parameter values for $\bar{\phi} = 0.5$, see Fig. 3.17.

Note that the vesicles in the phase diagrams have the same input, "bare" surface tension in the simulations but not exactly the same effective surface tension, which is modified by the curvature coupling (see Section 3.3).

3.2.4 Continuous behaviors at the transition

We performed simulations below and above the critical Ising parameter $\tilde{J}_{I,c}$. Correlation functions, structure factors and domain size distributions are plotted for different Ising parameters below and above the transition in Fig. 3.21. In the correlation functions, the undulations are far stronger above the transition with a prominent first undulation, but are still present below it, although weaker. One has to set the Ising parameter much lower to see them vanish, where the system becomes fully disordered. In the same way for size distribution, a second peak is clearly visible above the transition enhanced while increasing J_I (with bigger typical domain size). This peak is still visible below the transition but the typical domain size decreases while decreasing J_I, and the second peak eventually merges with the first peak corresponding to monomers. One does not notice any kind of discontinuity in the observable behavior at the transition. This is consistent with a smooth transition, which can be explained by the fact that the system does not undergo an actual thermodynamic phase transition owing to the finite size of the domains, as predicted in Ref. [Des10].

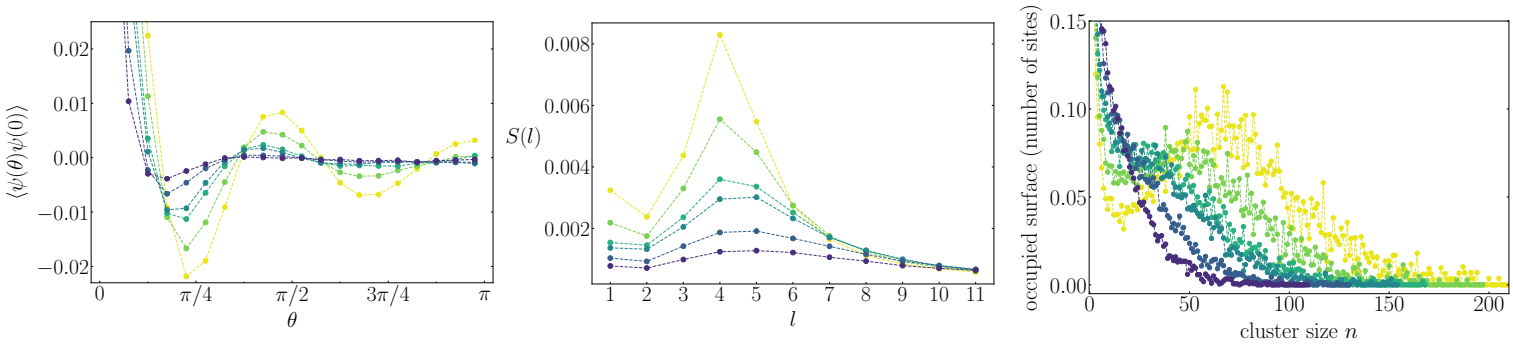

FIGURE 3.21 – Correlation functions, structure factor ($\bar{\phi} = 0.5$) and size distribution ($\bar{\phi} = 0.2$), from left to right, below and above $J_{I,c}^{-1} \approx 3.62$ (≈ 3.45 for $\bar{\phi} = 0.2$). $J_{I,c}^{-1} = 3.0$, 3.25, 3.5, 3.62, 4.0 and 4.5 from yellow to dark blue. Other parameters are $\tilde{\sigma} = 300$ and $c_1 = 3.0$. Color lines are guides to the eye.

3.3 Surface tension renormalization by curvature coupling and system size

In their article, Gueguen et al. (2017) explored the effect of renormalization of surface tension depending on the numerical parameters. They found that the effective surface tension actually "felt" by the vesicle $\tilde{\sigma}_{\text{eff}}$ and measured in its fluctuation spectrum is different from the "bare" surface tension in input of the simulations. For uniform spontaneous curvature c, the effective surface tension depends on c and on the number of sites N as

$$\tilde{\sigma}_{\text{eff}} = \tilde{\sigma} + \frac{1}{2}\tilde{\kappa}_0(2-c)^2 - \epsilon\frac{N}{8\pi} \tag{3.13}$$

$\tilde{\sigma}$ being the bare input surface tension in the simulation. Eq. (3.13) has been found by doing renormalization calculations of u^4 terms in [GDM17], Eqs. (15) and (73). In this work the local curvature c did not depend on ϕ. We then write here a mean-field extension of this expression by using the mean value of the curvature $\bar{c} = c_0 + c_1\bar{\phi}$.

Furthermore the value of the numerical prefactor ϵ depends on the type of vertex elementary moves chosen in the Metropolis algorithm. For radial moves used in our work we have $\epsilon = 3$. If in addition $c_0 = 2$, then we get

$$\tilde{\sigma}_{\text{eff}} = \tilde{\sigma} + \frac{1}{2}\tilde{\kappa}_0 c_1^2\bar{\phi}^2 - \frac{3N}{8\pi} \tag{3.14}$$

Note that this is a rough estimate for inhomogeneous membrane composition. A more precise expression should be obtained using renormalization calculations in future works.

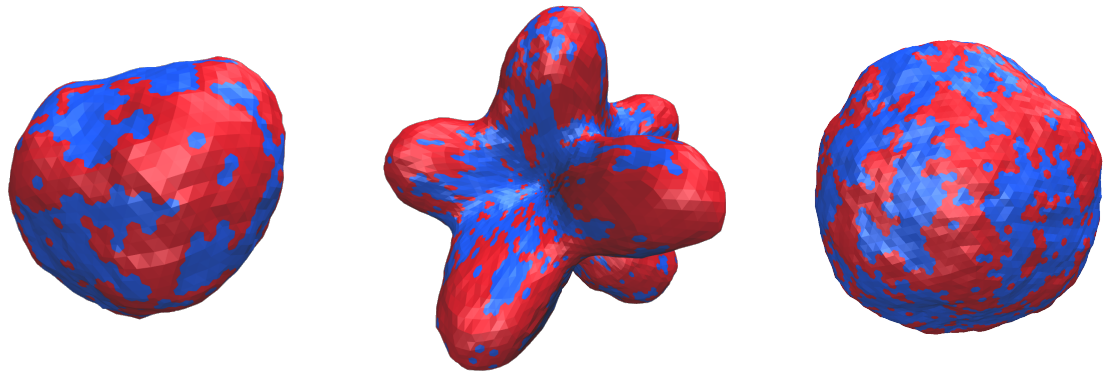

FIGURE 3.22 – Numerical verification of surface tension renormalization. Snapshots of 3 vesicles run with the same following parameters $\bar{\phi} = 0.5$, $\tilde{J}_I^{-1} = 4.0$ and $c_1 = 2.0$. The leftmost vesicle and the middle one were both run with $\tilde{\sigma} = 300$ but differ in their total number of sites, $N = 2562$ (left) and $N = 10242$ (center). The center vesicle and the rightmost one have the same number of sites $N = 10242$ but different input surface tensions, $\tilde{\sigma} = 1217$ (right).

Fig. 3.22 shows vesicles with different number of sites N and input surface tension $\tilde{\sigma}$. The leftmost vesicle and the middle one were both run with $\tilde{\sigma} = 300$ but differ in their total number of sites. The first one has $N = 2562$ vertices and is inflated, showing a quasi-spherical shape nevertheless close to the buckling transition ($\tilde{\sigma}_{\text{eff}} \simeq 4$), whereas the second one has $N = 10242$ vertices and appears deflated showing a star shape and strong deformations (here $\tilde{\sigma}_{\text{eff}} \simeq -913$).

The vesicle in the middle and the rightmost one have the same number of sites $N = 10242$ but different input surface tensions. The input surface tension of the rightmost vesicle ($\tilde{\sigma} = 1217$) was calculated so that it undergoes the same effective tension as the leftmost one ($\tilde{\sigma}_{\text{eff}} \simeq 4$) with the help of Eq. (3.13). It now shows a quasi-sherical shape and is as inflated as the leftmost vesicle. Comparing the two first vesicles that have the same input surface tension $\tilde{\sigma}$ but different number of sites N, we can numerically confirm the influence of the number of sites in the surface tension renormalization: the effective surface tension is lowered by the number of sites in the system as predicted by Eq. (3.13) by the term $-\frac{3N}{8\pi} \approx -300$ for $N = 2562$. Note that the coupling term $\frac{1}{2}\tilde{\kappa}_0 c_1^2 \bar{\phi}^2 = 10$ for $c_1 = 2.0$ and $\bar{\phi} = 0.5$ has a negligible contribution in comparison to the rightmost term implying the system size N. In order to obtain vesicles that keep the same level of inflation and a quasi-spherical shape when increasing the number of sites, one needs to compute the input surface tensions $\tilde{\sigma}$ using Eq. (3.13) so that the vesicles with different N "feel" the same effective surface tension $\tilde{\sigma}_{\text{eff}}$ as it was done for the rightmost vesicle in Fig. 3.22. We thus could numerically check the global behavior of surface tension renormalization depending on the system size provided by [GDM17] although more precise calculations need to be performed in the case of multi-component membrane.

Chapter 4

Bridging the scales: from coarse-grained to mescoscale simulations

Contents

We present here the work that we carried out with coarse-grained simulations in order to study the mechanisms at play in a patch of membrane, extract the membrane parameters, and make the connection with the upper scale, the mesoscale simulations previously described in Chapter 3. From a biophysical perspective, motivated by recent experimental findings [SIT16], we address the question of the role, in terms of local spontaneous curvature, of the glycosphingolipid GM1 inserted in the outer leaflet of a vesicle made of a lipid mixture featuring Lo and Ld phases. The gangliosides, the molecule family of GM1, are abundant in animal neurons and play important roles in several neuronal processes and diseases [Sch15; Aur+16]. They also act as membrane anchors for different toxins, bacteria and viruses [Ewe+10; Aur+16]. Contrary to phospholipids, the main components of biomembranes that have relatively small head groups, GM1 has a bulky head comprised of four monosaccharides [Mar10]. The shape conferred by its head makes GM1 able to generate locally strong curvature in a lipid bilayer, even at low concentration, when inserted in one of the two leaflets and thus resulting in bilayer asymmetry [Ewe+10; SL18]. The reported spontaneous curvature of GM1 (in a pure system) is 0.17 nm^{-1} [SIT16]. In their paper, Shimobayashi et al. (2016) studied GUVs made of DOPC - DPPC - cholesterol which undergo phase separation into Lo and Ld phases (see Section 6.2). They then added GM1 in the solution

that spontaneously inserted in the outer leaflet, preferentially in the Lo phase, and locally bent the membrane giving rise to smaller curved domains as shown in Fig. 4.1.

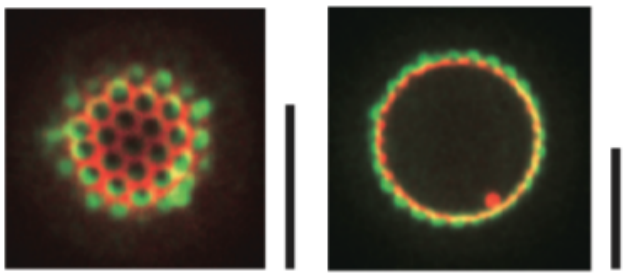

FIGURE 4.1 – Experiment of GM1 insertion in the Lo phase (green) locally bending the membrane in GUVs [SIT16]. Scale bars are 10 μm.

Adopting a multi-scale approach, we will extract parameter values from molecular-dynamics (MD) MARTINI simulations that will be useful for the larger scale Monte Carlo simulations as described above, in order to give a theoretical basis to these experimental findings. We use the methods presented in Section 2.2.

The systems studied are bilayers of 43 nm side length with periodic boundary conditions surrounded by 4 nm of water thickness at a temperature of 310 K and were simulated over 20 μs. Here we study a mixture DPPC (C16:0 dipalmitoyl) - DIPC (C18:2(9c,12c) dilinoleoyl) - cholesterol with concentration ratios 30:58:12 and with varying concentration of GM1 (C(d18:1/18:0) N-stearoyl-D-erythro) in the upper leaflet (see Figs. 4.2 and 4.3).

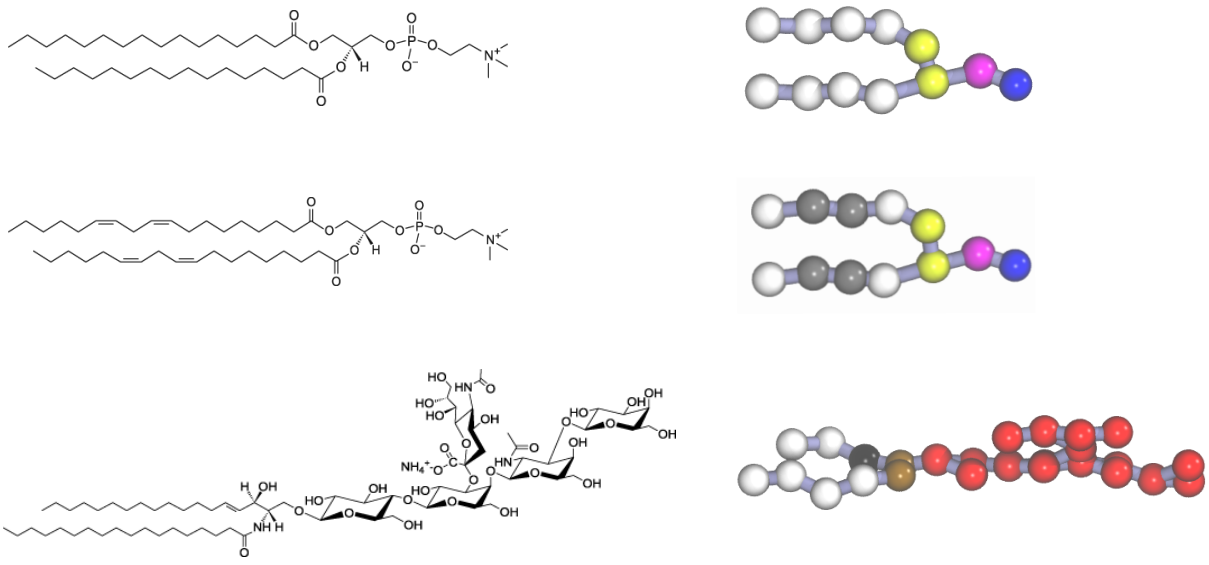

FIGURE 4.2 – Chemical formulas (left) and MARTINI representations (right) of the lipids used in the simulations. From top to bottom DPPC (C16:0 dipalmitoyl), DLPC (C18:2(9c,12c) dilinoleoyl, DIPC in MARTINI) and GM1 (C(d18:1/18:0) N-stearoyl-D-erythro, DPG1).

We checked that the bilayer upper and lower leaflet equilibrium areas were equal. We measured that they differed by $\sim 1\%$ at most which is low as compared to our measurement errors. In addition, the area per lipid values that we used in this calculations are only estimates provided

by CHARMM-GUI (2018) and are sensitive to the presence of cholesterol (that can diminish their values by 10 to 20% [CHA18]), which is our case.

4.1 Coarse-grained simulations analysis results

Qualitatively we can already observe that GM1 molecules colocalize with Lo phase (DPPC + cholesterol). This might result from hydrophobic mismatch effects. Indeed GM1 and DPPC have comparable carbonated chain length and nature. One also observes that GM1 tend to locally bend the bilayer as shown in Fig. 4.3. In order to compute different observables to study the

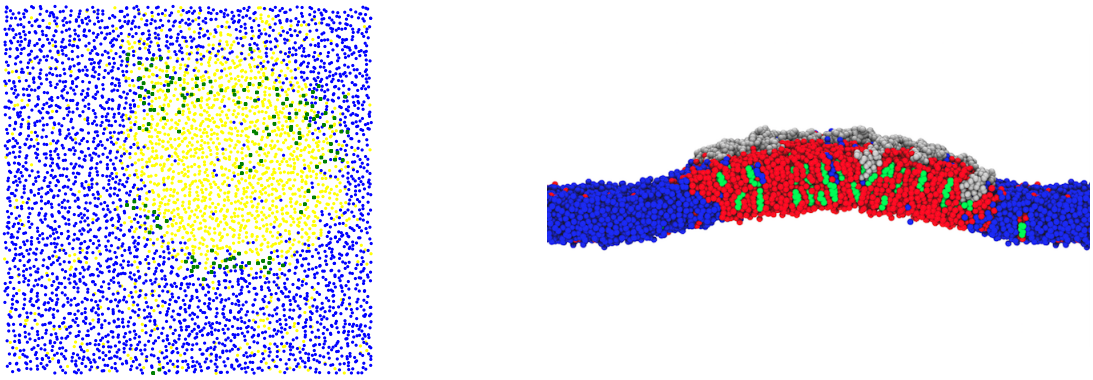

FIGURE 4.3 – Simulation of a bilayer of 43 nm side-length made of a mixture DPPC-DIPC-chol (30:58:12) and 5% of GM1 in the upper leaflet. **Left:** Spatial repartition of the species, top view of the last frame. Each molecule position is identified by the position of one bead in the leaflet plane (see text). DPPC (Lo) in yellow, DIPC (Ld) in blue and GM1 in green. **Right:** Simulation last frame cut. DPPC (Lo) in red, DIPC (Ld) in blue, cholesterol in green and GM1 in silver. One can notice the preferential localization of GM1 in the Lo phase and the important membrane local curvature.

role of GM1 in this mixture, we divide our membrane into a mesh of 15×15 zones (each box is then about 3 nm side). Each phospholipid position is identified by the coordinates of the bead corresponding to its phosphate group (pink bead in Fig. 4.2) and the GM1 positions by the coordinates of the bead labelled "GM5", which we checked to be located at a similar depth than the phosphate groups in the leaflet. We determine the centroid of the lipid heads in each box. The local composition of a box can then be computed as the ratio of DPPC molecules to the total number of molecules in the box (see Fig. 4.6).

4.1.1 Composition distribution

The composition distribution is computed as the fraction of DPPC molecules in each box as shown in Fig. 4.4. This enables us to determine the threshold above which a box is considered Lo (and Ld below). The threshold was set to a DPPC fraction of 0.6, where the composition distribution shows a marked minimum.

4.1.2 Quantification of phase segregation

In order to quantify phase separation degree, we compute the mean number of neighbors of the same species for each lipid throughout the simulation and plot it over time (see Fig. 4.5, left).

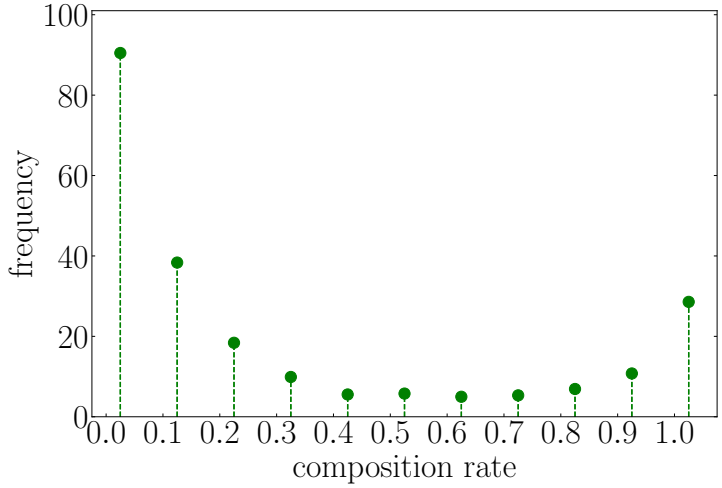

FIGURE 4.4 – Composition distribution. Fraction of DPPC in each box of the bilayer.

We use a cut-off distance d =13 Å to define the neighborhood zone, in order to have about six neighbors at equilibrium. One can see that this observable starts to reach a plateau but does not reach a stabilization close to the total number of neighbors. We can say that the phase separation is not total in this simulation and that at this temperature this mixture is not in the strong segregation regime.

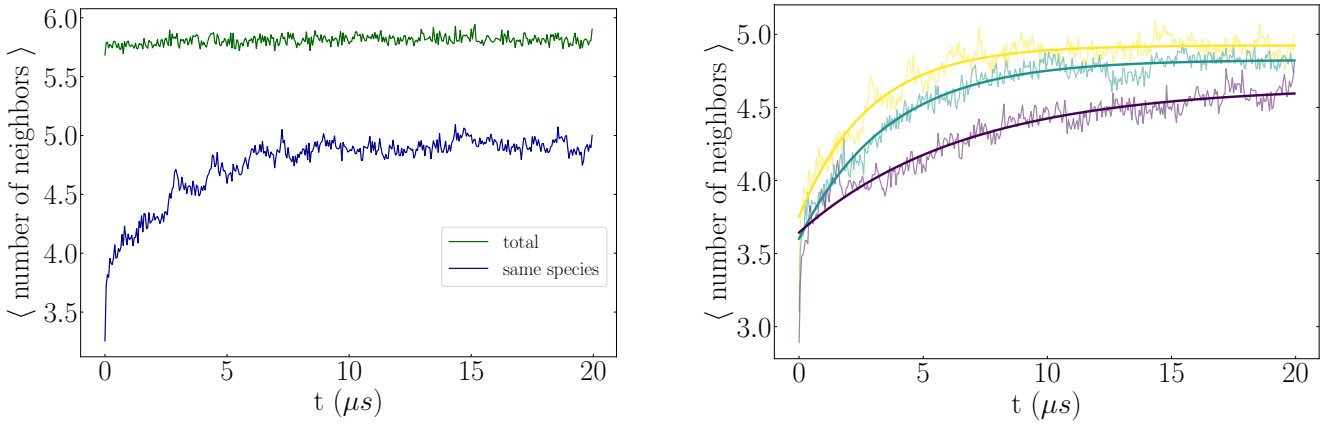

FIGURE 4.5 – **Left:** Mean number of neighbors of the same species for each lipid over simulation time in DPPC-DIPC-chol (30:58:12) mixture (blue). In green is represented the total number of neighbors. The cut-off distance d =13 Å was used to determine the neighbors of each lipid. **Right:** Mean number of neighbors of the same species fitted with $\langle n(t)\rangle = A - Be^{-t/\tau}$. This fit allows one to extract the typical equilibration time τ. One gets $\tau \simeq 2.8$, 3.6 and 6.6 μs for GM1 fractions 0 (yellow), 0.05 (green) and 0.1 (purple) respectively.

An equilibrium time on the order of few μs can be inferred from this measurement via the fit of this curve with $\langle n(t)\rangle = A - Be^{-t/\tau}$ (Fig. 4.5, right). We check that it is on the same order of magnitude than the typical time needed by a lipid to explore the whole simulated surface. One can notice that this equilibrium time increases with the concentration of GM1, suggesting that the presence of GM1 slows down the phase separation process (Fig. 4.5, right).

4.1.3 Local composition, thickness, curvature and their correlations

Over regular simulation steps the composition ratio is computed in each box and then binarized with the threshold defined in Section 4.1.1 so that the 2 different phases are identified. The boundary of the Lo phase is also identified. All the following measurements are performed after 5 μs so that phase separation is essentially reached. We compute local composition, thickness and curvature in the mesh grid (see examples in Fig. 4.6) and measure their correlation.

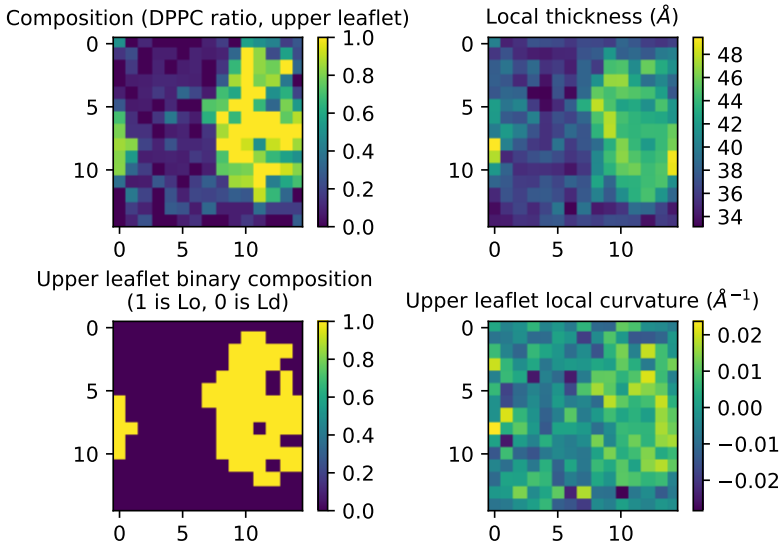

FIGURE 4.6 – Examples of analysis performed for a DPPC-DIPC-chol (30:58:12) mixture with 10% GM1 in the upper leaflet. The bilayer is divided into a 15×15 mesh. From left to right and top to bottom, composition repartition in terms of DPPC ratio, Lo-Ld binarization, local thickness and local curvature, computed for each box.

The local thickness is calculated via the difference of position of the corresponding box centroids in the two leaflets, for the Ld and the Lo phase (Fig. 4.7). We find an average membrane thickness for all GM1 concentration of approximately 4 nm. As expected, the Lo phase is thicker than the Ld one (see Section 6.2).

In order to compute the local curvature of the upper leaflet for the different phases, we use a 2D discrete Laplacian (4 nearest neighbors) applied on the mesh height field. Note that here the sign convention is the opposite of the one in the rest of the manuscript, i.e. a negative curvature is associated to a zone bending outwards the bilayer. Note also that we measure the curvature of the upper leaflet and not of the whole bilayer. The upper leaflet shows a Lo domain thicker than the surrounding Ld phase as shown above. This results in a weak negative curvature induced by the Lo domain, even in the absence of GM1 inclusions. Because of periodic boundary conditions, the total curvature averaged on the whole system exactly vanishes. We see in Fig. 4.8 (left) that we indeed measure a higher curvature for the Lo phase, where GM1 are mainly inserted, than in the Ld one. When increasing the GM1 fraction in the upper leaflet (Fig. 4.8, right), the Lo domain curvature gets more important.

We also measure the correlations between these observables. We measure the composition correlation between the two leaflets (when the same species are facing each other, which is named

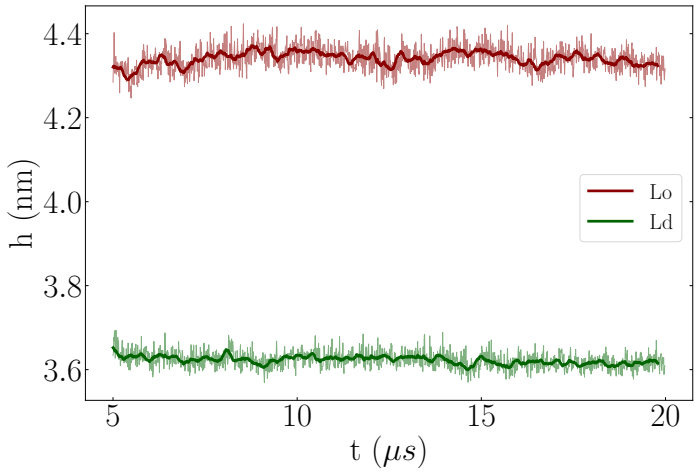

FIGURE 4.7 – Local thickness measurement through time, averaged for Lo and Ld phase separately. DPPC-DIPC-chol (30:58:12) mixture. Here and in the following figures, the thick lines are sliding averages on a 0.2 μs window.

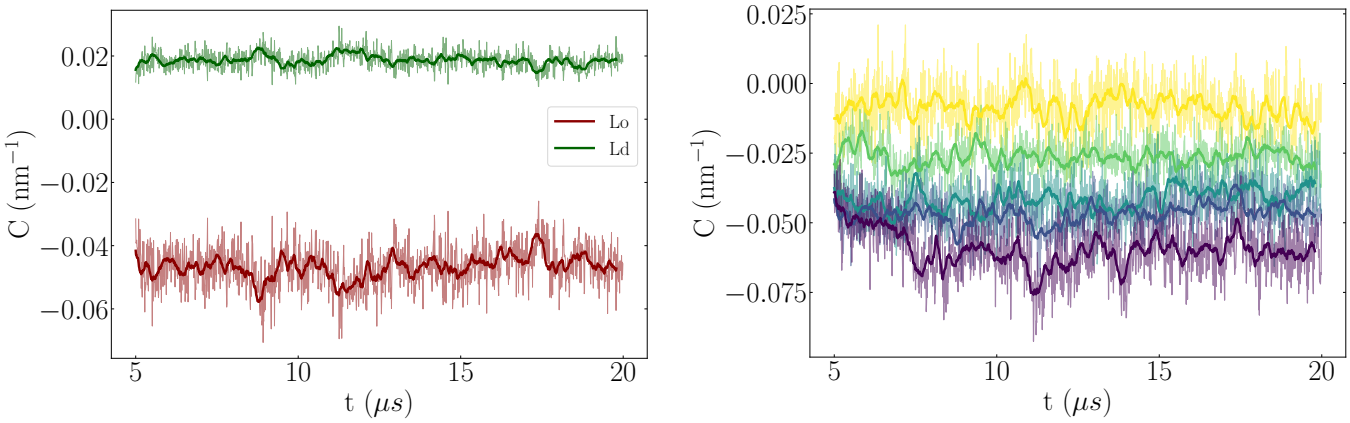

FIGURE 4.8 – **Left:** Local curvature measurement through time, averaged for Lo and Ld phase separately, in the upper leaflet. DPPC-DIPC-chol (30:58:12) mixture with 7.5% GM1 in the upper leaflet. **Right:** Curvature of the Lo phase from 0 to 10% GM1 in the upper leaflet (by increments of 2.5) from yellow to purple.

registration) at a given time step following

$$g(\phi^0, \phi^1) = \frac{1}{N} \sum_{i,j} \frac{\phi^0_{ij}\phi^1_{ij} - \langle\phi^0\rangle\langle\phi^1\rangle}{s(\phi^0)s(\phi^1)} \tag{4.1}$$

with ϕ^0 and ϕ^1 being the binarized compositions in the upper and lower leaflet respectively, s the standard deviation and N the number of sites of the mesh taken into account (here 225). We normalize by the standard deviation so to get a value ranging from 0 to 1. We check in Fig. 4.9, left, that the leaflet composition are quite in register.

In an equivalent manner, we compute the correlation between the local thickness and the local composition ϕ of the bilayer (average box composition of both leaflets) defined as

$$g(h,\phi) = \frac{1}{N}\sum_{i,j}\frac{h_{ij}\phi_{ij} - \langle h\rangle\langle\phi\rangle}{s(h)s(\phi)} \tag{4.2}$$

with h the local bilayer thickness. We notice in Fig. 4.9, right, a strong correlation between the local thickness and the binarized composition of the bilayer, as expected.

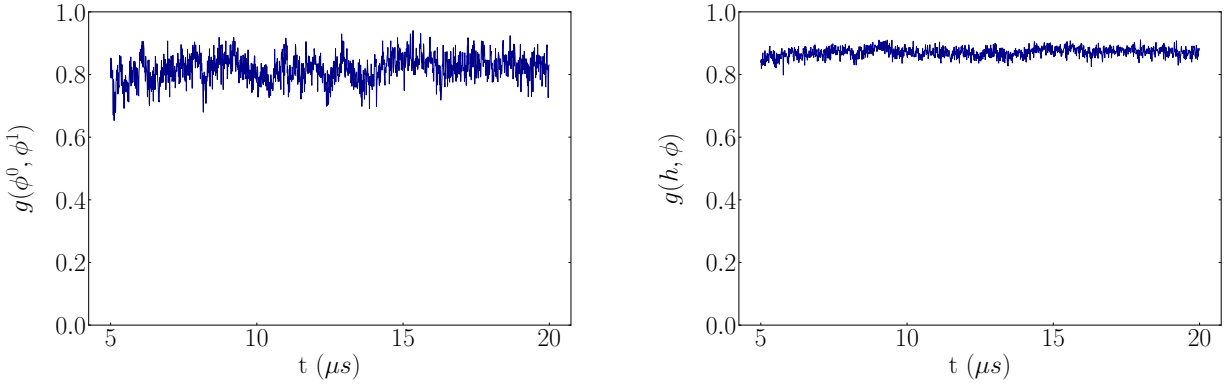

FIGURE 4.9 – Correlation between the binarized composition fields of the 2 leaflets (registration), left, and between the binarized composition field of the bilayer and the local thickness through time, right. DPPC-DIPC-chol (30:58:12) mixture.

We also compute $g(C,\phi^0)$ providing information about the correlation between the local curvature and the composition of the upper leaflet:

$$g(C,\phi^0) = \frac{1}{N}\sum_{i,j}\frac{C_{ij}\phi^0_{ij} - \langle C\rangle\langle\phi^0\rangle}{s(C)s(\phi^0)} \tag{4.3}$$

with C being the local upper leaflet curvature. We can see as well in Fig. 4.10 a correlation between the composition of the upper leaflet and the local curvature, which appears to be higher in the Lo phase where GM1 are inserted. This correlation increases with GM1 fraction (Fig. 4.10).

We finally measure the relative ratios of GM1 molecules that are located in the Lo and Ld phases and at the Lo phase boundary, weighted by the corresponding area ratios (Fig. 4.11). We compute for instance the number of GM1 molecules in the Lo phase over the Lo domain area and divide it by the total number of GM1 molecules over the leaflet area. This confirms that in our simulations, the GM1 molecules preferentially partition into the Lo phase as observed experimentally by Shimobayashi et al. (2016). We conduct the same measurement for the GM1 molecules located in the Lo domain boundary zone in order to verify if GM1 preferentially get located at the boundary. Our results indicate that they are roughly homogeneously distributed in the domain, the ensuing curvature is then quasi-uniform in the domain.

We are now interested in studying the local curvature as a function of GM1 concentration (Fig. 4.12). The reference curvature chosen is the local curvature imposed to the leaflet by the Lo domain without GM1 insertions ($C \simeq 0.0087$ nm^{-1}). We thus plot the difference of curvature between the Lo domains enriched in GM1 and this reference system against the GM1 fraction.

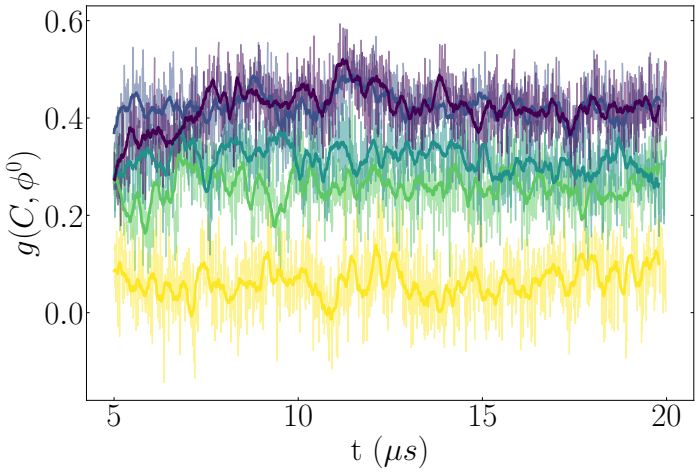

FIGURE 4.10 – Correlation between the binarized composition field of the upper leaflet and the local curvature through time. DPPC-DIPC-chol (30:58:12) mixture with percentage of GM1 in the upper leaflet varying from 0 (yellow) to 10 (purple).

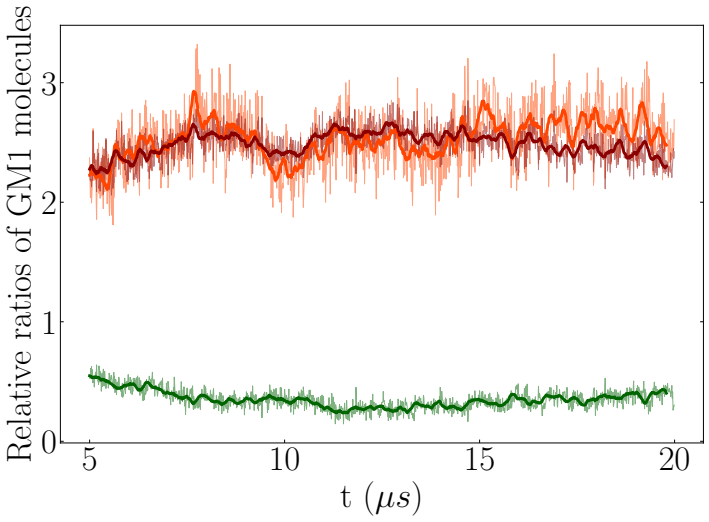

FIGURE 4.11 – Relative ratios of GM1 molecules located in the Ld (green) and Lo (red) phases and at the Lo phase boundary (orange) weighted by the corresponding area ratios. DPPC-DIPC-chol (30:58:12) mixture with 10% GM1 in the upper leaflet.

The curvature values are averaged on the measurements shown in Fig. 4.8 (right) from 10 to 20 μs to ensure that they are extracted from equilibrated domains. We find that the difference of curvature C_1 between the Lo domain with GM1 insertions and the reference depends linearly on the GM1 fraction ϕ_{GM1} as $C_1 \simeq 0.5\,\phi_{\text{GM1}}$ nm^{-1}. It confirms our assumption that the local curvature increases linearly with large-head lipid inclusion concentration and thus with the bilayer compositional asymmetry. Sreekumari et al. (2018) also performed coarse-grained simulations of bilayer composed of small-head lipids and large-head lipid inclusions in the upper leaflet and also found a linear law between large-head lipid fraction and curvature: $C_1 \simeq 0.4\,\phi_{\text{GM1}}$ nm^{-1} with a bilayer thickness of 4 nm.

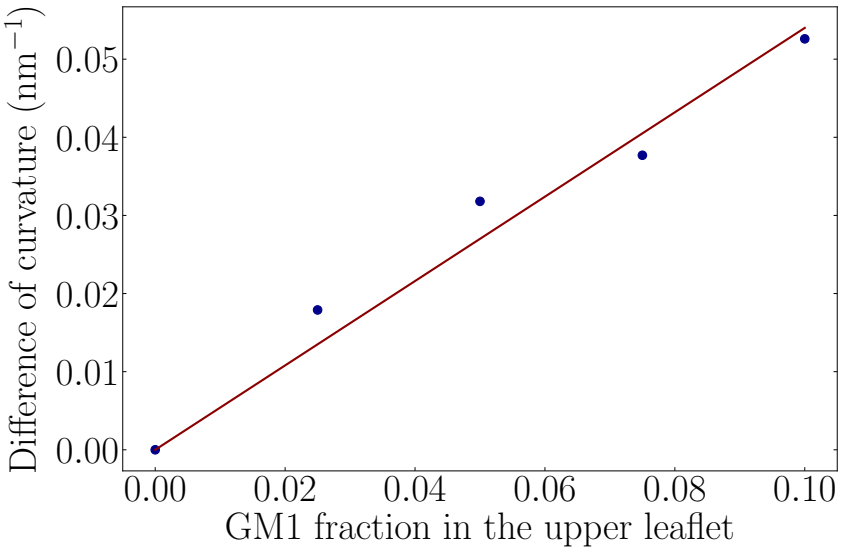

FIGURE 4.12 – Difference of curvature between the Lo domain with GM1 and the reference Lo domain without GM1. DPPC-DIPC-chol (30:58:12) mixture with 0, 0.025, 0.05, 0.075 and 0.1 GM1 fraction in the upper leaflet.

4.1.4 Line tension measurement

To measure the line tension at the boundary of Lo and Ld phases in a mixture without GM1, we measure the fluctuations of the Lo domain boundary. We use the same method as the one applied on fluorescence microscopy images in [Esp+07] or in mesoscale simulations [EPS11]. We apply a threshold (see above) in order to delineate the Lo-Ld boundary and use a polar (r, θ) discretization [1] to write it as a function of θ (see Fig. 4.13, left). We then calculate the Fourier series of this function $\langle u_n \rangle$. We use Eq. 3 of Ref. [Esp+07] to directly link the power spectrum of the boundary fluctuations to the line tension λ of the mixture. With our convention for the Fourier coefficients, we obtain

$$\langle |u_n|^2 \rangle = \frac{k_B T}{2\pi\lambda R_0 (n^2 - 1)} \tag{4.4}$$

with R_0 the equivalent radius of a non-fluctuating domain defined as $\langle r(\theta) \rangle = R_0(1 - \frac{1}{4}\sum_{n>0}\langle |u_n|^2 \rangle$, $\langle r(\theta) \rangle$ being the average radius of the domain.

We plot $\langle |u_n|^2 \rangle$ against $1/(n^2 - 1)$ and measure the slope from a linear fit (see Fig. 4.13, right). We consider only the first modes to avoid discretization effects. We get a value for the line tension $\lambda \simeq 3$ pN for a DPPC-DIPC-chol (30:58:12) mixture at $T = 310$ K. This order of magnitude is in agreement with line tension measured experimentally in GUVs with Lo and Ld domains [DMC18].

1. We use concentric circles of radii separated by 2 nm and 20 angular sectors.

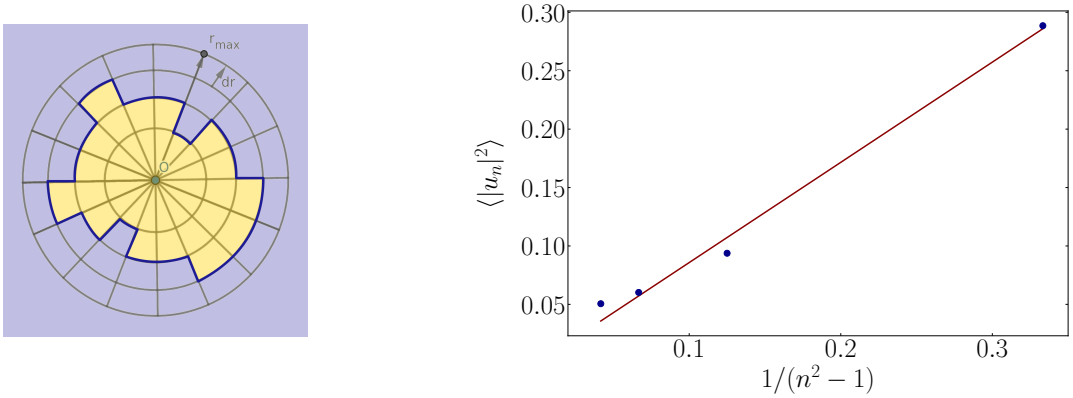

FIGURE 4.13 – **Left:** Scheme of the polar discretization (r, θ) applied to a Lo domain and determination of the Lo-Ld boundary as a function $r(\theta)$. Courtesy of Nelly Coulonges. **Right:** Power spectrum of the Lo-Ld boundary in a DPPC-DIPC-chol mixture from which the line tension λ is extracted. The values of the y-axis must be divided by $2\pi^2$.

4.2 Link between the extracted parameters at the coarse-grained scale and the parameters of the mesoscale model

In order to bridge the two modeling scales, coarse-grained and mesoscale, we need to establish the link between the parameters that we measure in the MD simulations with the input parameter of the mesoscale description.

After measuring the line tension λ, we can have access to the Ising parameter at the molecular scale as explained in Section 2.1.1. Close to the critical point, λ depends algebraically on $J_{I,0} - J_{I,c}$ and vanishes at the critical point. Renormalization arguments show that both quantities are in fact proportional for the 2D Ising model universality class. More precisely,

$$\lambda = \frac{4\sqrt{3}}{l_0}(J_{I,0} - J_{I,c}). \tag{4.5}$$

The prefactor depends on the lattice and is equal to $4\sqrt{3}$ on a triangular lattice [SZ01]. Owing to Eq. (2.5), we also have

$$\lambda = \frac{4\sqrt{3}}{a}(J_I - J_{I,c}). \tag{4.6}$$

This enables us to establish the link between the molecular and the mesoscale simulations. We can relate the Ising parameter and the line tension with the lattice spacing a through Eq. (4.6). As an example, with an Ising parameter $J_I = 0.5 k_B T$ as used in Chapter 3 and the line tension measured above in Section 4.1.4 $\lambda \approx 0.15$ pN one gets $a \simeq 40$ nm. Using $a = (8\pi/\sqrt{3})^{\frac{1}{2}} R/\sqrt{N}$, one can then calculate the corresponding radius associated to the N-vertices vesicle simulated at the mesoscale, $R \simeq 500$ nm (for $N = 2562$). For a measured local curvature of $C_1 \simeq 0.04$ nm^{-1}, for example at 8% GM1 in the leaflet, one gets $c_1 = RC_1 \simeq 20$ as an input value for the A-species spontaneous curvature in the mesoscale simulations. Another possible pathway is to start from a c_1 value used in mesoscale simulations and to infer the consequent real-unit curvature C_1. For instance, $c_1 = 15$ (see Fig. 3.8) leads to $C_1 \simeq 0.03$ nm^{-1} for this vesicle radius. Owing to

the relation drawn from Fig. 4.12, $C_1 \simeq 0.5\,\phi_{\mathrm{GM1}}$ nm^{-1}, one can estimate the GM1 fraction responsible for this curvature, $\phi_{\mathrm{GM1}} \simeq 0.06$.

The analysis of bilayer simulations at the molecular level thus provides us with reprensentative membrane parameter values that can be injected into the mesoscale model. In this way, the simulations can then be tuned in order to tackle different biologically relevant systems at large length and time scales. In the near future, my supervisors and M. Chavent and E. Haanappel (IPBS) intend to confront the so-obtained numerical predictions of the mesoscale model to fluorescence microscopy experiments on real GUVs, by using the same protocol as Shimobayashi et al. (2016).

Chapter 5

Domain shape study and comparison to experimental virus receptor trajectories

Contents

The project described in this chapter started in an amusing way: during my Master program course "programming", we had to develop a data analysis program, using biological data of our choice. I asked Nicolas, who had been collaborating with Laurence Salomé's group for a long time, and I was lucky to get interesting unpublished data. In their experiments of SPT (Single Particle Tracking) on cell membrane proteins, Fabrice Dumas and his coworkers had noticed that some confinement domains seemed to appear more elongated when these proteins were overexpressed. They were interested in quantifying the domain shapes to investigate whether and how protein concentration could influence domain morphologies, a higher concentration leading to domain elongation. This chapter is then the fruit of our collaborative work starting from this question. In the following, all the experiments mentioned were performed in Laurence Salomé's group of the IPBS, Toulouse, by Fabrice Dumas and his coworker Pascal Preira.

5.1 Experimental data analysis

We study the trajectories of transmembrane proteins CD4 (glycoprotein) and its coreceptors CCR5 and CXCR4 confined into domains. The two latest are GPCRs (G protein-coupled receptors) members of the largest family of membrane receptors [LP09]. These are transmembrane proteins involved in cell signalling and then in a variety of physiological processes. HIV infection requires the sequential interaction of the viral protein gp120 with the CD4 protein and then

the CCR5 or CXCR4 coreceptors of CD4 T cells (for review see [TP07] and [DH17]). The infection is not only determined by the presence of these proteins since the fusion is a cooperative process requiring the availability of several receptor and co-receptor molecules. For instance, it has been shown that the efficiency of infection depends on the surface density of receptors and corecepteors [Via+02; Her+07; MD11]. Moreover, it has also been shown that the distribution of CD4 on the surface of the plasma membrane of the target cells is heterogeneous and depends on the nature of the membrane lipids [Sin+01; Jun+16]. The location of these receptors into rafts during viral entry is still controversial. They have been suggested to be located in rafts in some studies [TP07] whereas other works as Gaibelet et al. (2006) showed that CD4-CCR5 interaction takes place outside raft domains. It has been shown experimentally that CD4 and CCR5 do interact into membrane domains (not necessarily rafts), with statistically one CD4 molecule interacting with about 5 CCR5 ones, and that this interaction is strengthened by viral protein action [Kuh+00; Bak+07]. These various observations have led some authors to propose the existence of domains which, by concentrating the receptors for the virus, would favour its entry into the target cells [SH03; Gai+06; DH17]. To verify this hypothesis, non-invasive methods such as single particle tracking have been used to study the compartmentalization of these receptors within membrane domains and the consequence of this concentration on membrane organization.

Thanks to the cell-line system developed by Johnston et al. (2009) described in Appendix C, F. Dumas and his coworkers have been able to generate cells presenting a high ($\sim 10^5$) or a low ($\sim 10^4$) number of copies of each protein (CD4, CCR5 and CXCR4) at their surface with any possible combination. It is important to note that this model is relevant regarding HIV infection since, whatever the expression level of the three proteins, even though they are not lymphocytes, the cells can be infected by HIV (F. Dumas, private communication). These cell lines - which were initially set up to study the interdependent function of CD4, CCR5 and CXCR4 during infection - are ideal for studying the influence of protein expression on the shape of membrane domains.

5.1.1 Observations and quantification methods of membrane domain shape

In our study, the proteins described above are labelled and tracked by Single Particle Tracking (SPT) technique as illustrated in Fig. 5.1. SPT is a technique of choice to study the dynamics of membrane proteins, to identify a confinement zone of these proteins and to determine its size and shape (for review see [AGT09]). It allows one to access a membrane molecule trajectory by binding a dye to it and tracking the dye by videomicroscopy coupled to image analysis. Thanks to this technique, F. Dumas and coworkers were able to acquire the trajectories of CD4, CCR5 and CXCR4 proteins at the surface of live cells for different combinations of expression level of these proteins.

The confined part of the trajectories were isolated thanks to the method developed in Meilhac et al. (2006). The proteins diffuse in the lipid membrane and their diffusion regime differs according to their freedom of motion. They can diffuse freely in the membrane plane or can be transiently trapped into relatively stable membrane domains (transient confinement zones). The trajectories of proteins diffusing in a constrained area show a noticeable fast diffusion regime at

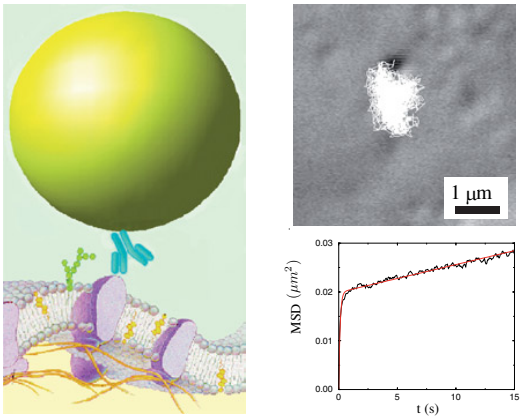

FIGURE 5.1 – **Left:** illustrative principle scheme of the SPT technique. The membrane molecule of interest, a lipid or a protein, is labelled with a dye bound via an antibody. The dye is tracked by videomicroscopy. **Right, top:** acquired trajectory by this technique over 2 min. **Right, bottom:** the mean square displacement of the dye position against time computed from this trajectory. At large timescales the diffusion is slow whereas at short timescale it is fast and confined. Figure drawn from [SLD06].

short timescales (see Fig. 5.1) and confined sequences can be identified based on their confinement index suggesting that the proteins are trapped in membrane domains (see [Mei+06] for more details about this detection method). The data collected give the (x, y) coordinates of the confined parts of the trajectories of the tracked proteins every 40 ms. The localization precision has been measured over 80 seconds to be of 7 nm in x and y directions [Mas12]. See examples in Fig. 5.2.

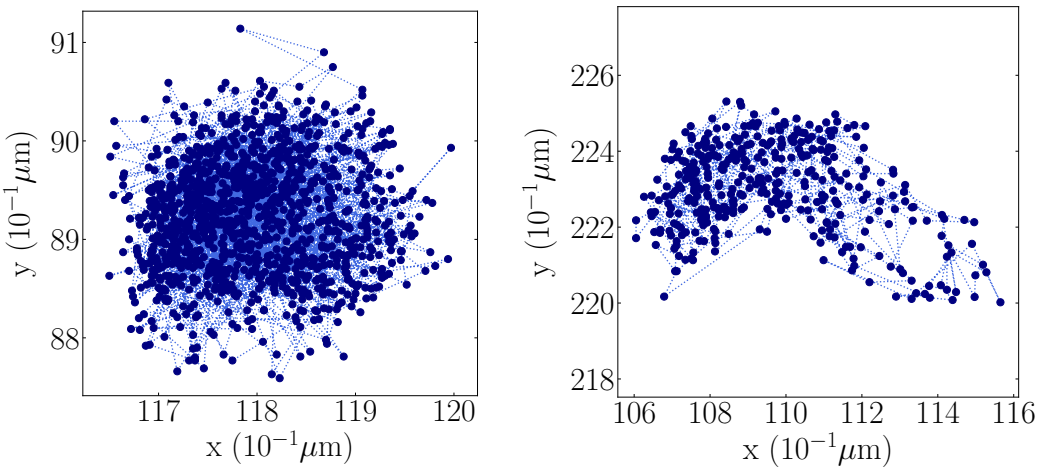

FIGURE 5.2 – Examples of trajectories of proteins confined in domains. The tracked protein here is the GPCR CCR5. In the data we observe domains that are more roundish when the proteins are not overexpressed (left) and more elongated ones, notably when the proteins are overexpressed (right).

These trajectories give us information about domain size and shape. We are especially interested in domain shape since it has been noted that the domains seemed to be more elongated when the proteins were overexpressed in the membrane, whereas they were more roundish in the

case of basal state expression. The same kind of elongated clusters were also observed for other membrane proteins, for example for overexpressed syntaxin clusters observed by superresolution microscopy [Mer+17] (compare Figures 5 and 5S therein) or μ-opioid receptors (h-MOP) tracked by SPT (Laurence Salomé, private communication). To quantify this shape, we decided to study the aspect ratio of the observed domains, drawn from a principal component analysis. We compute it from the eigenvalues of the covariance matrix that characterizes domain anisotropy:

$$\begin{pmatrix} \sigma_x^2 & \mathrm{cov}(x,y) \\ \mathrm{cov}(x,y) & \sigma_y^2 \end{pmatrix} \tag{5.1}$$

$$\text{with } \sigma_x^2 = \frac{1}{N}\sum_{i=1}^{N} x_i^2 - \left(\frac{1}{N}\sum_{i=1}^{N} x_i\right)^2 \text{ and } \mathrm{cov}(x,y) = \frac{1}{N}\sum_{i=1}^{N} x_i y_i - \left(\frac{1}{N}\sum_{i=1}^{N} x_i\right)\left(\frac{1}{N}\sum_{i=1}^{N} y_i\right), \tag{5.2}$$

N being the number of points forming the trajectory and (x, y) their Cartesian coordinates in the membrane plane.

Let us name λ_1 and λ_2 the eigenvalues of this matrix with $\lambda_1 > \lambda_2 > 0$. The aspect ratio (AR) of the domain is defined as the square root of the ratio of the major axis and the minor axis of the domain:

$$\mathrm{AR} = \sqrt{\frac{\lambda_1}{\lambda_2}} \tag{5.3}$$

The eigenvalues are equivalent to position variance. After diagonalization, in the new basis, we have

$$\sigma'_x = \sqrt{\lambda_1} \quad \text{and} \quad \sigma'_y = \sqrt{\lambda_2} \tag{5.4}$$

Now we want to relate the area of the domain to these eigenvalues. We begin with a circle where

$$\langle r^2 \rangle = \langle x^2 \rangle + \langle y^2 \rangle = \frac{1}{\pi R^2}\int_0^R r^2 2\pi r \mathrm{d}r = \frac{R^2}{2} \tag{5.5}$$

Hence

$$\sigma_x'^2 = \sigma_y'^2 = \langle x^2 \rangle = \langle y^2 \rangle = \frac{R^2}{4} \tag{5.6}$$

Then the domain area $\mathcal{A}$ writes

$$\mathcal{A} = \pi R^2 = 4\pi \sigma'_x \sigma'_y = 4\pi\sqrt{\lambda_1 \lambda_2} \tag{5.7}$$

when the point distribution is uniform in the domain. The same can be written for an ellipse after a dilation in the x or y direction.

We have to set a threshold for this aspect ratio above which domains are considered elongated and roundish below. We set this threshold value to 2, characterizing a domain with a principal dimension twice bigger than the other one, above which we consider that the domain is elongated. This threshold comes from the numerical distribution showing a "hinge point" for this value when concentration is increased and domains start to become more elongated, see below.

We plot the aspect ratio distribution for different experimental conditions. In some SPT experiments one type of receptor is tracked (CD4, CCR5 or CXCR4) and is present in the membrane with basal expression or overexpression. We can then study the influence of overexpression of one receptor on the shape of its own domains. In other cases, we can quantify the domain shape of one receptor and study it in function of the overexpression or not of one of the other receptors. The study of the correlation between one receptor overexpression and the domain shape of another one can be a hint for our understanding of their interaction and possible colocalization into nano-domains. We then compute the p-values based on the aspect ratio lists of two samples with the help of the Student t-test tool provided by Wolfram Mathematica [KA13] (unpaired two-tailed t-test) and used the significance threshold $p < 5 \times 10^{-2}$. In the figure captions, the p-values are indicated in green when they are below this threshold and in red otherwise.

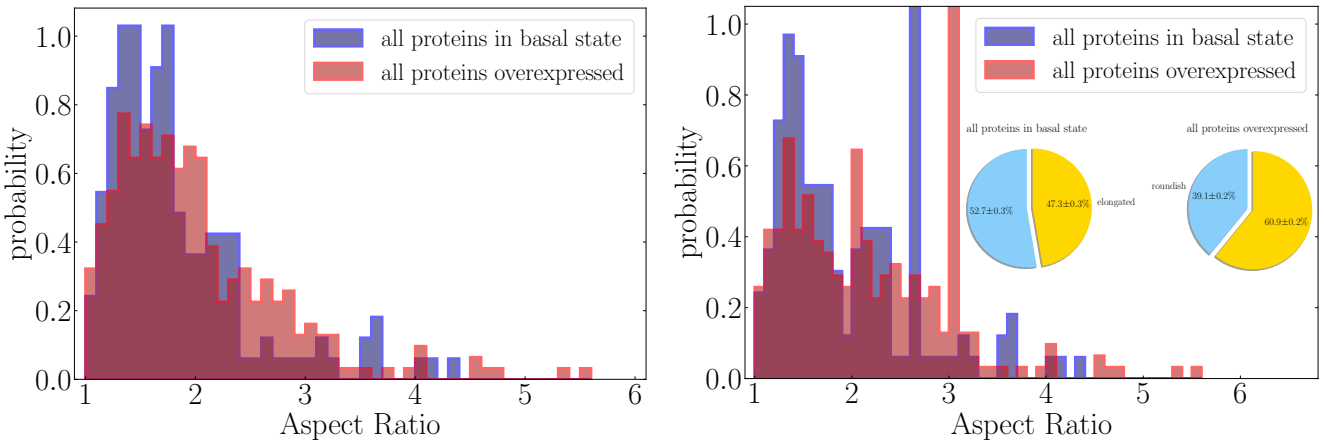

FIGURE 5.3 – Experimental aspect ratio cumulated distributions for all the conditions where proteins are at basal state expression and all the conditions where proteins are overexpressed without correction (left) and after applying the correction for the false roundish domains (right). **Inset:** pie charts representing the relative quantities of roundish or elongated domains detected with an aspect ratio threshold of 2. Blue: roundish, AR ≤ 2; yellow: elongated, AR > 2. The errors given on the percentages are the SEM (Standard Error of the Mean). The p-value computed for this comparison is $p \approx 8 \times 10^{-6}$ ($N_b = 165$ and $N_o = 317$, see text).

In Fig. 5.3 (left) we compute the aspect ratio distributions of the cumulated data of all the proteins expressed at basal state versus the cumulated data of all the proteins overexpressed. We note that the domains in overexpressed conditions show an aspect ratio distribution shifted towards higher values.

In some cases, we noticed by the eye that for some domains, the aspect ratio was not a relevant measurement to characterize their shape. First of all, some ring-shaped or spiral-shaped domains would lead to an aspect ratio close to 1, since they appear as globally roundish, but the human eye can notice that they are in fact coiled elongated domains. We cannot numerically discriminate these domains in our analysis, they are very sparse though. In some less extreme cases, some elongated domains are coiled but the global shape is not closed, as for instance horseshoe-shaped domains (Fig. 5.4). For these domains the computed aspect ratio value will also be close to 1 and we cannot classify them as "elongated" with the sole criterion of its aspect ratio. To detect such "hidden" elongated domains, we implemented a second verification in our analyses, carried out on the domains that are classified by their aspect ratio as roundish (AR < 2): we calculate the domain barycenter and divide the domain into regular angular sectors emerging

from the barycenter. We then compute the number of points per sector. We are interested in characterizing the fact that some sectors might contain no or a few points, less than in the other sectors, corresponding to a hole. We compute the power spectrum of this quantity, see Fig. 5.4. The mode $n = 0$ of the power spectrum characterizes the average number of points per sector. We normalize the measurements by this value. We notice that the horseshoe-shaped domains have a high value for the mode $n = 1$ compared to the "real roundish" ones [1] and then set a threshold of 0.03 for this value above which we consider that the domain has a hole and is then an elongated coiled one.

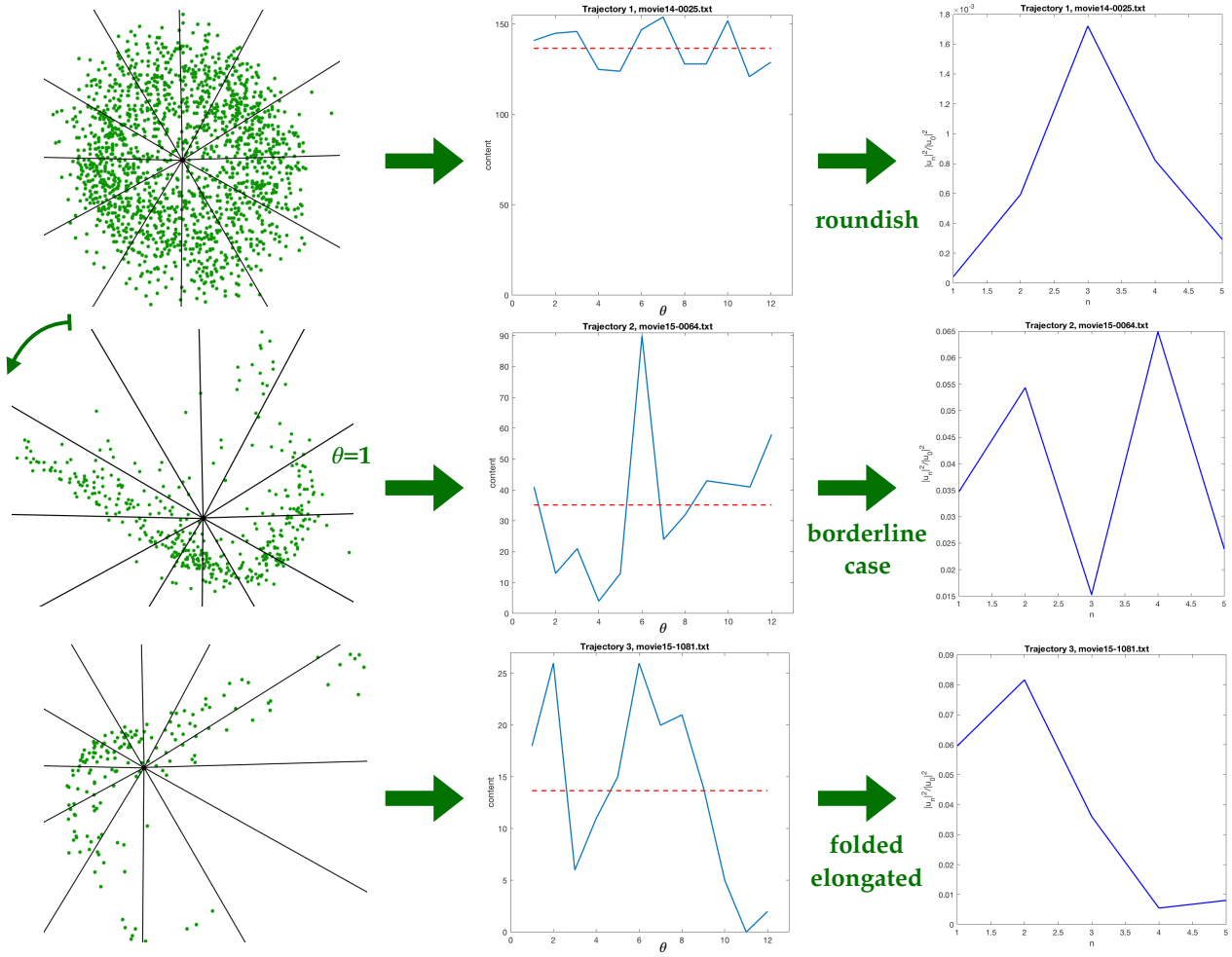

FIGURE 5.4 – Illustrative examples of the method used to discriminate the "false roundish" domains with the study of the power spectrum of the number of points per sector. The space is divided into regular angular sectors indexed by $\theta = 1$ to 12 (left) and the number of points per sector is computed and plotted as an histogram (center). The average value of the number of points per sector is depicted with a red dashed line in these plots. This function is then computed in the Fourier space where we take the square of its modulus (power spectrum) and normalize it by the value of its first mode (right). We then consider the mode $n = 1$ and set the threshold to 0.03 for its value to discriminate the roundish domains, being considered as "false roundish" above this value.

We also studied another criterion described in Fig. 5.5: we still divide the domain into regular angular sectors, and we compute the mean number of points per sector. We set a threshold value

1. Indeed, the mode $n = 1$ corresponds in real space to a distribution of points where a sector with few points is opposite to a sector with numerous points, as in horseshoe-shaped domains.

below which the domain is considered to have a hole if at least one of its sectors contains less points than this value, and then considered as coiled elongated. We tried different threshold values and chose to set it to 30% of the average number of points per sector checking visually that it was discriminating most of the hidden elongated domains and including very few "real roundish" domains. We found this criterion could supersede the power spectrum one detailed above and was more effective to detect the majority of the hidden elongated domains.

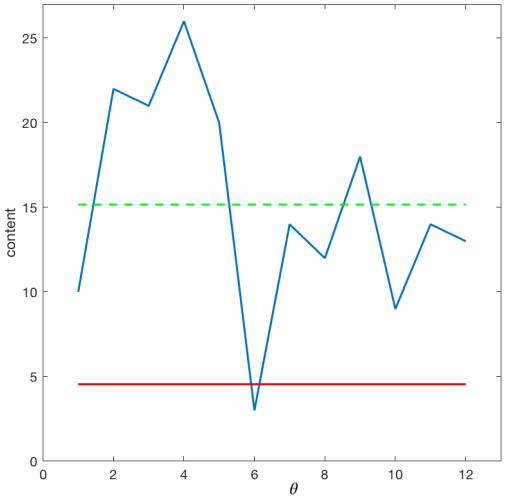

FIGURE 5.5 – Illustrative examples of the method used to discriminate the "false roundish" domains with a minimum threshold applied to the number of points per sector. Here the domains for which one sector contained less than 30% of the average number of points per sector were considered to have a hole and then to be coiled elongated. The average value is represented in green and the threshold one in red.

The errors generated by this correction were taken into account into the error on shape determination which is on the order of a few percents. For example, for the experimental condition tracking CXCR4 with all the proteins at low expression, the characterization of the domain shape with the aspect ratio criterion and the correction described above led to 43% of roundish domains. We checked by the eye the domains that were possibly badly identified in both the "false roundish" and "real roundish" categories and adjusted the proportions accordingly. It gave 46% of roundish domains. We then set that the error for this characterization was on the order of 1.5% even though this is a somewhat disputable approach. The sole aspect ratio is not relevant for characterizing this domain shape. However, we want to take these hidden elongated domains into account in the distributions. We thus assign to them an aspect ratio value reflecting the fact that they are elongated, unlike their original one. We adopted a "mean-field" approach and assigned to them the average aspect ratio value of the initially detected elongated domains (verifying $AR > 2$). Figure 5.3 (right) shows the same comparison as the case shown in the left figure but after applying the correction for the false roundish domains. It can be seen that the correction is captured in the aspect ratio distributions in Fig. 5.3 (right) inducing a higher peak for the mean aspect ratio value of the elongated domains in each condition, around 2.6 for the basal level of expression and around 3.1 for the overexpression level respectively.

Note that we then tested the different criteria described above that were more or less relevant

to detect these coiled elongated domains, however we could check that our conclusions (in terms of proportions of elongated domains and significance based on the p-value computation) were robust to modifications in criterion type and threshold values. We also performed the same analysis with an aspect ratio threshold of 1.8 and checked that the same conclusions hold with marginal influence on the trajectory classification.

5.1.2 Experimental results analysis

In the next results we use the following notations for the experimental conditions:

- when a protein is expressed at a basal level, its name is written in lowercase letters,
- when a protein is overexpressed, its NAME is written in uppercase letters,
- when a protein is tracked with SPT, its <u>name</u> is underlined.

In total, we have accumulated 165 trajectories, confined parts of a longer SPT trajectory, in the basal state (i.e. all proteins are weakly expressed) and 317 trajectories when all proteins are overexpressed. Let us name N_b and N_o the number of studied trajectories in each comparison where the proteins are in the basal state or overexpressed, respectively. Note that to interpret the analysis we focus on the pie charts showing the proportion of elongated versus roundish domains in each condition. In what follows, the correction based on the number of points per sector minimum threshold is applied for the false roundish domains. We provide here the aspect ratio distributions for information in order to bring out the slide towards higher AR values when concentration is increased, however we do not interpret them in-depth since they are biased by the correction applied to false roundish domains. However the p-value is based on the lists of the aspect ratio values.

Effect of the overexpression of all proteins on the cumulated domain shape data

First we pool all the trajectories into two categories, the cumulated data of all the proteins expressed at basal state ($N_b = 165$) versus the cumulated data of all the proteins overexpressed ($N_o = 317$) (Fig. 5.3). The domains in overexpressed conditions show an aspect ratio distribution shifted towards higher values, i.e. are in average more elongated than the domains in the conditions at basal level of expression. The effect of overexpression is here clear and the distributions differ in a very significant way, characterized by a p-value of $p \approx 8 \times 10^{-6}$. This effect is also highlighted in the inset of Fig. 5.3 comparing the proportion of elongated domains for the cumulated data obtained with an aspect ratio threshold of 2.

Effect of the overexpression of all proteins simultaneously on each type of protein domain

When the three proteins (CD4, CCR5 and CXCR4), tracked separately, are overexpressed at the cell surface, a significant increase in the proportion of elongated domains is also observed. This increase is observed regardless of the protein whose trajectory was studied (Fig. 5.6). It is interesting to note that this effect is seemingly more marked for the seven transmembrane-spanning proteins (GPCRs) CCR5 ($p = 0.0005$) and CXCR4 ($p = 0.005$) than for the single transmembrane-spanning protein CD4 ($p = 0,0121$).

Effect of the overexpression of each type of protein on its own domain shape

To go further in this study, we have decided to focus our interest on the CD4 and CCR5 receptors that have been shown to be predominantly used upon HIV-1 infection and that have been abundantly studied in literature ([Gai+06; DPS14; Bea+17; Sha+19]). Our approach was to analyze changes of the shape of the confinement domains of each of these proteins when it is the only one to be overexpressed. As shown in Fig. 5.7 **a)**, we have observed that overexpression of the CCR5 protein is accompanied by a significant lengthening of its confinement domains (i.e. an increase of the proportion of elongated domains at the expense of circular ones). This reinforces the observations we had previously made in Figs 5.3 and 5.6 and is in agreement with our simulations (see Section 5.2). However, for the CD4 protein (Fig. 5.7 **b)**), we have only observed a slight increase of the proportion of elongated domains that was not statistically significant. Several explanations can be put forward to explain this point: CD4 has only one transmembrane segment and the impact of overexpression of this protein on the local membrane curvature might be less important than for CCR5 which has seven transmembrane segments (see discussion below, Section 5.3). This may also explain why the effect of global protein overexpression affects more significantly CCR5 proteins than CD4 proteins (Fig. 5.6). Furthermore, previous works carried out by the IPBS team have shown that there exist several subpopulations of CD4 proteins on the surface of T lymphocytes [Mas+12]. The dynamics of these CD4 sub-populations were diversely affected by temperature changes inducing a significant heterogeneity in the dynamic behaviors of these proteins. We can hypothesize that the presence of several subpopulations of CD4 has "diluted" the effect of overexpression of the protein and minimized its impact on domain shape rearrangement.

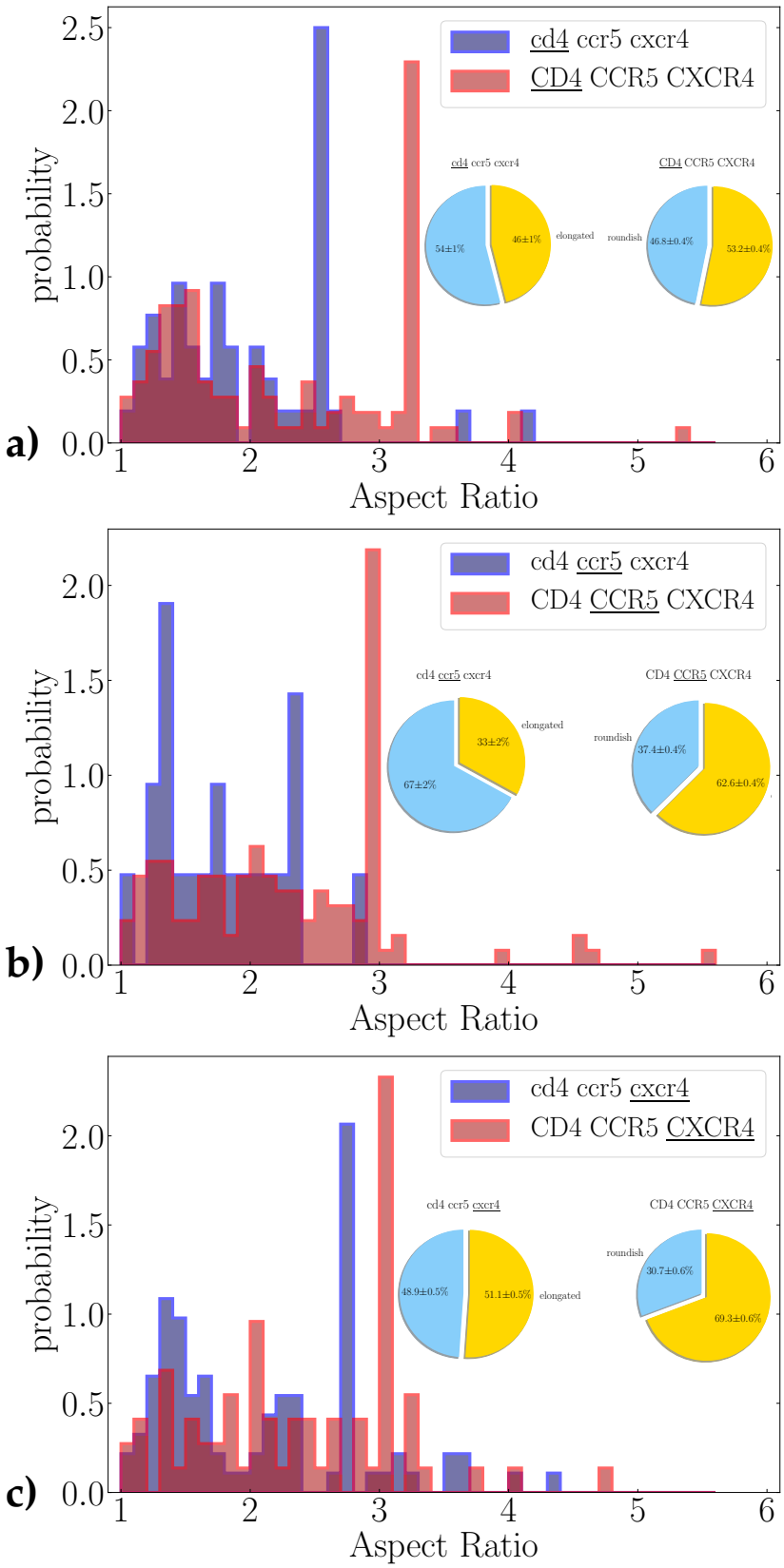

FIGURE 5.6 – Experimental aspect ratio distributions for two compared conditions for the three types of proteins. Here the proteins were tracked separately and we compare the case where they are all overexpressed to the reference case where they are all at basal state expression. **Insets:** pie charts representing the relative quantities of roundish or elongated domains detected with an aspect ratio threshold of 2. The errors given on the percentages are the SEM (Standard Error of the Mean). The p-value computed for these comparisons are respectively **a)** $p \approx 1.2 \times 10^{-2}$ ($N_b = 52$ and $N_o = 111$), **b)** $p \approx 5 \times 10^{-5}$ ($N_b = 21$ and $N_o = 131$) and **c)** $p \approx 5 \times 10^{-3}$ ($N_b = 92$ and $N_o = 75$).

Cross-effect of the overexpression of some protein types on other protein types domain shape

Previous works have shown that there are constitutive interactions between CD4 and CCR5 and that these interactions could take place in specific membrane domains ([Gai+06; Yan+17]). The last point we wanted to study was whether there could be a visible cross-effect of overexpression of these proteins. In other words, can CD4 overexpression affect the shape of CCR5 domains and vice versa? To verify this point we have studied the shape of the CD4 confining domains when CCR5 was overexpressed and inversely. We observed that there was no significant mutual influence of these two proteins (Fig. 5.7 **c)**, **d)**, **e)** and **f)**). This suggests that these proteins are not systematically confined in the same domains in the cellular model we have used. In this study, in order to be able to control the expression rate of the proteins of interest without being hindered by the presence of naturally expressed proteins, we have performed the measurements on Human embryonic kidney 293 cells (HEK-293), which do not naturally express CD4, CCR5 nor CXCR4. It is therefore difficult to compare these results with those obtained in the literature that have mostly been performed with T lymphocytes and it might be interesting, in future works, to establish stable T cell lines expressing various level of CD4 and CCR5 to check whether such a cross-effect can be observed.

Note that if we naively calculate the surface ratio occupied by the proteins on a typical cell membrane in the case of overexpression based on the number of proteins (see Appendix C) and protein diameter, this surface ratio is low: approximately, with a spherical cell of 6 μm of radius and 10^5 copies of proteins of radius 2 nm, the membrane surface ratio occupied by proteins is less than 1%. However, one should consider that a real cell is a far more complex system. For instance the proteins do not cluster alone but also recruit certain lipids and partner proteins so that the area increase of the concerned domains is probably higher than this value considering the sole tracked proteins. In addition, it has been demonstrated by analytical arguments that domains of different type "ignore" each others in the case of cluster phases [Des08]. Thus, if the membrane is enriched in one type of proteins, the domains of this type can in principle elongate independently of domains of other types. This point is addressed below in the discussion in Section 5.3.

This experimental study then shows that there is a general trend of an increase in the number of elongated membrane domains when the proteins they comprise are overexpressed. In the following we use our mesoscale model in order to perform numerical simulations with the aim of confirming this effect and providing a suggestion of a mechanism driving this effect. We then compare the experimental results to simulations where the concentration of the curvature-generating species is increased to mimick protein overexpression.

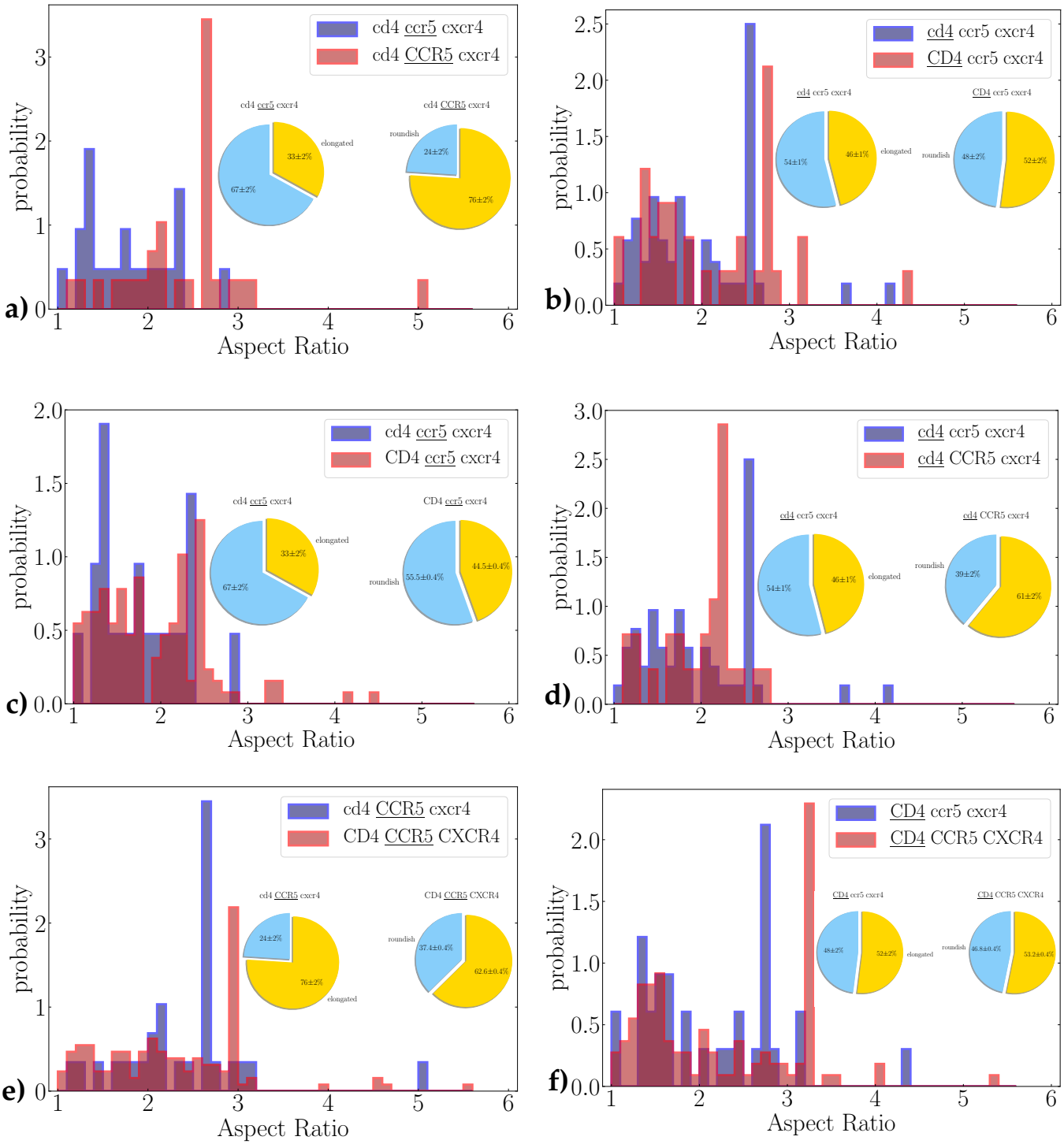

FIGURE 5.7 – Experimental aspect ratio distributions for different compared conditions. **Insets:** pie charts representing the relative quantities of roundish or elongated domains detected with an aspect ratio threshold of 2. The errors given on the percentages are the SEM (Standard Error of the Mean). The p-value computed for these comparisons are respectively **a)** $p \approx 8 \times 10^{-4}$ ($N_b = 21$ and $N_o = 29$), **b)** $p \approx 2.8 \times 10^{-1}$ ($N_b = 52$ and $N_o = 33$), **c)** $p \approx 3.4 \times 10^{-1}$ ($N_b = 21$ and $N_o = 128$), **d)** $p \approx 9.0 \times 10^{-1}$ ($N_b = 52$ and $N_o = 28$), **e)** $p \approx 8.8 \times 10^{-1}$ ($N_b = 29$ and $N_o = 131$) and **f)** $p \approx 1.7 \times 10^{-1}$ ($N_b = 33$ and $N_o = 111$).

5.2 Qualitative comparison to simulations

To study the effect of concentration on domain shape and to compare the results to the previous experimental data analysis, we used our bicomponent vesicle mesoscale model. In these simulations, the A species can be considered as a phase containing particular lipids and some transmembrane proteins that has different spontaneous curvatures than the major phase (species B), mimicking the receptors (see discussion 5.3 on this particular point). The range of parameters we could explore to have qualitatively comparable systems to the experimental results was quite restricted. Indeed, we want to study rather small and numerous domains, which implies that the coupling c_1 has to be strong enough as shown previously. On the other hand, if c_1 is too large the domains get as small as the lattice spacing. Our theory is then not applicable anymore since the domains have to be significantly greater than lattice size. Besides, the line tension of the domain boundary has to be high enough to prevent ample boundary fluctuations and then to have well-defined domains as in the experiments. We then had to choose a high interaction parameter $\tilde{J}_I$ for the mixture. We ran longer simulations, up to 3.10^{10} MC steps, to cope with the fact that the Kawasaki dynamic is slowed at this parameter value so to have enough independent configurations and good enough measurement sampling. We then focus on simulations with $c_1 = 10.0$ and $\tilde{J}_I^{-1} = 2.0$ (and $\tilde{\sigma} = 300$), and study a rather low A species concentration $\bar{\phi} = 0.20$ versus a higher one $\bar{\phi} = 0.35$.

As described above, we implemented a cluster detection algorithm to identify each domain and measure its size on independent system configurations throughout the simulation. To measure the aspect ratio of these domains lying on a quasi-spherical surface, we had to project each of them onto the plane tangent to the average sphere at the domain center of mass to get rid of the third dimension and to compute the domain anisotropy matrix with its in-plane coordinates (x, y). We also divided each domain into regular angular sectors to study the number of sites in each sector, so that we can identify the "false roundish" domains that are not discriminated as elongated by their aspect ratio value. Note that in the simulations we did not apply the correction described in 5.1 since they were extremely rare. The first explanation for their scarcity in our simulations might be that projecting the domains results in altering their shape. The other point to take into account is that several factors that can give rise to such folded domains in real cell membranes such as actin meshwork or other cellular processes are not integrated in our model. In the experimental trajectories however we noticed that these domains were quite numerous ($>$ 10%) which motivated us to introduce the correction for them not to bias the elongated/roundish domain classification.

Figure 5.8 shows the simulation results at two different concentrations $\bar{\phi} = 0.20$ and $\bar{\phi} = 0.35$ and the corresponding aspect ratio distributions of their domains identified throughout the simulation. We find here that the increase in concentration leads to an increase in the proportion of elongated domains, from 28.2% at $\bar{\phi} = 0.20$ to 40.3% at $\bar{\phi} = 0.35$. This analysis was also performed for the same parameters with slightly different curvature coupling values leading to very similar results. With $c_1 = 9.0$ it led to 24.5% of elongated domains at $\bar{\phi} = 0.20$ and 37.0% at $\bar{\phi} = 0.35$, and with $c_1 = 11.0$ we got 31.1% of elongated domains at $\bar{\phi} = 0.20$ and 40.8% at $\bar{\phi} = 0.35$, with an aspect ratio threshold value equal to 2. In the distribution plot in Fig. 5.8, we

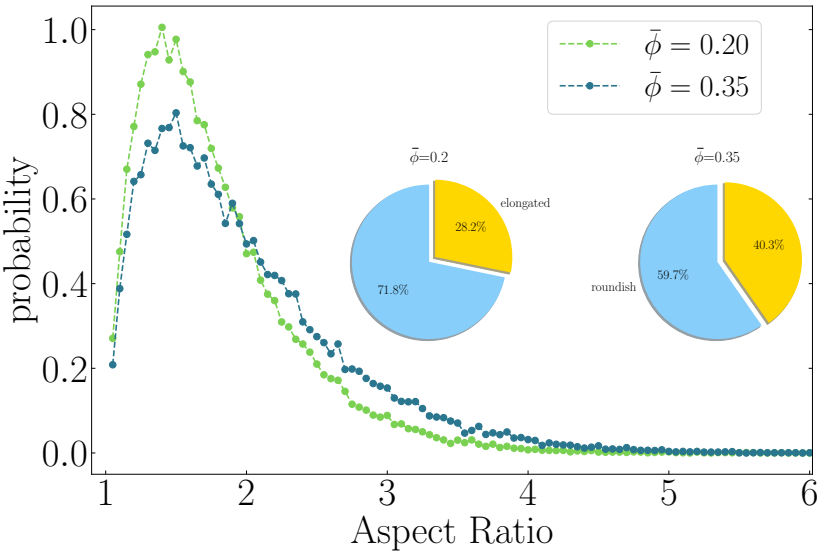

FIGURE 5.8 – Simulation aspect ratio distributions of A (red) domains for vesicles with $\bar{\phi} = 0.20$ and $\bar{\phi} = 0.35$. Other parameters are $c_1 = 8.0$, $\tilde{\sigma} = 300$ and $\tilde{J}_I^{-1} = 2.0$. **Inset:** pie charts representing the classified domain shape with an aspect ratio threshold of 2 for vesicles with $\bar{\phi} = 0.20$ (left) and $\bar{\phi} = 0.35$ (right). The p-value is below the computer accuracy.

note that the curve at $\bar{\phi} = 0.35$ crosses the one at $\bar{\phi} = 0.20$ around an aspect ratio value of 2. This was also verified in the simulations with $c_1 = 9.0$ and $c_1 = 11.0$ and provides a simulation-driven argument to set the aspect ratio threshold to 2. We find results qualitatively similar to the experimentally observed phenomenon, with enhanced large aspect ratio values for the system with a higher concentration. The p-values computed for these aspect ratio samples were found to be below the computer accuracy, ensuring that the elongation effect is a real phenomenon in the simulations.

We can measure the typical cluster sizes with the help of the cluster size distribution and compare them for the two concentrations. As expected, the domains for $\bar{\phi} = 0.35$ have a significantly larger typical size than the ones at $\bar{\phi} = 0.20$ as depicted in Fig. 5.9 (around 30 sites as against 20), and their largest values found are bigger (they reach 15% of the total system size at $\bar{\phi} = 0.35$ as against $\sim 4\%$ at $\bar{\phi} = 0.20$). However one can see in Fig. 5.10 where are plotted the spatial correlation function and the associated structure factor that the systems are characterized by very close spatial wavelengths. The oscillations of the spatial correlation functions are almost in phase and the two systems have a maximum in their structure factor for the same mode ($l = 8$). The differences in amplitudes for the correlation functions and in the peak widths in the structure factors arise from the different input concentrations. Although the correlation function is computed from an average measurement in every direction, we can qualitatively interpret these observations as the fact that the domains elongate in one direction only and that their typical spacing and thus width remain roughly constant. This has also been observed in the experimental data were the domain minor axis is thinly varying and their major axis varying more significantly with concentration (minor and major axes were measured through the eigenvalues λ_1 and λ_2). For example, in the condition where CCR5 is tracked and all protein expression levels are low, the semi-minor axis of the domains was in average equal to 127 ± 13 nm, and it shifted to 150 ± 8

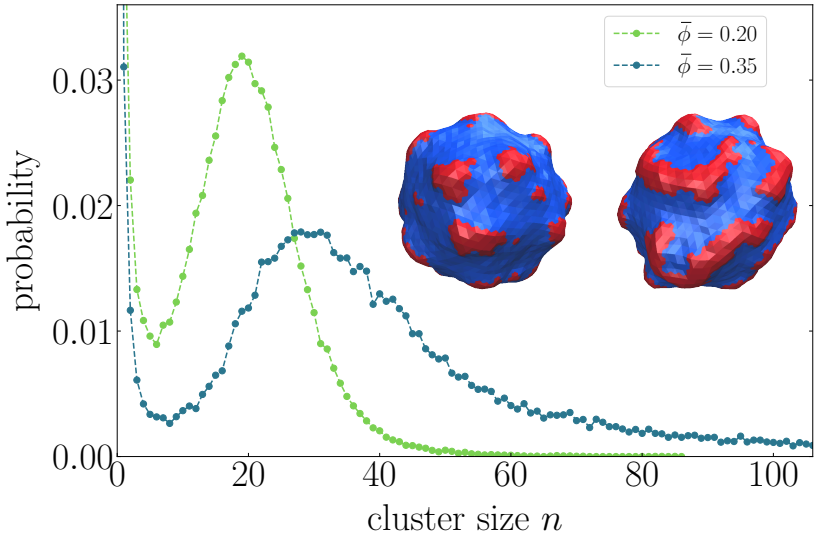

FIGURE 5.9 – Domain size distribution for vesicles with $\bar{\phi} = 0.20$ and $\bar{\phi} = 0.35$ in terms of number of sites. The typical domain size for a system corresponds to the position of the peak. The system at higher concentration ($\bar{\phi} = 0.35$) shows domains with a higher typical size (by $\sim 50\%$) than the one at lower concentration ($\bar{\phi} = 0.20$). Its largest domains are also bigger than the ones at lower concentration (not shown) and can reach ~ 400 sites (about 15% of the total system size, whereas the biggest ones at lower concentration reach $\sim 4\%$ of the system size). Other parameters are $c_1 = 8.0$, $\tilde{\sigma} = 300$ and $\tilde{J}_I^{-1} = 2.0$. **Inset:** simulations snapshots of the corresponding vesicles with $\bar{\phi} = 0.20$ (left) and $\bar{\phi} = 0.35$ (right).

nm in the case where all the protein were overexpressed. In comparison, the semi-major axis mean value shifted from 218 ± 26 nm to 288 ± 14 nm, a more pronounced increase.

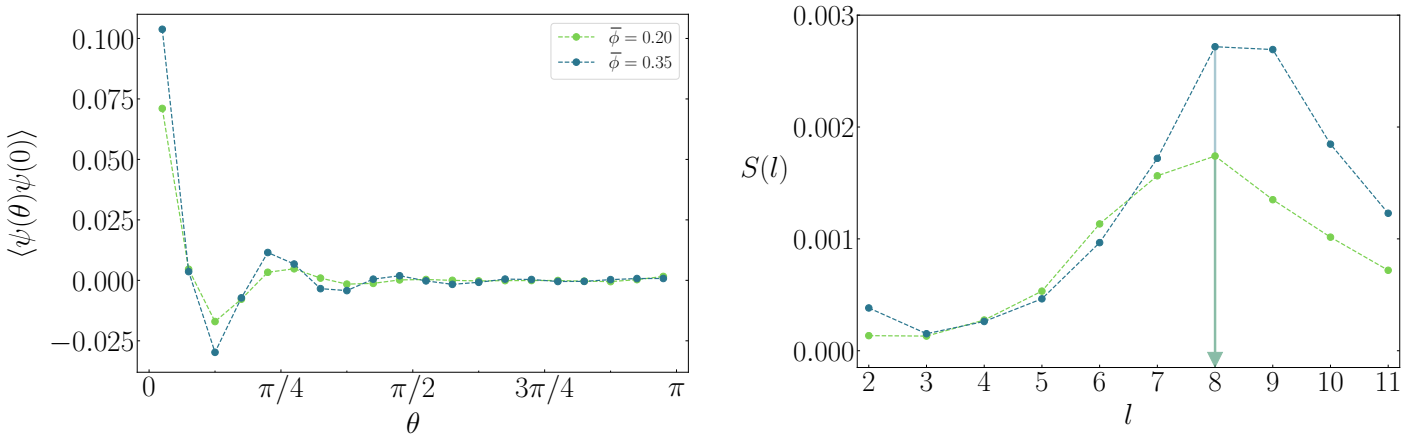

FIGURE 5.10 – Correlation functions and structure factor for vesicles with $\bar{\phi} = 0.20$ and $\bar{\phi} = 0.35$. The two systems are characterized by very close spatial wavelengths. Other parameters are $c_1 = 8.0$, $\tilde{\sigma} = 300$ and $\tilde{J}_I^{-1} = 2.0$.

Other simulations performed on planar membranes with the model of interacting "proteins" of Destainville (2008) also show such elongated patterns when the concentration is high enough (see inset in Fig. 5.11) whereas they show roundish "bubbles" at lower concentrations. In these simulations, the pairwise potential described in [Des08] comes into play:

$$U(r) = -\varepsilon_a e^{-\gamma_a r} + \varepsilon_r e^{-\gamma_r r} \tag{5.8}$$

r being the distance between the proteins, in addition to hard-core repulsion. The parameters used for the simulations therein are $\varepsilon_a = 21.3 k_\mathrm{B}T$, $\varepsilon_r = 0.31 k_\mathrm{B}T$, $\gamma_a = 2$ and $\gamma_r = 0.25$ in inverse units of molecule diameter. The density $\bar{\phi}$ is computed at null temperature, with all the beads considered to be condensed in a perfect triangular lattice. Note that the long-range repulsions between the proteins are explicitly introduced in these simulations whereas they indirectly result from the difference of curvature in a curvature-composition coupling model [WD13]. Yet, it is interesting to notice that the phenomenon of domain shape elongation with concentration increase is commonly shared by these different cases. In addition, we observe in Fig. 5.11 that the aspect ratio distributions of these domains also tend to slide towards higher values when the concentration is increased, which supports our model results. Again the "hinge point" in the aspect ratio distributions is close to 2.

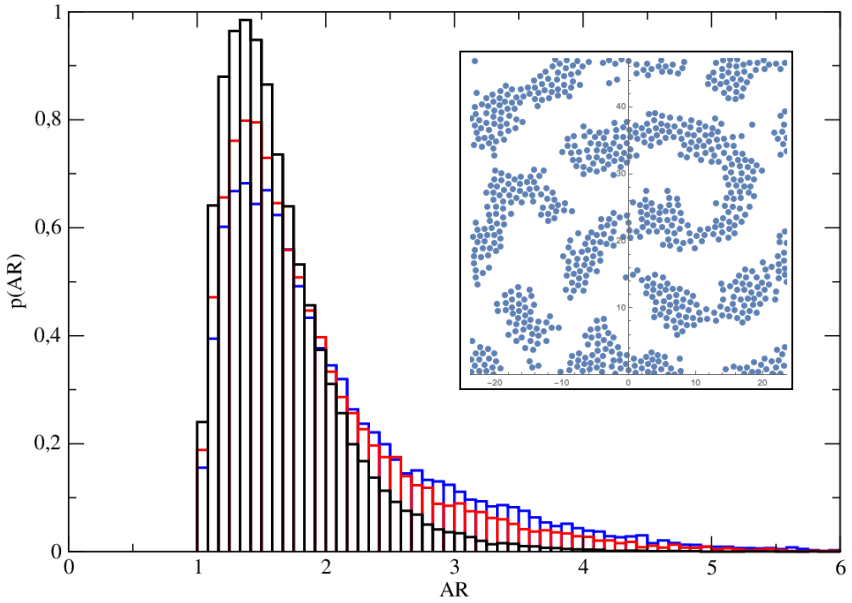

FIGURE 5.11 – Aspect ratio distributions for the domains observed in the in-plane simulations with explicit short-range attraction and long-range repulsion [Des08] as defined in Eq. (5.8) with $\bar{\phi} \simeq 0.18$ (black), $\bar{\phi} \simeq 0.25$ (red) and $\bar{\phi} \simeq 0.27$ (blue). **Inset:** simulation snapshot showing similar elongated patterns when the concentration is increased to $\bar{\phi} \simeq 0.31$. N=800 proteins.

5.3 Discussion

We then propose the following illustrative scenario: an elongated domain at higher concentration is a lengthwise merge of several roundish small ones, i.e. domains growth induced by concentration increase happens in one direction only. Such a mechanism has been found to modulate domain shape elongation in membrane systems in theoretical studies [LA87; KGL99; HMO05] and experiments [Kon+11a] as well as in other systems such as nanoparticles at the air-water interface [Sea+99]. An aspect ratio of 2 for a domain would then typically correspond to a merge of 2 roundish small domains, and a higher aspect ratio to a merged alignment of more than 2 of them. In Ref. [HMO05] it is indeed shown by approximate analytical arguments [2] that the transition from "bubbles" to "stripes" when increasing $\bar{\phi}$ can happen at more or less enhanced concentration, depending on the parameter combination, and notably the line tension value. The author build a phase diagram (see Fig. 5.12) characterizing the different morphologies in function of the concentration and the parameter τ, related to the product of the line tension and the surface tension. The cases where one observes the elongated domains might correspond to the coexistence zone of these "bubbles" and "stripes" shapes (indicated in orange in Fig. 5.12). In the case of our simulations, $\tau \approx 0.07$ which allows the transition around $\phi \approx 0.35$, consistently with our simulation observations. The transition can happen at rather low concentration values in a certain parameter regime, which could explain the experiment results discussed here where domains of one species remain scarce (low $\bar{\phi}$), in spite of overexpression. In Ref. [Kon+11b], the authors also highlight a coexistence zone between "bubbles" and "stripes" showing elongated domains similar to those observed in our experimental and numerical systems, using simulations with explicit electrostatic repulsions comparable to the model of Destainville (2008) and analogous to our model with implicite long-range repulsion induced by curvature.

Pointing out the analogy between experimental and numerical domain morphologies implicitly assumes that a curvature-composition coupling mechanism is at play in the case of HIV receptors nano-domains, at least GPCR ones as underlined above. This point now deserves to be discussed more thoroughly. As we have stressed it in [DMC18], "the transmembrane part of an integral protein has no reason to be up-down symmetric (...). This is either apparent in the molecular shape of transmembrane proteins or can be inferred from their behavior in biophysical experiments". In the case of GPCRs, they all share structural similarities in their transmembrane part, more precisely seven transmembrane helices connected by three intracellular loops as well as three extracellular ones. The N-terminus is extracellular and the C-terminus is intracellular. This does not mean that they all exert the same mechanical constraints on the membrane, but analogies can legitimately be expected. The spontaneous curvature induced by one class of GPCRs has very recently been investigated in detail, namely the class-A GPCRs [Ros+17], by studying their partitioning into tubular filopodia, in live cells. A spontaneous curvature of about 0.04 nm^{-1} is deduced. According to the authors, this is related to the crystal structures of those GPCRs that reveal their transmembrane part to be up-down asymmetric across the bilayer. This spontaneous

2. In this study, the only morphologies under consideration are roundish bubbles and regular stripes. Their respective stabilities are determined through comparison of their energies. The occurrence of elongated or coiled domains is not envisaged. The theory ought to be refined to take them into consideration.

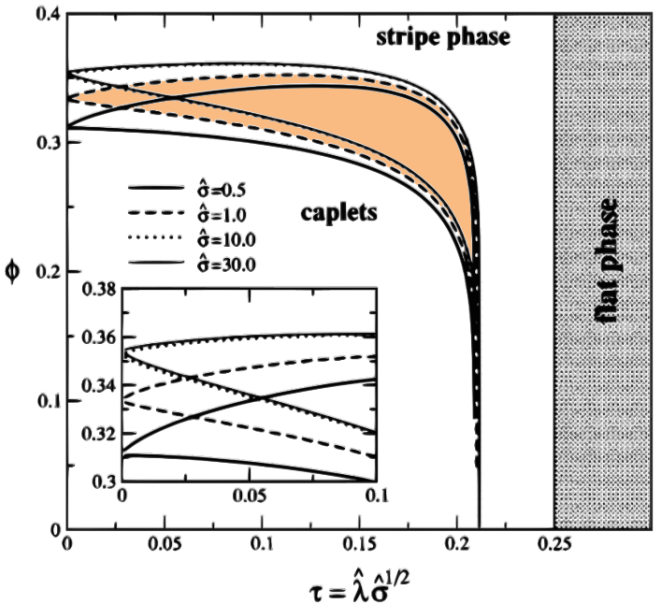

FIGURE 5.12 – Phase diagram from [HMO05] showing the existence of different patterns in function of the concentration ϕ and of a parameter τ, related to the product of the line tension and the surface tension. The existence of "stripes" and "caplets" (bubbles) phases is predicted as well as a coexistence zone (in orange). Here ϕ is our $\bar{\phi}$ and $\hat{\lambda}$ and $\hat{\sigma}$ are the reduced line and surface tensions.

curvature is typically in the range of values that can promote sub-micrometric nanodomains, as expected [DMC18]. To our knowledge, no such measurements have been performed on CCR5 or CXCR4. But they belong to the same class A [LP09] and thus share structural similarities with those of Rosholm et al. (2017). Those recent experiments make realistic that a curvature-composition coupling mechanism also promotes nanodomains of the GPCRs involved in HIV infection.

The present work then shows that the accumulation of proteins into domains can conduce to a change of their morphology. This has been observed with 3 receptors CD4, CCR5 and CXCR4 and can probably be extrapolated to numerous membrane proteins since such "abnormal" domain shape has already been observed with other proteins in different cell types without being explained. The numerical simulations performed suggest a theoretical mechanism to explain this shape elongation that is consistent with the experimental conclusions. The "classical" parameters commonly acquired when studying protein dynamics at the surface of cell membranes are the diffusion modes (random, directed, permanently or transiently confined) and the diffusion rate inside and outside domains. We propose to include a new parameter of interest: the aspect ratio of membrane domains. Combined with the others this might give interesting information regarding the level of accumulation of specific proteins in the cell membrane and the biological processes that might be associated with such an accumulation.

Chapter 6

Model extensions

Contents

In this chapter we present some exploratory very recent works done with our model. In the first section we study the response of vesicles with curvature-composition coupling to the application of external forces. In the second section, we explore the effect of bending modulus-composition coupling only.

6.1 Vesicle simulations with curvature-composition coupling and applied forces

In this section we study the effect of the application of external forces on vesicles modelled at the mesoscale using Monte Carlo simulations. Besides the curiosity of confronting our model with theoretical physics principles (such as verifying the linear response theory and the Green-Kubo theorem [Cha87; KTH91]), this work is also of biophysical interest. Indeed, in cells, various processes resulting in membrane deformation involve forces application, exerted by actin meshwork for example [Sim+19], or tubulin. Microtubule forces are for instance crucial in the correct positioning of the nucleus in yeast division [Tra+01]. The biological case that motivated our present study is mitosis. During anaphase cell elongation, forces are applied on the cell membrane by the microtubules of the mitotic spindle. This might participate in inducing membrane component rearrangement for mechanical reasons and account for experimental observations of Roubinet et al. (2011). This molecular rearrangement is a first step of a cascade of events eventually leading to cell division by contributing to the correct positioning of the cell division plane. The work presented in this section was mainly realized by Nicolas Gaudy that I was fortunate to supervise in the context of his Master 1 internship.

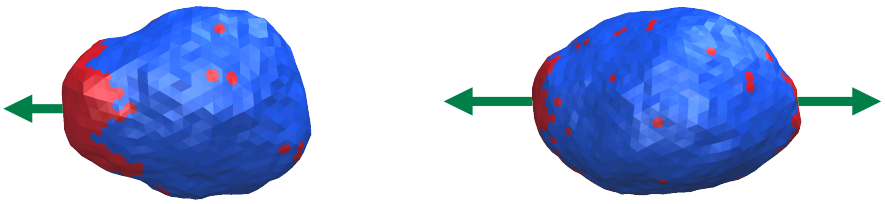

FIGURE 6.1 – **Left:** Low force application on one pole of the vesicle. The opposite force is applied to the center of mass. **Right:** Higher force application on two opposite sites of the vesicle.

On the strength of the results obtained previously on vesicles subject to the same surface tension $\tilde{\sigma} = 300$ as the systems in the phase diagram Fig. 3.17, we investigate the effect of forces the values of which span over tens to hundreds of pico-Newtons (for vesicle of about 10 μm of radius). It can indeed be measured in biological systems that a pushing force of 3-4 pN can be generated by an individual microtubule growth [Dog+05; VKD16] and the astral microtubules reaching the cell cortex in mouse stem cell division are around 20 [MMH14].

6.1.1 Low force application on one pole and verification of the linear response

We first start with applying a low force on one site of the vesicle as described in Section 2.1.3 in order to attest the linear response of our system as illustrated in Fig. 6.1 (left). To do so we use the Green-Kubo theorem that establishes the proportionality relationship between the linear response of an observable to a perturbation of the Hamiltonian and the correlation function of this observable in an unperturbed system at equilibrium. The demonstration of this theorem is presented in Appendix D.

We associate the perturbation δH to the modification of the height fluctuation induced by a force f applied to the pole so that $\delta H = -fR\, u_{\text{pole}}$ where u_{pole} is the radial displacement of the pole.

Our observable is the local composition $\phi(\theta, \varphi)$. We then compare the correlation function between membrane height and composition $C_{\{u,\phi\}_0}(\gamma)$ without force perturbation (noted with 0 subscript) with the angular composition $s(\gamma)$ computed with respect to the site on which the force is applied. See 2.1.5 for the definition of these functions. In our case, the Green-Kubo theorem can then be written following Eq. (D.6) as

$$s(\gamma) = \beta f R C_{\{u,\phi\}_0}(\gamma) \tag{6.1}$$

We recall that we use the dimensionless parameter $\tilde{f} = Rf/k_{\text{B}}T$ (Section 2.1.3). One can see in Fig. 6.2 that we indeed recover proportionality between our two measurements. However, one can notice that we need to add a prefactor by hand different from 1 ($\simeq 40$). The origin of this prefactor is still investigated [1]. Fig. 6.3 shows the angular composition for different applied forces. We note that with the same value of c_1 the induced patterns keep the same typical wavelength while $\tilde{f}$ is increased. The intensity of the concentration in A species close to the site where the

1. *Corrigendum:* We eventually understood that this prefactor was ensuing from an erroneous weighting of the correlation function $C_{\{u,\phi\}}$ in the code. A corrective prefactor $\sqrt{N} \simeq 50$ must applied to these functions when displayed in the figures. This solves the apparent discrepancy between the correlation and the response functions.

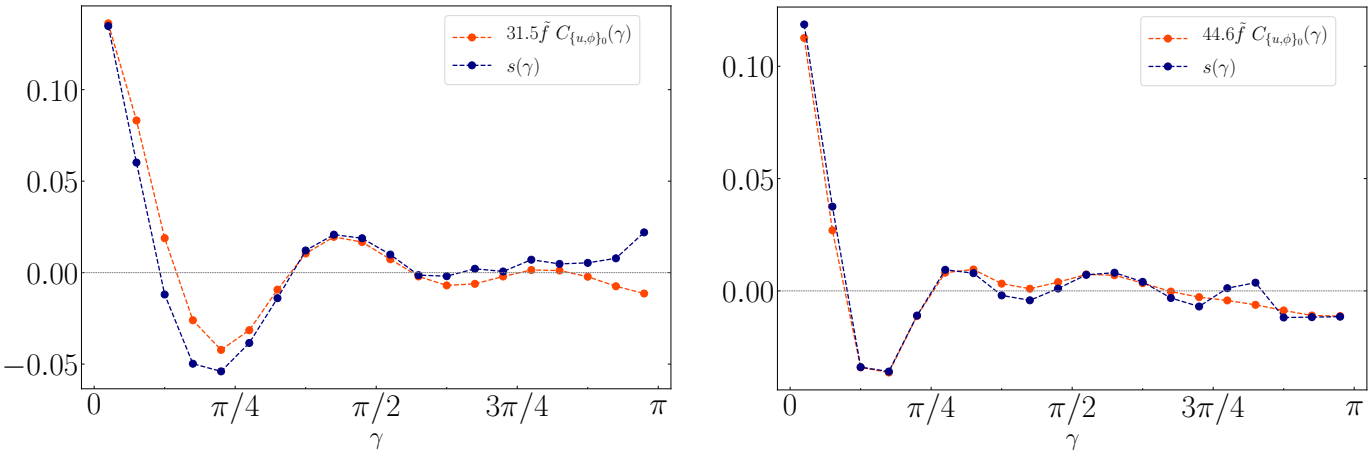

FIGURE 6.2 – Comparison of the angular composition $s(\gamma)$ and the correlation function between membrane height and composition $C_{\{u,\phi\}_0}(\gamma)$ multiplied by the force value and the prefactor for $c_1 = 4.0$ (left) and $c_1 = 6.0$ (right). Other parameters are $\bar{\phi} = 0.5$, $\tilde{\sigma} = 300$, $\tilde{J}_I^{-1} = 2.5$ and $\tilde{f} = 15$.

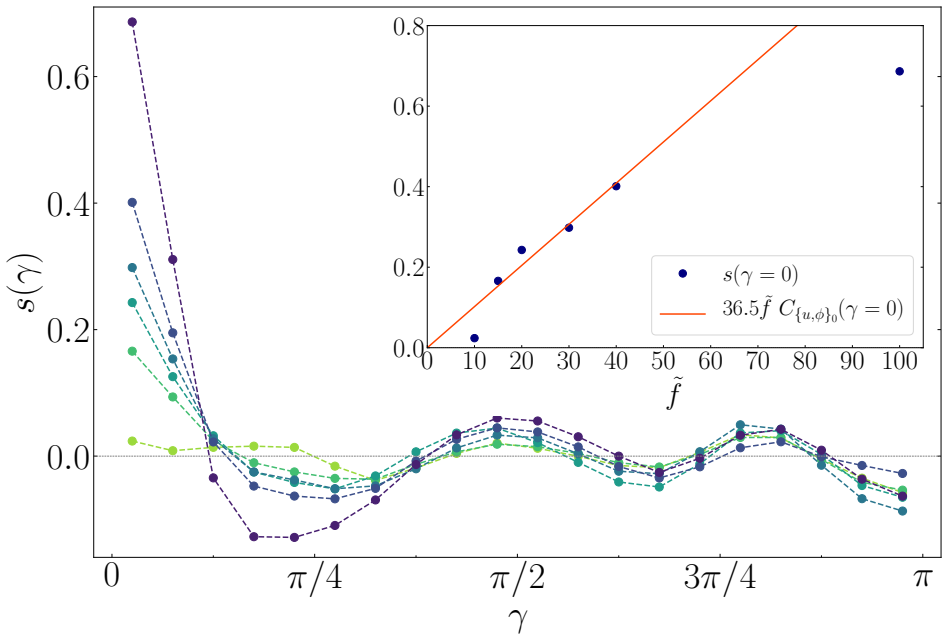

FIGURE 6.3 – Angular composition $s(\gamma)$ for different applied force values $\tilde{f}$. The inset shows the angular composition values $s(\gamma = 0)$ and the correlation function values $C_{\{u,\phi\}_0}(\gamma = 0)$ multiplied by the force value and the prefactor. The value $C_{\{u,\phi\}_0}(\gamma = 0)$ is measured in a system with the same simulation parameters but with zero force. Other parameters are $\bar{\phi} = 0.2$, $\tilde{\sigma} = 300$, $c_1 = 4.0$ and $\tilde{J}_I^{-1} = 2.5$.

force is applied (i. e. for $\gamma = 0$) though increases with $\tilde{f}$. This attests the fact that the force application tends to create a more curved region around its point of application whose curvature is favorable for the red species with higher spontaneous curvature than the blue one. In the inset, we compare the angular composition values for $s(\gamma = 0)$ to the correlation function $C_{\{u,\phi\}_0}(\gamma = 0)$ multiplied by the force value and the prefactor evaluated numerically. We check that for low enough forces ($\tilde{f} < 40$) the system is in the linear regime. At too low forces however ($\tilde{f} = 10$), we note the the agreement between the two observables is degraded. This probably comes from the fact that numerical errors coming from the sphere tesselation influence species repartition

and are predominant in this very low force regime. Although these comparisons were done for systems in which the force is applied on a vertex belonging to a face of the initial icosahedron and not to its vertices, which lowers the bias, the effect is still present (see Section 2.1.6 for more detailed explanations about this effect).

6.1.2 Force application on two opposite poles

We now explore the effect of higher applied forces on our system to analyse the consequences on membrane component spatial organization (see Fig. 6.1, right). Motivated by the biological case of cell division, we chose to apply two equal forces on two opposite sites of the vesicle. We compute the distance separating the two poles and check that it saturates after equilibration.

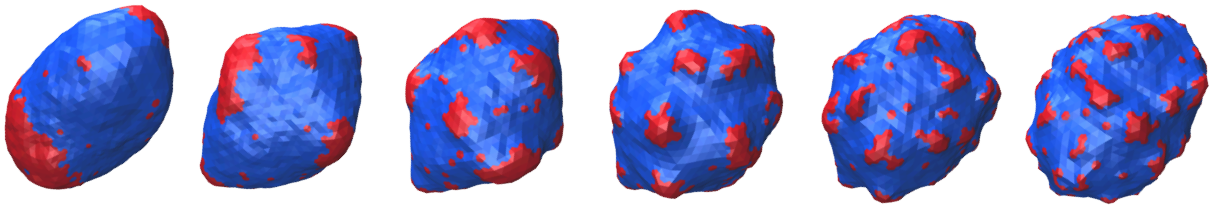

FIGURE 6.4 – Force application on two opposite poles of the vesicle with increasing c_1 value (from 2.0 to 12.0 by 2.0 increment). Other parameters are $\bar{\phi} = 0.2$, $\tilde{\sigma} = 300$, $\tilde{J}_I^{-1} = 2.5$ and $\tilde{f} = 100$.

Under forces, the system behavior in term of pattern formation remains globally close to its behavior without forces described in the phase diagram Fig. 3.17. However, in Fig. 6.4 we notice a few interesting effects induced by this perturbation. The first noticeable fact is that macrophases become unstable at high enough forces. The application of a force on two opposite poles results in the vesicle elongation and locally induces an increased curvature at the two poles. For example, at low curvature coupling and high $\tilde{J}_I$, set of parameters leading to a single macrodomain formation without forces, one can observe two red domains located at the vesicle poles under the application of force ($c_1 = 2.0$, $\tilde{f} = 100$, see leftmost vesicle in Fig. 6.4).

The other observation is that membrane patterning seems to be reorganized by the force application. Indeed, as one can see in Fig. 6.4, the red domains form as in the unperturbed case but tend to locate to particular latitudes only, as "necklaces" of domains, lying on circles of latitudes (parallel to the equator). To quantitatively characterize this phenomenon, we use the plot of the angular composition. We can see in the oscillations in Fig. 6.5 that the domains indeed have a higher probability to be located at certain latitudes and that the number of "necklaces" increases with the curvature coupling. For example, the vesicle with $c_1 = 6.0$ exhibits 2 latitudes enriched in A domains (besides the two poles), a number that seems to reach 5 for $c_1 = 10.0$ or 12.0. This is coherent with the fact that c_1 coupling increase leads to the formation of smaller and more numerous curved domains that repel each-others as shown in Chapter 3 and depicted in Fig. 3.9. The vesicles then become polarized under force application as are the cells in the division process [Rou+11].

We found that another way to induce the formation of such "necklaces" in the membrane is to keep the curvature coupling c_1 constant and decrease the Ising parameter as shown in Fig. 6.6,

also consistent with the fact that decreasing $\tilde{J}_I$ decreases the line tension, thus facilitating domain fragmentation.

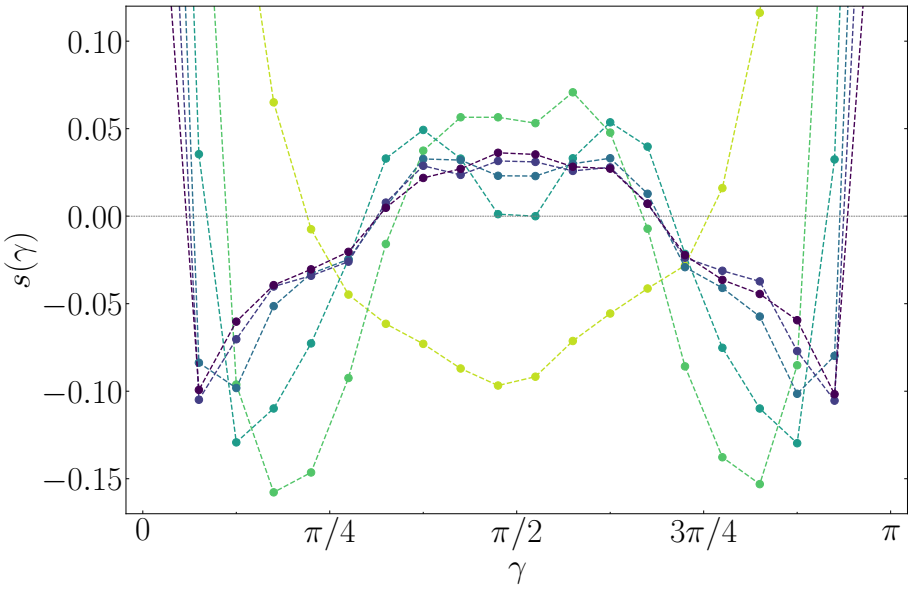

FIGURE 6.5 – Angular composition $s(\gamma)$ for increasing c_1 coupling values (from 2.0 to 12.0 by increments of 2.0, from light green to dark blue). Other parameters are $\bar{\phi} = 0.2$, $\tilde{\sigma} = 300$, $\tilde{J}_I^{-1} = 2.5$ and $\tilde{f} = 100$.

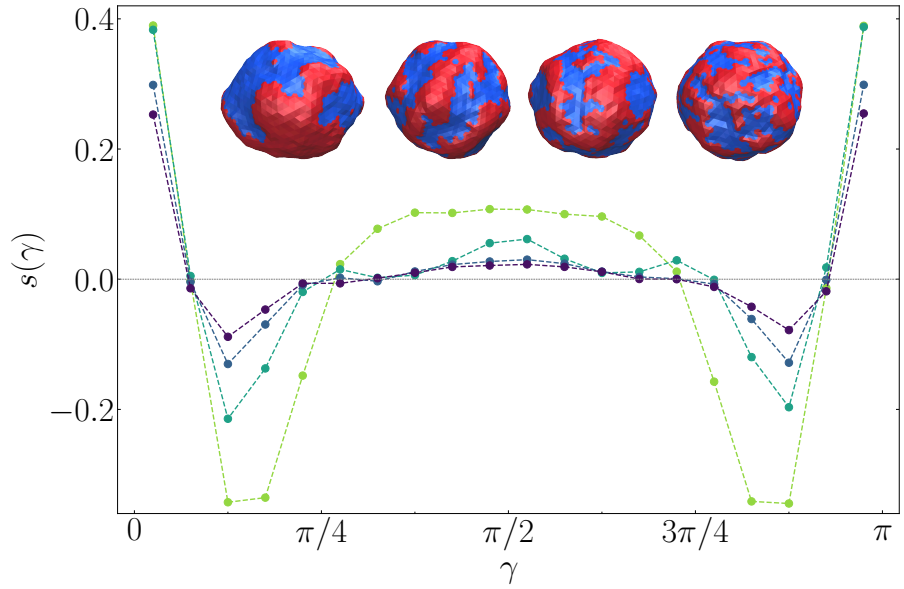

FIGURE 6.6 – Angular composition $s(\gamma)$ for increasing $\tilde{J}_I^{-1}$ values (from 2.0 to 3.5 by increments of 0.5, from green to dark blue). Other parameters are $\bar{\phi} = 0.5$, $\tilde{\sigma} = 600$, $c_1 = 6.0$ and $\tilde{f} = 100$.

We check that the effect of surface tension is countering strong deformations. Indeed, vesicles with applied force $\tilde{f} = 100$ at $\tilde{\sigma} = 600$ (Fig. 6.6) are less elongated than those simulated at $\tilde{\sigma} = 300$. We measure this difference by comparing the values of $u(\gamma = 0)$ which is found to be around 3 times higher at $\tilde{\sigma} = 300$ than at $\tilde{\sigma} = 600$.

With this study we thus could verify the linear response of our system under force application. We also found interesting patterning behaviors in the membrane with the application of forces driving domain reorganization and location on preferential latitudes on the vesicle. This work needs to be continued more in-depth guided by the motivation of comparison with biological cases involving an interplay between membrane component organization and local force application such as cell division.

6.2 Preliminary results on vesicles with bending modulus-composition coupling

In this part we investigate the effect of a bending modulus - composition coupling. For sake of clarity and in order to understand in detail the role of each kind of coupling, we chose to study separately the local curvature coupling and the bending modulus one. Consequently, in this case C_1 is set to 0 as well as C_0 (so $C = C_0 = 0$) and the bending modulus dependance on composition is introduced as $\kappa = \kappa_0 + \kappa_1\phi$. We note $\bar{\kappa}$ the ratio between the bending moduli of the two phases. This coupling implies that one of the two lipid species has a higher bending modulus, associated with a higher thickness and rigidity (in red in the figures). This case can correspond to the well known liquid ordered Lo and liquid disordered Ld phases formed in lipid mixtures [KA14; Mou05; Mar09; Sch17]. The first one is formed by saturated lipids (ordered tails at low enough temperature) making it thick and is enriched in cholesterol, which reinforces its rigidity, and the second one is formed by unsaturated lipids (disordered tails) which makes it more flexible. These phases undergo phase separation below a critical temperature [CL95; Onu02; VK05; HVK09]. However, different patterns can be observed in lipid mixtures presenting such Lo and Ld phases as illustrated in Fig. 6.7 in certain parameter ranges. In experiments, thicker Lo phases are measured to have higher bending rigidities than Ld phases. For example, measured ratios are $\kappa_{\text{Lo}}/\kappa_{\text{Ld}} \simeq 5$ in [Bau+05] and $\simeq 4$ in [Sem+09], a range of values confirmed in more recent studies measuring ratios up to 10 [Nic+15; Use+17a], depending on the precise lipids at play.

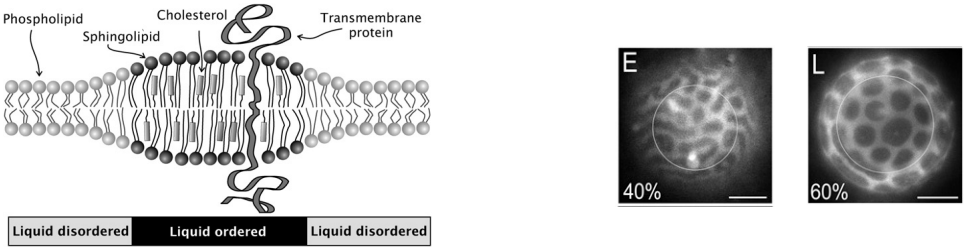

FIGURE 6.7 – **Left:** Liquid disordered (Ld) phase and liquid ordered (Lo) phase enriched with cholesterol, undergoing total phase separation. Image from [SS09]. **Right:** examples of different kinds of patterning in biosystems due to differences in bending modulus [GAF13]. The GUVs are observed in fluorescence microscopy. The bright phase is the Ld one. The Ld phase here is rich in DOPC and POPC lipids whereas the Lo one is rich in DSPC and cholesterol. The compositions ratios DSPC/(DOPC+POPC)/CHOL are respectively 0.283/0.45/0.267, left, and 0.395/0.30/0.305, right. The percentage given is the DOPC/(DOPC+POPC) ratio. Scale bars are 10 μm.

A consequence of this difference in bending modulus is that the more rigid phase is then more difficult to bend and encounters difficulties to accommodate to a globally curved spherical shape [DMC18]. Above the critical Ising parameter, large rigid and flat macrophases are then unstable. They break into smaller domains whose arrangement on the sphere allows a better shape accommodation and a lower bending energy cost in spite of the increased line energy at domain boundaries. This mechanism is illustrated in Fig. 6.8. This pattern formation has been observed experimentally as for example in [GAF13] as visible in the rightmost GUV image in Fig. 6.7. We indeed observe this phenomenon in our simulations as shown in Fig. 6.9, rightmost vesicle. The bending modulus coupling can also imply membrane deformation leading to the formation of thicker and flatter zones arranged into stripes as experimentally observed, see for example the left vesicle in Fig. 6.7. We indeed observe in Fig. 6.9, center vesicle, that this can lead to the formation of flat stripes with a vanishing curvature. The surrounding flexible phase is deformed to enable the flat stripes formation. In Fig. 6.9, the leftmost vesicle has a ratio of $\bar{\kappa} = 5$ between the A and B phases. At this Ising parameter ($\tilde{J}_I^{-1} = 2.5$) and this $\bar{\kappa}$ value, the fragmentation of the rigid phase into only two large regions is stable. We show that they are two ways to get a more important fragmentation and more interesting patterns. The first way is intuitive and consist in keeping the Ising parameter constant and to increase the bending modulus coupling. The center vesicle in Fig. 6.9 is an example of this case with $\tilde{J}_I^{-1} = 2.5$ and $\bar{\kappa} = 10$. It shows modulated phases with stripes, characterized by oscillations in the spatial correlation function and a peak in the structure factor for $l^* = 6$. The second way is to keep constant the bending modulus coupling and to lower the Ising parameter, which lowers the line tension and facilitates energetically the fragmentation as predicted in [DMC18]. The rightmost vesicle in Fig. 6.9 is an example of this case, showing modulated phases characterized by a peak in $l^* = 3$ in the structure factor.

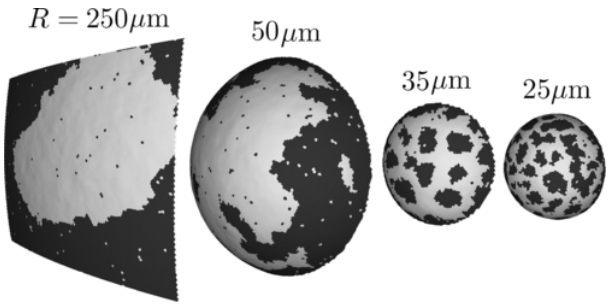

FIGURE 6.8 – Illustration of the "tortoise shell" effect [AF14]. When the vesicle curvature increases (i.e. its radius decresaes), the energy cost to bend the more rigid phase to accommodate the sphere becomes high since it tends to be flat. This phase then breaks into an arrangement of smaller flat pieces separated by the more flexible phase that can then better adjust to the global shape constraint.

In order to test our model, we tried to qualitatively recover results obtained in the literature with a similar model [HWL11] (Figs. 6.10 and 6.11). Note that the models differ in several ways. First, in the simulations of Ref. [HWL11], the vesicle volume is free to fluctuate and the triangle areas are locally constrained, whereas the volume is constrained in our case and the total vesicle area is globally controlled by surface tension (see Section 2.1.1). Second, the composition patches stand on the middle of the triangular faces in their model and not on the tesselation vertices

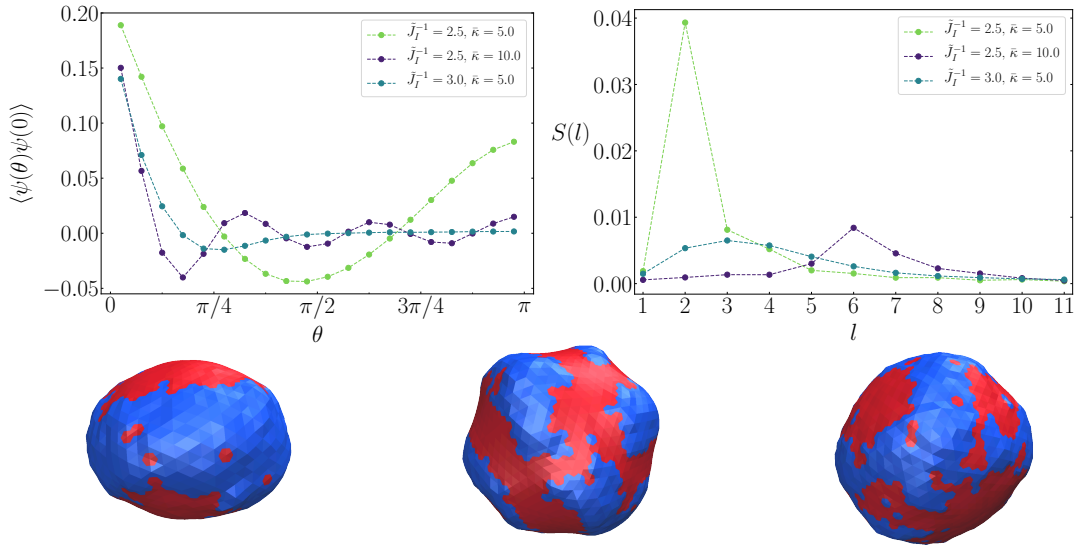

FIGURE 6.9 – Correlation functions, structure factors and corresponding vesicle snapshots for systems with bending modulus coupling below $\tilde{J}_{I,c}^{-1}$. Left: $\tilde{J}_I^{-1} = 2.5$, $\bar{\kappa} = 5.0$; center: $\tilde{J}_I^{-1} = 2.5$, $\bar{\kappa} = 10.0$; right: $\tilde{J}_I^{-1} = 3.0$, $\bar{\kappa} = 5.0$. Other parameters are $\bar{\phi} = 0.5$ and $\tilde{\sigma} = 1000$.

contrary to our case, thus their lattice and ours are dual networks. This, however, should not play any role in the continuous limit, when N is large, even though the critical Ising parameter value is then different. Last, the system size is also different, which also renormalizes the critical Ising parameter value. For these reasons, a direct comparison has not been performed a this stage. We can however conclude that we find qualitatively similar morphologies when varying $\bar{\kappa}$ as shown in Figs. 6.10 and 6.11. Note that Hu et al. (2011) have shows that these morphologies have very close free energies, they therefore probably correspond to metastable states (see Fig. 3 therein).

For lack of time, we could not explore this mechanism further in this work. Complementary simulations should be carried out in the future. The model can be improved further with a 4-state system fully accounting for the bilayer nature of the membrane and the four possible combinations of A and B species on each site. It is of interest to study numerically the case of vesicles with bending modulus-composition and curvature-composition couplings simultaneously and compare them to the analytical predictions of Gueguen et al. (2014).

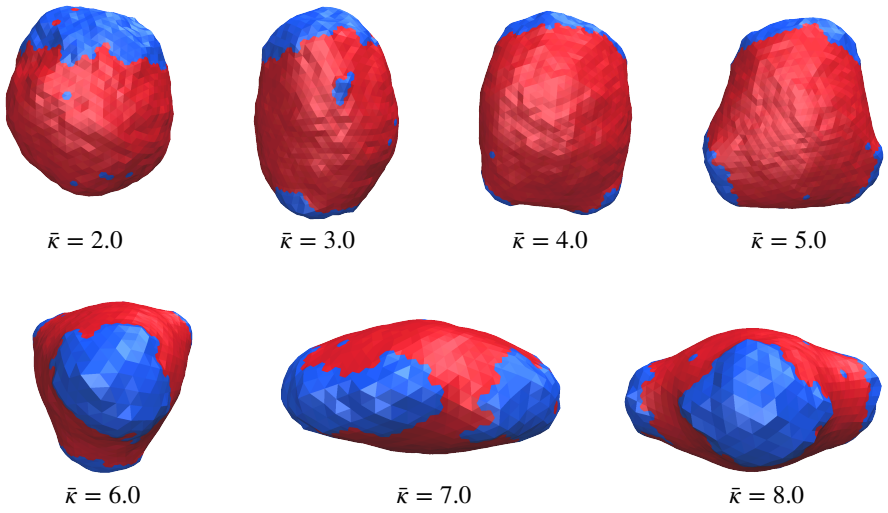

FIGURE 6.10 – Morphologies obtained by numerical simulations with κ coupling. $\bar{\phi} = 0.8$, $\tilde{J}_I^{-1} = 2.0$, $\tilde{\sigma} = 300$ and, from left to right, $\bar{\kappa} = 2$ to 8.

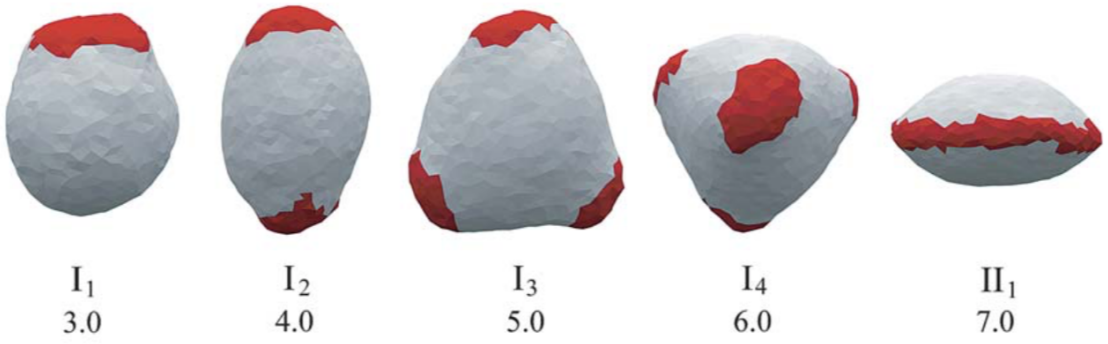

FIGURE 6.11 – Morphologies obtained by numerical simulations with κ coupling drawn from [HWL11]. The values under the images corresponds to the values of $\bar{\kappa}$.

Conclusion and outlooks

The curvature-composition coupling mechanism studied in this work is a good candidate to explain the formation of certain mesodomains in biomembranes. In [DMC18] we argued that it is one of the few most suitable mechanisms to explain the existence of membrane domains whose size is shorter than optical resolution, provided that some molecular species break the up/down symmetry of the membrane, inducing local curvature. Below the demixing temperature (strong segregation limit), aggregation is stopped before a macrophase emerges because curvature makes too large domains unstable. Above the demixing temperature (weak segregation limit), density fluctuations stabilized by curvature coupling have a typical size corresponding to a maximum of the structure factor, whereas their size distribution would decay exponentially without any coupling to curvature (Orstein-Zernicke behavior in a dilute phase [CL95]).

We were able to validate numerically the theoretical phase diagram proposed in Ref. [GDM14] below $J_{I,c}$. Furthermore, we completed the phase diagram above $J_{I,c}$ where no analytical solutions can easily be obtained. In addition to the modulation wavelength that is accessible through the maximum of the structure factor, we calculated the typical cluster size in the low-concentration region were clusters are well-defined. We checked that both approaches are mutually consistent. Contrary to the analytical single mode approximation used in Refs. [HMI98; KGL99; JLS00; HMO05], one observes qualitatively, by looking at the snapshots, and also quantitatively through the structure factor wide peak shape, that the resulting patterns are actually far from being regular stripes or periodically organized roundish domains. One rather obtains deformable domains with a liquid (i.e. short range) order.

Besides recovering qualitative correspondence with experimentally observed domains, we also provide quantitative predictions about their size. Concerning the question raised in the Introduction of their small size, below the diffraction limit, we proposed a scaling law for the typical domain size r in function of the spontaneous curvature C_1 imposed by the minority species, $r \simeq 1.4/C_1$ when $\bar{\phi} = 0.2$ and $\tilde{J}_I^{-1} = 2.0$. We can extrapolate this scaling law drawn from the simulation results to go beyond the spatial cut-off numerical limitation. For instance, for a vesicle of radius $R = 10$ μm, a typical domain size $r \approx 50$ nm, commonly observed by super-resolution microscopy, would lead to $C_1 \approx 0.03$ nm^{-1}. This curvature value can be reached for asymmetric lipid leaflets [PS11; HD20; Ste+20], lipid domains with glycolipid inclusions [Das+18] or protein domains [ZK06; BSL14], notably GPCR ones [Ros+17]. As a consequence, experimentally observed domain sizes can be accounted for by the model presented in this work. Further experiments on well-controlled model systems, reaching the sub-wavelength resolution (such as cryo-EM, AFM, superresolution fluorescence microscopy) will be useful to ascertain our predictions on the relationship between spontaneous curvature and domain size. Our IPBS colleagues are planning to carry out experiments on biphasic GUVs with GM1 insertion in

the outer leaflet promoting curvature [SIT16] to complete the link between experiments, molecular scale simulations and mesoscale ones.

This work also brought insight into the understanding of the effect of concentration increase on domain shape, from roundish domains to elongated ones that can fuse together. This morphological transition can be of particular biophysical interest because membrane cell domains are often supposed to be disjoint. However, in some experiments, some proteins are highly overexpressed in order to get a strong enough fluorescent signal. This might lead to an undesired change in domain morphologies, a possible experimental bias that should be quantified further in the future.

Note that some studies include Gaussian curvature and the associated saddle-splay modulus κ_G in membrane modeling [Sem+09; GGL09; HWL11]. It is generally assumed that $\kappa_G \approx -\kappa$ to ensure membrane stability [GGL09]. However, in most analytical and numerical works, the corresponding term in the Canham-Helfrich free energy is neglected, by arguing that at fixed topology, its integral over the whole membrane surface is an invariant due to the Gauss-Bonnet theorem. But if κ_G turns out to depend significantly on the lipid phase, this argument fails and a more rigorous approach is needed. Julicher et al. (1996) have tackled this question using the fact that when $\kappa_{G,Lo} \neq \kappa_{G,Ld}$, the integral over the whole surface can be simplified, still owing to the Gauss-Bonnet theorem. It is proportional to $\kappa_{G,Lo} - \kappa_{G,Ld}$ and can be written as the integral of the geodesic curvature along the interface between both phases, see Eq. (24) of Ref. [JL96]. It can potentially favor a longer interface and thus a mesophase [AZ17]. However, Julicher et al. (1996) study was only dedicated to the shape of vesicles undergoing macrophase separation, and not to the stability of mesophases. To our knowledge, a systematic study of the interplay between the different contributions to the membrane energy remains to be done to ascertain the precise role played by the Gaussian curvature and clarify when it can be neglected or not.

We also note that the Ising model that we use in this work does not take into account the distance between two lattice sites. This can affect the real line energy when the distance between sites is significantly modified. For example, in an elongated vesicle zone, this can then favor the formation of curved domains close to the tips by artificially locally reducing the line energy cost. However, this can only occur in the case of large deformations, which is beyond the framework of this study.

The fact that the phase diagram frontiers match the theory with the bare input value of $\tilde{\sigma}$ whereas $\tilde{\sigma}_{\text{eff}}$ is close to 0 when $\tilde{\sigma} = 300$ indicates that the renormalization of the surface tension in the coupled case is not well understood at this stage. We can use the spatial correlation function of the membrane height field (or equivalently the fluctuation spectrum) in order to measure the effective surface tension $\tilde{\sigma}_{\text{eff}}$. By integrating the composition degrees of freedom, we have in this case

$$H_{\text{tot,eff}} = \frac{\kappa_0}{2} \sum_{\lambda} M_u(l) |u_{l,m}|^2 \quad \text{and} \quad M_u(l) = H(l) - \frac{c_1^2 \left[l(l+1) - 2\right]^2}{\hat{m} + c_1^2 + \hat{J} l(l+1)} \tag{6.2}$$

with $H(l) = \left[l(l+1) - 2\right] \left[l(l+1) - 2 + \hat{\sigma}\right]$ as defined in Chapter 1.

When trying to fit the numerical data, we face the same numerical limitations as for the structure factor as detailed in Appendix A. We thus fix the values of two fit parameters, c_1 and $\hat{J}$ and constrain the accessible values of $\hat{m}$ in a small interval (Fig. 1). We note that in general we

get better fits with an input surface tension $\tilde{\sigma} = 600$ than at $\tilde{\sigma} = 300$. In order to test numerically

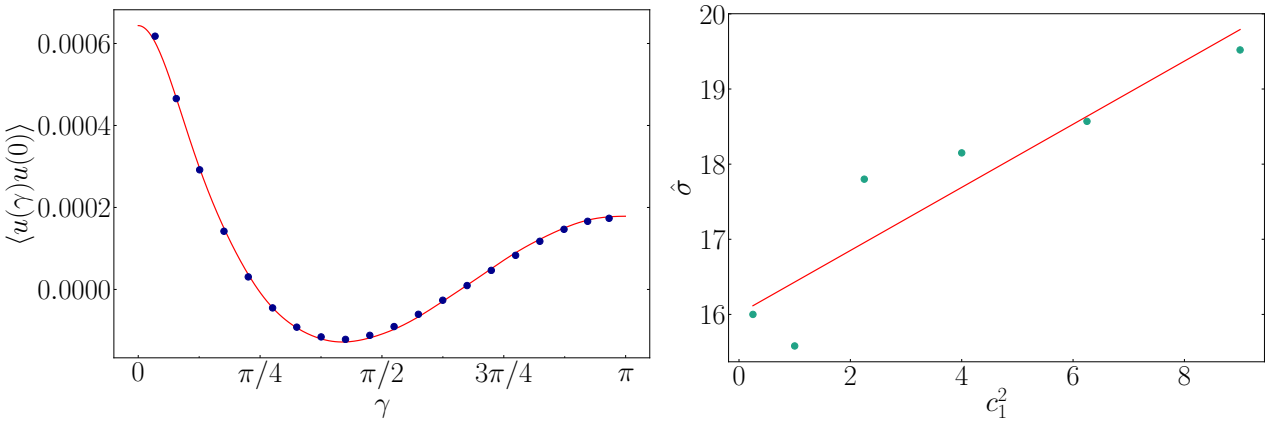

FIGURE 1 – **Left:** Example of a fit of the spatial correlation function of the vertex positions plotted in real space with $c_1 = 2.0$ and $\tilde{\sigma} = 600$. The fitted value of $\tilde{\sigma} \simeq 360$. **Right:** plot of the fitted surface tension $\hat{\sigma}$ against c_1^2 for simulations at input surface tension $\tilde{\sigma} = 600$ and thus $\hat{\sigma} = 30$. Other parameters are $N = 2562$, $\tilde{J}_I^{-1} = 4.0$ and $\bar{\phi} = 0.5$ in both figures.

the validity of the approximate relation 3.13 for $\tilde{\sigma}_{\text{eff}}$ we study the behavior of the fitted surface tension when varying c_1^2 only and N only. With an input surface tension of $\tilde{\sigma} = 600$ and for c_1 varying from 0.5 to 3, we fit in Fig. 1, right, the effective surface tension and plot it against c_1^2. We get a rough affine law with a slope of approximately 0.4. This is larger than the slope proposed in Eq. (3.13), expected to be $\frac{1}{2}\bar{\phi}^2 = 0.125$. In another test, we follow the same fitting procedure for two different system sizes $N = 2562$ and 10242 with the same parameters, $\bar{\phi} = 0.5$, $c_1 = 2.0$, $\tilde{J}_I^{-1} = 4.0$ and the input surface tension $\tilde{\sigma} = 1217$ as in Section 3.3. We find a slope in N of 0.006 whereas the expected one is $3/(8\pi) \approx 0.12$. This suggests that Eq. (3.13) is not valid for bicomponent vesicles, although this must be confirmed by additional simulations. It also indicates that the effective surface tension in our simulations is "less" renormalized than expected, especially for high c_1 values. This could explain why the theoretical frontiers computed with the bare input tension match the numerically obtained ones. Contrary to mean-field analytical Hamiltonians, the numerical energies are not limited to quadratic terms and contain all the coupling terms. The complementary terms they embrace might compensate and attenuate the renormalization terms of Eq. (3.13). This will have to be elucidated in future works by calculating how the surface tension is renormalized in the coupled model.

When studying the bending modulus-composition coupling, we also ran preliminary simulations below the critical Ising parameter $\tilde{J}_{I,c}$, where the mixture would be disordered in the absence of coupling, so to compare our results to the analytical predictions of Gueguen et al. (2014). The introduction of a bending modulus-composition coupling has been shown theoretically to stabilize small flat domains in this case [GDM14]. In our simulations, we qualitatively observe small A-species domains as shown in Fig. 2. However, these systems show the same size distribution as the ones observed in a system with no coupling and no typical domain size emerges (Fig. 2, left) as it would have been expected. Nevertheless, we can see in the plot of the structure factors (Fig. 2, right) that contrary to the structure factor of a similar system without coupling which maximum is in $l = 1$, the ones with bending modulus coupling unambiguously

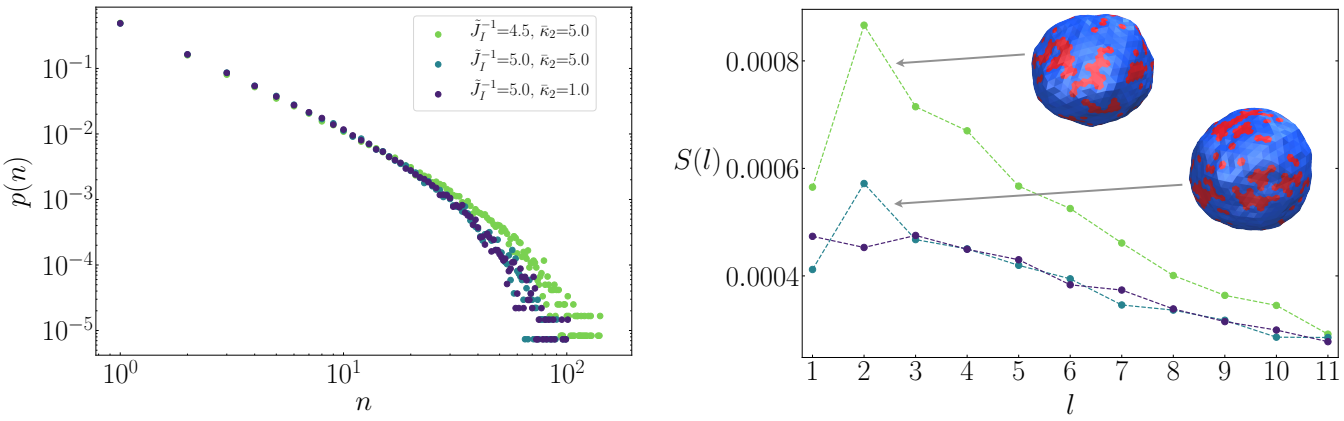

FIGURE 2 – **Left:** Domain size distribution in log-log scale in vesicles with bending modulus coupling ($\bar{\kappa} = 5.0$) for $\tilde{J}_I^{-1} < \tilde{J}_{I,c}^{-1}$ compared to an uncoupled system ($\bar{\kappa} = 1.0$, $\tilde{J}_I^{-1} = 5.0$). **Right:** Associated structure factors and vesicle snapshots, $\tilde{J}_I^{-1} = 4.5$ (green) and 5.0 (blue). Other parameters are $\bar{\phi} = 0.2$, $\tilde{\sigma} = 300$ and $c_0 = c_1 = 0$.

show a peak in $l = 2$. This suggest vesicle deformation towards a more prolate shape that could contribute to minimize the bending energy. The mixture may remain disordered as it is without coupling but the more rigid A-species patches may get located to particular zones of the vesicle in this case, promoting the prolate shape. Note that these preliminary simulations are performed at $\bar{\phi} = 0.2$ whereas the theoretical predictions are drawn at $\bar{\phi}_c = 1/2$.

The next step of this work will be to continue to explore models where not only the spontaneous curvature depends on local concentration, but also the bending rigidity κ, because the membrane thickness depends on its phase state. Some numerical works have tackled this issue (see Ref. [DMC18] for a review), but no systematic study has explored the corresponding phase diagrams and the entanglement between spontaneous curvature and bending modulus. From a numerical perspective, this leads to consider a 4-state Potts model coupled to the membrane shape to explicitly deal with the two membrane leaflet compositions, which leads to much more complex phase diagrams [GDM14]. This would provide a more accurate model for biomembranes, made of two asymmetric leaflets. As for now, we started to explore this question with a 3-state model as first step. We wrote a version of the program with 3 species (Fig. 3), corresponding to a lipid species with no spontaneous curvature ($C_0 = 2$, in blue) and 2 protein inclusions imposing local curvatures of opposite sign ($C_n < 0$, in green, and $C_p > 0$ in red), at $\bar{\phi}_p = \bar{\phi}_n = 0.2$. Clusters of such inclusions are supposed to repel each other (see [WD13]) but we observed that they arrange in a way that their boundaries are into contact, leading to alternative zones of positive and negative local curvature (Fig. 3, **a)**). It comes from the fact that by positioning this way, the total boundary length is smaller than with distant domains of positive and negative preferred curvature since the same Ising interaction parameter $\tilde{J}_I$ is at play between all the species. The long-range repulsion is not strong enough to counter the short-range attraction. We then performed simulations of systems with higher Ising parameter between the two species oppositely curving (Fig. 3, **b)**): $\tilde{J}_{p-n} = 10\tilde{J}_I$ and $\tilde{J}_{p-0} = \tilde{J}_{n-0} = \tilde{J}_I$ (where the subscript 0 corresponds to the species with $c_0 = 2.0$). In this case, the positive and negative inclusions arrange on the sphere with thin stripes of base-curvature species (blue) disconnecting them, strongly deforming the vesicle, but do not repel each other. Increasing the surface tension forces the vesicle to

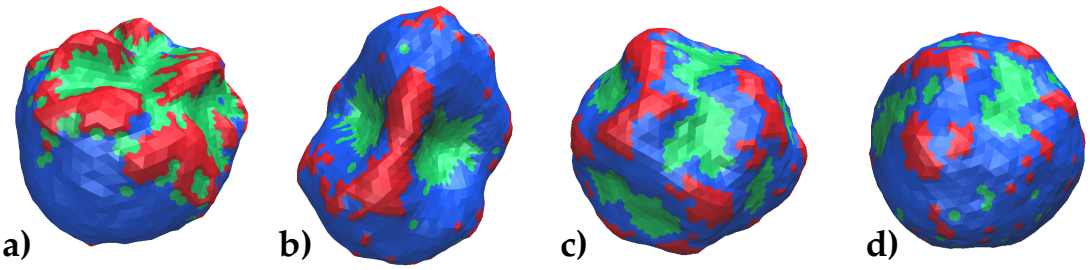

FIGURE 3 – Snapshots of 3-state simulated vesicles with $c_p = 6.0$ (red), $c_n = -6.0$ (green) and $\tilde{J}_I^{-1} = 2.5$. From left to right , **a)** $\tilde{J}_{p-n} = \tilde{J}_{p-0} = \tilde{J}_{n-0} = \tilde{J}_I$, $\tilde{\sigma} = 300$; **b)** $\tilde{J}_{p-n} = 10\tilde{J}_I$ and $\tilde{J}_{p-0} = \tilde{J}_{n-0} = \tilde{J}_I$, $\tilde{\sigma} = 300$; **c)** $\tilde{J}_{p-n} = 10\tilde{J}_I$ and $\tilde{J}_{p-0} = \tilde{J}_{n-0} = \tilde{J}_I$, $\tilde{\sigma} = 900$; **d)** $\tilde{J}_{p-n} = 10\tilde{J}_I$ and $\tilde{J}_{p-0} = \tilde{J}_{n-0} = \tilde{J}_I$, $\tilde{\sigma} = 1200$. $\bar{\phi}_p = \bar{\phi}_n = 0.2$ for the first three vesicles **a)** to **c)**, and $\bar{\phi}_p = \bar{\phi}_n = 0.1$ for the rightmost one **d)**.

be quasi-spherical (Fig. 3, **c)**) but the upwards and downwards inclusions still do not seem to undergo long-range repulsion. We eventually tried to decrease the inclusion concentration to $\bar{\phi}_p = \bar{\phi}_n = 0.1$ (Fig. 3, **d)**) and we still observe that the red and green inclusions tend to get localized close to one another. Indeed, the "hidden faces" of vesicles **c)** and **d)** are rich in blue species and do not present numerous red and green domains. They might arrange in this way since we deal with spherical geometry with volume and area constraints. This study will have to be continued and then enriched so as to achieve a biologically relevant 4-state model.

We also need to pursue our multiscale approach by using the links established between coarse-grained and mesoscale membrane parameters to run Monte Carlo simulations fed from realistic molecular input parameters. We can also consider applying a backmapping from mesoscale to coarse-grained as recently done by Pezeshkian et al. (2020). This would allow us to equilibrate slow large-scale membrane conformational changes at the mesoscale with Monte Carlo simulations, and then check their stability at the coarse-grained level and explore in further details the local properties at this resolution. One difficulty will be to control the value of the membrane surface tension in MARTINI simulations in spherical topology. Indeed in this case the only control parameter is the number of solvent molecules encapsulated in the vesicle, which sets the pressure difference across the membrane, and thus the surface tension owing to the Laplace law.

All in all, this work illustrates how simulating vesicles at the mesoscale enables one to address questions of biological and biophysical relevance, which cannot be tackled with more refined, however much more ressource-demanding simulations at the atomic or molecular scale. This thesis is an additional step of the efforts made in the group to fill the gap between experiments and modeling, that will undoubtedly be pursued in the future.

Appendix A

Numerical issues

We present here several numerical limitations encountered in this work and the way we addressed them.

A.1 Finite-size effects

The coupled theory developed in [GDM14] that was tested numerically in Chapter 3 is valid for infinite-size systems, whereas we study finite-size ones. This has some consequences on physical observables. The position of the second maximum in the structure factor indicates which mode is the most excited in the spatial species repartition $\phi(\theta, \varphi)$. This characterizes the patterns observed on the vesicle. The $l = 1$ mode is associated with the case where the species are totally separated, leading to one hemisphere rich in one species and one rich in the other.

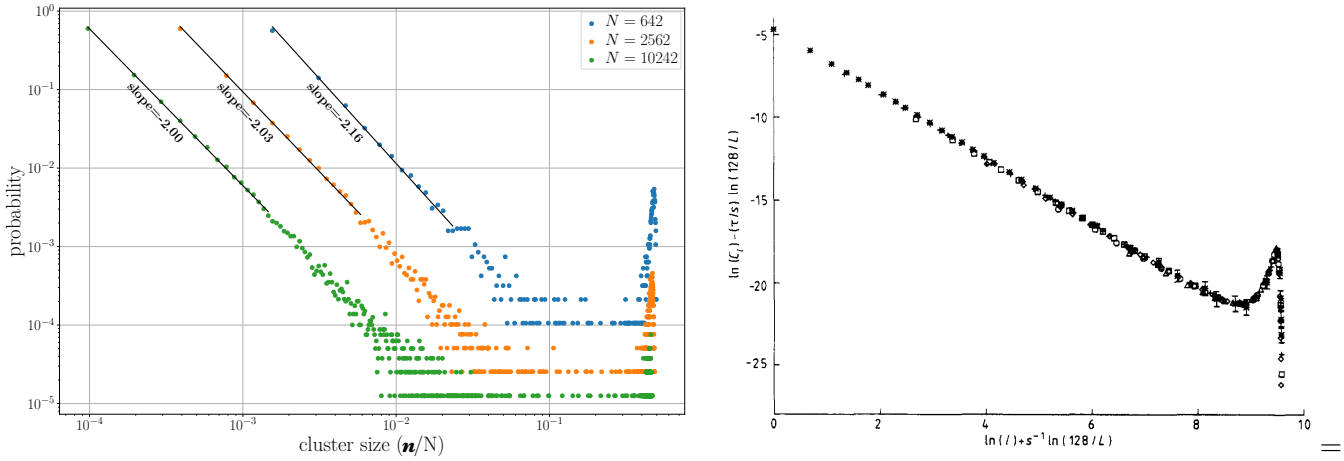

FIGURE 1 – **Left:** size distribution in log-log scale. The simulations are performed in the uncoupled case (pure Ising model, $c_1 = 0$) at the critical point ($\tilde{J}_I^{-1} = \tilde{J}_{I,c}^{-1} \simeq 3.62$ and $\bar{\phi} = \bar{\phi}_c = 1/2$). The bigger the system size, the lower the amplitude of the peak corresponding to big domain sizes (macrocluster). **Right:** this effect was already underlined by Toral et al. (1987) (figure reproduced from this work).

Close to the critical point, large density fluctuations make possible the occurrence of very large clusters in an infinite system. In a finite-size system, this leads to an over-abundance of macro-clusters, as thoroughly studied, for example, in [TW87]. This implies that the probability of having big domains covering half of the sphere (at $\bar{\phi} = \bar{\phi}_c$) is increased compared to the infinite-size system case, as illustrated in Fig. 1. When increasing the system size, one decreases this big domain occurrence. This effect artificially increases the contribution of $l = 1$ in the

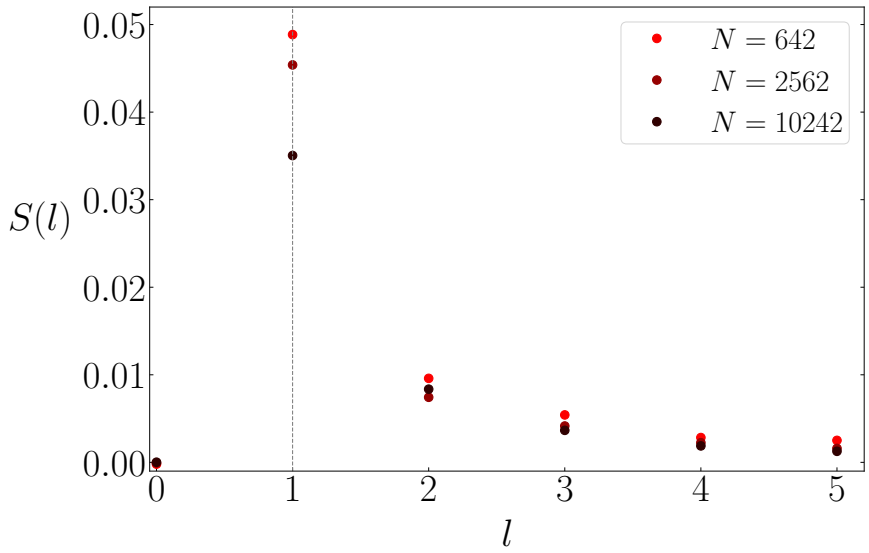

FIGURE 2 – Structure factor for different system sizes $N = 642$, 2562 and 10242, in the decoupled case (pure Ising model) at the critical point ($\tilde{J}_I^{-1} = \tilde{J}_{I,c}^{-1} \simeq 3.62$ and $\bar{\phi} = \bar{\phi}_c = 1/2$). The bigger the system size, the lower the amplitude of the $l = 1$ mode. Its value is overestimated along with system smallness.

structure factor $S(l)$, as depicted in Fig. 2 where the uncoupled case is studied for three different system sizes N. One observes that the bigger the system size, the lower the amplitude of the $l = 1$ mode corresponding to a macrocluster.

This finite-size effect is the reason why we do not take this point into account when fitting $S(l)$.

A.2 Fit of the structure factor: degenerescence of the parameter minimum

When fitting the structure factors, we minimize the square of the distance between the theoretical expression of $S(l)$ in Eq. (1.19) and the numerical data $S_{\rm num}(l)$, denoted by d^2. To do so, we used the GOSA software [GFR94; CCH06] that performs simulated annealing. As explained in Chapter 3, we obtained good fitted values of the parameter $\hat{J}$, with small error bars (provided by the software). In contrast, the fitted values of $\hat{m}$ and $\hat{\sigma}$ were quite far from the expected ones, with large error bars, suggesting that d^2 has a degenerate minimum in the parameter set. This can be understood thanks to the following argument.

The squared distance d^2 is defined as

$$d^2(\hat{J},\hat{m},\hat{\sigma}) = \sum_{l\geq 2} \left[S(l) - S_{\rm num}(l)\right]^2 . \tag{A.1}$$

The data $S_{\rm num}(l)$ are fixed and we look for the the parameter values of the variables $\hat{J}$, $\hat{m}$, and $\hat{\sigma}$, appearing implicitly in $S(l)$ that minimize d^2. Denoting generically these variables as x_i, we have the partial derivatives

$$\frac{\partial d^2}{\partial x_i} = 2\sum_{l\geq 2} \frac{\partial S(l)}{\partial x_i}\left[S(l) - S_{\rm num}(l)\right] \tag{A.2}$$

that must vanish at the minimum of d^2. We also need the second order derivatives to characterize this minimum:

$$\frac{\partial^2 d^2}{\partial x_i \partial x_j} = 2\sum_{l\geq 2} \left\{ \frac{\partial^2 S(l)}{\partial x_i \partial x_j}\left[S(l) - S_{\rm num}(l)\right] + \frac{\partial S(l)}{\partial x_i}\frac{\partial S(l)}{\partial x_j} \right\}. \tag{A.3}$$

We focus on the most favorable case where the measured values are close to the exact ones, in which case $S(l) \simeq S_{\rm num}(l)$ at the minimum of d^2. It follows that the first derivatives in Eq. (A.1) vanish, as expected. Owing to Eq. (1.19), the second derivatives become

$$\frac{\partial^2 d^2}{\partial x_i \partial x_j} = \frac{2}{\pi^2 \tilde{\kappa}_0^2} \sum_{l\geq 2} \frac{1}{M^4(l)} \frac{\partial M(l)}{\partial x_i}\frac{\partial M(l)}{\partial x_j}. \tag{A.4}$$

If we assume now that $M(l)^{-1}$ has a pronounced peak at position l^*, as explained in the main text, then $M^{-4}(l)$ is even more peaked, and the sum is dominated by $l = l^*$:

$$\frac{\partial^2 d^2}{\partial x_i \partial x_j} \simeq \frac{2}{\pi^2 \tilde{\kappa}_0^2} \frac{1}{M^4(l^*)} \frac{\partial M(l^*)}{\partial x_i}\frac{\partial M(l^*)}{\partial x_j}. \tag{A.5}$$

We now focus on the $(\hat{m},\hat{\sigma})$ subspace where the fit degeneracy arises. We recall that

$$M(l) = \hat{m} + \frac{c_1^2 \hat{\sigma}}{l(l+1) - 2 + \hat{\sigma}} + 2\hat{J}l(l+1). \tag{A.6}$$

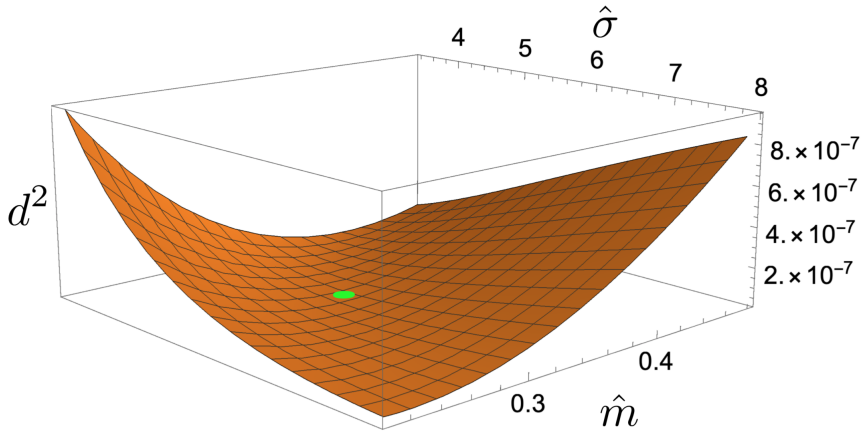

FIGURE 3 – Valley of quasi-degenerate minima of the squared differences $d^2(\hat{J}, \hat{m}, \hat{\sigma})$ between the theoretical structure factor $S(l)$ and some measured values, plotted in the $(\hat{m}, \hat{\sigma})$ subspace. The green dot represents the value found by the GOSA algorithm [GFR94; CCH06]. Here $c_1 = 1$, $\bar{\phi} = 0.5$, $\tilde{J}_I^{-1} = 4$ and $\tilde{\sigma} = 300$.

We get the Hessian matrix at the minimum of d^2:

$$\text{Hess}(l^*) = \frac{2}{\pi^2 \tilde{\kappa}_0^2} \frac{1}{M^4(l^*)} \begin{pmatrix} (\frac{\partial M}{\partial \hat{m}})^2 & \frac{\partial M}{\partial \hat{m}} \frac{\partial M}{\partial \hat{\sigma}} \\ \frac{\partial M}{\partial \hat{\sigma}} \frac{\partial M}{\partial \hat{m}} & (\frac{\partial M}{\partial \hat{\sigma}})^2 \end{pmatrix} \tag{A.7}$$

$$= \begin{pmatrix} 1 & A(l^*) \\ A(l^*) & A^2(l^*) \end{pmatrix}, \tag{A.8}$$

where

$$A(l) = \frac{2}{\pi^2 \tilde{\kappa}_0^2} \frac{c_1^2}{M^4(l)} \frac{l(l+1) - 2}{[l(l+1) - 2 + \hat{\sigma}]^2}. \tag{A.9}$$

This matrix has a trivial vanishing eigenvalue[1], which is the signature of a degenerate minimum, more precisely a valley of minima in the $(\hat{m}, \hat{\sigma})$ subspace parallel to the corresponding eigenstate. Figure 3 illustrates this result. This implies that if the numerical data are slightly different, we will not find the same minimum. Since we have measurement errors in our $S(l)$, we cannot reach the "real" minimum. The results are then not easily fittable and this explains why we get large error bars for $\hat{m}$ and $\hat{\sigma}$.

1. This comes here from the fact that $\frac{\partial M}{\partial \hat{m}} = 1$.

Appendix B

Role of the amplitude of the spatial step in the Monte Carlo random move

In this appendix we study the effect of the amplitude of the spatial displacement dr in the radial Monte Carlo random moves applied to vertex positions. In the simulations presented in this manuscript the displacement amplitude is $dr = 0.007R$. We compute the distribution of the difference of energy ΔE_u in the Monte Carlo random moves applied to vertex positions only over 10^6 moves after equilibration for two different dr values (Fig. 1). We note that distribution for $dr = 0.007R$ is not centered on zero and is shifted to a positive value on the order of 1.5 $k_{\mathrm{B}}T$. In this case the acceptance rate for the vertex position moves is around 42%. This energy difference can be induced by the curvature contribution in the elastic energy. For a triangle of area δx^2, this contribution reads

$$E = \frac{\kappa}{2}\,(H - C)^2\,\delta x^2 \tag{B.1}$$

$$|\delta E| \simeq \kappa\,|(H - C)\,\delta H|\,\delta x^2 \tag{B.2}$$

with C the local spontaneous curvature. One can estimate the discrete Laplacian and get $|\delta H| \approx 4\frac{\delta h}{\delta x^2}$ leading to

$$|\delta E| \approx 4\kappa\,|H - C|\,\delta h \tag{B.3}$$

$$\approx 0.6\,|H - C|\,R \tag{B.4}$$

in $k_{\mathrm{B}}T$ units. With $\kappa = 20$ and $\delta h = dr = 0.007R$ we get $|\delta E| \sim 1 k_{\mathrm{B}}T$ when H is different enough from C, as in the simulations presented in this work. This is indeed what what we observe in Fig. 1, left.

We check that with a smaller displacement amplitude, $dr = 0.002$ (Fig. 1, right), the distribution is now centered close to zero and the acceptance rate is around 81%. However using a smaller displacement amplitude implies running longer simulations in order to reach equilibrium and to get good statistical sampling.

Figure 2 shows two examples of structure factors of vesicles simulated with the same set of parameters but with different dr values. One can note that above $\tilde{J}_{I,c}^{-1}$ the structure factor is

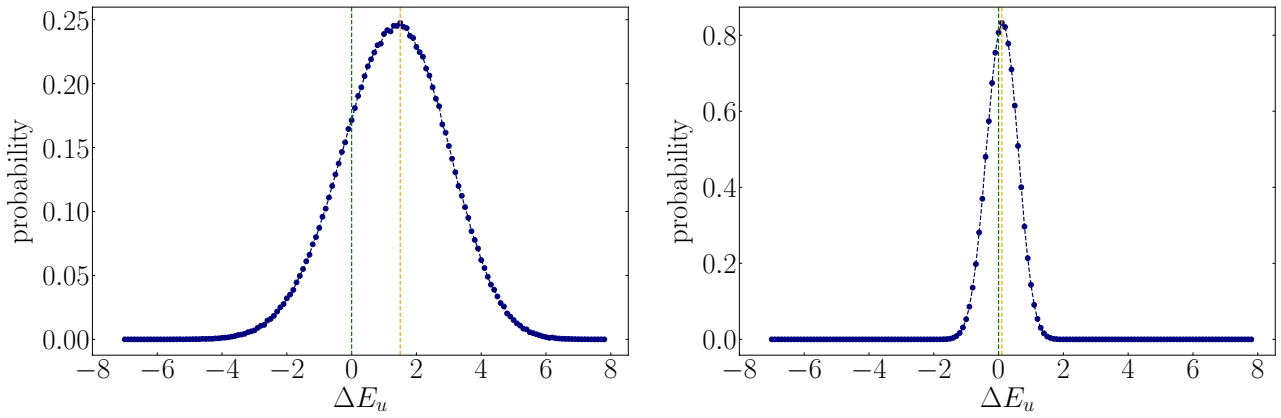

FIGURE 1 – Distribution of the difference of energy ΔE_u (whether the move be accepted or not) in $k_{\mathrm{B}}T$ units in the Monte Carlo random move applied to vertex positions only for $dr = 0.007$ (left) and $dr = 0.002$ (right), computed over 10^6 moves after equilibration. Mean values are indicated by the orange dotted lines. Simulation parameters are $\bar{\phi} = 0.5$, $\tilde{\sigma} = 300$, $c_1 = 2.0$ and $\tilde{J}_I^{-1} = 4.0$.

almost not affected by dr variation (left), however below $\tilde{J}_{I,c}^{-1}$ and with a stronger curvature coupling, they show slight differences (right).

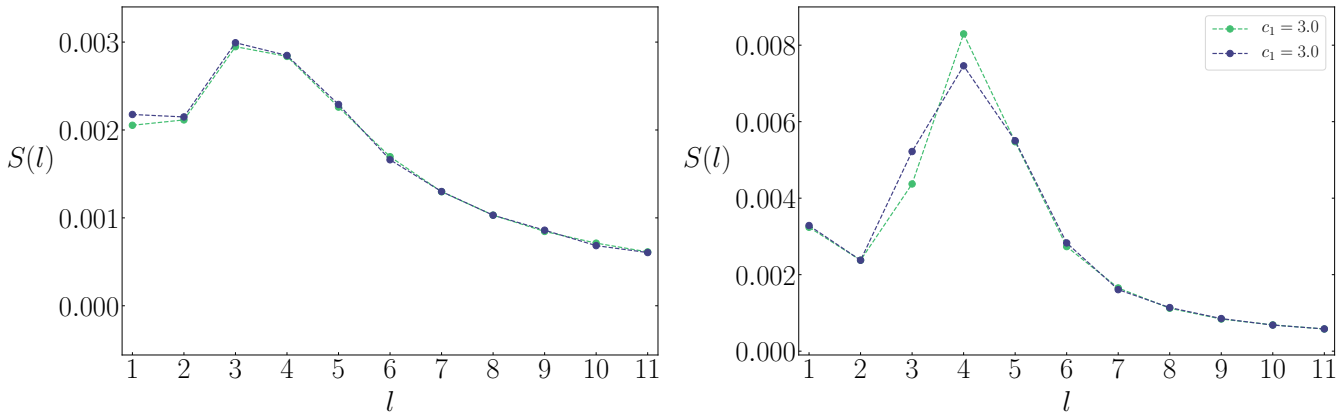

FIGURE 2 – Structure factors of vesicles simulated with the same set of parameters but with different radial displacement values, $dr = 0.007$ and 0.002. The vesicles are simulated with $c_1 = 2.0$ and $\tilde{J}_I^{-1} = 4.0$, left, and $c_1 = 3.0$ and $\tilde{J}_I^{-1} = 3.0$, right. Other parameters are $\bar{\phi} = 0.5$ and $\tilde{\sigma} = 300$ and the simulations were both run for 10^{10} MC steps.

In conclusion, the effect of the dr value has no noticeable consequences on the present results, especially since when the structure factor characteristics were in a borderline case we indicated the corresponding simulations with a specific color in the phase diagrams. However, note that if one wants to study refined effects one should better use a smaller displacement and run longer simulations.

Appendix C

Supplementary information about cells used in SPT experiments

In the appendix we provide some supplementary information about the cells used in the SPT experiments presented in Chapter 5. All these experiments were performed by Fabrice Dumas and his coworkers in Laurence Salomé's team. The following information was supplied by Fabrice Dumas.

To study HIV infection processes, Johnston et al. (2009) have developed an inducible cell line in which two membrane proteins (CD4 and CCR5) can be simultaneously and independently regulated with a large range of surface expression. F. Dumas and his coworkers used the Human Embryonic Kidney 293 cells (HEK-293) and have stably transfected this cell line to express the third membrane protein that can be involved in HIV infection, CXCR4. They have established two stable cell lines, one expressing a low number (15 000 $\pm$ 2000 per cell) of CXCR4 and one expressing a high number (120 000 $\pm$ 7000) of this protein. Figure 1 shows that the expression of CD4 and CCR5 can be simultaneously and independently controlled in these cell lines with various concentrations of minocycline and ponasterone, respectively. At basal state (i.e. without drug stimulation), cells express 2600 $\pm$ 300 copies of CD4 and 3600 $\pm$ 800 copies of CCR5. The number or both proteins increases upon the addition of the drugs to reach a maximum of 100 000 $\pm$ 13 000 copies of CD4 and 126 000 $\pm$ 8 000 copies of CCR5 (Figs. 1 and 2).

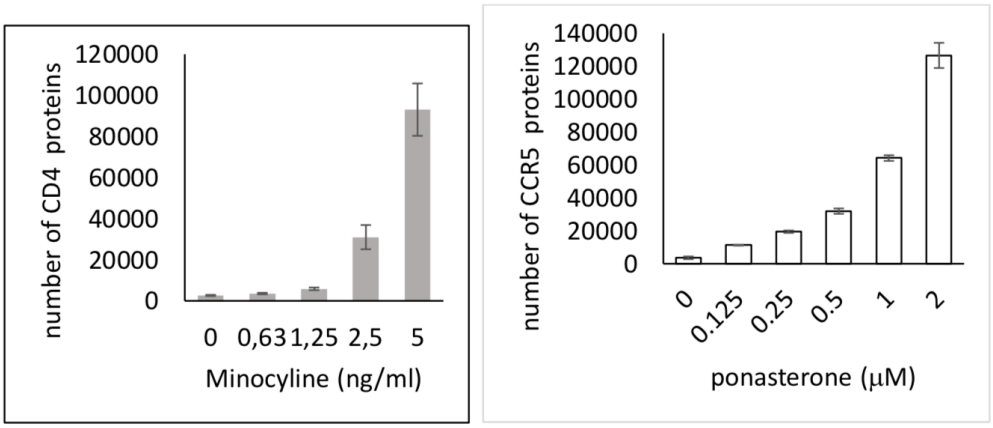

FIGURE 1 – CD4 and CCR5 can be regulated in the dually inducible 293-Affinofile cell line. Minocycline (left) and ponasterone (right) induce CD4 and CCR5 expression in a dose-dependent manner. The data are represented as mean values ± s.e.m of at least 5 independent measurements for each concentration. The inducible cells were seeded in 24-well plates 24 h before induction with the indicated concentrations of minocycline or ponA. At 18 h after induction, CD4 and CCR5 expression levels were determined by Fluorescence-Activated Cell Sorting (FACS) analysis.

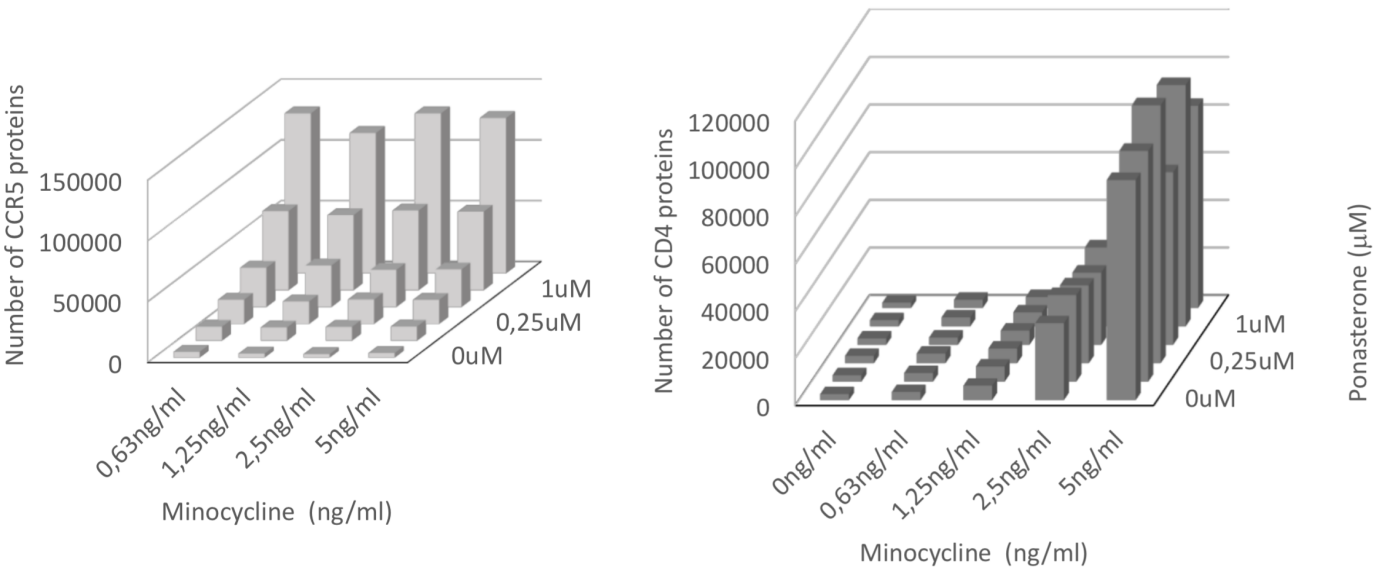

FIGURE 2 – CD4 and CCR5 can be independently and simultaneously regulated. **Left:** ponasterone induces the expression of CD4 proteins on the same manner whatever the minocycline concentration. **Right:** Minocycline induces the expression of CCR5 proteins on the same manner whatever the ponasterone concentration.

Appendix D

Green-Kubo theorem

This appendix provides the demonstration of the Green-Kubo theorem used in Section 6.1. The present demonstration is drawn from the book "*Introduction to Modern Statistical Mechanics*" by D. Chandler [Cha87].

We consider a perturbed Hamiltonian H such as

$$H = H_0 + \delta H \tag{D.1}$$

with H_0 the unperturbed Hamiltonian and δH the perturbation applied to the system.

We are here interested in the linear response, i.e. the case where the applied perturbation is low such as $\delta H \ll H_0$.

We consider an observable A and its equilibrium average value $\langle A \rangle_0$ so that

$$\langle A \rangle_0 = \int_\Omega dX p_0(X) A(X) \quad \text{where} \quad p_0(X) = \frac{e^{-\beta H_0(X)}}{Z} \tag{D.2}$$

with Ω the phase space, Z the partition function and X the canonical ensemble variables.

The average value of the observable A is defined as

$$\langle A \rangle = \frac{\int dX A(X) e^{-\beta[H_0(X)+\delta H(X)]}}{\int dX e^{-\beta[H_0(X)+\delta H(X)]}} \tag{D.3}$$

Using here the fact that $\delta H \ll H_0$, we get at the first order

$$e^{-\beta[H_0(X)+\delta H(X)]} \simeq e^{-\beta H_0(X)} (1 - \beta \delta H) \tag{D.4}$$

Finally, $\langle A \rangle$ is given by

$$\langle A \rangle \simeq \frac{\langle A \rangle_0 - \beta \langle A \delta H \rangle_0}{1 - \beta \langle \delta H \rangle_0} \tag{D.5}$$

After rearranging the previous equation, we get an equation establishing the proportionality between the shift of the average value of the observable A when the system is perturbed and the correlation function of A and the perturbation δH in equilibrium when the system is unperturbed:

$$\langle A \rangle - \langle A \rangle_0 = -\beta \left[\langle A \delta H \rangle_0 - \langle A \rangle_0 \langle \delta H \rangle_0 \right]. \tag{D.6}$$

Bibliography

[Abr+15] M. J. Abraham, T. Murtola, R. Schulz, S. Pall, J. C. Smith, B. Hess, and E. Lindahl. "GROMACS: High performance molecular simulations through multi-level parallelism from laptops to supercomputers". In: *SoftwareX* 1-2 (2015), pp. 19–25.

[ASR88] M. Abramowitz, I. A. Stegun, and R. H. Romer. *Handbook of mathematical functions with formulas, graphs, and mathematical tables*. United States Department of Commerce, 1988.

[AZ17] M. R. Adkins and Y. C. Zhou. "Geodesic curvature driven surface microdomain formation". In: *Journal of Computational Physics* 345 (2017), pp. 260–274.

[Ala+16] A. Alastuey, M. Clusel, M. Magro, and P. Pujol. *Physics and mathematical tools: Methods and examples*. World Scientific, 2016.

[Alb+02] B. Alberts, A. Johnson, J. Lewis, M. Raff, K. Roberts, and P. Walter. *Molecular biology of the cell (4th ed.)* ResearchGate. Garland Science, 2002.

[AGT09] D. Alcor, G. Gouzer, and A. Triller. "Single-particle tracking methods for the study of membrane receptors dynamics". In: *The European Journal of Neuroscience* 30.6 (2009). Number: 6, pp. 987–997.

[AF14] J. J. Amazon and G. W. Feigenson. "Lattice simulations of phase morphology on lipid bilayers: Renormalization, membrane shape, and electrostatic dipole interactions". In: *Physical Review E* 89.2 (2014), p. 022702.

[AKK92] D. Andelman, T. Kawakatsu, and K. Kawasaki. "Equilibrium shape of two-component unilamellar membranes and vesicles". In: *Europhysics Letters (EPL)* 19.1 (1992). Publisher: IOP Publishing, pp. 57–62.

[Aur+16] M. Aureli, L. Mauri, M. G. Ciampa, A. Prinetti, G. Toffano, C. Secchieri, and S. Sonnino. "GM1 ganglioside: Past studies and future potential". In: *Molecular Neurobiology* 53.3 (2016), pp. 1824–1842.

[Bak+07] A.-M. Baker, A. Sauliere, G. Gaibelet, B. Lagane, S. Mazères, M. Fourage, F. Bachelerie, L. Salomé, A. Lopez, and F. Dumas. "CD4 interacts constitutively with multiple CCR5 at the plasma membrane of living cells. A fluorescence recovery after photobleaching at variable radii approach". In: *The Journal of Biological Chemistry* 282.48 (2007), pp. 35163–35168.

[BS18] P. Bassereau and P. Sens. *Physics of Biological Membranes*. Springer International Publishing, 2018.

[BSL14] P. Bassereau, B. Sorre, and A. Levy. "Bending lipid membranes: Experiments after W. Helfrich's model". In: *Advances in Colloid and Interface Science*. Special issue in honour of Wolfgang Helfrich 208 (2014), pp. 47–57.

[Bau+05] T. Baumgart, S. Das, W. W. Webb, and J. T. Jenkins. "Membrane elasticity in giant vesicles with fluid phase coexistence". In: *Biophysical Journal* 89.2 (2005), pp. 1067–1080.

[Bax82] R. Baxter. *Exactly solved models in statistical mechanics*. Academic Press, 1982.

[Bea+17] D. Beauparlant, P. Rusert, C. Magnus, C. Kadelka, J. Weber, T. Uhr, O. Zagordi, C. Oberle, M. J. Duenas-Decamp, P. R. Clapham, K. J. Metzner, H. F. Gunthard, and A. Trkola. "Delineating CD4 dependency of HIV-1: Adaptation to infect low level CD4 expressing target cells widens cellular tropism but severely impacts on envelope functionality". In: *PLoS pathogens* 13.3 (2017). Number: 3, e1006255.

[Big+20] L. M. Biga, S. Dawson, A. Harwell, R. Hopkins, J. Kaufmann, M. LeMaster, P. Matern, K. Morrison-Graham, D. Quick, and J. Runyeon. *Anatomy and physiology*. OpenStax - Oregon State University, 2020.

[BT16] J. A. Bollinger and T. M. Truskett. "Fluids with competing interactions. I. Decoding the structure factor to detect and characterize self-limited clustering". In: *The Journal of Chemical Physics* 145.6 (2016), p. 064902.

[Can70] P. B. Canham. "The minimum energy of bending as a possible explanation of the biconcave shape of the human red blood cell". In: *Journal of Theoretical Biology* 26.1 (1970), pp. 61–81.

[Ceb+18] M. Cebecauer, M. Amaro, P. Jurkiewicz, M. J. Sarmento, R. Sachl, L. Cwiklik, and M. Hof. "Membrane Lipid Nanodomains". In: *Chemical Reviews* 118.23 (2018). Publisher: American Chemical Society, pp. 11259–11297.

[CL95] P. M. Chaikin and T. C. Lubensky. *Principles of condensed matter physics*. Cambridge University Press, 1995.

[Cha87] D. Chandler. *Introduction to modern statistical mechanics*. 1 edition. New York: Oxford University Press, 1987.

[CHA18] CHARMM-GUI. *Membrane builder*. Online; accessed June 26, 2020. 2018.

[Cha+18] M. Chavent, A. L. Duncan, P. Rassam, O. Birkholz, J. Helie, T. Reddy, D. Beliaev, B. Hambly, J. Piehler, C. Kleanthous, and M. S. P. Sansom. "How nanoscale protein interactions determine the mesoscale dynamic organisation of bacterial outer membrane proteins". In: *Nature Communications* 9.1 (2018). Number: 1 Publisher: Nature Publishing Group, p. 2846.

[CDS16] M. Chavent, A. L. Duncan, and M. S. Sansom. "Molecular dynamics simulations of membrane proteins and their interactions: from nanoscale to mesoscale". In: *Current Opinion in Structural Biology* 40 (2016), pp. 8–16.

[Con+13] S. D. Connell, G. Heath, P. D. Olmsted, and A. Kisil. "Critical point fluctuations in supported lipid membranes". In: *Faraday Discussions* 161.0 (2013). Publisher: The Royal Society of Chemistry, pp. 91–111.

[CDM20] J. Cornet, N. Destainville, and M. Manghi. "Domain formation in bicomponent vesicles induced by composition-curvature coupling". In: *The Journal of Chemical Physics* 152.24 (2020). Publisher: American Institute of Physics, p. 244705.

[CCH06] J. Czaplicki, G. Cornelissen, and F. Halberg. "GOSA, a simulated annealing-based program for global optimization of nonlinear problems, also reveals transyears". In: *Journal of applied biomedicine* 4.2 (2006), pp. 87–94.

[Das+18] R. Dasgupta, M. S. Miettinen, N. Fricke, R. Lipowsky, and R. Dimova. "The glycolipid GM1 reshapes asymmetric biomembranes and giant vesicles by curvature generation". In: *Proceedings of the National Academy of Sciences* 115.22 (2018), pp. 5756–5761.

[Dau+03] F. Daumas, N. Destainville, C. Millot, A. Lopez, D. Dean, and L. Salomé. "Confined diffusion without fences of a g-protein-coupled receptor as revealed by single particle tracking". In: *Biophysical Journal* 84.1 (2003), pp. 356–366.

[DM06] D. S. Dean and M. Manghi. "Fluctuation-induced interactions between domains in membranes". In: *Physical Review E* 74.2 (2006). Publisher: American Physical Society, p. 021916.

[Des10] N. Destainville. "An alternative scenario for the formation of specialized protein nano-domains (cluster phases) in biomembranes". In: *EPL (Europhysics Letters)* 91.5 (2010). Publisher: IOP Publishing, p. 58001.

[DF08] N. Destainville and L. Foret. "Thermodynamics of nanocluster phases: A unifying theory". In: *Physical Review E* 77 (2008), p. 051403.

[Des08] N. Destainville. "Cluster phases of membrane proteins". In: *Physical Review E* 77.1 (2008). Publisher: American Physical Society, p. 011905.

[DMC18] N. Destainville, M. Manghi, and J. Cornet. "A rationale for mesoscopic domain formation in biomembranes". In: *Biomolecules* 8.4 (2018).

[Dim14] R. Dimova. "Recent developments in the field of bending rigidity measurements on membranes". In: *Advances in Colloid and Interface Science* 208 (2014), pp. 225–234.

[Dog+05] M. Dogterom, J. W. Kerssemakers, G. Romet-Lemonne, and M. E. Janson. "Force generation by dynamic microtubules". In: *Current Opinion in Cell Biology* 17.1 (2005), pp. 67–74.

[DH17] F. Dumas and E. Haanappel. "Lipids in infectious diseases - The case of AIDS and tuberculosis". In: *Biochimica et Biophysica Acta (BBA) - Biomembranes*. Membrane Lipid Therapy: Drugs Targeting Biomembranes 1859.9 (2017). Number: 9, Part B, pp. 1636–1647.

[DPS14] F. Dumas, P. Preira, and L. Salomé. "Membrane organization of virus and target cell plays a role in HIV entry". In: *Biochimie* 107, Part A (2014), pp. 22–27.

[Dun+17] A. L. Duncan, T. Reddy, H. Koldso, J. Helie, P. W. Fowler, M. Chavent, and M. S. P. Sansom. "Protein crowding and lipid complexity influence the nanoscale dynamic organization of ion channels in cell membranes". In: *Scientific Reports* 7 (2017).

[EPS11] J. Ehrig, E. P. Petrov, and P. Schwille. "Phase separation and near-critical fluctuations in two-component lipid membranes: Monte Carlo simulations on experimentally relevant scales". In: *New Journal of Physics* 13.4 (2011). Publisher: IOP Publishing, p. 045019.

[Esp+08] C. Espenel, E. Margeat, P. Dosset, C. Arduise, C. Le Grimellec, C. A. Royer, C. Boucheix, E. Rubinstein, and P.-E. Milhiet. "Single-molecule analysis of CD9 dynamics and partitioning reveals multiple modes of interaction in the tetraspanin web". In: *The Journal of Cell Biology* 182.4 (2008), pp. 765–776.

[Esp+07] C. Esposito, A. Tian, S. Melamed, C. Johnson, S.-Y. Tee, and T. Baumgart. "Flicker spectroscopy of thermal lipid bilayer domain boundary fluctuations". In: *Biophysical Journal* 93.9 (2007), pp. 3169–3181.

[Ewe+10] H. Ewers, W. Romer, A. E. Smith, K. Bacia, S. Dmitrieff, W. Chai, R. Mancini, J. Kartenbeck, V. Chambon, L. Berland, A. Oppenheim, G. Schwarzmann, T. Feizi, P. Schwille, P. Sens, A. Helenius, and L. Johannes. "GM1 structure determines SV40-induced membrane invagination and infection". In: *Nature Cell Biology* 12.1 (2010). Number: 1 Publisher: Nature Publishing Group, pp. 11–18.

[FB01] G. W. Feigenson and J. T. Buboltz. "Ternary phase diagram of dipalmitoyl-PC/dilauroyl-PC/cholesterol: nanoscopic domain formation driven by cholesterol." In: *Biophysical Journal* 80.6 (2001), pp. 2775–2788.

[Flo53] P. Flory. *Principles of polymer chemistry*. Cornell University Press, 1953.

[Gai+06] G. Gaibelet, T. Planchenault, S. Mazères, F. Dumas, F. Arenzana-Seisdedos, A. Lopez, B. Lagane, and F. Bachelerie. "CD4 and CCR5 constitutively interact at the plasma membrane of living cells: a confocal fluorescence resonance energy transfer-based approach". In: *The Journal of Biological Chemistry* 281.49 (2006), pp. 37921–37929.

[GCS07] A. J. Garcia-Saez, S. Chiantia, and P. Schwille. "Effect of line tension on the lateral organization of lipid membranes". In: *The Journal of Biological Chemistry* 282.46 (2007), pp. 33537–33544.

[GFR94] W. L. Goffe, G. D. Ferrier, and J. Rogers. "Global optimization of statistical functions with simulated annealing". In: *Journal of Econometrics* 60.1 (1994), pp. 65–99.

[GAF13] S. L. Goh, J. J. Amazon, and G. W. Feigenson. "Toward a better raft model: Modulated phases in the four-component bilayer, DSPC/DOPC/POPC/CHOL". In: *Biophysical Journal* 104.4 (2013), p. 853.

[GK95] G. Gompper and D. M. Kroll. "Phase diagram and scaling behavior of fluid vesicles". In: *Physical Review E* 51.1 (1995). Publisher: American Physical Society, pp. 514–525.

[Gow+16] R. J. Gowers, M. Linke, J. Barnoud, T. J. E. Reddy, M. N. Melo, S. L. Seyler, J. Domanski, D. L. Dotson, S. Buchoux, I. M. Kenney, and O. Beckstein. "MDAnalysis: A Python package for the rapid analysis of Molecular Dynamics simulations". In: *Proceedings of the 15th Python in Science Conference* (2016). Conference Name: Proceedings of the 15th Python in Science Conference, pp. 98–105.

[Gra+11] S. L. Grage, A. M. Keleshian, T. Turdzeladze, A. R. Battle, W. C. Tay, R. P. May, S. A. Holt, S. A. Contera, M. Haertlein, M. Moulin, P. Pal, P. R. Rohde, V. T. Forsyth, A. Watts, K. C. Huang, A. S. Ulrich, and B. Martinac. "Bilayer-Mediated Clustering and Functional Interaction of MscL Channels". In: *Biophysical Journal* 100.5 (2011), pp. 1252–1260.

[GRO16] GROMACS. *GROMACS Reference Manual*. Online; accessed June 26, 2020. 2016.

[Gue16] G. Gueguen. "Vésicules lipidiques sous tension : des mésophases aux transitions de formes". PhD thesis. Université de Toulouse, Université Toulouse III - Paul Sabatier, 2016.

[GDM14] G. Gueguen, N. Destainville, and M. Manghi. "Mixed lipid bilayers with locally varying spontaneous curvature and bending". In: *The European Physical Journal E* 37.8 (2014), p. 76.

[GDM17] G. Gueguen, N. Destainville, and M. Manghi. "Fluctuation tension and shape transition of vesicles: renormalisation calculations and Monte Carlo simulations". In: *Soft Matter* 13.36 (2017), pp. 6100–6117.

[GGL09] E. Gutlederer, T. Gruhn, and R. Lipowsky. "Polymorphism of vesicles with multi-domain patterns". In: *Soft Matter* 5.17 (2009), pp. 3303–3311.

[Han06] J. F. Hancock. "Lipid rafts: Contentious only from simplistic standpoints". In: *Nature Reviews. Molecular Cell Biology* 7.6 (2006), pp. 456–462.

[HMI98] P. L. Hansen, L. Miao, and J. H. Ipsen. "Fluid lipid bilayers: Intermonolayer coupling and its thermodynamic manifestations". In: *Physical Review E* 58.2 (1998). Publisher: American Physical Society, pp. 2311–2324.

[HMO05] J. L. Harden, F. C. Mackintosh, and P. D. Olmsted. "Budding and domain shape transformations in mixed lipid films and bilayer membranes". In: *Physical Review. E, Statistical, Nonlinear, and Soft Matter Physics* 72.1 (2005), p. 011903.

[Har03] T. Harder. "Formation of functional cell membrane domains: The interplay of lipid- and protein-mediated interactions." In: *Philosophical Transactions of the Royal Society B: Biological Sciences* 358.1433 (2003), pp. 863–868.

[Har12] E. E. Harrison. *Equal area spherical subdivision*. Master degree thesis, University of Calgary, 2012.

[Heb+13] F. A. Heberle, R. S. Petruzielo, J. Pan, P. Drazba, N. Kucerka, R. F. Standaert, G. W. Feigenson, and J. Katsaras. "Bilayer thickness mismatch controls domain size in model membranes". In: *Journal of the American Chemical Society* 135.18 (2013). Publisher: American Chemical Society, pp. 6853–6859.

[Heb+10] F. A. Heberle, J. Wu, S. L. Goh, R. S. Petruzielo, and G. W. Feigenson. "Comparison of three ternary lipid bilayer mixtures: FRET and ESR reveal nanodomains". In: *Biophysical Journal* 99.10 (2010), pp. 3309–3318.

[Hee02] H. Heerklotz. "Triton promotes domain formation in lipid raft mixtures." In: *Biophysical Journal* 83.5 (2002).

[Hel73] W. Helfrich. "Elastic properties of lipid bilayers: Theory and possible experiments." In: *Zeitschrift für Naturforschung C* 28 (1973), pp. 693–703.

[Her+07] A. Heredia, B. Gilliam, A. DeVico, N. Le, D. Bamba, R. Flinko, G. Lewis, R. C. Gallo, and R. R. Redfield. "CCR5 density levels on primary CD4 T cells impact the replication and Enfuvirtide susceptibility of R5 HIV-1". In: *AIDS (London, England)* 21.10 (2007). Number: 10, pp. 1317–1322.

[HKP16] C. S. Ho, N. K. Khadka, and J. Pan. "Sub-ten-nanometer heterogeneity of solid supported lipid membranes determined by solution atomic force microscopy". In: *Biochimica et Biophysica Acta (BBA) - Biomembranes* 1858.2 (2016), pp. 181–188.

[Hol+16] D. A. Holdbrook, R. G. Huber, T. J. Piggot, P. J. Bond, and S. Khalid. "Dynamics of crowded vesicles: Local and global responses to membrane composition". In: *PLOS ONE* 11.6 (2016). Publisher: Public Library of Science, e0156963.

[Hon+08] A. R. Honerkamp-Smith, P. Cicuta, M. D. Collins, S. L. Veatch, M. den Nijs, M. Schick, and S. L. Keller. "Line tensions, correlation lengths, and critical exponents in lipid membranes near critical points". In: *Biophysical Journal* 95.1 (2008), pp. 236–246.

[HVK09] A. R. Honerkamp-Smith, S. L. Veatch, and S. L. Keller. "An introduction to critical points for biophysicists; observations of compositional heterogeneity in lipid membranes". In: *Biochimica Et Biophysica Acta* 1788.1 (2009), pp. 53–63.

[Hon+14] A. Honigmann, V. Mueller, H. Ta, A. Schoenle, E. Sezgin, S. W. Hell, and C. Eggeling. "Scanning STED-FCS reveals spatiotemporal heterogeneity of lipid interaction in the plasma membrane of living cells". In: *Nature Communications* 5 (2014), p. 5412.

[HD20] A. Hossein and M. Deserno. "Spontaneous curvature, differential stress, and bending modulus of asymmetric lipid membranes". In: *Biophysical Journal* 118 (2020), pp. 624–642.

[Hou+18] R. Houmadi, D. Guipouy, J. Rey-Barroso, Z. Vasconcelos, J. Cornet, M. Manghi, N. Destainville, S. Valitutti, S. Allart, and L. Dupré. "The Wiskott-Aldrich Syndrome Protein Contributes to the Assembly of the LFA-1 Nanocluster Belt at the Lytic Synapse". In: *Cell Reports* 22.4 (2018), pp. 979–991.

[HWL11] J. Hu, T. Weikl, and R. Lipowsky. "Vesicles with multiple membrane domains". In: *Soft Matter* 7.13 (2011), pp. 6092–6102.

[IKK01] R. Iino, I. Koyama, and A. Kusumi. "Single molecule imaging of green fluorescent proteins in living cells: E-cadherin forms oligomers on the free cell surface". In: *Biophysical Journal* 80.6 (2001), pp. 2667–2677.

[Ing+16] H. I. Ingolfsson, C. Arnarez, X. Periole, and S. J. Marrink. "Computational 'microscopy' of cellular membranes". In: *Journal of Cell Science* 129.2 (2016). Publisher: The Company of Biologists Ltd Section: Commentary, pp. 257–268.

[Ips+87] J. H. Ipsen, G. Karlstrom, O. G. Mouritsen, H. Wennerstrom, and M. J. Zuckermann. "Phase equilibria in the phosphatidylcholine-cholesterol system". In: *Biochimica Et Biophysica Acta* 905.1 (1987), pp. 162–172.

[JL96] F. Julicher and R. Lipowsky. "Shape transformations of vesicles with intramembrane domains". In: *Physical Review E* 53.3 (1996), pp. 2670–2683.

[JL16] K. Jacobson and P. Liu. "Complexity revealed: A hierarchy of clustered membrane proteins". In: *Biophysical Journal* 111 (2016), pp. 1–2.

[JMA07] K. Jacobson, O. G. Mouritsen, and R. G. W. Anderson. "Lipid rafts: At a crossroad between cell biology and physics". In: *Nature Cell Biology* 9.1 (2007), pp. 7–14.

[JLS00] Y. Jiang, T. Lookman, and A. Saxena. "Phase separation and shape deformation of two-phase membranes". In: *Physical Review E* 61.1 (2000). Publisher: American Physical Society, R57–R60.

[Joh+09] S. H. Johnston, M. A. Lobritz, S. Nguyen, K. Lassen, S. Delair, F. Posta, Y. J. Bryson, E. J. Arts, T. Chou, and B. Lee. "A quantitative affinity-profiling system that reveals distinct CD4/CCR5 usage patterns among human immunodeficiency virus type 1 and simian immunodeficiency virus strains". In: *Journal of Virology* 83.21 (2009), pp. 11016–11026.

[Jon+13] D. H. de Jong, G. Singh, W. F. D. Bennett, C. Arnarez, T. A. Wassenaar, L. V. Schafer, X. Periole, D. P. Tieleman, and S. J. Marrink. "Improved parameters for the martini coarse-grained protein force field". In: *Journal of Chemical Theory and Computation* 9.1 (2013). Publisher: American Chemical Society, pp. 687–697.

[Jun+16] Y. Jung, I. Riven, S. W. Feigelson, E. Kartvelishvily, K. Tohya, M. Miyasaka, R. Alon, and G. Haran. "Three-dimensional localization of T-cell receptors in relation to microvilli using a combination of superresolution microscopies". In: *Proceedings of the National Academy of Sciences of the United States of America* 113.40 (2016). Number: 40, E5916–E5924.

[Kaw+93] T. Kawakatsu, D. Andelman, K. Kawasaki, and T. Taniguchi. "Phase transitions and shapes of two component membranes and vesicles I: Strong segregation limit". In: *Journal de Physique II* 3 (1993), pp. 971–997.

[KKS15] S. Kawamoto, M. L. Klein, and W. Shinoda. "Coarse-grained molecular dynamics study of membrane fusion: Curvature effects on free energy barriers along the stalk mechanism". In: *The Journal of Chemical Physics* 143.24 (2015). Publisher: American Institute of Physics, p. 243112.

[KK15] P. Khakbaz and J. B. Klauda. "Probing the importance of lipid diversity in cell membranes via molecular simulation". In: *Chemistry and Physics of Lipids* 192 (2015), pp. 12–22.

[KWT09] V. Kiessling, C. Wan, and L. K. Tamm. "Domain coupling in asymmetric lipid bilayers". In: *Biochimica Et Biophysica Acta* 1788.1 (2009).

[KS13] E. Klotzsch and G. J. Schutz. "A critical survey of methods to detect plasma membrane rafts". In: *Philosophical Transactions of the Royal Society B: Biological Sciences* 368.1611 (2013).

[KA14] S. Komura and D. Andelman. "Physical aspects of heterogeneities in multi-component lipid membranes". In: *Advances in Colloid and Interface Science* 208.C (2014), pp. 34–46.

[Kon+11a] T. M. Konyakhina, S. L. Goh, J. Amazon, F. A. Heberle, J. Wu, and G. W. Feigenson. "Control of a Nanoscopic-to-Macroscopic Transition: Modulated Phases in Four-Component DSPC/DOPC/POPC/Chol Giant Unilamellar Vesicles". In: *Biophysical Journal* 101.2 (2011), p. L8.

[Kon+11b] T. M. Konyakhina, S. L. Goh, J. Amazon, F. A. Heberle, J. Wu, and G. W. Feigenson. "Control of a nanoscopic-to-macroscopic transition: modulated phases in four-component DSPC/DOPC/POPC/Chol Giant Unilamellar Vesicles". In: *Biophysical Journal* 101.2 (2011), p. L8.

[KA13] M. Krzywinski and N. Altman. "Points of significance: Significance, P values and t-tests". In: *Nature methods* 10.11 (2013). Publisher: Nature Publishing Group, pp. 1041–1042.

[KTH91] R. Kubo, M. Toda, and N. Hashitsume. *Statistical physics II: Nonequilibrium statistical mechanics*. 2nd ed. Springer Series in Solid-State Sciences, Springer Ser.Solid-State Statistical Physics. Berlin Heidelberg: Springer-Verlag, 1991.

[Kuh+00] S. E. Kuhmann, E. J. Platt, S. L. Kozak, and D. Kabat. "Cooperation of multiple CCR5 coreceptors is required for infections by human immunodeficiency virus type 1". In: *Journal of Virology* 74.15 (2000), pp. 7005–7015.

[KGL99] P. B. S. Kumar, G. Gompper, and R. Lipowsky. "Modulated phases in multicomponent fluid membranes". In: *Physical Review E* 60.4 (1999). Publisher: American Physical Society, pp. 4610–4618.

[LR10] T. Lang and S. O. Rizzoli. "Membrane protein clusters at nanoscale resolution: More than pretty pictures". In: *Physiology* 25.2 (2010), pp. 116–124.

[Lei86] S. Leibler. "Curvature instability in membranes". In: *Journal de Physique (France)* 47 (1986), pp. 507–516.

[LA87] S. Leibler and D. Andelman. "Ordered and curved meso-structures in membranes and amphiphilic films". In: *Journal de Physique* 48.11 (1987), pp. 2013–2018.

[Les11] M. Leslie. "Do lipid rafts exist?" In: *Science* 334 (2011), pp. 1046–1047.

[LV16] I. Levental and S. Veatch. "The continuing mystery of lipid rafts". In: *Journal of Molecular Biology* 428 (2016), pp. 4749–4764.

[LM13] D. Levy and P.-E. Milhiet. "Imaging of Transmembrane Proteins Directly Incorporated Within Supported Lipid Bilayers Using Atomic Force Microscopy". In: *Nanoimaging* (2013). Publisher: Humana Press, Totowa, NJ, pp. 343–357.

[LS10] D. Lingwood and K. Simons. "Lipid rafts as a membrane-organizing principle". In: *Science (New York, N.Y.)* 327.5961 (2010), pp. 46–50.

[LP09] D. T. Lodowski and K. Palczewski. "Chemokine receptors and other GPCRs". In: *Current opinion in HIV and AIDS* 4.2 (2009), pp. 88–95.

[Lop+13] C. A. Lopez, Z. Sovova, F. J. van Eerden, A. H. de Vries, and S. J. Marrink. "Martini force field parameters for glycolipids". In: *Journal of Chemical Theory and Computation* 9.3 (2013), pp. 1694–1708.

[Lou+10] M. Louhivuori, H. J. Risselada, E. v. d. Giessen, and S. J. Marrink. "Release of content through mechano-sensitive gates in pressurized liposomes". In: *Proceedings of the National Academy of Sciences* 107.46 (2010). Publisher: National Academy of Sciences Section: Biological Sciences, pp. 19856–19860.

[Mar+19] S. J. Marrink, V. Corradi, P. C. Souza, H. I. Ingolfsson, D. P. Tieleman, and M. S. Sansom. "Computational modeling of realistic cell membranes". In: *Chemical Reviews* (2019).

[Mar+07] S. J. Marrink, H. J. Risselada, S. Yefimov, D. P. Tieleman, and A. H. de Vries. "The MARTINI force field: Coarse grained model for biomolecular simulations". In: *The Journal of Physical Chemistry B* 111.27 (2007), pp. 7812–7824.

[MT13] S. J. Marrink and D. P. Tieleman. "Perspective on the Martini model". In: *Chemical Society Reviews* 42.16 (2013), pp. 6801–6822.

[Mar09] D. Marsh. "Cholesterol-induced fluid membrane domains: A compendium of lipid-raft ternary phase diagrams". In: *Biochimica Et Biophysica Acta* 1788.10 (2009), pp. 2114–2123.

[Mar10] D. Marsh. "Molecular volumes of phospholipids and glycolipids in membranes". In: *Chemistry and Physics of Lipids* 163.7 (2010), pp. 667–677.

[Mas+12] P. Mascalchi, A. S. Lamort, L. Salomé, and F. Dumas. "Single Particle Tracking reveals two distinct environments for CD4 receptors at the surface of living T lymphocytes". In: *Biochemical and Biophysical Research Communications* 417.1 (2012), pp. 409–413.

[Mas12] P. Masclachi. "Analyse par suivi de particule unique a la surface de lymphocytes vivants de l'organisation dynamique des récepteurs CD4 et CCR5 impliqués dans l'infection par le VIH". PhD thesis. Université de Toulouse, Université Toulouse III - Paul Sabatier, 2012.

[Mei+06] N. Meilhac, L. Le Guyader, L. Salomé, and N. Destainville. "Detection of confinement and jumps in single-molecule membrane trajectories". In: *Physical Review E* 73.1 (2006). Publisher: American Physical Society, p. 011915.

[Mer+17] E. Merklinger, J.-G. Schloetel, P. Weber, H. Batoulis, S. Holz, N. Karnowski, J. Finke, and T. Lang. "The packing density of a supramolecular membrane protein cluster is controlled by cytoplasmic interactions". In: *eLife* 6 (2017). Ed. by R. Jahn. Publisher: eLife Sciences Publications, Ltd, e20705.

[Mey+03] M. Meyer, M. Desbrun, P. Schröder, and A. H. Barr. *Discrete differential-geometry operators for triangulated 2-manifolds*. Berlin, Heidelberg: Springer Berlin Heidelberg, 2003, pp. 35–57.

[MK15] V. Monje-Galvan and J. B. Klauda. "Modeling yeast organelle membranes and how lipid diversity influences bilayer properties". In: *Biochemistry* 54.45 (2015), pp. 6852–6861.

[Mon+08] L. Monticelli, S. K. Kandasamy, X. Periole, R. G. Larson, D. P. Tieleman, and S.-J. Marrink. "The MARTINI coarse-grained force field: Extension to proteins". In: *Journal of Chemical Theory and Computation* 4.5 (2008). Publisher: American Chemical Society, pp. 819–834.

[MMH14] F. Mora-Bermudez, F. Matsuzaki, and W. B. Huttner. "Specific polar subpopulations of astral microtubules control spindle orientation and symmetric neural stem cell division". In: *eLife* 3 (2014). Ed. by F. Miller. Publisher: eLife Sciences Publications, Ltd, e02875.

[Mou05] O. G. Mouritsen. *Life - as a matter of fat: The emerging science of lipidomics*. The Frontiers Collection. Berlin Heidelberg: Springer-Verlag, 2005.

[MD11] S. N. Mulampaka and N. M. Dixit. "Estimating the threshold surface density of gp120-CCR5 complexes necessary for HIV-1 envelope-mediated cell-cell fusion". In: *PLoS ONE* 6.5 (2011). Number: 5.

[Mun03] S. Munro. "Lipid rafts: elusive or illusive?" In: *Cell* 115.4 (2003), pp. 377–388.

[Nel13] P. Nelson. *Cell biology by the numbers*. Macmillan Publishers, 2013.

[NP95] R. R. Netz and P. Pincus. "Inhomogeneous fluid membranes: Segregation, ordering, and effective rigidity". In: *Physical Review E* 52.4 (1995), pp. 4114–4128.

[NB99] M. E. J. Newman and G. T. Barkema. *Monte Carlo Methods in Statistical Physics*. Oxford, New York: Oxford University Press, 1999.

[Nic+15] J. D. Nickels, X. Cheng, B. Mostofian, C. Stanley, B. Lindner, F. A. Heberle, S. Perticaroli, M. Feygenson, T. Egami, R. F. Standaert, J. C. Smith, D. A. A. Myles, M. Ohl, and J. Katsaras. "Mechanical properties of nanoscopic lipid domains". In: *Journal of the American Chemical Society* 137.50 (2015), pp. 15772–15780.

[Onu02] A. Onuki. *Phase transition dynamics*. Cambridge: Cambridge University Press, 2002.

[Pen+15] S. Penic, A. Iglic, I. Bivas, and M. Fosnaric. "Bending elasticity of vesicle membranes studied by Monte Carlo simulations of vesicle thermal shape fluctuations". In: *Soft Matter* 11.25 (2015), pp. 5004–5009.

[PS11] J. D. Perlmutter and J. N. Sachs. "Interaction and asymmetry in phase separated lipid bilayers: molecular dynamics simulations". In: *Journal of the American Chemical Society* 133 (2011), pp. 6563–6577.

[Pez+20] W. Pezeshkian, M. Konig, T. A. Wassenaar, and S. J. Marrink. "Backmapping triangulated surfaces to coarse-grained membrane models". In: *Nature Communications* 11.1 (2020). Number: 1 Publisher: Nature Publishing Group, p. 2296.

[PM15] R. Phillips and R. Milo. *Cell biology by the numbers*. Garland Science, 2015.

[Pik06] L. J. Pike. "Rafts defined: A report on the Keystone Symposium on lipid rafts and cell function". In: *Journal of Lipid Research* 47.7 (2006), pp. 1597–1598.

[Pov+08] J. A. Poveda, A. M. Fernandez, J. A. Encinar, and J. M. Gonzalez-Ros. "Protein-promoted membrane domains". In: *Biochimica et Biophysica Acta (BBA) - Biomembranes*. Protein Modulation of Membrane Structure 1778.7 (2008), pp. 1583–1590.

[Ros+17] K. R. Rosholm, N. Leijnse, A. Mantsiou, V. Tkach, S. L. Pedersen, V. F. Wirth, L. B. Oddershede, K. J. Jensen, K. L. Martinez, N. S. Hatzakis, P. M. Bendix, A. Callan-Jones, and D. Stamou. "Membrane curvature regulates ligand-specific membrane sorting of GPCRs in living cells". In: *Nature Chemical Biology* 13.7 (2017). Number: 7 Publisher: Nature Publishing Group, pp. 724–729.

[Rou+11] C. Roubinet, B. Decelle, G. Chicanne, J. F. Dorn, B. Payrastre, F. Payre, and S. Carreno. "Molecular networks linked by Moesin drive remodeling of the cell cortex during mitosis". In: *Journal of Cell Biology* 195.1 (2011). Publisher: The Rockefeller University Press, pp. 99–112.

[Saf18] S. Safran. *Statistical thermodynamics of surfaces, interfaces, and membranes*. CRC Press, 2018.

[SLD06] L. Salomé, P.-F. Lenne, and N. Destainville. "Membranes biologiques : vers un modele physique". In: 2006.

[Sch15] C.-L. Schengrund. "Gangliosides: glycosphingolipids essential for normal neural development and function". In: *Trends in Biochemical Sciences* 40.7 (2015), pp. 397–406.

[Sch12] M. Schick. "Membrane heterogeneity: Manifestation of a curvature-induced microemulsion". In: *Physical Review E* 85 (2012), p. 031902.

[Sch17] F. Schmid. "Physical mechanisms of micro- and nanodomain formation in multicomponent lipid membranes". In: *Biochimica et Biophysica Acta (BBA) - Biomembranes* 1859.4 (2017). arXiv: 1611.04202, pp. 509–528.

[Sea+99] R. P. Sear, S. W. Chung, G. Markovich, W. M. Gelbart, and J. R. Heath. "Spontaneous patterning of quantum dots at the air-water interface". In: *Physical Review. E, Statistical Physics, Plasmas, Fluids, and Related Interdisciplinary Topics* 59.6 (1999), R6255–6258.

[Sem+09] S. Semrau, T. Idema, T. Schmidt, and C. Storm. "Membrane-mediated interactions measured using membrane domains". In: *Biophysical Journal* 96.12 (2009), pp. 4906–4915.

[SS09] S. Semrau and T. Schmidt. "Membrane heterogeneity - from lipid domains to curvature effects". In: *Soft Matter* 5.17 (2009). Publisher: The Royal Society of Chemistry, pp. 3174–3186.

[SA95] M. Seul and D. Andelman. "Domain shapes and patterns: The phenomenology of modulated phases". In: *Science* 267.5197 (1995), pp. 476–483.

[Sez+17] E. Sezgin, I. Levental, S. Mayor, and C. Eggeling. "The mystery of membrane organization: Composition, regulation and roles of lipid rafts". In: *Nature Review Molecular Cell Biology* 18 (2017), pp. 361–374.

[Sha+19] M. M. Shaik, H. Peng, J. Lu, S. Rits-Volloch, C. Xu, M. Liao, and B. Chen. "Structural basis of coreceptor recognition by HIV-1 envelope spike". In: *Nature* 565.7739 (2019). Number: 7739, pp. 318–323.

[SIT16] S. F. Shimobayashi, M. Ichikawa, and T. Taniguchi. "Direct observations of transition dynamics from macro- to micro-phase separation in asymmetric lipid bilayers induced by externally added glycolipids". In: *EPL* 113.5 (2016), p. 56005.

[SS13] R. Shlomovitz and M. Schick. "Model of a raft in both leaves of an asymmetric lipid bilayer". In: *Biophysical Journal* 105 (2013), pp. 1406–1413.

[SZ01] V. A. Shneidman and R. K. P. Zia. "Wulff shapes and the critical nucleus for a triangular Ising lattice". In: *Physical Review B* 63.8 (2001). Publisher: American Physical Society, p. 085410.

[Sim+19] C. Simon, R. Kusters, V. Caorsi, A. Allard, M. Abou-Ghali, J. Manzi, A. Di Cicco, D. Levy, M. Lenz, J.-F. Joanny, C. Campillo, J. Plastino, P. Sens, and C. Sykes. "Actin dynamics drive cell-like membrane deformation". In: *Nature Physics* 15.6 (2019). Number: 6 Publisher: Nature Publishing Group, pp. 602–609.

[Sin+01] I. I. Singer, S. Scott, D. W. Kawka, J. Chin, B. L. Daugherty, J. A. DeMartino, J. DiSalvo, S. L. Gould, J. E. Lineberger, L. Malkowitz, M. D. Miller, L. Mitnaul, S. J. Siciliano, M. J. Staruch, H. R. Williams, H. J. Zweerink, and M. S. Springer. "CCR5, CXCR4, and CD4 Are Clustered and Closely Apposed on Microvilli of Human Macrophages and T Cells". In: *Journal of Virology* 75.8 (2001). Publisher: American Society for Microbiology Journals Section: VIRUS-CELL INTERACTIONS, pp. 3779–3790.

[Sin+19] A. Singharoy, C. Maffeo, K. H. Delgado-Magnero, D. J. K. Swainsbury, M. Sener, U. Kleinekathofer, J. W. Vant, J. Nguyen, A. Hitchcock, B. Isralewitz, I. Teo, D. E. Chandler, J. E. Stone, J. C. Phillips, T. V. Pogorelov, M. I. Mallus, C. Chipot, Z. Luthey-Schulten, D. P. Tieleman, C. N. Hunter, E. Tajkhorshid, A. Aksimentiev, and K. Schulten. "Atoms to Phenotypes: Molecular Design Principles of Cellular Energy Metabolism". In: *Cell* 179.5 (2019). Publisher: Cell Press, 1098–1111.e23.

[SSS03] A.-S. Smith, E. Sackmann, and U. Seifert. "Effects of a pulling force on the shape of a bound vesicle". In: *Europhysics Letters* 64.2 (2003). Publisher: IOP Publishing, p. 281.

[Sou+20] P. C. T. Souza, S. Thallmair, P. Conflitti, C. Ramirez-Palacios, R. Alessandri, S. Raniolo, V. Limongelli, and S. J. Marrink. "Protein-ligand binding with the coarse-grained Martini model". In: *Nature Communications* 11.1 (2020), p. 3714.

[SL18] A. Sreekumari and R. Lipowsky. "Lipids with bulky head groups generate large membrane curvatures by small compositional asymmetries". In: *The Journal of Chemical Physics* 149.8 (2018), p. 084901.

[SA94] D. Stauffer and A. Aharony. *Introduction To Percolation Theory: Revised Second Edition*. 2 edition. London: Taylor & Francis, 1994. 192 pp.

[SH03] C. M. Steffens and T. J. Hope. "Localization of CD4 and CCR5 in living cells". In: *Journal of Virology* 77.8 (2003). Number: 8, pp. 4985–4991.

[Ste+20] J. Steinkuhler, T. Bhatia, Z. Zhao, R. Lipowsky, and R. Dimova. "Super-elasticity of plasma- and synthetic membranes by coupling of membrane asymmetry and liquid-liquid phase separation". In: *bioRxiv* (2020). Publisher: Cold Spring Harbor Laboratory Section: New Results.

[TP07] E. Teissier and E.-I. Pecheur. "Lipids as modulators of membrane fusion mediated by viral fusion proteins". In: *European Biophysics Journal* 36.8 (2007), pp. 887–899.

[TW87] R. Toral and C. Wall. "Finite-size scaling study of the equilibrium cluster distribution of the two-dimensional Ising model". In: *Journal of Physics A Mathematical General* 20 (1987), pp. 4949–4965.

[Tra+01] P. Tran, L. Marsh, V. Doye, S. Inoue, and F. Chang. "A Mechanism for Nuclear Positioning in Fission Yeast Based on Microtubule Pushing". In: *The Journal of Cell Biology* 153.2 (2001), pp. 397–412.

[Use+17a] R. D. Usery, T. A. Enoki, V. P. Nguyen, B. N. Francisco, and G. W. Feigenson. "F4,5GWALP partitioning, orientation, and effect on bending moduli in models of the plasma membrane". In: *Biophysical Journal* 112.3 (2017). Publisher: Elsevier, 377a.

[Use+17b] R. D. Usery, T. A. Enoki, S. P. Wickramasinghe, M. D. Weiner, W.-C. Tsai, M. B. Kim, S. Wang, T. L. Torng, D. G. Ackerman, F. A. Heberle, J. Katsaras, and G. W. Feigenson. "Line tension controls liquid-disordered + liquid-ordered domain size transition in lipid bilayers". In: *Biophysical Journal* 112.7 (2017), pp. 1431–1443.

[Vea+08] S. L. Veatch, P. Cicuta, P. Sengupta, A. Honerkamp-Smith, D. Holowka, and B. Baird. "Critical Fluctuations in Plasma Membrane Vesicles". In: *ACS Chemical Biology* 3.5 (2008). Publisher: American Chemical Society, pp. 287–293.

[VK03] S. L. Veatch and S. L. Keller. "Separation of Liquid Phases in Giant Vesicles of Ternary Mixtures of Phospholipids and Cholesterol". In: *Biophysical Journal* 85.5 (2003). Publisher: Elsevier, pp. 3074–3083.

[VK05] S. L. Veatch and S. L. Keller. "Seeing spots: Complex phase behavior in simple membranes". In: *Biochimica Et Biophysica Acta* 1746.3 (2005), pp. 172–185.

[Via+02] M. Viard, I. Parolini, M. Sargiacomo, K. Fecchi, C. Ramoni, S. Ablan, F. W. Ruscetti, J. M. Wang, and R. Blumenthal. "Role of Cholesterol in Human Immunodeficiency Virus Type 1 Envelope Protein-Mediated Fusion with Host Cells". In: *Journal of Virology* 76.22 (2002). Publisher: American Society for Microbiology Journals Section: VIRUS-CELL INTERACTIONS, pp. 11584–11595.

[VKD16] M. Vleugel, M. Kok, and M. Dogterom. "Understanding force-generating microtubule systems through in vitro reconstitution". In: *Cell Adhesion & Migration* 10.5 (2016). Publisher: Taylor & Francis, pp. 475–494.

[WD13] S. Weitz and N. Destainville. "Attractive asymmetric inclusions in elastic membranes under tension: cluster phases and membrane invaginations". In: *Soft Matter* 9.32 (2013), pp. 7804–7816.

[WP15] A. M. Whited and P. S.-H. Park. "Nanodomain organization of rhodopsin in native human and murine rod outer segment disc membranes". In: *Biochimica et biophysica acta* 1848.1 (2015), pp. 26–34.

[WLN07] M. Widom, J. Lidmar, and D. R. Nelson. "Soft modes near the buckling transition of icosahedral shells". In: *Physical Review E* 76.3 (2007). Publisher: American Physical Society, p. 031911.

[Wik12] WikiDoc. *Cell membrane*. Online; accessed June 24, 2020. 2012.

[Wu+14] E. L. Wu, P. J. Fleming, M. S. Yeom, G. Widmalm, J. B. Klauda, K. G. Fleming, and W. Im. "E. coli outer membrane and interactions with OmpLA". In: *Biophysical Journal* 106.11 (2014), pp. 2493–2502.

[Yan+17] S.-T. Yang, A. J. B. Kreutzberger, V. Kiessling, B. K. Ganser-Pornillos, J. M. White, and L. K. Tamm. "HIV virions sense plasma membrane heterogeneity for cell entry". In: *Science Advances* 3.6 (2017). Number: 6, e1700338.

[ZK06] J. Zimmerberg and M. M. Kozlov. "How proteins produce cellular membrane curvature". In: *Nature Reviews Molecular Cell Biology* 7.1 (2006), pp. 9–19.

Résumé en français

La membrane plasmique, en plus de constituer une enveloppe pour la cellule, est impliquée dans de nombreux processus biologiques clés pour son fonctionnement (signalisation, adhésion...). Il est connu depuis longtemps (et les récents développements en technique d'imagerie ont permis de le confirmer [Hou+18]) que les constituants de ces membranes (principalement lipides et protéines) ne sont pas répartis spatialement de façon homogène mais sont organisés en nanodomaines. Les mécanismes de formations de si petits domaines sont encore sujets de nombreuses questions, d'autant plus que ces domaines forment souvent des unités fonctionnelles jouant des rôles déterminants dans les fonctions biologiques mentionnées ci-dessus. Le travail de ma thèse consiste à continuer l'exploration d'un mécanisme candidat potentiel : le couplage entre la composition et la courbure locales. Une étude analytique de ce mécanisme a déjà été menée dans mon équipe [GDM14 ; Gue16] ainsi que le début d'une étude numérique sur un système simplifié, une vésicule constituée d'un mélange homogène dans une premier temps afin d'étudier ses transitions de forme [GDM17] puis une vésicule lipidique à 2 espèces dans un second temps afin d'étudier le couplage entre la forme de la membrane et sa composition. Le but de mes travaux est de continuer cette étude, de mener des simulations numériques (programmation C, modèle mésoscopique) et d'en comparer les résultats à ceux obtenus analytiquement (fonctions de corrélation, diagramme de phases), mais également de la prolonger en modifiant le programme afin de simuler des systèmes plus biologiquement réalistes et de vérifier la validité de nos modèles. Je réalise également des mesures quantitatives sur ces simulations. Nous menons des comparaisons de nos modèles aux données expérimentales obtenues par Fabrice Dumas et son équipe à l'IPBS sur la question de la forme des domaines membranaires. Enfin, la collaboration avec Matthieu Chavent de l'IPBS maîtrisant des outils de simulation tout-atome et gros-grains va nous permettre d'établir des correspondances entre les 2 échelles et de fournir un modèle pertinent.

Grâce aux récents développements des techniques d'imagerie et notamment de la microscopie de super-résolution [Hou+18], il est aujourd'hui bien connu que les constituants des membranes biologiques s'organisent en motifs spatiaux comme cela est visible dans la figure 1. Dans les cellules, ces motifs sont parfois des domaines enrichis en certaines espèces chimiques de quelques dizaines à quelques centaines de nanomètres et remplissant des fonctions biologiques bien précises. Les mécanismes de formation de ces domaines ainsi que les explications de leur petite taille sont encore des questions actives de recherche [DMC18]. Le présent travail explore un mécanisme potentiel pouvant expliquer ces phénomènes, en utilisant un couplage entre la forme et la composition de la membrane.

La description suivante de la membrane est depuis longtemps largement utilisée dans le domaine de la modélisation des biomembranes. Un membrane biologique peut-être vue comme une

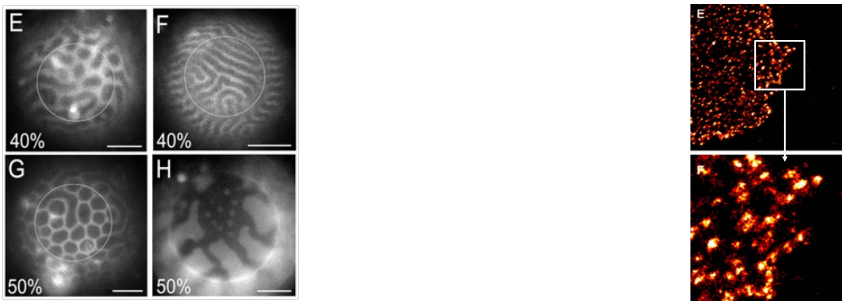

FIGURE 1 – **Gauche :** Différents motifs observés dans des GUVs en microscopie de fluorescence. Les barres d'échelle correspondent à 10 μm. Images tirées de [GAF13]. **Droite :** Domaines de protéines transmembranaires (LFA-1) dans des membranes de lymphocytes T (microscopie de super-résolution dSTORM). Le côté du zoom carré mesure environ 1 μm. Images fournies par Raïssa Houmadi.

surface élastique sur laquelle vit un mélange de différentes espèces chimiques. Afin d'étudier le lien entre la forme de la membrane et sa composition, on s'intéresse aux configurations correspondant à des minima d'énergie libre de ce système. L'énergie libre élastique de la membrane est décrite grâce au Hamiltonien de Canham-Helfrich [Can70 ; Hel73] :

$$H_{\text{Helf}} = \frac{1}{2}\int_{\mathcal{A}} \kappa(2H - C)^2 dS + \sigma\mathcal{A} \tag{1}$$

avec $\mathcal{A}$ l'aire totale de la membrane, H la courbure locale, C la courbure spontanée, κ le module de rigidité ou de courbure et σ la tension de surface de la membrane, qui contraint son aire totale. On considère une vésicule de forme quasi-sphérique subissant de faibles fluctuations de surface autour de la sphère de référence de rayon R.

Avec une approche champ-moyen, on peut décrire l'énergie libre de mélange des constituants de la membrane grâce au Hamiltonien de Ginzburg-Landau [CL95]

$$H_{\text{GL}}[\phi] = \int_{\mathcal{A}} \mathrm{d}S \left[\frac{m}{2}(\phi - \phi_c)^2 + \frac{b}{2}(\nabla\phi)^2\right] \tag{2}$$

Dans notre modèle on choisit un couplage linéaire en première approximation entre la courbure locale C et la composition locale ϕ de la membrane de la forme

$$C = C_0 + C_1\phi \tag{3}$$

c'est à dire que l'on considère que la courbure locale est directement dépendante de la composition à cet endroit de la membrane comme l'illustre la figure 2.

Notre travail repose sur les travaux de thèse de Guillaume Gueguen [Gue16] et les travaux menés précédemment dans le groupe [GDM14]. cette étude analytique fournit les outils nécessaires à l'étude d'une membrane régie par ce mécanisme de couplage courbure-composition et les prévisions théoriques de son comportement en fonction des différents paramètres impliqués dans sa description. Les paramètres adimensionnés introduits sont répertoriés dans le tableau 1.

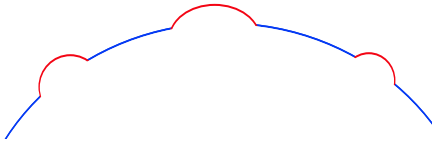

FIGURE 2 – Les deux espèces imposent différentes courbures spontanées locales à la membrane. Dans cet exemple, le rayon de courbure préféré de l'espèce bleue est le rayon de la sphère de référence R, l'espèce bleue a donc une courbure spontanée de $C_0 = 2/R$. L'espèce rouge impose une courbure spontanée plus élevée que la bleue, c'est-à-dire que sa courbure spontanée est supérieure à $C_0 = 2/R$ et son rayon de courbure préféré a une valeur inférieure à R. Le terme C_1 désigne la différence de courbure entre les espèces rouge et bleue de sorte que la courbure de l'espèce rouge est donnée par $C_0 + C_1$. Ceci est la description du cas qui est principalement étudié dans ce travail.

TABLE 1 – Les paramètres sans dimension suivants sont introduits, les longueurs étant divisées par le rayon de la vésicule R. La notation $\hat{\cdot}$ indique que les énergies sont divisées par le module de rigidité moyen κ_0 tandis que la notation $\tilde{\cdot}$ indique qu'elles sont divisées par $k_\mathrm{B}T$.

Paramètre	**Expression**
Courbure spontanée	$c_0 = C_0 R\,;\; c_1 = C_1 R$
Module de rigidité	$\tilde{\kappa}_0 = \kappa_0/k_\mathrm{B}T$
Tension de surface	$\tilde{\sigma} = \sigma R^2/k_\mathrm{B}T\,;\; \hat{\sigma} = \sigma R^2/\kappa_0$
Paramètre d'Ising	$\tilde{J}_I = J_I/k_\mathrm{B}T$ $\hat{J} = 2\sqrt{3}J_I/\kappa_0$
Paramètre de Ginzburg-Landau	$\hat{m} = mR^2/\kappa_0$ $= \alpha_0 N(1 - J_I/J_{I,c})/\tilde{\kappa}_0$

Le travail mené dans [GDM14] nous donne l'expression de la fonction de corrélation spatiale (angulaire) de la composition

$$\langle \psi(\theta)\psi(0)\rangle = \frac{k_\mathrm{B}T}{4\pi\kappa_0}\sum_{l\geq 1}\frac{(2l+1)P_l(\cos\theta)}{M(l)} \tag{4}$$

où P_l sont les polynômes de Legendre [ASR88], ainsi que son équivalent dans l'espace réciproque, le facteur de structure, définit par

$$S(l) = \frac{k_B T}{2\pi\kappa_0}\frac{1}{M(l)} \tag{5}$$

avec

$$M(l) = \hat{m} + \frac{c_1^2\hat{\sigma}}{l(l+1) - 2 + \hat{\sigma}} + 2\hat{J}l(l+1). \tag{6}$$

Ces deux outils permettent de caractériser de manière quantitative le degré d'ordre du système.

Afin de mener une étude numérique de ce système, il nous faut le discrétiser. On considère

donc notre vésicule comme une sphere tessélée ou triangulée possédant N sommets. L'énergie libre élastique Eq. (1) est discrétisée comme suis

$$H_{\text{Helf}} = \frac{1}{2}\sum_i \kappa_0[2H_i - C_i]^2\mathcal{A}_i + \sigma\sum_i \mathcal{A}_i \tag{7}$$

avec $\mathcal{A}_i$ l'aire associée à un sommet. Le terme $2H_i$ est la norme de l'opérateur de Laplace-Beltrami $\mathbf{K}_i$ (courbure totale) calculée selon [Mey+03] comme

$$\mathbf{K}_i = \frac{1}{2\mathcal{A}_i}\sum_j (\cot\alpha_{ij} + \cot\beta_{ij})(\mathbf{x}_i - \mathbf{x}_j) \tag{8}$$

où $\mathbf{x}_i$ est la position du sommet i, la somme étant réalisée sur les sommets j voisins de i. Les angles α_{ij} et β_{ij} sont les angles des deux triangles partageant l'arête $\mathbf{x}_i\mathbf{x}_j$ et opposé à cette arête. Voir [GDM17] et Fig. 3 pour une illustration. Le module de rigidité est considéré dans ce travail comme constant et identique pour les deux espèces, fixé à $\tilde{\kappa} = 20$. Le cas où celui-ci depend de l'espèce sera étudié par la suite. Notons que pour éviter que la vésicule ne diffuse globalement tout au long du processus de Monte Carlo (voir ci-dessous), son centre de position est lié à l'origine par un potentiel quadratique [Gue16 ; GDM17].

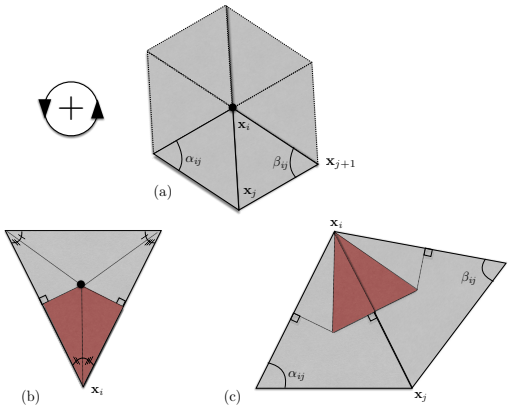

FIGURE 3 – Aire de Voronoï associée à un sommet et prise en compte dans le calcul de l'énergie libre de courbure, et définition des angles α_{ij} et β_{ij}. Figure tirée de [Gue16].

Pour l'énergie libre de mélange, on utilise un modèle d'Ising très adéquat pour décrire les phénomènes de transition de phases, ici sur un réseau triangulaire illustré Fig. 4. On écrit son Hamiltonien comme suit

$$H_{\text{Ising}} = -J_I\sum_{\langle i,j\rangle} s_i s_j \tag{9}$$

avec $s_i = \pm 1$. La composition moyenne sur un sommet i du réseau est $\phi_i = 0$ ou 1, reliée à s_i par $\phi_i = (1 + s_i)/2$.

Suivant les considérations de renormalisation [AF14], assez proche de sa valeur critique, le paramètre d'Ising dépend du niveau d'"àgraindissement" du système. On note

- a le paramètre de maille des simulations à l'échelle mésoscopique, $a = (8\pi/\sqrt{3})^{\frac{1}{2}}\, R/\sqrt{N}$,
- $l_0 \sim 1$ nm la distance typique entre deux lipides,

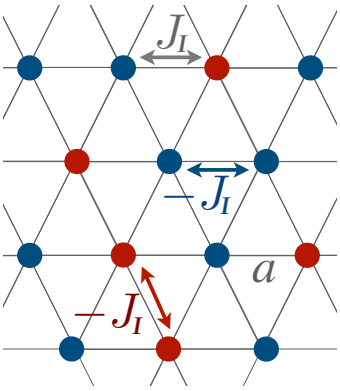

FIGURE 4 – Modèle d'Ising 2D sur un réseau triangulaire avec J le paramètre d'Ising.

- $J_{I,0}$ le paramètre d'Ising à l'échelle moléculaire.

On suppose que le réseau d'interaction à l'échelle moléculaire peut être assimilé à un réseau triangulaire, du fait des symétries des liquides bidimensionnels. Proche du point critique, on obtient

$$J_I - J_{I,c} = \frac{a}{l_0}\left(J_{I,0} - J_{I,c}\right) \tag{10}$$

reliant les deux échelles [AF14]. Cette relation sera utile pour relier les résultats des simulations MARTINI présentées plus bas et les paramètres mésoscopiques. Notez que sur ce réseau $k_\mathrm{B}(T_c - T) = (4/\ln 3)\left(J_{I,0} - J_{I,c}\right)$, où $T_c - T$ peut être mesuré soit dans des expériences, soit dans des simulations de dynamique moléculaire.

Le couplage entre la courbure et la composition est introduit de la manière suivante dans les simulations numériques

$$C_i = C_0 + C_1\phi_i \tag{11}$$

avec C_i la courbure locale assignée à un sommet calculée avec l'équation 8.

Pour minimiser l'énergie libre de ce système ainsi décrit, on procède à des simulations Monte Carlo. Plus précisément, on utilise l'algorithme de Metropolis impliquant deux mouvements locaux dans notre cas : (1) un sommet est déplacé radialement, ce qui modifie l'énergie élastique du système ; (2) les valeurs de composition de deux sites voisins sont échangées, ce qui modifie l'énergie d'interaction. Ces mouvements locaux sont acceptés si la différence d'énergie entre les configurations avant et après mouvement ΔE est négative ou avec la probabilité $\mathrm{e}^{-\beta\Delta E} < 1$ lorsqu'elle est positive. L'itération de ce procédé permet de converger vers les configurations d'équilibre de la membrane en terme de forme et de répartition spatiale de ses composants comme l'illustre la figure 5.

Pour créer la sphère discrétisée, un icosaèdre initial est successivement tesselé. Cela conduit à une liste restreinte de valeurs accessibles pour le nombre total de sommets (voir [GDM14]). Un point important à noter est que cette discrétisation conduit également à quelques défauts dans la structure. En effet, le nombre de coordination de tous les sommets n'est pas égal à 6 pour

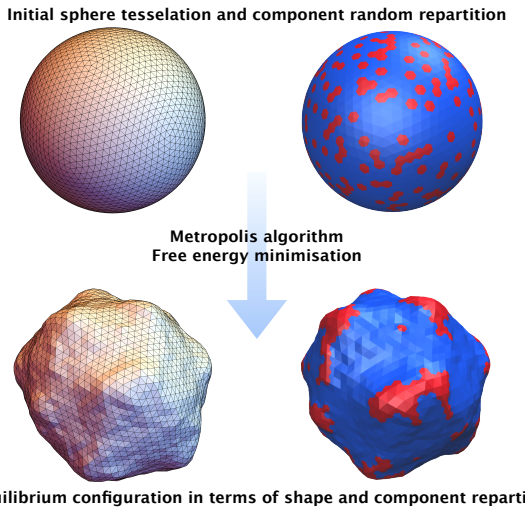

FIGURE 5 – Principe de simulation Monte Carlo. Snapshot d'une vésicule tessélée avant simulation et après (à l'équilibre) en utilisant l'algorithme Metropolis / Kawasaki, montrant le champ de hauteur de la membrane u (gauche) et celui de la composition ϕ (droite), A (resp. B) espèce rouge (resp. bleue). Les itérations de l'algorithme conduisent à un état d'équilibre pour un ensemble de paramètres.

tous, à cause des 12 sommets de l'icosaèdre initial qui n'ont que 5 voisins. Cette caractéristique doit être prise en compte lors du calcul de l'énergie locale (Helfrich ou Ising) d'un sommet. Cette brisure de symétrie sphérique a également un impact global qui impacte les résultats en terme de nombre de clusters formés dans le cas des mésophases. En effet, après chaque subdivision des faces de l'icosaèdre initial, les points nouvellement créés sont projetés sur la sphère. Les triangles projetés ont alors une surface plus grande que les triangles initiaux (Fig. 6). Il en résulte des triangles avec des surfaces différentes dans la sphère initiale. Les triangles proches des centres des faces initiales de l'icosaèdre ont alors une surface plus grande que ceux proches des sommets initiaux. Il en résulte des triangles avec des surfaces différentes dans le réseau, les plus grands triangles étant généralement 10% plus grands que les plus petits. L'aire de Voronoï associée à chaque sommet [GDM17] prise en compte dans les calculs d'énergie locale dépend des triangles environnants. Ils sont par conséquent localement plus petits près des sommets de l'icosaèdre, impliquant des énergies locales calculées localement plus faibles puisque l'énergie de courbure d'un sommet est proportionnelle à l'aire de Voronoï qui lui est associée. Ainsi, les régions d'espèce A les plus courbées ont tendance à s'ancrer sur les plus petits triangles, proches des 12 sommets initiaux, ce qui biaise la minimisation de l'énergie libre et donc nos résultats.

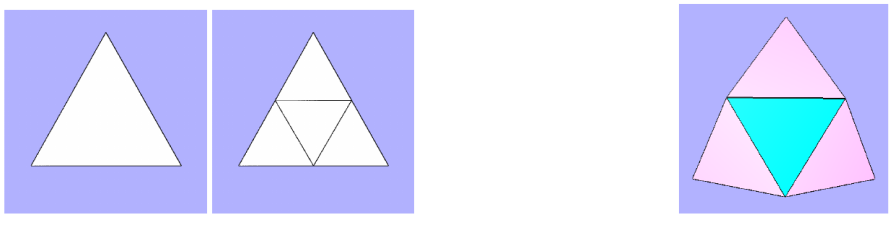

(a) Starting Face (b) Level 1 Face

FIGURE 6 – Subdivision d'une face (gauche). Après projection (droite), le triangle projeté bleu a une aire plus grande que celle des triangles roses. Figures tirées de [Har12].

Pour corriger cet effet, nous avons essayé de créer une sphère discrétisée initiale avec tous les triangles de taille égale. Nous n'avons trouvé aucune approche déterministe pour faire cela et, comme cela semble être un problème ouvert [Har12], nous avons abordé ce problème numériquement et stochastiquement. Nous sommes partis de la configuration générée par la tesselation décrite ci-dessus. Ensuite, nous avons utilisé un algorithme de Metropolis à température nulle (descente de gradient) minimisant l'écart-type des aires des triangles du réseau, dont les déplacements locaux sont de petits déplacements des sommets sur la sphère. Nous avons ensuite vérifié que nous obtenions une distribution très piquée autour d'une aire triangulaire caractéristique, ayant une dispersion d'aire réduite d'un facteur ~ 100 (Fig. 7).

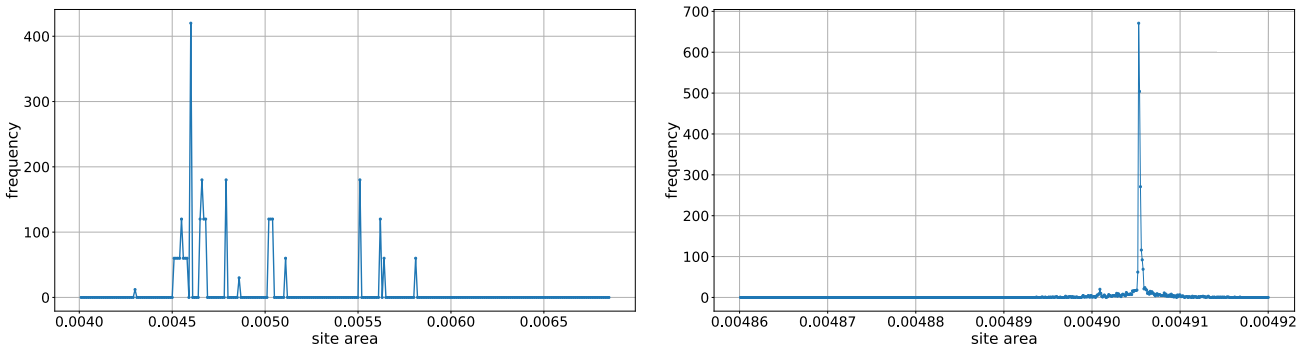

FIGURE 7 – Distribution d'aire des triangles avant (gauche) et après correction (droite). Notez que les échelles de l'axe des x sont différentes.

Dans un premier temps, les résultats de ces simulations nous permettent de confirmer les résultats analytiques obtenus dans [GDM14] : au-dessus de la température critique ou en-dessous du paramètre d'Ising critique $\tilde{J}_{I,c}$ sans couplage à la courbure, le système est désordonné. Lorsque la composition est localement couplée à la courbure, le couplage tend à stabiliser des fluctuations de composition comme le montre la figure 8.

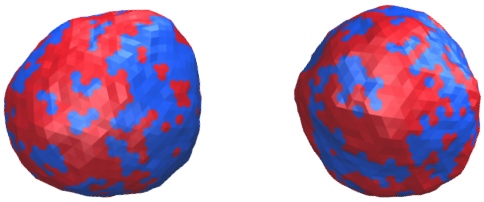

FIGURE 8 – Snapshots de vésicules simulées montrant l'effet de la différence de courbure spontanée $c_1 = c_2 - c_0$ entre les deux espèces à faible $\tilde{J}_I$ ($\tilde{J}_I^{-1} = 4.0$) , $\bar{\phi} = 0.5$, $\tilde{\sigma} = 300$) : $c_1 = 0$ (à gauche) et $c_1 = 3$ (à droite). Pour l'espèce bleue, $c_0 = 2$ dans toutes les simulations. Les deux espèces tendent à se mélanger mais le couplage c_1 stabilise des phases modulées, bien que difficiles à détecter à l'œil (voir texte).

Les simulations numériques nous offrent également la possibilité d'aller au-delà des prévisions théoriques en permettant d'accéder à une région de paramètres où les résultats analytiques ne sont pas accessibles par des calculs en champ moyen : au-dessus du paramètre d'Ising critique $\tilde{J}_{I,c}$. Dans ce cas, sans couplage, la vésicule subit une séparation de phases totale (visible dans la vésicule de gauche Fig. 9) comme attendu. Lorsque l'on augmente le couplage, les grands domaines de l'espèce courbante A (en rouge) deviennent de plus en plus courbés induisant un

fort coût en énergie élastique, la membrane étant sous tension. Ils deviennent instables et il est donc plus favorable énergétiquement de former de plus nombreux et plus petits domaines courbés, l'énergie élastique augmentant plus vite que l'énergie de ligne (voir Fig. 9).

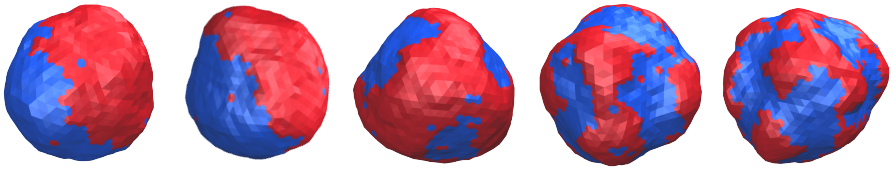

FIGURE 9 – Mêmes paramètres que pour la Fig. 8 à haut $\tilde{J}_I$ avec $c_1 = 0, 2, 3, 4, 6$ de gauche à droite. Les autres valeurs de paramètre sont $\tilde{J}_I^{-1} = 2.5$, $\bar{\phi} = 0.5$, $\tilde{\sigma} = 300$.

Les mesures statistiques sont réalisées sur environ 1000 configurations indépendantes une fois l'équilibre atteint. Comme introduit précédemment, la fonction de corrélation spatiale de la composition ainsi que le facteur de structure, son équivalent dans l'espace réciproque, nous permettent de caractériser de manière quantitative les domaines émergeants (voir Fig. 10). Ils nous permettent de distinguer les systèmes ordonnés de desordonnées et nous donnent notamment la longueur d'onde caractéristique du système lorsque celui-ci est ordonné. Les fonctions de corrélation montrent une première décroissance exponentielle correspondant à la largeur du motif et des oscillations secondaires liées à l'espacement des motifs. Les facteurs de structure présentent un maximum pour une abscisse l^* (flèches), correspondant à la longueur d'onde du motif dans l'espace réel, qui augmente à mesure que c_1 augmente et que les motifs s'amincissent.

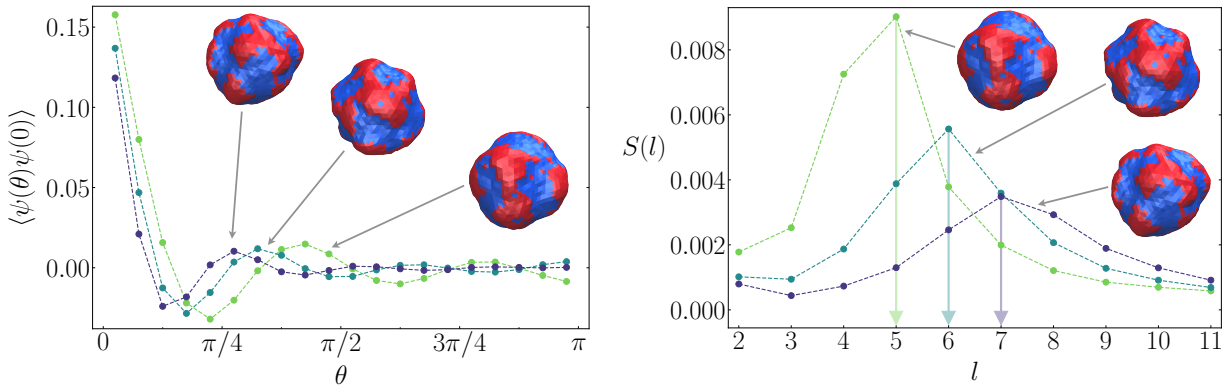

FIGURE 10 – Fonctions de corrélation mesurées numériquement (gauche) et facteurs de structure correspondants (droite) pour différentes valeurs de couplage en courbure $c_1 = 4$, 5 et 6 du vert au bleu ($\tilde{J}_I^{-1} = 2.5$, $\bar{\phi} = 0.5$, $\tilde{\sigma} = 300$). Les lignes de couleur servent de guide pour l'œil.

La figure 11 nous permet de vérifier quantitativement le fait que le couplage de la composition à la courbure "ordonne" le mélange en-dessous du paramètre d'Ising critique, ce qui est difficilement discernable à l'œil. Cette information s'obtient en observant la position du maximum du facteur de structure, possédant une valeur supérieure à 1 pour $c_1 = 3.0$, signal d'ordre dans le système.

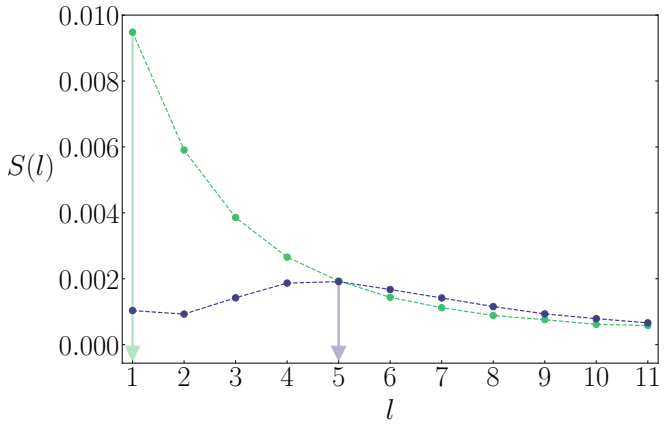

FIGURE 11 – Facteurs de structure pour deux valeurs de couplage en courbure différentes $c_1 = 0$ (vert, pas de couplage) et $c_1 = 3.0$ (bleu), courbes des deux vésicules présentées dans Fig. 8 à faible valeurs de $\tilde{J}_I$ (les valeurs des paramètres sont celles données dans Fig. 8). Les lignes de couleur servent de guide pour l'œil.

Les résultats théoriques de [GDM14] ont été obtenus à $\bar{\phi} = 0.2$ ce qui nous a motivé à réaliser de nombreuses simulations à cette concentration afin de comparer nos résultats aux prédictions analytiques. Nous nous sommes aussi intéressés à une concentration d'espèce courbante minoritaire plus réaliste des systèmes biologiques, $\bar{\phi} = 0.5$. La figure 12 montre un exemple de vésicule obtenue à cette concentration avec un fort couplage en courbure qui nous permet de retrouver des tailles de domaines comparables à celles obtenues expérimentalement [SIT16]. Un autre outil nous

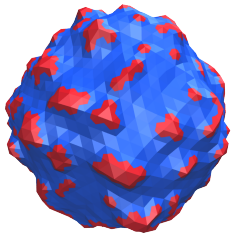

FIGURE 12 – Snapshot d'une vésicule simulée pour $\bar{\phi} = 0.2$ et $c_1 = 15$. ($\tilde{J}_I^{-1} = 2.5$ et $\tilde{\sigma} = 300$). De nombreux petits domaines courbés sont observés, comme attendu.

permettant de mieux caractériser les domaines est la distribution de tailles. Pour l'obtenir, nous avons implémenté dans le code un algorithme de détection de domaines (Depth First Search algorithm), afin d'identifier chaque domaine et d'en lister la taille. La distribution de tailles a un pic autour de la taille caractéristique des domaines comme le montre la figure 13.

On peut vérifier que le couplage à la courbure induit la formation de domaines de plus en plus nombreux et petits (voir figure 14), résultat cohérent avec la théorie et avec des résultats expérimentaux [SIT16].

D'autre part, les effets de la tension de surface $\tilde{\sigma}$ et du paramètre d'Ising $\tilde{J}_I$ sur la formation de domaines sont étudiés. La tension de surface a pour effet de s'opposer à l'effet du couplage, une tension plus forte induisant un coût énergétique pour déformer la membrane plus fort (Fig. 15). Le paramètre d'Ising module la taille des domaines (Fig. 16) : plus $\tilde{J}_I$ est important, plus les

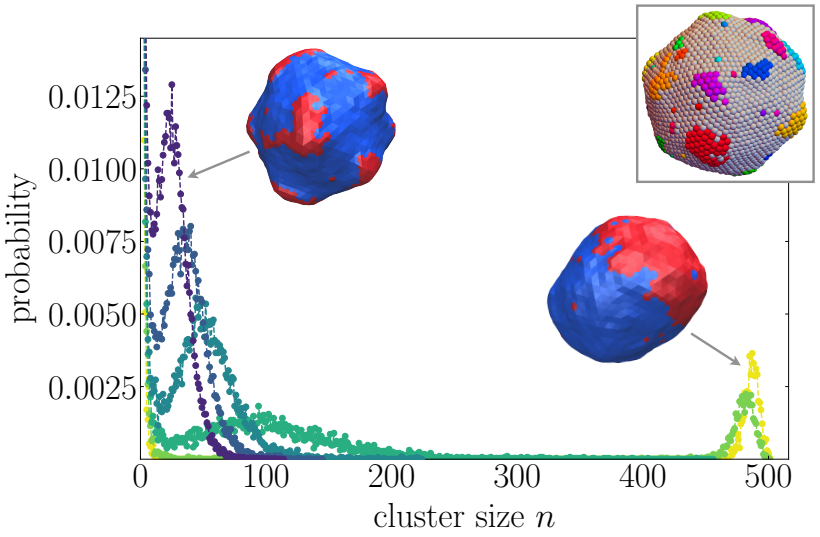

FIGURE 13 – Distribution de taille des domaines $p(n)$ pour c_1 passant de 1 à 6 (du jaune au violet). On peut distinguer les macrophases (à droite) et les mésophases (à gauche) via l'abscisse du maximum qui correspond à la taille typique des domaines n^*. La taille des domaines est mesurée en unités de nombre de sites. $\bar{\phi} = 0.2$, $\tilde{J}_I^{-1} = 2.5$ et $\tilde{\sigma} = 300$. Les lignes de couleur servent de guide pour l'œil.)

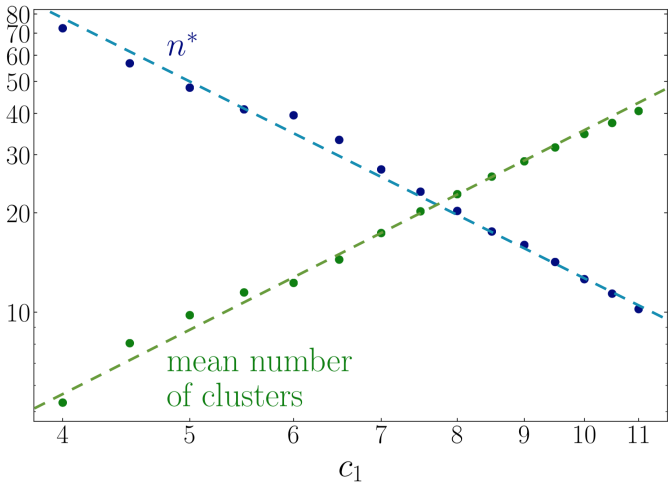

FIGURE 14 – Effet du couplage en courbure c_1 sur la taille typique des domaines n^* extraite de Fig. 13 et sur le nombre moyen de domaines pour les domaines de taille $n \geq 5$ ($\bar{\phi} = 0.2$, $\tilde{J}_I^{-1} = 2.0$ et $\tilde{\sigma} = 300$). Coordonnées log-log. Les lignes pointillées ont respectivement pour pente 2 et -2 et servent de guides pour l'œil.

domaines sont gros. Ces résultats qualitatifs sont également confirmés quantitativement par les analyses des facteurs de structure et des distributions de tailles de domaines.

Un fois l'effet de chaque paramètre sur la formation de domaines dans le système compris, on peut en dresser un diagramme de phase. On se place ici à tension de surface constante $\tilde{\sigma} = 300$ et à concentration $\bar{\phi} = 0.5$. On peut distinguer trois régions au lieu de deux dans un cas non couplé :

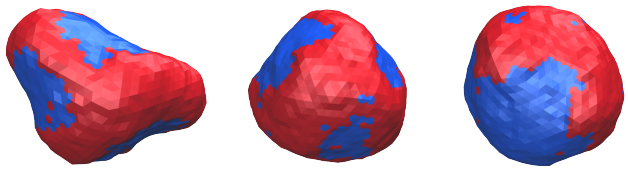

FIGURE 15 – Snapshots de vésicules simulées avec une tension de surface croissante $\tilde{\sigma}$ (respectivement de gauche à droite 150, 300 et 600). Les autres valeurs de paramètres sont $\tilde{J}_I^{-1} = 2.5$, $\bar{\phi} = 0.5$ et $c_1 = 3$.

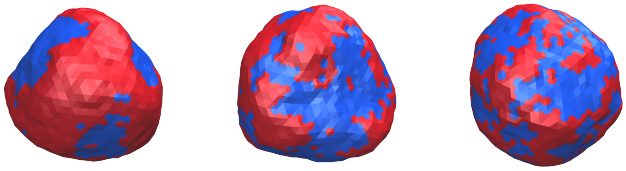

FIGURE 16 – Rôle du paramètre d'Ising sur la séparation de phases et la formation de domaines. $\tilde{J}_I^{-1}$ vaut respectivement de gauche à droite 2.5, 3.5 et 4.5. Les autres paramètres sont $\bar{\phi} = 0.5$, $\tilde{\sigma} = 300$ et $c_1 = 3$ pour toutes ces simulations.

— une région désordonnée pour de faibles valeurs de $\tilde{J}_I$ et c_1, où le mélange est homogène et ne présente pas d'ordre sous-jacent (croix bleue) ;
— une région macrophase pour de fortes valeurs de $\tilde{J}_I$ et de faibles valeurs de c_1 dans laquelle le mélange subit une séparation de phases totale (croix vertes) ;
— une région de phases modulées, pour d'assez grandes valeurs de c_1 et de faibles valeurs de $\tilde{J}_I$, dans laquelle la vésicule présente plus d'un seul domaines et où le mélange est donc ordonné ou modulé (croix rouges).

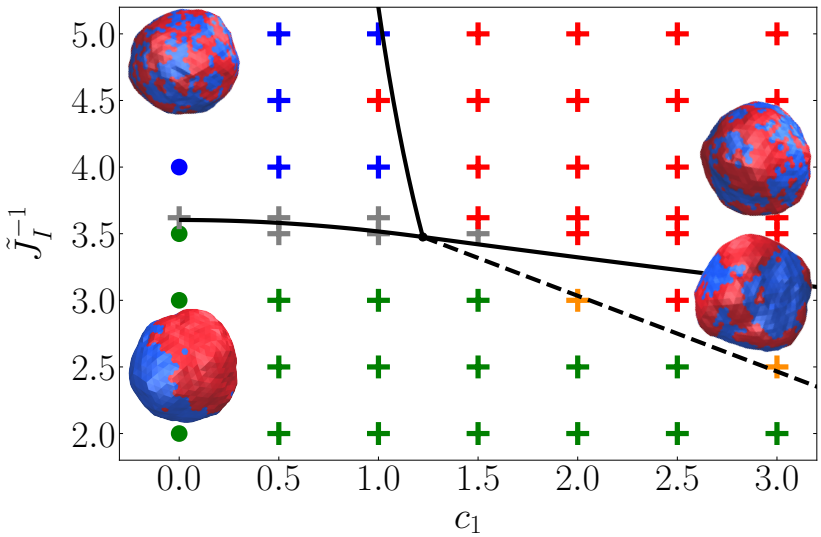

FIGURE 17 – Diagramme de phases dans l'espace de paramètres (c_1, $\tilde{J}_I^{-1}$) avec $\tilde{\sigma} = 300$ et $\bar{\phi} = 0.5$. Les croix vertes sont les macrophases, les rouges les phases modulées et les bleues les phases désordonnées. Les points pour $c_1 = 0$ sont le cas sans couplage (résultats exacts [Bax82]). Les lignes noires pleines sont les expressions analytiques des frontières. La ligne pointillée (déterminée numériquement) sépare la régions des macrophases et celles des phases structurées ordonnées [GDM14].

Parallèlement, grâce à la collaboration avec Matthieu Chavent (IPBS), nous nous sommes intéressés à l'étude de ce mécanisme à une échelle inférieure. Nous avons utilisé des simulations gros-grains de dynamique moléculaires (MARTINI) afin de simuler une bicouche lipidique (voir Fig. 18) dans laquelle sont insérés des lipides particuliers (GM1, un glycolipide), dans le feuillet supérieur uniquement, induisant une asymétrique dans la membrane et donc une courbure locale [SIT16].

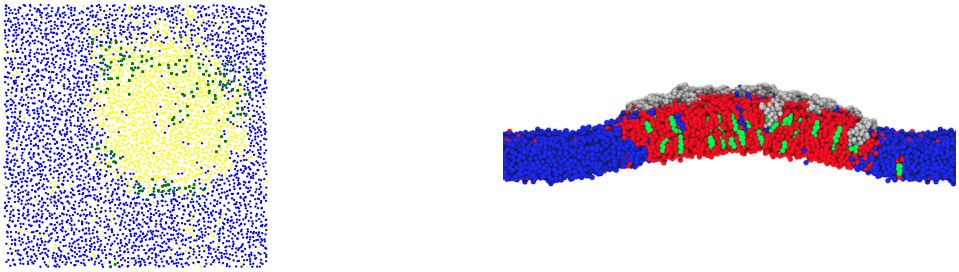

FIGURE 18 – Simulation d'une bicouche de 43 nm de côté constituée d'un mélange DPPC-DIPC-chol (30 :58 :12) et 5% de GM1 dans le feuillet supérieur. **Gauche :** Répartition spatiale des espèces, vue de dessus de la dernière étape. DPPC (Lo) en jaune, DIPC (Ld) en bleu et GM1 en vert. **Droite :** Image de la dernière étape de simulation. DPPC (Lo) en rouge, DIPC (Ld) en bleu, cholestérol en vert et GM1 en argenté. On peut remarquer la localisation préférentielle de GM1 dans la phase Lo et l'importante courbure locale de la membrane. La visualisation est produite en utilisant VMD.

Nous avons développé différents scripts d'analyse afin d'extraire les valeurs des paramètres de la membrane à cette échelle. La figure 19 (gauche) montre que la courbure de la phase Lo comprenant la majorité des inclusions de GM1 augmente avec la concentration de GM1. On montre également (Fig. 19, droite) que la différence de courbure entre le domain Lo avec des GM1 et le domaine de référence sans GM1 augmente linéairement avec la concentration de GM1 suivant $C_1 \simeq 0.5\,\phi_{\mathrm{GM1}}$ nm^{-1}.

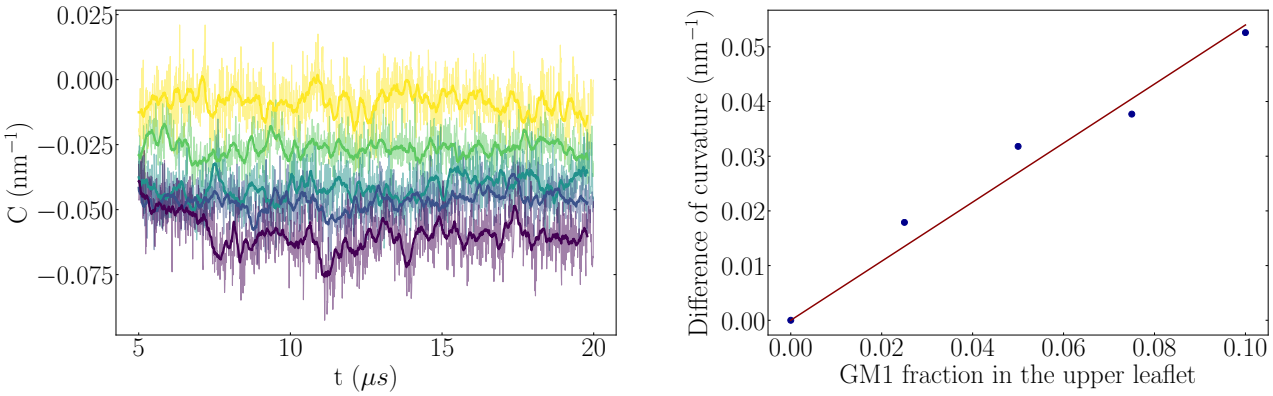

FIGURE 19 – À gauche, la courbure du domaine Lo contenant les insertions de GM1 pour différentes concentrations de GM1, de 0 à 10% par pas de 2.5, du jaune au bleu foncé. À droite, la différence de courbure mesurée entre le domaine Lo avec GM1 et le domaine Lo de référence sans GM1 en fonction de la concentration en GM1. Mélange DPPC-DIPC-cholestérol (30 :58 :12) avec une concentration de GM1 dans le feuillet supérieur variant de 0 à 10% par pas de 2.5.

D'autre part, ces simulations nous permettent de mesurer la tension de ligne à la frontière entre les phases Lo et Ld. Dans l'espace de Fourier, les fluctuations de la frontière du domaine

Lo et la tension de ligne λ peuvent être reliés par la relation

$$\langle |u_n|^2 \rangle = \frac{k_B T}{\lambda \pi R_0 (n^2 - 1)} \tag{12}$$

La mesure de cette quantité présentée en figure 20 nous permet d'extraire la valeur de la tension de ligne $\lambda \simeq 0.15$ pN pour ce mélange à $T = 310$ K.

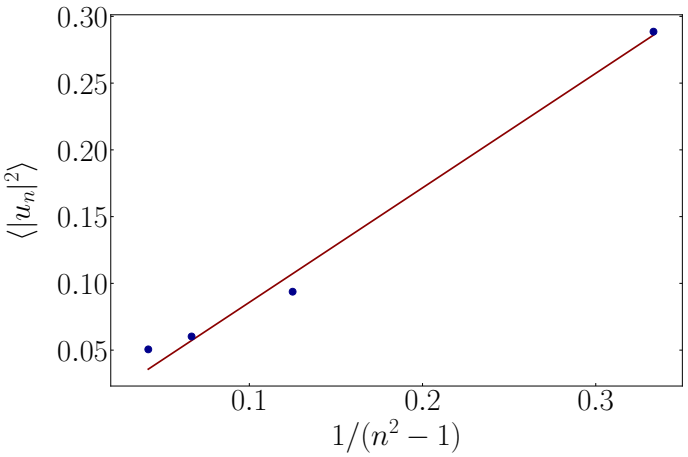

FIGURE 20 – Mesure de la tension de ligne Lo-Ld via les fluctuations de la frontière du domaine Lo. Mélange DPPC-DIPC-cholestérol (30 :58 :12).

Après avoir mesuré la tension de ligne λ, nous pouvons avoir accès au paramètre d'Ising à l'échelle moléculaire comme expliqué ci-dessus. Près du point critique, λ dépend algébriquement de $J_{I,0} - J_{I,c}$ et s'annule au point critique. Les arguments de renormalisation montrent que les deux grandeurs sont en fait proportionnelles pour la classe d'universalité du modèle Ising 2D. Plus précisément,

$$\lambda = \frac{4\sqrt{3}}{l_0}(J_{I,0} - J_{I,c}). \tag{13}$$

Le préfacteur dépend du réseau et vaut $4\sqrt{3}$ sur un réseau triangulaire [SZ01]. Suivant Eq. (10), on a également la relation

$$\lambda = \frac{4\sqrt{3}}{a}(J_I - J_{I,c}). \tag{14}$$

Cela nous permet d'établir le lien entre les simulations à l'échelle moléculaire et mésoscopique et de proposer un mécanisme pertinent aux différentes échelles.

Par ailleurs, nous nous sommes aussi intéressés à la forme des domaines observés, en collaboration avec Fabrice Dumas de l'équipe de Laurence Salomé (IPBS). Les expériences de suivi de particule unique menées dans leur équipe permettent d'obtenir la trajectoire de protéines membranaires confinées dans des domaines et donnent donc accès à des informations sur la forme de ces domaines (voir Fig. 21) [Mas+12]. Les protéines suivies sont des récepteurs au VIH. Il a été remarqué que les domaines observés étaient plutôt arrondis habituellement, mais prenaient statistiquement plus souvent des formes allongées lorsque les protéines étaient surexprimées dans la cellules, soit en plus grande concentration.

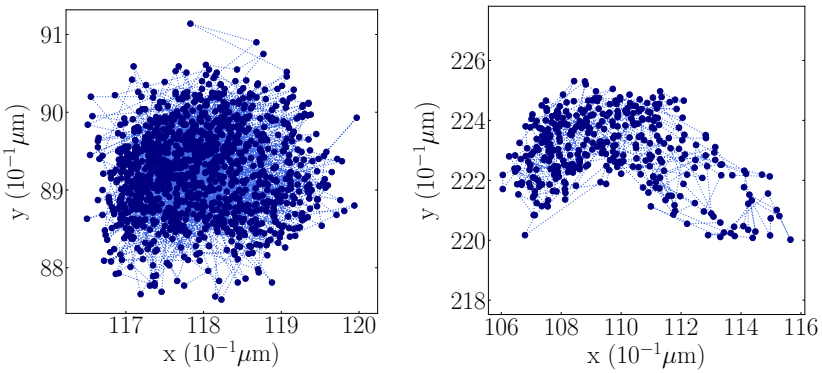

FIGURE 21 – Exemples de trajectoires de protéines confinées dans des domaines. La protéine suivie ici est le GPCR CCR5. Dans les données, nous observons des domaines statistiquement plus arrondis lorsque les protéines ne sont pas surexprimées (à gauche) et plus allongés lorsque les protéines sont surexprimées.

Nous avons développé un outil pour caractériser quantitativement l'allongement de ces domaines, basé sur la mesure du rapport d'aspect, définit par la racine du rapport des dimensions du domaine dans les deux directions principales. Nous avons ainsi pu confirmer statistiquement que les domaines tendaient à être plus allongés lorsque les protéines étaient surexprimées (Fig. 22). Nous avons comparé ces observations expérimentales à nos résultats numériques en considérant

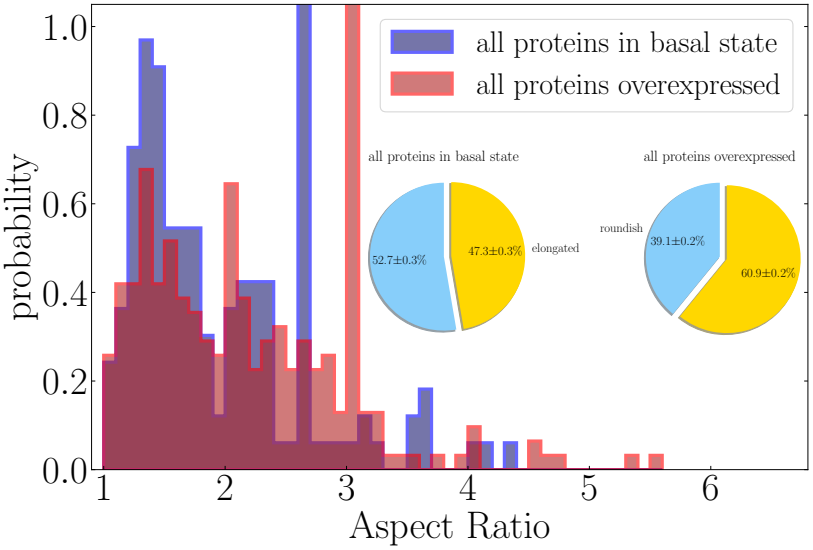

FIGURE 22 – Distributions expérimentales des rapports d'aspects cumulées pour toutes les conditions où les protéines sont à l'état basal et toutes les conditions où les protéines sont surexprimées. Les domaines dans des conditions surexprimées montrent une distribution de rapports d'aspect décalée vers des valeurs plus élevées. Encart : Diagrammes circulaires représentant les quantités relatives de domaines arrondis ou allongés détectés avec un seuil de rapport d'aspect de 2. Les erreurs données sur les pourcentages sont le SEM. La p-value calculée pour cette comparaison est $p \approx 5.0 \times 10^{-3}$.

une concentration en espèce minoritaire relativement faible $\bar{\phi} = 0.20$ pour représenter l'état d'expression basal des protéines et une concentration plus élevée $\bar{\phi} = 0.35$ pour représenter leur surexpression. Les figures 23 et 24 montrent que nos résultats sont qualitativement cohérents avec

les expériences et confirment notre hypothèse que l'augmentation de la concentration induirait l'allongement des domaines. À $\bar{\phi} = 0.35$ les domaines observés ont une taille caractéristique plus importante qu'à $\bar{\phi} = 0.20$ Fig. 23 et présentent des rapports d'aspect statistiquement plus grands (Fig. 24).

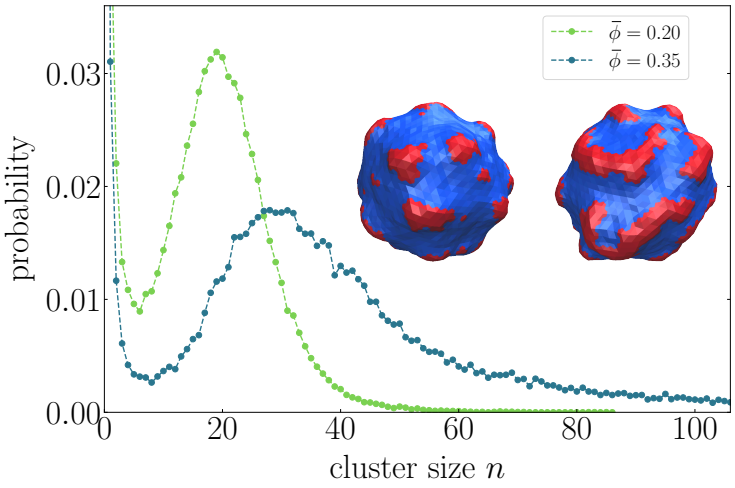

FIGURE 23 – Distribution de tailles de vésicules simulées avec $\bar{\phi} = 0.20$ (à gauche) et $\bar{\phi} = 0.35$ (à droite) et les snapshots correspondants. Les autres paramètres sont $c_1 = 8.0$, $\tilde{\sigma} = 300$ et $\tilde{J}_I^{-1} = 2.0$.

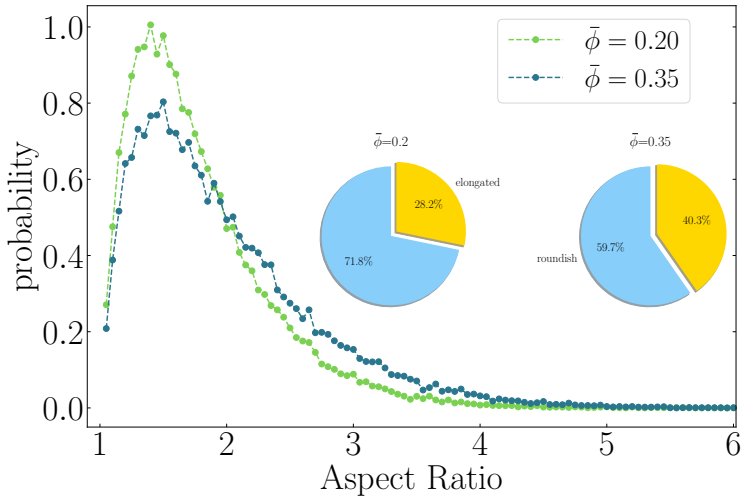

FIGURE 24 – Distributions des rapports d'aspect de simulations de vésicules avec $\bar{\phi} = 0.20$ et $\bar{\phi} = 0.35$. Encart : forme de domaine classifiées avec un seuil de rapport d'aspect de 2 pour des vésicules avec $\bar{\phi} = 0.20$ et $\bar{\phi} = 0.35$. Les autres paramètres sont $c_1 = 8.0$, $\tilde{\sigma} = 300$ et $\tilde{J}_I^{-1} = 2.0$.

Dans une dernière partie de mes travaux de thèse, j'ai eu la chance de participer à l'encadrement d'un stagiaire de M1, Nicolas Gaudy, dont le travail nous a permis d'explorer un nouvel aspect de nos simulations de vésicules : l'applications de forces extérieures à la membrane. Une des motivations biologiques qui ont guidé ce travail est la mitose ou division cellulaire lors de laquelle le fuseau mitotique applique une force sur deux pôles opposés de la membrane cellulaire. Pour prendre en compte la force dans les simulations Monte Carlo, on considère le travail de la

force sur un déplacement dr. On définit la force appliquée sans dimension comme $\tilde{f} = Rf/k_{\mathrm{B}}T$. Dans le processus de déplacement aléatoire de Metropolis sur la position des sommets, lorsqu'un site où l'on veut appliquer la force est choisi au hasard, on ajoute la variation d'énergie potentielle associée à la force à la variation d'énergie de sorte que

$$\Delta E = \Delta E_{\text{élastique}} \pm \tilde{f} dr \tag{15}$$

où $\Delta E_{\text{élastique}}$ est calculé pour la contribution d'énergie élastique lorsqu'aucune force n'est appliquée comme décrit plus haut, et le signe est choisi au hasard avec une probabilité égale. La force est ainsi appliquée vers l'extérieur de la vésicule qui est ici étudiée dans l'ensemble f. Nous rappelons que le centre de position de la vésicule est lié à l'origine par un potentiel quadratique agissant comme force opposée lors de l'application de la force externe sur un seul côté de la vésicule. Notre cas est donc comparable à une étude théorique d'une force de traction sur une vésicule liée, comme cela a été fait par exemple dans [SSS03]. Pour éviter que les sommets où la force est appliquée ne divergent et ne se séparent du reste de la surface de manière non physique, nous appliquons la force de manière distribuée sur un site et sur ses voisins. On applique donc factuellement sur ces sommets la force par site $\tilde{f}_s = \tilde{f}/(\nu + 1)$, ν étant le nombre de premiers voisins du site central.

En modifiant le programme pour appliquer premièrement une seule force localement, nous avons pu vérifier la réponse linéaire de notre système dans un régime de faibles forces.

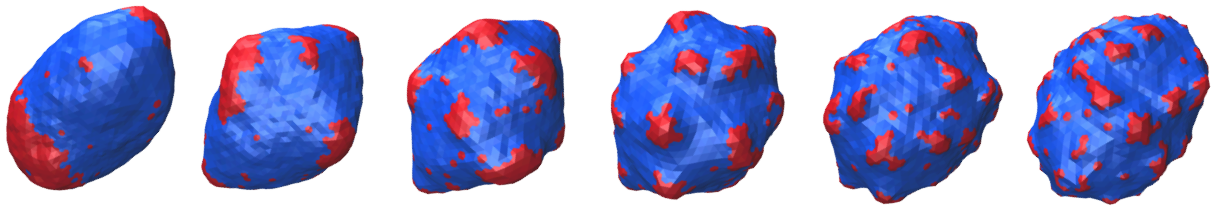

FIGURE 25 – Application de forces sur deux "pôles" opposés de la vésicule et effet du couplage en courbure c_1. Les autres paramètres sont $\bar{\phi} = 0.2$, $\tilde{\sigma} = 300$ et $\tilde{J}_I^{-1} = 2.5$.

Puis, en appliquant la force sur deux sites opposés, nous avons montré que cette perturbation extérieure induit la ré-organisation des domaines le long de certaines latitudes privilégiées (voir figures Fig. 25 et Fig. 26. Cela est comparé à l'enrichissement local aux pôles et à l'équateur en lipides et protéines particuliers au cours de la division cellulaire.

Enfin, nous avons commencé à explorer le cas d'un couplage de la composition non pas à la courbure locale mais au module de rigidité, représentatif des phases L_o/L_d, "liquid ordered" (épaisse et rigide) et "liquid disordered" (moins épaisse et plus souple), observées dans les bicouches lipidiques. On définit $\bar{\kappa}$ comme le ratio des modules de rigidité des deux phases A et B.

Une conséquence de cette différence de module de rigidité est que la phase la plus rigide est alors plus difficile à courber et rencontre des difficultés pour s'accommoder à une forme globalement sphérique. Au-dessus du paramètre d'Ising critique, les grandes macrophases rigides et plates sont alors instables. Elles se fragmente en domaines plus petits dont la disposition sur

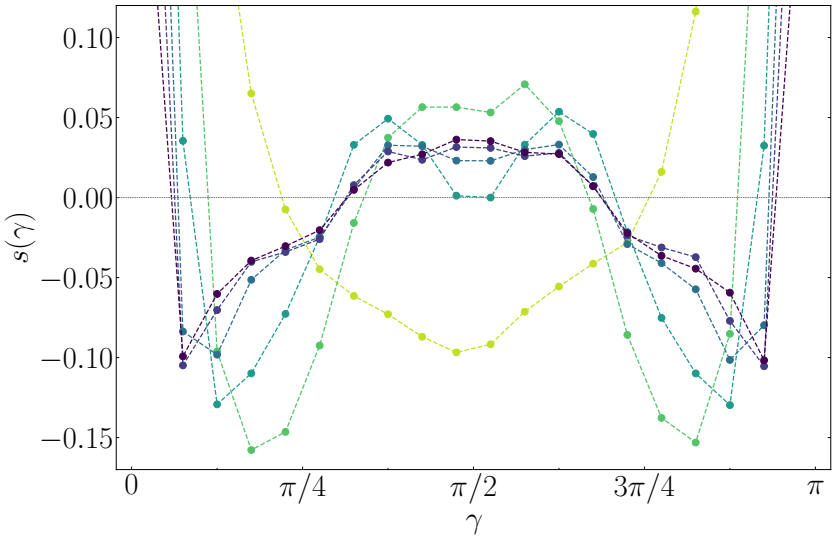

FIGURE 26 – Mesure de la composition angulaire lorsque des forces sont appliquées sur deux "pôles" opposés de la vésicule et effet du couplage en courbure c_1. Les autres paramètres sont $\bar{\phi} = 0.2$, $\tilde{\sigma} = 300$ et $\tilde{J}_I^{-1} = 2.5$.

la sphère permet une meilleure adaptation de la forme et un coût en énergie de courbure plus faible. Cette formation de motifs a été observée expérimentalement comme par exemple dans [GAF13]. On observe en effet ce phénomène dans nos simulations comme le montre la figure Fig. 27 (vésicule la plus à droite).

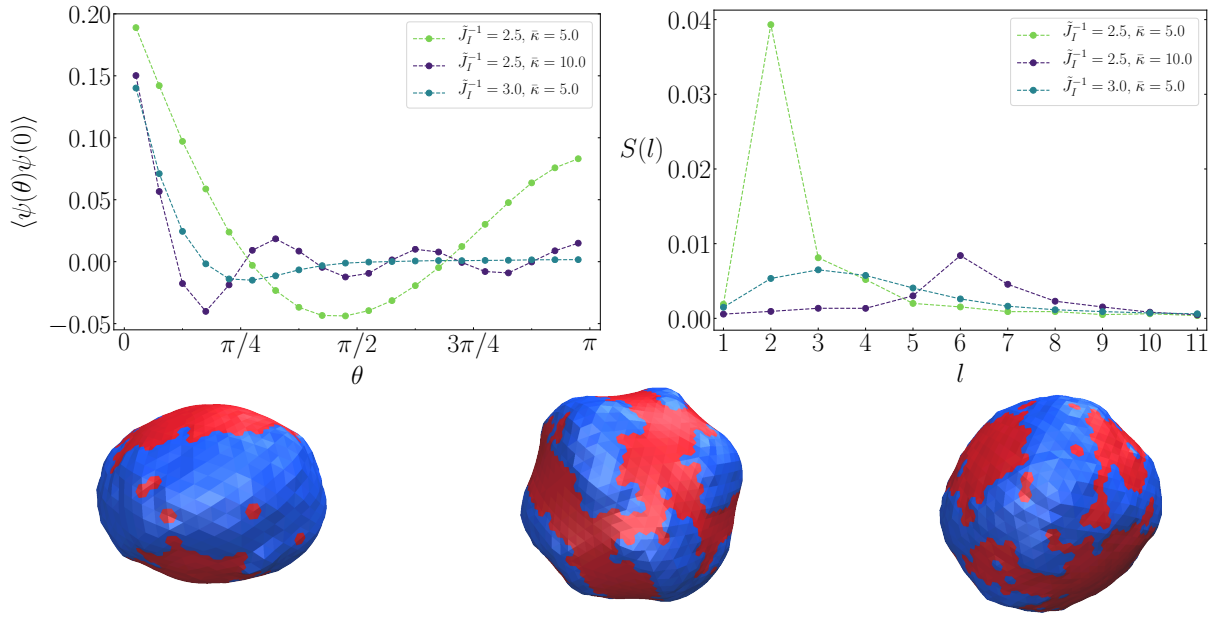

FIGURE 27 – Fonctions de corrélation, facteurs de structure et snapshots de vésicules correspondants pour des systèmes avec un couplage en module de rigidité, au-dessus de $\tilde{J}_{I,c}^{-1}$. Les autres paramètres sont $\bar{\phi} = 0.5$ and $\tilde{\sigma} = 1000$.

Le couplage au module de courbure peut également impliquer une déformation de la membrane conduisant à la formation de zones plus épaisses et plus plates disposées en bandes comme observé expérimentalement [GAF13]. On observe en effet dans la figure Fig. 27, vésicule centrale,

que cela peut conduire à la formation de bandes plates à courbure tendant vers zéro. La phase flexible environnante est déformée pour permettre la formation de bandes plates. Dans la figure Fig. 27, la vésicule la plus à gauche a un rapport de $\bar{\kappa} = 5$ entre les phases A et B. À ce paramètre d'Ising ($\tilde{J}_I^{-1} = 2.5$) et à cette valeur de $\bar{\kappa}$, la fragmentation de la phase rigide en seulement deux grandes régions est stable. On montre qu'il existe deux façons d'obtenir une fragmentation plus importante et des motifs plus intéressants. La première manière est intuitive et consiste à garder constant le paramètre d'Ising et à augmenter le couplage du module de rigidité. La vésicule centrale dans la figure Fig. 27 est un exemple de ce cas avec $\tilde{J}_I^{-1} = 2.5$ et $\bar{\kappa} = 10$. Il montre des phases modulées avec des bandes, caractérisées par des oscillations dans la fonction de corrélation spatiale et un pic dans le facteur de structure pour $l^* = 6$. La deuxième façon est de garder fixe le couplage en module de rigidité et d'abaisser le paramètre d'Ising, ce qui abaisse la tension de la ligne et facilite énergiquement la fragmentation comme prévu dans [DMC18]. La vésicule la plus à droite dans la figure Fig. 27 est un exemple de ce cas, montrant des phases modulées caractérisées par un pic en $l^* = 3$ dans le facteur de structure.

Le mécanisme de couplage courbure-composition étudié dans ce travail est donc un bon candidat pour expliquer la formation de certains mésodomaines dans les biomembranes. Dans [DMC18], nous avons fait valoir que c'est l'un des rares mécanismes les plus appropriés pour expliquer l'existence de domaines membranaires dont la taille est plus petite que la résolution optique, à condition que certaines espèces moléculaires brisent la symétrie haut/bas de la membrane, induisant localement une courbure. En dessous de la température de démixtion (limite de forte ségrégation), l'agrégation est arrêtée avant qu'une macrophase n'émerge car la courbure rend instables les domaines trop grands. Au-dessus de la température de démixtion (limite de faible ségrégation), les fluctuations de densité stabilisées par couplage de courbure sont caractérisées par une taille typique correspondant au maximum du facteur de structure, alors que leur distribution de taille décroîtraient exponentiellement sans couplage à la courbure (comportement d'Orstein-Zernicke en phase diluée [CL95]).

Nous avons pu valider numériquement le diagramme de phase théorique proposé dans la réf. [GDM14] en dessous de $J_{I,c}$. De plus, nous avons complété le diagramme de phases au-dessus de $J_{I,c}$ où aucune solution analytique ne peut être obtenue. En plus de la longueur d'onde de modulation de phase, accessible par le maximum du facteur de structure, nous avons mesuré la taille typique des clusters typique dans le régime de faible concentration où les clusters sont bien définis. Nous avons vérifié que les deux approches sont cohérentes.

La prochaine étape de ce travail sera de continuer à explorer des modèles où non seulement la courbure spontanée dépend de la concentration locale, mais aussi le module de rigidité κ, car l'épaisseur de la membrane dépend localement de la phase. Certains travaux numériques ont abordé ce problème (voir Ref. [DMC18] pour une revue), mais aucune étude systématique n'a exploré les diagrammes de phases correspondants et l'intrication entre courbure spontanée et module de rigidité. D'un point de vue numérique, cela conduit à considérer un modèle de Potts à 4 états couplé à la forme de la membrane pour traiter explicitement les deux compositions de feuillets membranaires, ce qui conduit à des diagrammes de phase beaucoup plus complexes [GDM14]. Cela fournirait un modèle plus précis pour les biomembranes, composées de deux feuillets asymétriques.

Pour l'instant, nous avons commencé à explorer cette question avec un modèle à 3 états comme première étape. Nous avons écrit une version du programme avec 3 espèces (Fig. 28), correspondant à une espèce lipidique sans courbure spontanée ($C_0 = 2$, en bleu) et 2 inclusions protéiques imposant des courbures locales de signe opposé ($C_n < 0$, en vert, et $C_p > 0$, en rouge) à $\bar{\phi}_p = \bar{\phi}_n = 0.2$. Les cluster de telles inclusions sont censés se repousser (voir [WD13]) mais nous avons observé qu'ils s'arrangent de manière à ce que leurs frontières soient en contact, conduisant à des zones alternatives de courbure locale positive et négative (Fig. 28, **a)**). Cela vient du fait qu'en se positionnant de cette manière, la longueur totale de la frontière est plus petite qu'avec des domaines distants de courbure préférentielle positive et négative puisque le même paramètre d'interaction d'Ising $\tilde{J}_I$ est en jeu entre toutes les espèces.

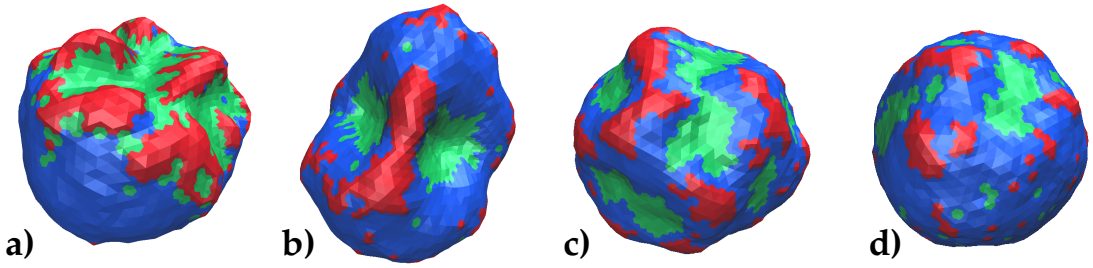

FIGURE 28 – Snapshots de vésicules simulées à 3 états avec $c_p = 6.0$ (rouge), $c_n = -6.0$ (vert) et $\tilde{J}_I^{-1} = 2.5$. De gauche à droite, **a)** $\tilde{J}_{p-n} = \tilde{J}_{p-0} = \tilde{J}_{n-0} = \tilde{J}_I$, $\tilde{\sigma} = 300$; **b)** $\tilde{J}_{p-n} = 10\tilde{J}_I$ et $\tilde{J}_{p-0} = \tilde{J}_{n-0} = \tilde{J}_I$, $\tilde{\sigma} = 300$; **c)** $\tilde{J}_{p-n} = 10\tilde{J}_I$ et $\tilde{J}_{p-0} = \tilde{J}_{n-0} = \tilde{J}_I$, $\tilde{\sigma} = 900$; **d)** $\tilde{J}_{p-n} = 10\tilde{J}_I$ et $\tilde{J}_{p-0} = \tilde{J}_{n-0} = \tilde{J}_I$, $\tilde{\sigma} = 1200$. $\bar{\phi}_p = \bar{\phi}_n = 0.2$ pour les 3 premières vésicules **a)** à **c)**, et $\bar{\phi}_p = \bar{\phi}_n = 0.1$ pour la plus à droite **d)**.

Nous avons ensuite effectué des simulations de systèmes avec un paramètre d'Ising plus élevé entre les deux espèces à courbure opposée (Fig. 28, **b)**) : $\tilde{J}_{p-n} = 10\tilde{J}_I$ et $\tilde{J}_{p-0} = \tilde{J}_{n-0} = \tilde{J}_I$ (où l'indice 0 correspond à l'espèce avec $c_0 = 2.0$). Dans ce cas, les inclusions positives et négatives s'organisent sur la sphère avec de fines rayures de l'espèce de courbure de base (bleues) les déconnectant, déformant fortement la vésicule, mais ne se repoussent pas. L'augmentation de la tension de surface force la vésicule à être quasi-sphérique (Fig. 28, **c)**) mais les inclusions courbant positivement et négativement ne semblent toujours pas subir de répulsion à longue portée. Nous avons finalement essayé de diminuer la concentration d'inclusions à $\bar{\phi}_p = \bar{\phi}_n = 0.1$ (Fig. 28, **d)**) et nous observons toujours que les inclusions rouges et vertes ont tendance à se localiser proches les unes des autres. En effet, les "faces cachées" des vésicules **c)** et **d)** sont riches en espèces bleues et ne présentent pas de nombreux domaines rouges et verts. Ils pourraient s'organiser de cette manière du fait de la géométrie sphérique avec des contraintes de volume et de surface. Cette étude devra être poursuivie puis enrichie pour aboutir à un modèle à 4 états biologiquement pertinent.

Nous devons également poursuivre notre approche multi-échelles en utilisant les liens établis entre les paramètres de membrane gros-grain et mésoscopique pour réaliser des simulations de Monte Carlo alimentées en entrée par des paramètres moléculaires réalistes. Nous pouvons également envisager d'appliquer un backmapping de l'échelle mésoscopique au gros-grain comme récemment fait par PEZESHKIAN et al. (2020). Cela nous permettrait d'équilibrer les changements conformationnels de la membrane lents de grande échelle de la membrane à l'échelle

mésoscopique avec des simulations de Monte Carlo, puis de vérifier leur stabilité au niveau gros-grains et d'explorer plus en détail les propriétés locales à cette résolution. Une difficulté sera de contrôler la valeur de la tension de surface de la membrane dans les simulations MARTINI en topologie sphérique. En effet dans ce cas, le seul paramètre de contrôle est le nombre de molécules de solvant encapsulées dans la vésicule, qui fixe la différence de pression à travers la membrane, et donc la tension de surface grâce à la loi de Laplace.

Ainsi, ce travail illustre comment la simulation de vésicules à l'échelle mésoscopique permet d'aborder des questions de pertinence biologique et biophysique, qui ne peuvent être abordées avec des simulations plus raffinées, cependant beaucoup plus exigeantes en ressources, à l'échelle atomique ou moléculaire. Cette thèse est une étape supplémentaire des efforts déployés dans le groupe pour combler le fossé entre expérimentations et modélisation, qui sera sans aucun doute poursuivie dans l'avenir.

Abstract

Plasma membrane forms a selective barrier for the cell, yet its role goes far beyond a simple frontier. Indeed, it plays a crucial role in biological functions such as endo and exocytosis, cell communication or adhesion. It is now widely agreed that membrane lipid and protein spatial repartition is not homogeneous but that these components are organized into nanodomains, which have proven to be key players in the above-mentioned biological functions. Combining statistical physics analytical tools and numerical simulations, we propose in this work a physical mechanism for this membrane organization in a simple model bicomponent vesicle. At the mesoscale, we describe the membrane with a composition-curvature coupling mechanism. We perform extensive Monte Carlo simulations for different membrane parameters (concentration, spontaneous curvature, mixture affinity, surface tension) and study its equilibrium states. We characterize the range of parameters leading to phase modulations by drawing phase diagrams from the simulation results and compare them to the ones previously obtained by analytical field-theoretic techniques. Different observables are computed such as correlation functions and domain size distributions to extract information about the emerging membrane patterns, such as their typical shape, size or spacing. With respect to domain shape, we analyse experimental membrane protein (HIV receptors) trajectories to quantify domain shape and compare it to our simulations. In order to propose a valid rationale for membrane structuring at different scales, we also perform coarse-grained molecular dynamics simulations (MARTINI) of lipid bilayers including curvature-generating components from which we extract the physical membrane parameters that can be plugged into the mesoscale model. We extend our mesoscale model by studying the effect of applied forces to the vesicle, inspired by cell division process during which membrane components reorganize and such forces are at play.

Résumé

La membrane plasmique forme une barrière sélective pour la cellule, mais son rôle va bien au-delà d'une simple frontière. En effet, elle joue un rôle crucial dans les fonctions biologiques telles que l'endo et l'exocytose, la communication cellulaire ou l'adhésion. Il est actuellement largement admis que la répartition spatiale des lipides et des protéines membranaires n'est pas homogène mais que ces composants sont organisés en nanodomaines, qui se sont avérés être des acteurs clés des fonctions biologiques susmentionnées. Combinant des outils analytiques de physique statistique et des simulations numériques, nous proposons dans ce travail un mécanisme physique pour cette organisation membranaire dans un modèle simple de vésicule biphasique. À l'échelle mésoscopique, nous décrivons la membrane avec un mécanisme de couplage composition-courbure. Nous réalisons des simulations Monte Carlo extensives pour différents paramètres de la membrane (concentration, courbure spontanée, affinité du mélange, tension de surface) et étudions ses états d'équilibre. Nous caractérisons la gamme de paramètres conduisant à des modulations de phases en dressant des diagrammes de phases à partir des résultats numériques et les comparons à ceux obtenus précédemment par les techniques analytiques de la théorie des champs. Différentes observables sont mesurées telles que les fonctions de corrélation et les distributions de taille de domaines pour extraire des informations sur les structures membranaires émergentes, telles que leur forme, leur taille ou leur espacement typique. En ce qui concerne la forme des domaines, nous analysons les trajectoires expérimentales de protéines membranaires (récepteurs au VIH) pour quantifier la forme des domaines et la comparer à nos simulations. Afin de proposer un mécanisme pour la structuration de la membrane pertinent à différents échelles, nous effectuons également des simulations de dynamique moléculaire gros-grains (MARTINI) de bicouches lipidiques, incluant des composants générateurs de courbure, à partir desquelles nous extrayons les paramètres physiques membranaires qui peuvent être injectés dans le modèle mésoscopique. Nous étendons notre modèle mésoscopique en étudiant l'effet de forces appliquées à la vésicule, inspirés par le processus de division cellulaire au cours duquel les composants de la membrane se réorganisent et de telles forces sont en jeu.